Alma mater studiorum - Università di Bologna

Dottorato di ricerca in astrofisica

Ciclo XXXIV

Study of new particle acceleration mechanisms in galaxy clusters through low frequency radio observations

Presentata da: **Nadia Biava**

Supervisore:
Prof.ssa Annalisa Bonafede

Co-supervisore:
Dott. Marisa Brienza

Coordinatore di Dottorato:
Prof. Andrea Miglio

Esame finale anno 2022

Settore Concorsuale: 02/C1 - Astronomia, Astrofisica, Fisica della Terra e dei Pianeti

Settore Scientifico Disciplinare: FIS/05 - Astronomia e Astrofisica

Abstract

Diffuse radio emission in galaxy clusters has been observed with different size and properties. Giant radio halos (RH), Mpc-size sources found in merging clusters, and mini halos (MH), $\sim 0.1 - 0.5$ Mpc size sources located in relaxed cool-core clusters, are thought to be distinct classes of objects with different formation mechanisms. In the recent years, radio observations with the LOw Frequency ARray (LOFAR) are revealing the unexpected presence of emission on Mpc-scales in relaxed clusters that host a central MH and show no signs of major mergers. The study of these sources is still at the beginning and it is not yet clear what could be the origin of their unusual emission.

The main goal of this thesis is to test the occurrence of these peculiar sources and investigate their properties using low frequency radio observations. This thesis consists in the study of a sample of 12 cool-core galaxy clusters which present some level of dynamical disturbances on large-scale. The heterogeneity of sources in the sample allowed me to investigate under which conditions a halo-type emission is present in MH clusters; and also to study the connection between AGN bubbles and the local environment. Using high sensitivity LOFAR observations, I have detected large-scale emission in four non-merging clusters, in addition to the central MH. Combining LOFAR data with follow-up observations, I have performed detailed analysis of the most interesting sources. I have constrained for the first time the spectral properties of diffuse emission in these double radio component galaxy clusters. I have investigated the connection between thermal and non-thermal emission for a better comprehension of the acceleration mechanisms contributing to these sources. Furthermore, I derived upper limits to the halo power for the other clusters in the sample, which could present large-scale diffuse emission under the detection threshold. Finally, I have reconstructed the duty-cycle of one of the most powerful AGN known, located at the centre of a galaxy cluster of the sample. The results achieved in this Thesis evince the extraordinary potential of sensitive low frequency observations for the study of steep-spectrum radio emission in galaxy clusters.

The Thesis is structured as follows:

- In Chapter 1: I provide an overview on galaxy clusters, presenting the physics of the intracluster medium and the properties of the radio sources located at the centre of relaxed galaxy clusters.
- In Chapter 2: I provide technical information on LOFAR, underlying its potential in the domain of galaxy cluster science and presenting data reduction techniques.
- In Chapter 3: I present the sample of cool-core clusters studied in this Thesis and

the results based on LOFAR HBA observations. We detect a double component diffuse radio emission in four clusters. For the other clusters we provide upper limits to the halo power.

- In Chapter 4: I illustrate the detailed analysis performed on the cool-core cluster RX J1720.1+2638, which hosts a double component radio emission. We found the two components have different natures. We estimate for the first time the spectral index of the large-scale diffuse emission and test the minor merger scenario.

- In Chapter 5: I report the results based on radio and X-ray analysis of the clusters A1068 and MS 1455.0+2232. Both the clusters present a double radio component, but only A1068 shows a clear steepening of the spectral index outside the cluster core.

- In Chapter 6: I focused on the radio source at the centre of the cluster MS 0735.6+7421, performing spectral index analysis and reconstructing the duty cycle of the central AGN. The results are then compared with timescales derived from X-ray analysis.

- In the Thesis conclusions I summarise the highlights of this Thesis and discuss future developments.

Throughout the Thesis we use the convention $S \propto \nu^{-\alpha}$ for radio synchrotron spectrum and we adopt a ΛCDM cosmological model with $\Omega_\Lambda = 0.7$, $\Omega_m = 0.3$ and $H_0 = 70$ km s^{-1} Mpc^{-1}.

Part of the results obtained during the PhD project are reported in the following papers:

- **The ultra-steep diffuse radio emission observed in the cool-core cluster RX J1720.1+2638 with LOFAR at 54 MHz**
  Biava N., de Gasperin F., Bonafede A. , Edler H. W. , Giacintucci S., Mazzotta P. , Brunetti G. , Botteon A., Brüggen M., Cassano R. , Drabent A. , Edge A. C. , Enßlin T. , Gastaldello F., Riseley C. J. , Rossetti M. , Rottgering H. J. A. , Shimwell T. W. , Tasse C. , van Weeren R. J.
  2021, MNRAS, 508, 3995

- **Constraining the AGN duty cycle in the cool-core cluster MS 0735.6+7421 with LOFAR data**
  Biava N., Brienza M., Bonafede A., Gitti M., Bonnassieux E., Harwood J., Edge A.C., Riseley C.J., Vantyghem A.
  2021, A&A, 650, A170

- **A MeerKAT-meets-LOFAR Study of MS 1455.0+2232: A 590 kiloparsec 'Mini'-Halo in a Sloshing Cool-Core Cluster**
  C. J. Riseley, K. Rajpurohit, F. Loi, A. Botteon, R. Timmerman, **N. Biava**, A. Bonafede, E. Bonnassieux, G. Brunetti, T. Enßlin, G. Di Gennaro, A. Ignesti, T. Shimwell, C. Stuardi, T. Vernstrom, R. J. van Weeren
  2021, MNRAS, 512, 4210

Contents

1 Galaxy clusters **1**
- 1.1 X-ray radiation from clusters of galaxies . . . 3
  - 1.1.1 Cool-core clusters and AGN feedback . . . 5
- 1.2 Radio observations of galaxy clusters . . . 7
  - 1.2.1 Radio galaxies . . . 7
    - 1.2.1.1 Plasma radiative age . . . 7
  - 1.2.2 Diffuse radio emission . . . 11
    - 1.2.2.1 Giant radio halos . . . 11
    - 1.2.2.2 Mini halos . . . 13

2 The LOw Frequency ARray **15**
- 2.1 Stations . . . 15
- 2.2 Surveys . . . 18
- 2.3 Impact on galaxy cluster studies . . . 19
- 2.4 Data reduction . . . 20
  - 2.4.1 LBA data . . . 21
  - 2.4.2 HBA data . . . 22

3 Searching large-scale diffuse emission in cool-core clusters with LOFAR **23**
- 3.1 The sample . . . 23
- 3.2 Radio observations . . . 24
- 3.3 Results . . . 26
  - 3.3.1 Morphology . . . 26
  - 3.3.2 Radial profiles . . . 41
  - 3.3.3 Spectral index distribution . . . 43
  - 3.3.4 Radio power and upper-limits . . . 48
- 3.4 Discussion . . . 50
  - 3.4.1 Radio morphology . . . 50
  - 3.4.2 Morphological parameters . . . 51
- 3.5 Conclusions . . . 53

4 RX J1720.1+2638 **55**
- 4.1 Introduction . . . 55
- 4.2 Radio observations . . . 56
- 4.3 Results . . . 58
  - 4.3.1 Morphology . . . 58
  - 4.3.2 Spectral analysis . . . 58
- 4.4 Radio and X-ray comparison . . . 61

4.4.1 X-ray and radio surface brightness correlation . . . 62
4.4.2 X-ray surface brightness vs spectral index . . . 66
4.5 Discussion . . . 67
4.5.1 Central emission . . . 68
4.5.2 Diffuse emission outside the cluster core . . . 68
4.6 Conclusions . . . 70

5 A1068 & MS 1455.0+2232 71
5.1 Introduction . . . 71
5.2 Data . . . 72
5.2.1 Radio data . . . 72
5.2.2 X-ray data . . . 73
5.3 Results . . . 74
5.3.1 A1068 . . . 74
5.3.1.1 Radio morphology . . . 74
5.3.1.2 Radio spectral study . . . 74
5.3.1.3 X-ray features . . . 76
5.3.2 MS 1455.0+2232 . . . 78
5.3.2.1 Radio morphology . . . 78
5.3.2.2 Radio spectral study . . . 80
5.3.2.3 X-ray properties . . . 81
5.3.3 Radio and X-ray comparison . . . 81
5.3.3.1 Point-to-Point Correlation: Surface Brightness . . . 81
5.3.3.2 Point-to-Point Correlation: Spectral Index . . . 84
5.4 Discussion . . . 86
5.5 Conclusions . . . 87

6 MS 0735.6+7421 89
6.1 Introduction . . . 89
6.2 Data . . . 91
6.2.1 LOFAR observation . . . 91
6.2.2 VLA observations and data reduction . . . 92
6.2.3 GMRT observations and data reduction . . . 93
6.2.4 X-ray observations . . . 94
6.3 Results . . . 94
6.3.1 Radio morphology . . . 94
6.3.2 X-ray features . . . 98
6.3.3 Radio spectral study . . . 100
6.3.3.1 Spectral index maps . . . 102
6.3.4 Central emission . . . 102
6.3.5 Radiative age . . . 104
6.3.6 Correction for adiabatic losses . . . 110
6.4 Discussion . . . 111
6.4.1 Spectral ages and duty cycle . . . 112
6.4.2 Comparison with X-ray estimates . . . 113
6.4.3 Energetics . . . 114
6.5 Conclusions . . . 116

Thesis conclusions 120

Bibliography 130

Chapter 1

Galaxy clusters

Galaxy clusters are the largest gravitationally bound objects in the Universe, with typical total masses of the order of 10^{15} $M_{\odot}$ and linear sizes of a few Mpc, hosting hundreds to thousands of galaxies. The galaxies determine the optical appearance of a cluster, but they contribute to only a small fraction ($\sim$ 5%) of its total mass. The space in-between the galaxies is filled with a hot ($T \sim 10^7 - 10^8$ K) and rarefied gas (electron density $n_e \sim 10^{-3}\mathrm{cm}^{-3}$), the intracluster medium (ICM), which emits in the X-ray band through bremsstrahlung radiation (e.g. Mitchell et al., 1976; Serlemitsos et al., 1977; Forman & Jones, 1982). Radio observations of galaxy clusters reveal diffuse synchrotron emission, indicating the presence of relativistic particles and magnetic fields in the ICM. Galaxy clusters can also host active galactic nuclei (AGNs) that emit particles in two relativistic jets over large distances. These particles spiral along magnetic field lines emitting synchrotron radiation visible in the radio band. A composite image of the galaxy cluster Abell 2744 (Pearce et al., 2017) is shown in Fig. 1.1, illustrating all these different components. The ICM contains more baryons than the stars seen in the member galaxies and constitutes $\sim$ 15% of the total mass of a cluster, which is dominated for the $\sim$ 80% by dark matter (e.g., Blumenthal et al., 1984; White & Fabian, 1995; Jones & Forman, 1999; Arnaud & Evrard, 1999; Sanderson et al., 2003; Vikhlinin et al., 2006)

In the current paradigm of structure formation, galaxy clusters are thought to form by the hierarchical assembly of smaller structures in the gravitational field dominated by dark matter (e.g. Peebles & Yu, 1970; Press & Schechter, 1974). Cluster mergers are very energetic events, releasing energies up to $\sim 10^{64}$ erg on a few Gyr timescale. This energy is dissipated through shocks and turbulence in the ICM, which are expected to accelerate cosmic rays (CRs) to relativistic energies and may amplify cluster's magnetic fields (e.g., Markevitch & Vikhlinin, 2007).

Spectroscopic observations show that cluster members move with a typical velocity dispersion $\sigma_v \sim 10^3$ km s^{-1} (e.g., Ruel et al., 2014). The typical crossing time, t_{cross}, in a cluster of size R is thus:

$$t_{\mathrm{cross}} = \frac{R}{\sigma_v} \simeq \left(\frac{R}{1\mathrm{Mpc}}\right)\left(\frac{10^3 \text{ km s}^{-1}}{\sigma_v}\right) \text{ Gyr}. \tag{1.1}$$

This implies that in a Hubble time ($\sim$ 13.7 Gyr), the system has enough time to reach a dynamical equilibrium in its centre while its outskirts are still affected by the accretion physics (e.g., Walker et al., 2019, for a review). Clusters can then be divided in relaxed (undisturbed) or merging (disturbed) systems, depending on their dynamical state. As it traces the ICM distribution, the X-ray morphology of a galaxy cluster is indicative of its dynamical state (e.g., Rossetti et al., 2016; Lovisari et al., 2017). Relaxed clusters show a smooth and regular brightness distribution peaked at the centre, while disturbed

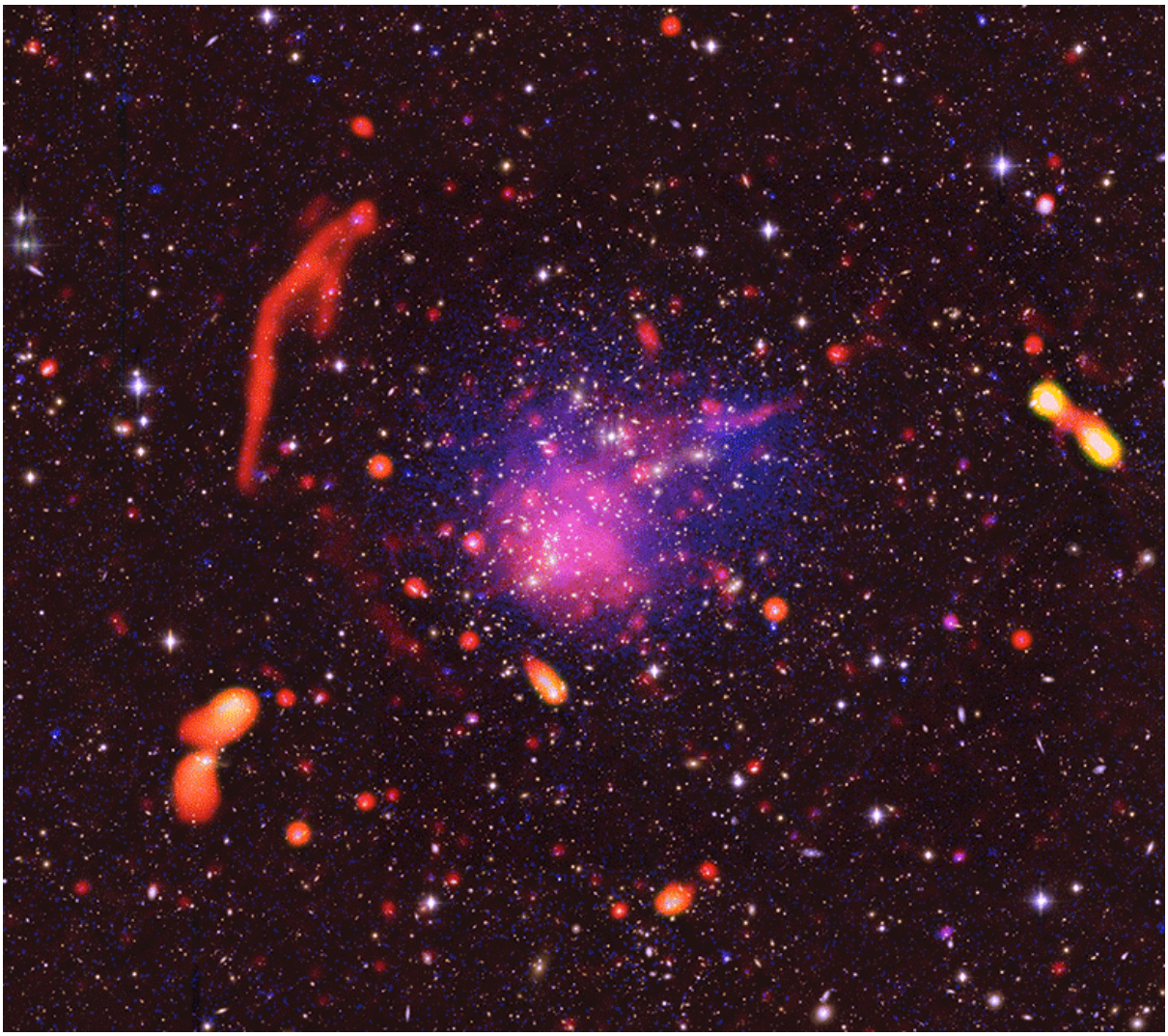

Figure 1.1: Composite image of the galaxy cluster Abell 2744, combining in white optical emission from star and galaxies, observed with the VLT and Subaru Telescopes, in blue X-ray emission from the ICM, observed with the *Chandra* satellite and in red synchrotron radio emission from cosmic rays and radio galaxies, observed with the Jansky Very Large Array. Credits: Pearce et al. (2017); Bill Saxton, NRAO/AUI/NSF; *Chandra*, Subaru; ESO

clusters have an irregular morphology, often showing an elongation along one axis and a number of sub-structures.

Under the assumption of dynamical equilibrium, it is possible to estimate the cluster virial mass:

$$M_{\rm vir} \simeq \frac{R_{\rm vir}\sigma_v^2}{G} \simeq \left(\frac{R}{1{\rm Mpc}}\right)\left(\frac{\sigma_v}{10^3 \text{ km s}^{-1}}\right)^2 \times 10^{15} \text{ M}_\odot \tag{1.2}$$

where G is the gravitational constant and $R_{\rm vir}$ is the virial radius. Otherwise, assuming spherical symmetry and hydrostatic equilibrium of the ICM in the cluster gravitational potential, it is possible to derive the cluster mass inside a given radius:

$$M(r) = -\frac{kT(r)r}{\mu m_p G}\left(\frac{d\log T(r)}{d\log r} + \frac{d\log \rho(r)}{d\log r}\right) \tag{1.3}$$

where k is the Boltzmann constant, μ is the mean molecular mass of the considered gas (typically $\mu = 0.6$ for the ICM), m_p is the proton mass, and the density $\rho(r)$ and temperature $T(r)$ profiles can be inferred from X-ray observations (e.g., Ettori et al., 2013, for a review). Typical scales used to estimate the cluster mass are R_{500} and R_{200}, defined as the radius within which the mean gas density is 500 and 200 times the critical density of the Universe, respectively. These methods are best used in relaxed systems, as they lead to large errors in the determination of the mass of merging clusters, where the system deviates from hydrostatical equilibrium and spherical symmetry (e.g., Rasia et al., 2006, 2012; Meneghetti et al., 2010).

1.1 X-ray radiation from clusters of galaxies

The X-ray emission coming from clusters of galaxies is spatially extended, so it does not originate in individual galaxies. The characteristic luminosity for the most massive clusters is $L_{\rm X} \sim 10^{43}-10^{45}$ erg s^{-1}. The radiation is produced by thermal bremsstrahlung (free–free radiation) from the hot gas which permeates the space between galaxies. Its emissivity is described by:

$$\epsilon_\nu \simeq Z^2 n_{\rm e} n_{\rm i} (kT)^{-1/2} g_{\rm ff} e^{h\nu/kT} \tag{1.4}$$

where Z is the charge of ions, $n_{\rm e}$ and $n_{\rm i}$ are the number density of electrons and ions, respectively and $g_{\rm ff}$ is the Gaunt factor, a slowly varying function of frequency and temperature (Sarazin, 1986). At low temperatures ($kT \leq 2$ keV) the X-ray emission of clusters becomes dominated by line emission from highly ionised atoms and it can be used to measure abundances of heavy elements and the cluster redshift. Temperature and density of the ICM can be determined from X-ray spectral analysis. Given the weak dependence of the ICM emission on the temperature, as a first approximation it can be assumed spatially constant ($T(r) = T$). Thus, under the assumption of isothermal distribution of gas in hydrostatic equilibrium within the potential well associated with a King profile (King, 1972), the gas density profile can be well described by the so-called β-model (Cavaliere & Fusco-Femiano, 1976, 1978):

$$n(r) = n_0\left[1 + \left(\frac{r}{r_{\rm c}}\right)^2\right]^{-3\beta/2} \tag{1.5}$$

where n_0 is the central number density and $r_{\rm c}$ is the core radius of the cluster. The β parameter comes from the ratio of the dynamical temperature, and the gas temperature ($\beta = \mu m_{\rm p}\sigma_{\rm v}^2/kT$). The surface brightness profile of the X-ray emission in this model is:

$$S(r) = S_0\left[1 + \left(\frac{r}{r_{\rm c}}\right)^2\right]^{-3\beta+1/2} \tag{1.6}$$

where S_0 is the X-ray surface brightness at the centre of the cluster. This model hence permits to derive the parameters of the density profile by fitting the X-ray profile.

As we will explain in the following section, the central regions of relaxed clusters have a cooling time shorter than the Hubble time, hence they are characterised by a cool-core, i.e. they present a peaked X-ray surface brightness and a drop in temperature in the central region (e.g., Molendi & Pizzolato, 2001; Hudson et al., 2010). Therefore, the X-ray emission of these clusters is inadequately described by the β-model, which produces a centrally flat density profile. Spectrally, cool-core clusters are well approximated by a two-temperature model, where the inner temperature represents the multiphase status of the core and the outer temperature is a measure of the ambient gas temperature. To account for that, their X-ray surface brightness should be modelled by a double β-model (e.g., Hudson et al., 2010; Giacintucci et al., 2017).

A dichotomy exists between cool-core and non cool-core clusters (e.g., Molendi & Pizzolato, 2001), depending whether their central region shows a drop in the temperature profile or not. This drop is due to the strongly peaked X-ray emissivity of relaxed systems that leads to efficient cooling of the gas in this dense environment. Conversely, disturbed systems exhibit shallower X-ray emissivity, hence lower cooling rates. Therefore, the properties of the cluster core are connected to its dynamical state: relaxed systems naturally form a cool-core while non cool-core are typically found in perturbed objects (e.g., Leccardi et al., 2010).

As mentioned before the X-ray morphology of a cluster can be used to classify its dynamical state (Rasia et al., 2013) and discriminate between relaxed or merging systems (Cassano et al., 2010). Various morphological parameters could be used to compute the dynamical state of a system. According to Lovisari et al. (2017) the morphological parameters more sensitive to the dynamical state of a cluster are:

- the concentration parameter, c, defined as the ratio of the X-ray surface brightness within 100 kpc over the X-ray surface brightness within 500 kpc (e.g. Santos et al., 2008):
$$c = \frac{S(r < 100 \text{ kpc})}{S(r < 500 \text{ kpc})}; \tag{1.7}$$
- the centroid shift, w, defined as the standard deviation of the projected separation Δ between the peak and the cluster X-ray centroid computed within N circles of increasing radius R (Böhringer et al., 2010),
$$w = \left[\frac{1}{N-1}\sum(\Delta_i - \langle\Delta\rangle)^2\right]^{1/2} \times \frac{1}{R}. \tag{1.8}$$

Cool-core clusters are characterised by a compact core, i.e. large values of c, and a spherically symmetric distribution of gas, i.e. small values of w. The opposite is the case for merging systems.

Cool-core clusters can be perturbed by minor mergers with a subcluster or a small group, causing the displacement of the gas from the central potential well, without disrupting the dense core. The cool gas then starts sinking towards the minimum of the gravitational potential setting a sloshing mechanism from which cold fronts develop (e.g. Markevitch & Vikhlinin, 2007). Cold fronts are sharp arc-shaped X-ray surface brightness discontinuities characterised by a jump in the temperature, with a lower temperature in the denser internal region and an higher temperature in the more rarefied external region. The pressure across the front, instead, is almost continuous. Sloshing lasts for several Gyr, so the perturbed cluster can appear quite relaxed excepted for the presence of cold fronts.

1.1.1 Cool-core clusters and AGN feedback

In the description of the thermal properties of the ICM presented in the previous section we have considered the simple assumption of hydrostatic equilibrium. In reality, the gas is subject to radiative losses, thus it will lose internal energy and the hydrostatic equilibrium cannot be maintained over arbitrarily long times. The cooling time is described by the following formula:

$$t_{\rm cool} \simeq 8.5 \times 10^{10} \left(\frac{10^{-3}\ {\rm cm}^{-3}}{n_{\rm e}}\right)\left(\frac{T}{10^{8}\ {\rm K}}\right)^{1/2}\ {\rm yr} \tag{1.9}$$

In general $t_{\rm cool}$ is longer than the Hubble time roughly everywhere in the cluster, thus the hydrostatic equilibrium should be established. However, the elevated gas density in the central regions of relaxed clusters can significantly reduce the cooling time, making it shorter than the Hubble time. It is possible to define a cooling radius ($R_{\rm cool}$), the radius at which $t_{\rm cool} \leq 3$ Gyr. Within this radius the cooling becomes so efficient that, in the absence of an external heating source, the mean temperature and pressure decrease dramatically, forming the so-called cool-core. Initially it was proposed that the pressure equilibrium in these systems could be re-established by the creation of a *cooling flow*, i.e. large quantities of gas flowing inwards towards the cluster centre (Fabian, 1994). During this process the gas is compressed by the external pressure and the increase of central density further accelerates the cooling process. The result is an evident decrease of temperature and increase of gas density within $R_{\rm cool}$ (e.g., Hudson et al., 2010), which, from an observational point of view, produces a peaked surface brightness profile.

In cooling flows the central gas is expected to reach temperatures significantly below 1 keV, emitting atomic lines. However, high resolution spectroscopic observations with *Chandra* and *XMM-Newton* X-ray telescopes did not detect such low temperatures. Another expectation of this cooling process is a large mass of cold gas at cluster centre, but no clear evidence has been found for it in optical observations. Furthermore, it is expected that an excess of cold gas should give rise to an enhancement in the star formation rate within the brightest cluster galaxy (BCG). However, the measured star formation rates and molecular gas quantities are an order of magnitude below the expectations (e.g., McNamara & O'Connell, 1989; Edge, 2001; McDonald et al., 2018). These pieces of evidence imply that some source of heating must balance the radiative losses (Peterson et al., 2003; Peterson & Fabian, 2006).

To date, feedback from AGN represents the most promising scenario to balance the cooling (e.g. Fabian, 2012, and references therein). The energy released by accretion of matter onto the central supermassive black hole of an AGN is of the order of $E = \eta M c^2 \sim 2 \times 10^{62}$ erg, for a black hole mass of $M = 10^9$ M$_\odot$ and an efficiency of mass-to-energy conversion of $\eta \sim 10\%$. The principal evidence of the impact of the AGN on the surrounding medium is represented by the detection of X-ray cavities at the centre of relaxed clusters, on scales approximately coincident with the lobes of the central radio galaxy (e.g., McNamara et al., 2000; Fabian, 2012; Hlavacek-Larrondo et al., 2012). The radio emitting plasma released by the central AGN creates a low-density bubble that rises buoyantly and expands, displacing the X-ray emitting gas and distributing energy to the surrounding medium. One of the clearest examples of AGN feedback is represented by the radio galaxy at the centre of the cluster MS 0735.6+7421 (Fig.1.2), studied in detail in Chapter 6.

X-ray cavities allow us to perform first order measurements of the non-radiative energy emitted by the jets. The AGN jets displace the ICM at the cavity location, doing work against the surrounding plasma. The total energy required to create a cavity is equal to

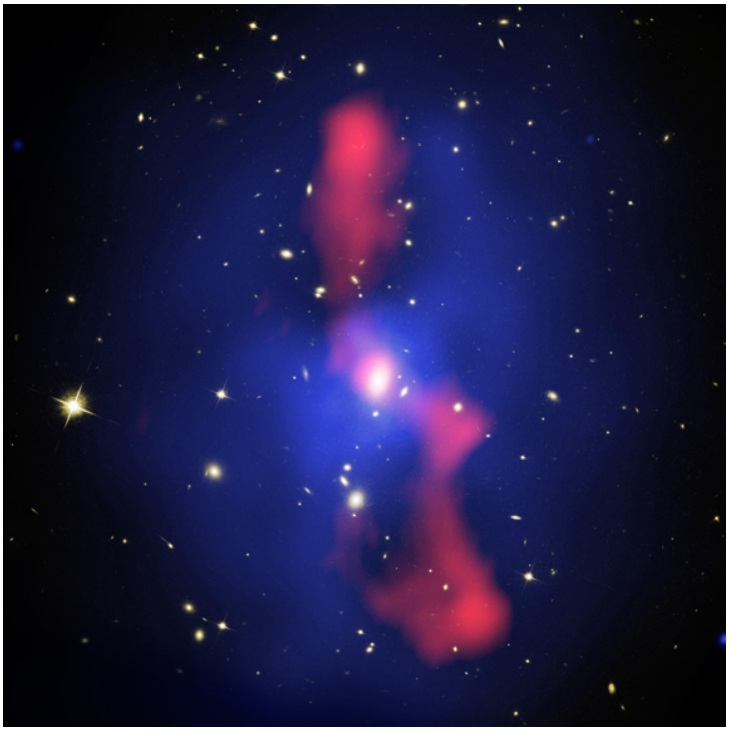

Figure 1.2: Composite image of the galaxy cluster MS 0735.6+7421, combining in white optical data from the Hubble Space Telescope, in blue X-ray data from the *Chandra* satellite and in red radio data from the Very Large Array (McNamara et al., 2009).

its enthalpy:

$$E_{\rm cav} = \frac{\gamma}{\gamma - 1} pV \tag{1.10}$$

where $\gamma = 4/3$ is the ratio of specific heats for a relativistic plasma, p is the pressure of the gas surrounding the cavity and V is the volume of the cavity. The location and size of a cavity can also be used to derive an estimate of its age (e.g., Bîrzan et al., 2004). Three different estimates are proposed in the literature:

- the sound-crossing timescale: the time required by the bubble to reach the cavity location (R) from the cluster centre, assuming it moves at the local sound speed $t_{\rm c_s} = R/v_{\rm c_s}$ (Omma et al., 2004);
- the buoyancy timescale: the time required by the bubble to rise buoyantly at its terminal velocity $v_{\rm t} = (2gV/SC)^{1/2}$, where g is the gravitational acceleration, V is the volume of the bubble, S the cross section and C is the drag coefficient ($C \sim 0.75$, see Churazov et al., 2001);
- the refilling timescale: the time required to refill the cavity volume as the bubble rises upward $t_{\rm refill} = 2R/\sqrt{r/GM(R)}$, where r is the cavity radius (McNamara et al., 2000; Nulsen et al., 2002).

In general, the cavity ages calculated using the sound speed are the shortest, the refilling timescales are the largest, and the buoyancy timescales lie in-between the two. When multiple systems of cavity are present in a single source, their ages could be used to measure the interval between the AGN outbursts. An outburst interval shorter than the cooling time ensures the heating of the surrounding medium. Multiple outbursts of short duration are also required by simulations of galaxy evolution to prevent too much cooling of gas from the galaxy's atmosphere or gas resulting from stellar mass loss (Ciotti et al., 2010, 2017). However, multiple cavity systems have only been observed in a few massive clusters and groups so far (e.g., Fabian et al., 2006; Vantyghem et al., 2014; Ubertosi et al., 2021; Randall et al., 2015), probably due in part to observational limitations.

1.2 Radio observations of galaxy clusters

Galaxy clusters show a large variety of radio sources with different size, morphology and spectral properties, which could either be associated with single galaxies or produced by the non-thermal component of the ICM.

1.2.1 Radio galaxies

Galaxy clusters often host a number of AGNs, called radio-loud, which emit relativistic plasma in two oppositely directed jets. The fast moving electrons spiral in magnetic fields, producing synchrotron emission visible at radio frequencies (De Young, 1984; de Young, 2002; Tadhunter, 2016). The sizes of these sources range from a few kiloparsec up to megaparsec scale, and extend well beyond the host galaxy. In powerful sources the jet inflates large radio lobes and ends in bright hotspots, where the relativistic jets impact with the ICM and the particles are accelerated. These sources are called FRII radio galaxies, according to the Fanaroff & Riley classification (Fanaroff & Riley, 1974). In the less powerful sources ($L_{1.4GHz} \leq 10^{32}$ WHz^{-1}), called FRI radio galaxies, the jets are sub-relativistic, so most of the acceleration takes place in the central regions, near the core. For this reason, these sources are also named edge-darkened (no hotspots). An example of these sources is reported in the upper panels of Fig. 1.3. More recently, the FR0 class (Ghisellini et al., 2011; Sadler et al., 2014; Baldi et al., 2015) has been proposed for those radio sources showing compact emission (<10 kpc), dominant at low redshift. The nuclear and host galaxy properties of these sources are similar to those of FRI radio galaxies, but their origin and possible connection with other classes is still to be understood. Radio galaxies in galaxy clusters and groups often show signs of interaction with the surrounding medium (e.g., Miley, 1980; Burns, 1998). The radio lobes of these radio galaxies are bent due to the relative movement of the lobes with respect to the ICM and the pressure exerted by the external gas, and are usually classified as wide-angle tail (WAT), narrow-angle tail (NAT) or head-tail (HT) radio sources, depending on the opening angle of the two jets. See Fig. 1.3 for various examples of radio galaxies.

Some radio galaxies show multiple radio lobes that are related to different phases of AGN activity (e.g., Schoenmakers et al., 2000; Brocksopp et al., 2007; Hota et al., 2011; Orrù et al., 2015). The spectral properties of the radio plasma can be used to estimate the age of a radio lobe and so to reconstruct the duty cycle of restarted sources, i.e. the fraction of time the AGN is active (e.g., Harwood et al., 2013, 2015; Brienza et al., 2020). This method is complementary to age estimates from X-ray cavities, presented in the previous section.

1.2.1.1 Plasma radiative age

An electron accelerated in a magnetic field emits synchrotron radiation. The power irradiated by the particle is given by the Larmor formula:

$$P_s = \frac{2e^4}{3m^2c^5}\gamma^2 v^2 B^2 \sin^2\theta, \tag{1.11}$$

where $\gamma = E/mc^2$ is the Lorentz factor, e, m, v are the particle charge, mass and velocity, B is the magnetic field and θ, called pitch angle, is the angle that the velocity vector makes with the magnetic field lines.

For a population of electrons, the total emissivity is the convolution of the emission of a single electron with the energy distribution of all particles. If the particle energy distribution is assumed to be a power-law of the form:

$$N(E)dE = N_0 E^{-\delta} dE \tag{1.12}$$

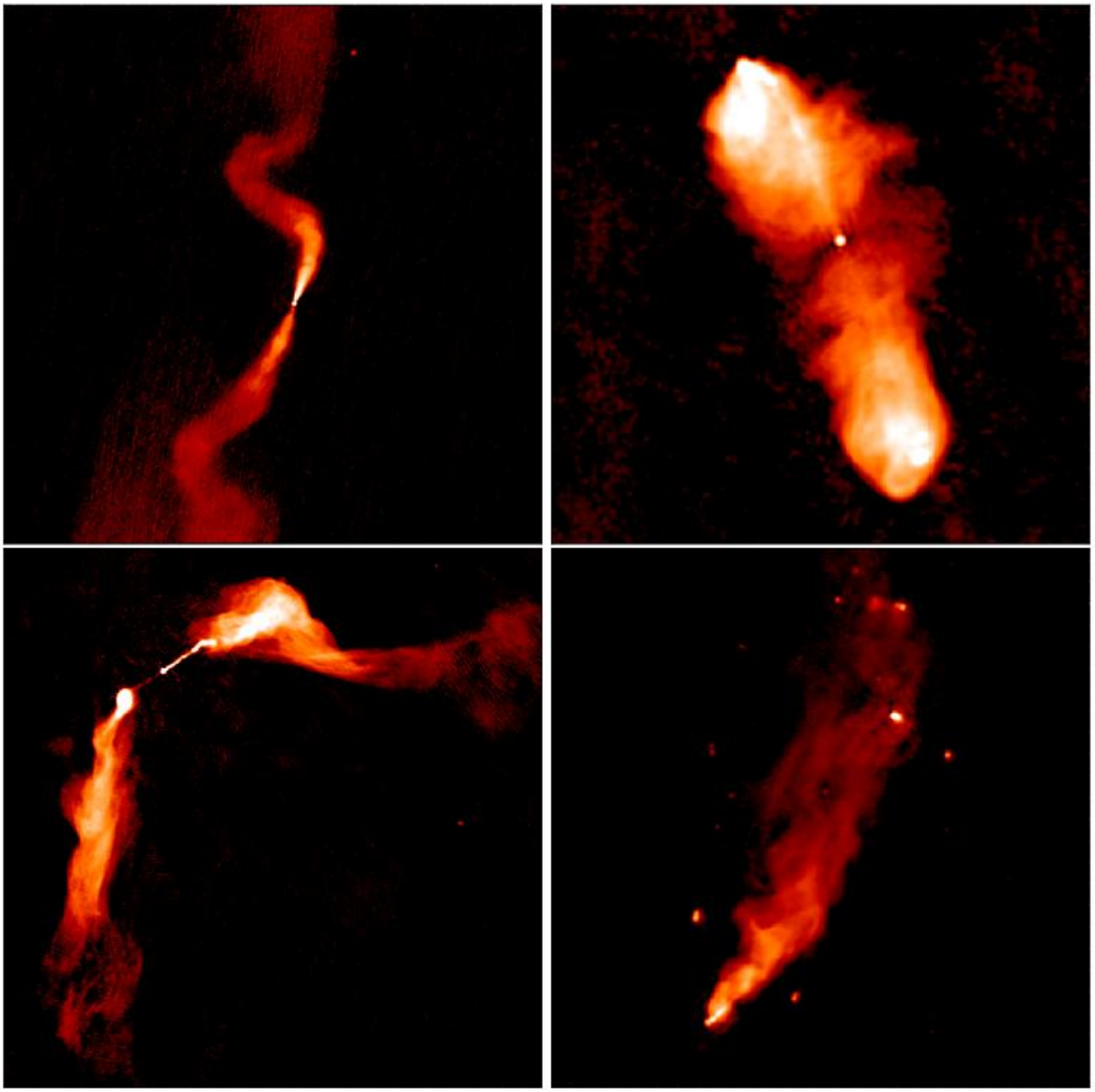

Figure 1.3: Different types of radio galaxies: FRI source 3C 31 (upper left), FRII source 3C 98 (upper right), WAT source 3C 465 (lower left) and HT source NGC 6109 (lower right). Adapted from Hardcastle & Croston (2020).

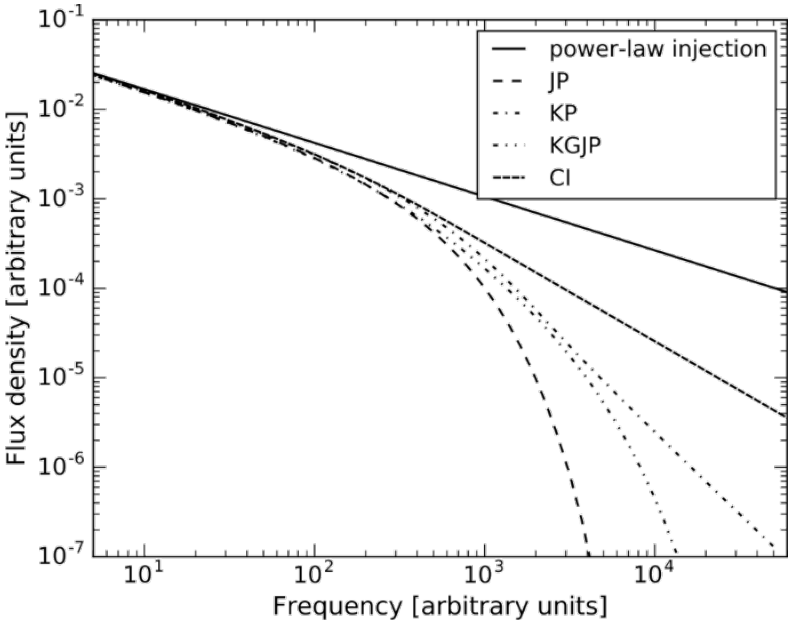

Figure 1.4: Radio spectral shapes of different spectral ageing models. All spectral models have $\alpha_{\rm inj} = 0.6$. The power-law spectrum depicts the spectral shape before any energy losses. From van Weeren et al. (2019)

then the total emissivity per unit frequency is:

$$S(\nu) = \int_{E1}^{E2} P_s(E,\nu) N(E) dE \propto \nu^{-\alpha_{\rm inj}}, \tag{1.13}$$

where the injection spectral index $\alpha_{\rm inj} = (\delta - 1)/2$ has typical values in the range 0.5-0.8 (see e.g. Jaffe & Perola, 1973; Carilli et al., 1991; Komissarov & Gubanov, 1994). Therefore, a power-law energy distribution of electrons produces a power-law spectrum and the two spectral indices are related. Hence the study of the spectra of radio sources gives us information on the energy distribution of the radiating electrons.

As particles radiate, they lose their energy according to $dE/dt \propto 1/E$. So, in absence of further particle acceleration (as could be in a radio lobe), there is a preferential cooling of higher energy electrons. The result is a spectrum which becomes steeper and increasingly curved over time. Therefore, the age of a radio source could be derived by the curvature of its spectrum, according to this formula:

$$t \propto \frac{B^{1/2}}{B^2 + B_{\rm CMB}^2} [\nu_{\rm b}(1+z)]^{1/2} \tag{1.14}$$

where B is the source magnetic field, $B_{\rm CMB} = 3.18(1+z)^2$ is the inverse-Compton (IC) equivalent magnetic field and $\nu_{\rm b}$ is the break frequency. A modern approach consists in fitting the observed radio spectrum with a modelled spectrum, obtained by numerical integration of the equations that describe the radiative losses of a particle population.

There are two main categories of spectral ageing models: the single injection models assume that the electrons are accelerated in a single event, while in the continuous injection models the particles are continuously emitted throughout the lifetime of the source. As the particles age, the radio spectrum steepens and curves at different frequencies according to the various models, as illustrated in Fig.1.4. The JP model (Jaffe & Perola, 1973) and KP model (Kardashev, 1962; Pacholczyk, 1970) are two classical single injection models and consider synchrotron and IC losses in a uniform magnetic field distribution, where the electron population has a fixed pitch angle (in the KP model) or a more realistic scenario with a randomised pitch angle (in the JP model). A third single injection model, the Tribble model (Tribble, 1993) considers a spatially non-uniform magnetic

field by integrating the standard JP losses over a Maxwell–Boltzmann magnetic field distribution. The continuous injection (CI) models, are instead a different class of models, where it is assumed that the source is fuelled constantly by freshly accelerated particles, and are constructed by combining individual JP or KP spectra of particle populations of different ages. The CI model (Pacholczyk, 1970) best describes active sources in which the injection of particles is still ongoing, while the so-called CIOFF or KGJP/KGKP model (Komissarov & Gubanov, 1994) assumes that the particle injection in the source switched off at a certain time. The assumption of a single injection works reasonably well for resolved spectral studies because on small scales, particles can likely be considered as part of a single acceleration event, while the continuous injection models are applicable only to integrated spectra of selected regions, where particles can be considered confined.

However, the proposed models only consider the energy losses due to synchrotron and IC emissions. Another effect that must be considered is the losses due to the adiabatic expansion of the radio lobes in the surrounding medium. The effect of adiabatic losses is to reduce the particle energy and the magnetic field in radio lobes (Scheuer & Williams, 1968), and so to shift the spectra towards lower (or higher) frequencies if there is a single (or continuous) injection of particles, without changing its shape (Kardashev, 1962; Murgia et al., 1999). So, the radiative ages derived from standard models could be corrected for this effect, simply multiplying the associated break frequency for a corrective factor, which depends on the linear expansion factor ($\Delta = r_1/r_0$ for a spherical bubble, where r_0 and r_1 are respectivelly the initial and final radius of the bubble) and the index of variation of the magnetic field (n, where $B(t) = B_0\Delta^{-n}$).

As previously mentioned, the spectral age also depends on the source magnetic field, which is difficult to constrain observationally. For this reason, it is often derived assuming the approximation of energy equipartition (e.g. Brunetti et al., 1997). This assumes that the energy density of the magnetic field is equal to the energy density of particle population (electrons + protons):

$$\begin{aligned} \epsilon_{\rm B} &= \epsilon_{\rm e} + \epsilon_{\rm p} = (1+k)\epsilon_{\rm e} \\ \frac{B^2}{2\mu_0} &= (1+k)\int_{\gamma_{min}}^{\gamma_{max}} N(\gamma)\gamma m_e c^2 \, d\gamma \end{aligned} \tag{1.15}$$

where B is the magnetic field, k is the ion to electron density energy ratio, and $N(\gamma)$ is the initial electron energy distribution, assumed to be a power-law. The value of k is typically assumed equal to 1, implying that energy is equally divided between electrons and ions. When direct measures of the magnetic field strength were possible, it has been shown that the typical values are a factor 2-3 below the equipartition values (Croston et al., 2005; Kataoka & Stawarz, 2005; Migliori et al., 2007; Ineson et al., 2017; Turner et al., 2018), suggesting the radio lobes contain higher electron energy densities than assumed by equipartition.

When both radio and X-ray observations are available, a comparison between synchrotron ages and cavity ages can be made. Bîrzan et al. (2008) found that the synchrotron and buoyancy ages are weakly consistent and computed that if the synchrotron ages would represent the true ages, the bubbles would be moving with a speed of $\sim 4-20$ times higher than the buoyancy speed, i.e. supersonically. As a result, in these systems we would expect to see shocks driven by the expanding bubbles. In fact, in some systems shocks have been discovered (e.g., McNamara & Nulsen, 2007; Vantyghem et al., 2014). However, this kind of investigation (radiative vs cavity age) remains limited and more studies are needed to put firmer constrains.

1.2.2 Diffuse radio emission

Diffuse radio emission, not directly associated with cluster member galaxies, indicates the presence of a non-thermal component of cosmic rays in the ICM, which emit synchrotron radiation in the presence of μG magnetic fields. This emission is classified as radio relics, giant radio halos or mini halos (van Weeren et al., 2019, for a review). Radio relics are located at the periphery of the cluster possibly tracing particles that are (re-)accelerated by shock waves. Radio halos and mini halos instead are diffuse sources located at the cluster centre. In this Thesis I focused mainly on mini halos and giant radio halos (Fig. 1.5), which I will further discuss in the next sections.

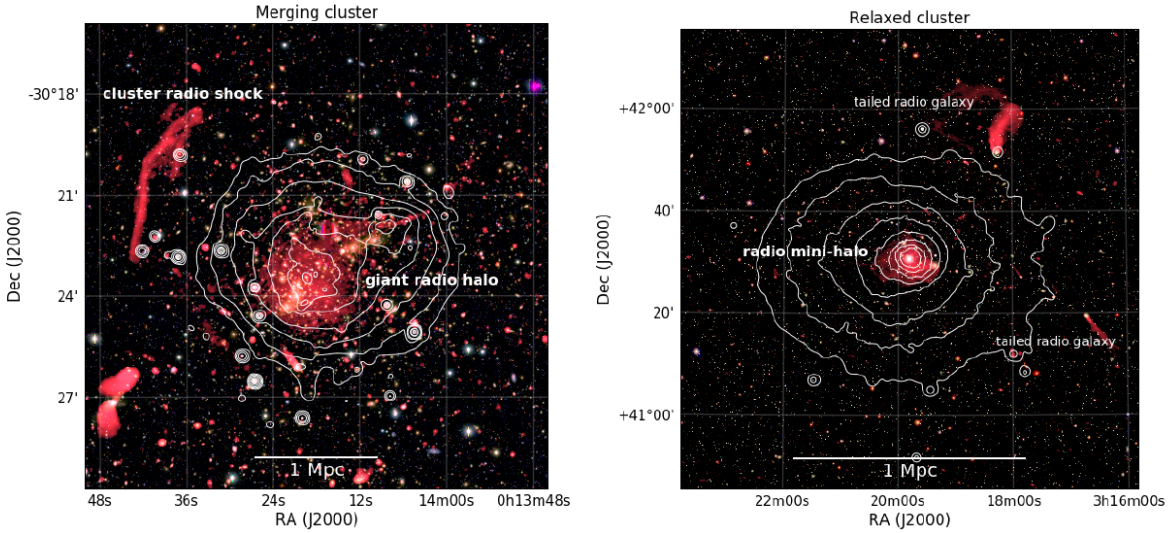

Figure 1.5: Diffuse radio emission in galaxy clusters. Giant radio halo at the centre of the merging cluster Abell 2744 (left) and mini halo at the centre of the relaxed cool-core Perseus cluster (right). X-ray contours are shown in white. From van Weeren et al. (2019).

1.2.2.1 Giant radio halos

Giant radio halos (RHs) are Mpc-size sources mostly found in massive, dynamically disturbed clusters. Their radio morphology is typically smooth and regular, approximately following the distribution of the thermal ICM. This is quantitatively confirmed by the detection of a sub/nearly-linear spatial correlation between the radio and the X-ray surface brightness, obtained through point-to-point analysis (Govoni et al., 2001; Botteon et al., 2020b; Rajpurohit et al., 2021a,b). RHs present integrated spectral indices in the range $1.1 \leq \alpha \leq 1.4$ (e.g., Giovannini et al., 2009). Spectral coverage with more than two frequencies is rare to obtain, so deviations from power-law spectra are difficult to investigate (Rajpurohit et al., 2021a, e.g.,). A spectral steepening is observed in the Coma cluster at frequencies higher than 1 GHz (Thierbach et al., 2003). Some halos instead present an ultra-steep spectrum, with a spectral index up to $\alpha \sim 2$ (e.g. Abell 521, Brunetti et al., 2008; Dallacasa et al., 2009). These are called ultra-steep spectrum radio halos (USSRHs). The existence of USSRHs is expected if the integrated spectra of radio halos present a cutoff, as a measure of the spectral index at frequency higher than the cutoff frequency will be very steep.

RHs are not ubiquitous in clusters: only 30% of the X-ray luminous clusters ($L_X \geq 5 \times 10^{44}$ ergs^{-1}) host a RH (Venturi et al., 2007, 2008). Cuciti et al. (2015) found the occurrence fraction of RHs depends on the cluster mass: 60-80% of RH detected in massive clusters ($M_{500} \geq 8 \times 10^{14}$ M$_\odot$) against 20-30% in clusters below this mass. Clusters with

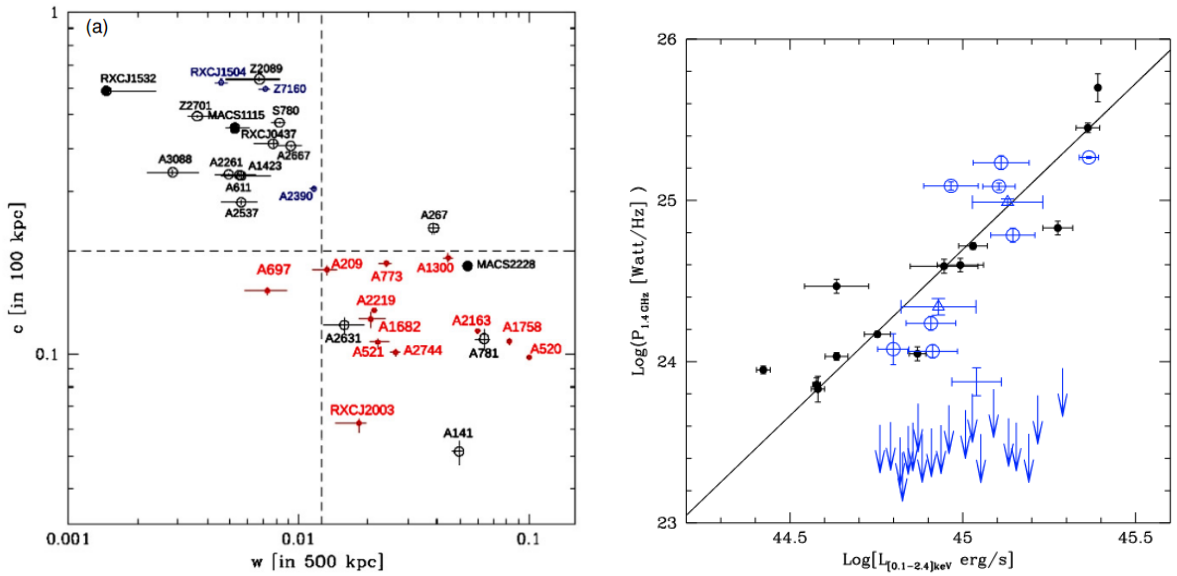

Figure 1.6: *Left panel:* Concentration parameter c vs. centroid shift w from Cassano et al. (2010). With different symbols are represented: giant radio halos (red filled dots), clusters without radio halos (black open dots), mini halos (blue open dots). *Right panel:* $P_{1.4}$ vs $L_{0.1-2.4keV}$ from Brunetti et al. (2009).

and without radio halos can be distinguished also according to their dynamical status, typically inferred from the cluster's X-ray morphology (Cassano et al., 2010). Almost all giant radio halos are found in dynamically disturbed clusters and clusters with RHs can be well separated from clusters without RHs and clusters with mini halos (Fig.1.6, left panel). The radio halo power correlates with the cluster X-ray luminosity (e.g., Brunetti et al., 2009; Cassano et al., 2013) and the cluster mass (Cassano et al., 2013; Cuciti et al., 2021; van Weeren et al., 2021), while the upper limits to the radio power of clusters with no detected RHs lie below the correlations (Fig.1.6, right panel). This bi-modality could be interpreted as due to two populations of clusters at different evolutionary stages (Brunetti et al., 2007, 2009). Merging clusters host RHs and follow the correlation, when clusters become dynamically relaxed, the RH synchrotron emission is gradually suppressed and clusters populate the region of the upper limits.

RH emission is suggested to originate from electrons re-accelerated by turbulence injected in the ICM during major merger events (Brunetti et al., 2001; Petrosian, 2001). As direct acceleration of CRe from the thermal ICM is a very inefficient mechanism (e.g., Petrosian & Bykov, 2008; Brunetti & Jones, 2014, for reviews), a population of seed electrons, mildly energetic particles present in the ICM, which are then re-accelerated, is required. CRe undergo radiative losses, due to synchrotron and IC emission, which prevent to reach Mpc-scale distances through slow diffusion, unless they are continuously generated or accelerated "in situ" throughout the radio halo volume (Jaffe, 1977). These particles may be injected in the ICM by AGN activity, supernovae, galactic winds or be generated by proton-proton interactions. Alternatively, it has been proposed that the electrons responsible of RH emission are produced in the hadronic interaction between CR protons and ICM protons (Dennison, 1980; Blasi & Colafrancesco, 1999). However, the non-detection of γ-rays in the Coma cluster, seem to disfavour this scenario (Brunetti et al., 2012, 2017). Therefore, the re-acceleration of electrons is the most promising explanation to date.

1.2.2.2 Mini halos

Mini halos (MHs) are diffuse radio sources with size typically $\leq 0.2\ R_{500} \approx 100 - 500$ kpc (Giacintucci et al., 2017, 2019), surrounding the central radio source associated to the brightest cluster galaxy. MHs are common in relaxed clusters with a cool-core: 80% of cool-core clusters with $M_{500} \geq 6 \times 10^{14}\ M_{\odot}$ host a mini halo (Giacintucci et al., 2017), while no mini halos are found in non cool-core systems. This suggests that cluster mergers do not play a major role in their origin. However, larger samples are required to obtain better statistics and confirm these results. A point-to-point radio and X-ray surface brightness correlation is observed also in MHs. Contrary to RHs, they show a super-linear behaviour, indicating a concentration of the ICM non-thermal component around the central AGN (Ignesti et al., 2020).

Although smaller than RHs, MHs also require in-situ acceleration given the short lifetime of synchrotron emitting electrons. The radio emission from MH does therefore not directly originate from the central AGN, which however could be the source of seed electrons. Similar to RHs, two possible scenarios have been proposed to explain the origin of MHs: the hadronic and the turbulent re-acceleration models. The hadronic model suggests that MHs are formed by the continuous injection of secondary electrons in the central regions by inelastic collisions of cosmic-ray protons with the cluster thermal proton population (Pfrommer & Enßlin, 2004). The decay chain for the injection of secondary particles also produces γ-rays. Accordingly, γ-rays emission is expected in galaxy clusters. However, γ-ray upper limits from the *Fermi* satellite and ground based Cherenkov telescopes are not yet deep enough to put strong constraints on the hadronic origin of MHs.

Another possibility is the re-acceleration of seed electrons in cluster cores by turbulence. Unlike giant radio halos, where the turbulence is induced by major cluster mergers, mini halos would trace turbulence in the cluster cores generated by gas sloshing in response to a gravitational perturbation by a minor/off-axis merger (ZuHone et al., 2013, 2015). The confinement of most of the MHs by spiral-shaped X-ray cold fronts supports this scenario (Mazzotta & Giacintucci, 2008).

One possibility to discriminate between the two models is to look for differences in the integrated spectrum and spectral index maps. The hadronic model predicts a rather uniform spectrum with $\alpha \sim 1$, while evidence for very steep spectra and/or for the presence of spectral breaks at high frequencies would favour a re-acceleration scenario (ZuHone et al., 2013, 2015). However, current MH observations cover a small frequency range that does not permit to constrain their spectral curvature. Furthermore, the separation between the contribution of the central AGN lobes and MH can be difficult, making good spectral measurements more challenging than in the case of giant radio halos.

Giant radio halos and mini halos have been considered since their discovery to be two different classes of sources. However, recent observations of radio emission with hybrid properties suggest RHs and MHs could be physically related to each other. For example, cluster merger events could transport CRe from cluster cores to larger scales, where they are re-accelerated again (see e.g., Brunetti & Jones, 2014). Therefore, mini halos could evolve into giant radio halos and vice-versa. Bonafede et al. (2014) discovered a radio halo with size 1.1 Mpc in the strong cool-core cluster CL1821+643. If this emission is caused by a merger event, the cluster is in a stage where the merger has not yet been able to disrupt the cool-core. Similarly, radio halos with scales of 0.8-1.0 Mpc are observed in the semi-relaxed clusters Abell 2261, RXCJ0232.2–4420 and SPT-CL J2031-4037 (Sommer et al., 2017; Savini et al., 2019; Kale et al., 2019; Raja et al., 2020), questioning the assumption that giant radio halos only occur in clusters

undergoing major mergers. Another peculiar case is the sloshing, minor-merger cluster Abell 2142, which presents a 2 Mpc radio halo with a double component (Farnsworth et al., 2013; Venturi et al., 2017). The inner component has a higher surface brightness, with properties similar to that of a mini halo. The outer larger component has a steeper spectrum. They proposed that the inner component is powered by gas sloshing, while the outer component might be re-accelerated by turbulence induced by a less energetic merger event. Alternatively, the different components are the result from a transition between hadronic and turbulent re-acceleration processes.

With the advent of the Low Frequency ARray (LOFAR, van Haarlem et al., 2013), two other cool-core clusters with steep-spectrum emission extending beyond the cool-core region were discovered (PSZ1 G139.61+24.20 and RX J1720.1+2638, Savini et al., 2018, 2019). In order to explain these sources, the authors have proposed that minor/off-axis mergers could accelerate particles on Mpc-scales, without disrupting the cool-core. In that case, both a giant radio halo and a mini halo could co-exist. As minor mergers are less energetic than the major ones, the diffuse emission on large scale should have a steep spectrum, with $\alpha \geq 1.5$ (Cassano et al., 2006; Brunetti et al., 2008; Cassano et al., 2012; Brunetti & Jones, 2014). However, due to observational limitations it has to-date been impossible to calculate the spectral index of the halo-like emission – it has only been possible to place limits. The study of this new type of sources could help to shed light on the origin of both giant radio halos and mini halos.

Chapter 2

The LOw Frequency ARray

The LOw-Frequency ARray (LOFAR, van Haarlem et al., 2013), is a new generation radio interferometer operated by ASTRON centred in the Netherlands and with stations distributed all around Europe. Using a new design, LOFAR covers the relatively unexplored low-frequency range from 10−240 MHz (corresponding to wavelengths of 30−1.2 m) and provides unique observing capabilities. LOFAR reaches sub-arcsecond resolution, thanks to the long interferometric baselines, while the dense core array, allows to recover, at the same time, very extended emission in the sky (Largest angular scale, LAS = 0.5 degrees). The effectively all-sky coverage of the dipoles gives LOFAR a large field-of-view (FoV), essential for surveys. This makes LOFAR a powerful instrument in many fields of astrophysics. Six Key Science Projects (KSP) determined the design, development and construction of LOFAR during its initial phase. Among these there is the Surveys KSP, whose aim is to conduct wide and deep surveys of the northern sky. This project involves a broad range of astrophysics topics such as: study the formation of massive galaxies, clusters and black holes, the non thermal emission and magnetic fields in galaxy clusters, star formation processes in the early Universe and exploring new parameter space for serendipitous discovery. More details on the LOFAR Surveys will be given in Section 2.2.

2.1 Stations

Currently, LOFAR comprises 52 individual stations distributed mainly in the northern countries of Europe (Fig. 2.1). Most of the stations are placed in the Netherlands (38 stations). 24 of these stations are concentrated in an area of 2 km, constituting the Core Stations (CS). Their distribution is optimised to achieve good instantaneous *uv*-coverage required by many of the KSPs. At the centre of the core, a 320m diameter region referred to as "the Superterp" contains 6 Core Stations, which provide the shortest baselines in the array. The remaining 14 stations in the Netherlands, called Remote Stations (RS), are approximately arranged in a logarithmic spiral distribution over an area roughly 180 km in diameter. Other 14 stations, named as International Stations (IS), are located between Germany (six stations), Poland (three stations), France, Ireland, Latvia, Sweden, and the United Kingdom (one station each). A station in Italy is also planned as part of the LOFAR2.0 upgrade, which will occur in the coming years.

LOFAR consists of an interferometric array of dipole antenna stations, which have no moving parts. Pointing and tracking are then achieved by combining signals from individual antennas to form a phased array. This allows for rapid re-pointing of the telescope and offers also the possibility to performed multiple simultaneous observations from a given station.

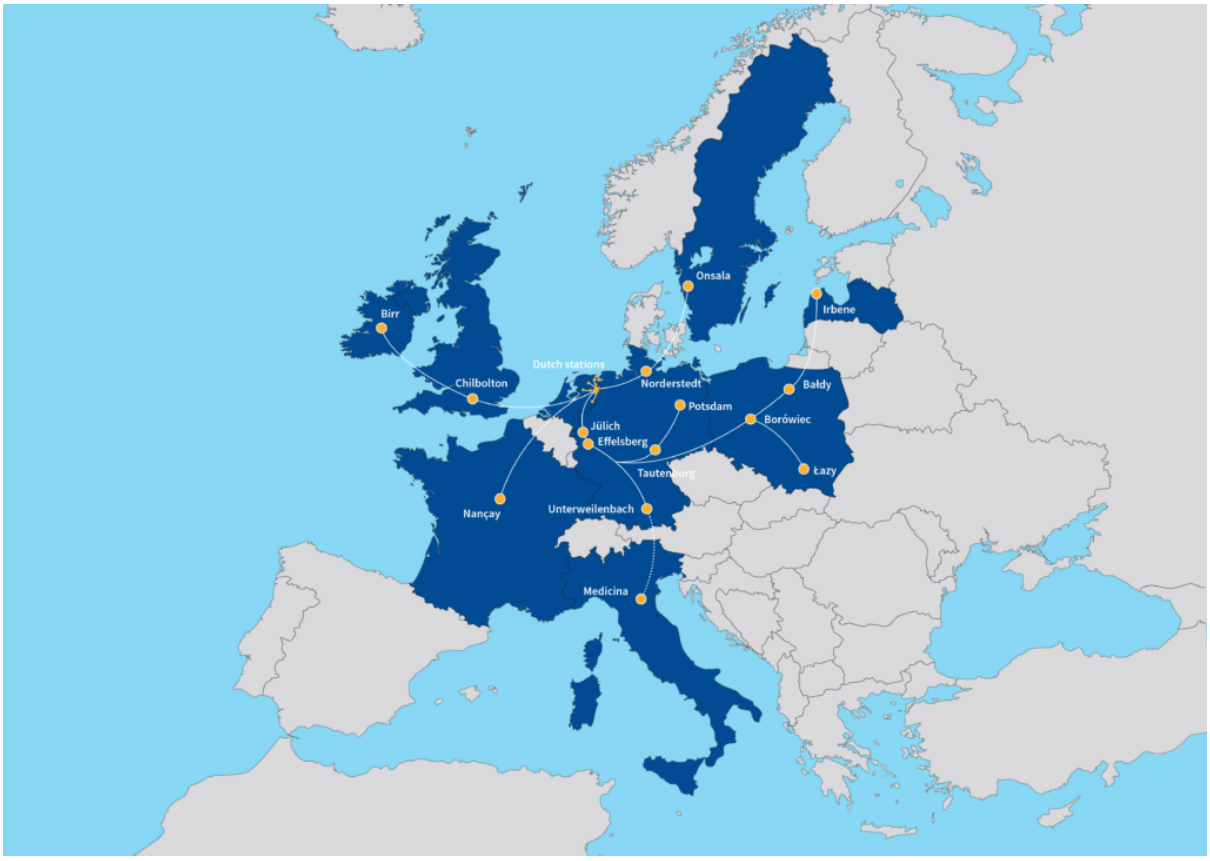

Figure 2.1: LOFAR stations.

We report the LOFAR performances at different frequencies in Table 2.1. To cover the $10 - 240$ MHz operating bandpass two different types of antenna are used, which I will describe in more detail below.

Low Band Antennas

The Low Band Antennas (LBA) are designed to operate from the ionospheric cutoff of the radio window, near 10 MHz, up to the onset of the commercial FM radio band at about 90 MHz. Due to the presence of strong interference at the lowest frequencies and the proximity of the FM band at the upper end, this range is operationally limited to $30-80$ MHz by default. A digital filter is employed to suppress the response outside of this band, with the option of deselecting it for observations below 30 MHz. An image of an LBA element and the LBA median response curve are reported in Fig. 2.2 (Upper panels). The LBA element, or dipole, is sensitive to two orthogonal linear polarisations. Due to hardware limitations (which will be removed in the LOFAR2.0 upgrade) in each station, only half of the LBA dipoles can be used during a single observation. Two configurations are possible, each consists of 48 dipoles that are grouped into an inner circle ("LBA Inner" mode) and an outer annulus ("LBA Outer" mode). The choice of the configuration has a large impact on the size and shape of the main lobe of the primary beam and on the positions and amplitudes of the side lobes, leading to different instrument responses, as reported in Table 2.1.

Freq. (MHz)	λ (m)	D (m)	$A_{\rm eff}$ (m^2)	$FWHM$ (deg)	FOV (deg^2)	D (m)	$A_{\rm eff}$ (m^2)	$FWHM$ (deg)	FOV (deg^2)	D (m)	$A_{\rm eff}$ (m^2)	$FWHM$ (deg)	FOV (deg^2)
		NL Inner				NL Outer				EU			
15	20.0	32.25	1284.0	39.08	1199.83	81.34	4488.0	15.49	188.62	65.00	3974.0	19.39	295.36
30	10.0	32.25	848.9	19.55	299.96	81.34	1559.0	7.75	47.15	65.00	2516.0	9.70	73.84
45	6.67	32.25	590.2	13.02	133.31	81.34	708.3	5.16	20.96	65.00	1378.0	6.46	32.82
60	5.00	32.25	368.5	9.77	74.99	81.34	399.9	3.88	11.78	65.00	800.0	4.85	18.46
75	4.00	32.25	243.6	7.82	47.99	81.34	256.0	3.10	7.55	65.00	512.0	3.88	11.81
		NL core				NL Remote				EU			
120	2.50	30.75	600.0	4.75	17.73	41.05	1200.0	3.56	9.95	56.50	2400.0	2.59	5.25
150	2.00	30.75	512.0	3.80	11.35	41.05	1024.0	2.85	6.37	56.50	2048.0	2.07	3.36
180	1.67	30.75	355.6	3.17	7.88	41.05	711.1	2.37	4.42	56.50	1422.0	1.73	2.33
200	1.50	30.75	288.0	2.85	6.38	41.05	576.0	2.13	3.58	56.50	1152.0	1.55	1.89
210	1.43	30.75	261.2	2.71	5.79	41.05	522.5	2.03	3.25	56.50	1045.0	1.48	1.72
240	1.25	30.75	200.0	2.38	4.43	41.05	400.0	1.78	2.49	56.50	800.0	1.29	1.31

Table 2.1: LOFAR effective area ($A_{\rm eff}$), full-width half-maximum (FWHM) and field of view (FOV) at different frequencies and for different station configurations (where D is the station diameter). From van Haarlem et al. (2013).

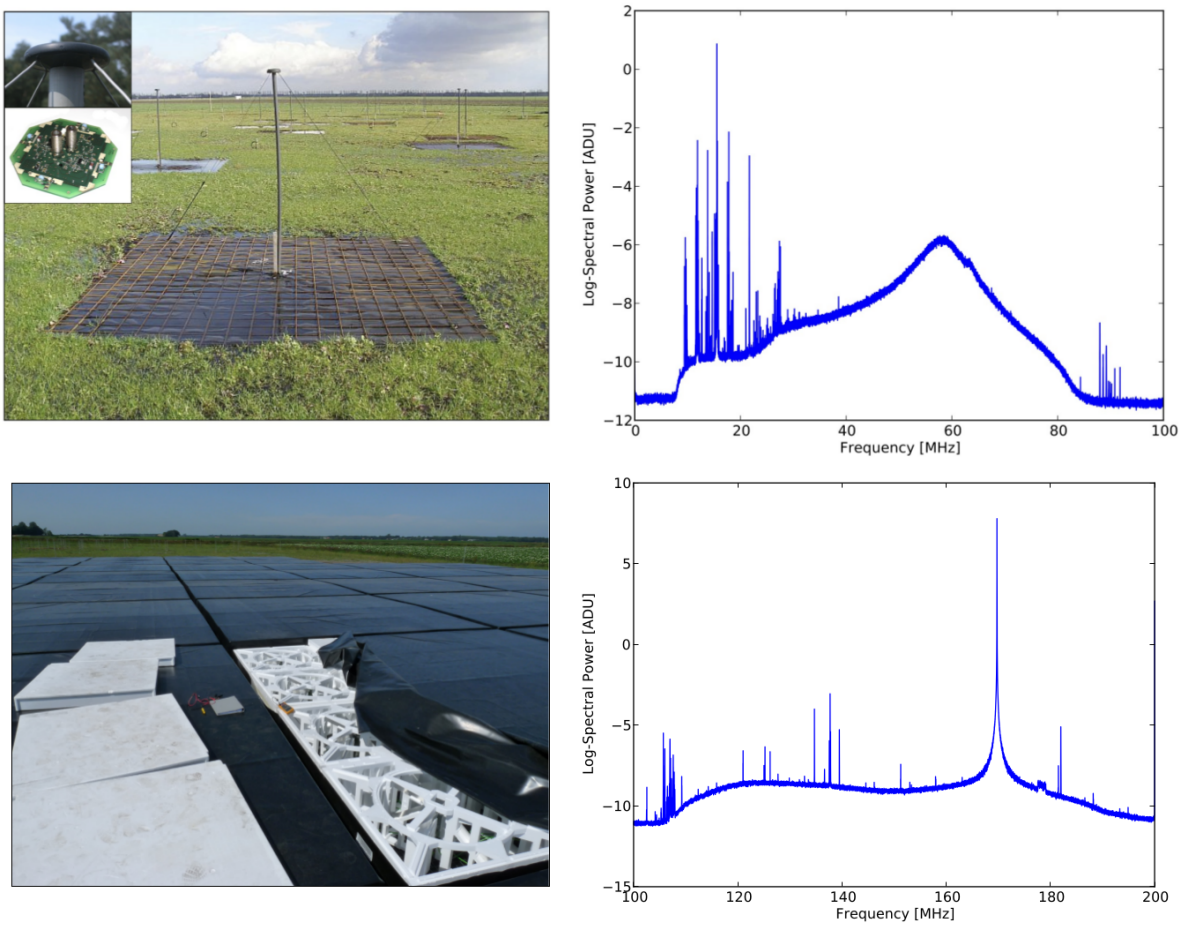

Figure 2.2: *Upper left*: a single LBA dipole. The inset images show the molded cap containing the electronics and the wires attachment points. *Upper right*: LBA median response curve for all LBA dipoles of a LOFAR station. The peak of the curve is near 58 MHz. The strong radio frequency interference (RFI) below 30 MHz and above 80 MHz are clearly visible. *Lower left*: image of a single HBA tile. The protective covering has been partially removed to show the dipole assembly. *Lower right*: HBA median response curve for the HBA LOW band for all HBA tiles of a LOFAR station. Various prominent RFI sources are clearly visible distributed across the band including the strong peak near 170 MHz corresponding to an emergency pager signal. From van Haarlem et al. (2013).

High Band Antennas

The High Band Antennas (HBA) are optimised to operate in the 110−250 MHz range. Due to heavy RFI contamination above 240 MHz, the band is operationally limited to the 110−240 MHz range. The total HBA frequency range is covered by three observing bands: 110-190 MHz (HBA LOW), 170-230 MHz (HBA MID), and 210-250 MHz (HBA HIGH). At these frequencies, the total system noise is no longer dominated by the sky noise as in the case for LBA, but by the electronics. Consequently, another design topology for the HBA antennas was required. The HBA elements are grouped in 16 dual dipole antennas and arranged in a 4×4 grid to form a single HBA "tile". A single "tile beam" is obtained by combining the signals from these 16 antenna elements in phase for a given direction on the sky. An image of an HBA tile and the HBA median response curve are reported in Fig 2.2 (Lower panels). The layout of HBA tiles within the core and remote stations is different. In the remote stations the 48 HBA tiles are contained in a single field, while in the core stations the HBA dipoles are grouped in two sub-stations of 24 tiles each. These sub-stations can be used together as a single station or separately as independent LOFAR stations. The latter option has the advantage of providing many more short baselines within the core and by extension and so more uniform *uv*-coverage, essential for science cases that depend critically on the use of short baselines, as the search for radio transients. In addition, many of the short baselines that result from the dual HBA sub-stations are redundant and therefore can be used as diagnostics for identifying bad phase and gain solutions during the calibration.

2.2 Surveys

LOFAR's design and capabilities make it a good survey instrument. The LOFAR Multifrequency Snapshot Sky Survey (MSSS) was the first wide-area northern-sky survey to be carried out with LOFAR. It surveyed the whole northern sky to a depth of around 10 mJy beam^{-1} with a resolution of 2 arcmin (Heald et al., 2015). Currently, four surveys are ongoing:

- LOFAR Two-metre Sky Survey (LoTSS): wide-area survey performed in the HBA frequency range 120−168 MHz. Its goal is to observe the whole northern sky at a resolution of 6″ and a sensitivity that depends on the declination and is typically around 100μJy beam^{-1}. It is a factor of 50 more sensitive and 5 times higher in resolution than the TIFR GMRT Sky Survey at 150 MHz (TGSS, Intema et al., 2017), and a factor of 10 more sensitive than the FIRST survey at 1.4 GHz (Faint Images of the Radio Sky at Twenty-cm), the current best high-resolution sky survey (see Fig. 2.3). A first data release covering an area of 424 square degrees (2% of the planned coverage) in the region of the HETDEX Spring Field has been released in 2019 (Shimwell et al., 2019). In Fig. 2.4 is reported the current status of the survey, a second data release is planned for the beginning of 2022.

  A stretch goal is to image large areas with the resolution of the International stations, around 0.5″.

- LoTSS deep fields: LoTSS is also performing repeated observations of selected fields with the same frequency coverage, aiming to reach a sensitivity of ~ 10 μJy beam^{-1} (roughly five times deeper than the best all-sky LoTSS pointing) over combined sky areas of many tens of square degrees. The first three fields being observed are Boötes, Elais-N1 and Lockman Hole, for each of which at least 100 hours of HBA data are already available; additional fields are planned. Combined with high-

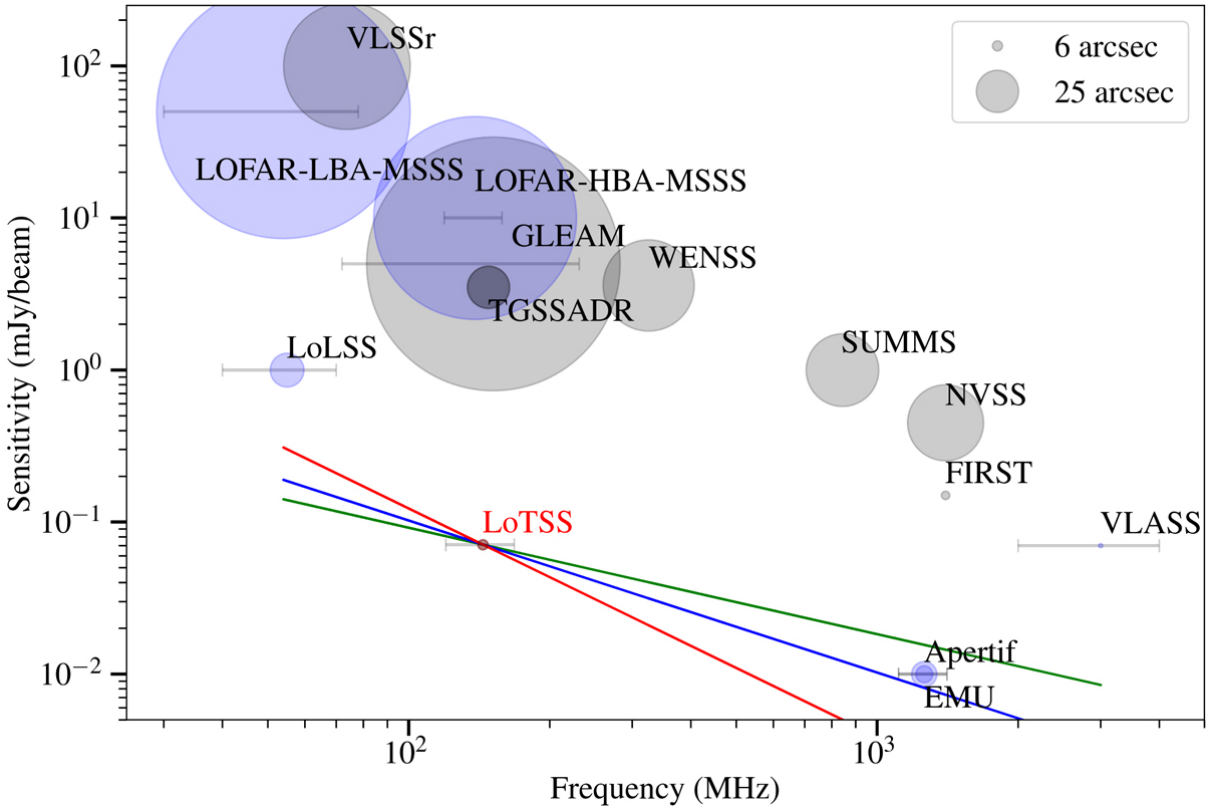

Figure 2.3: The image shows the rms, frequency and angular resolution (linearly proportional to the radius of the markers) of LoTSS and LoLSS in comparison to a selection of existing wide-area completed (grey) and upcoming (blue) radio surveys. The horizontal lines show the frequency coverage for surveys with large fractional bandwidths. The green, blue and red lines show an equivalent sensitivity to LoTSS for compact radio sources with spectral indices of 0.7, 1.0 and 1.5, respectively. From Shimwell et al. (2019).

quality ancillary data, this will allow to study star formation and AGN activity across cosmic time.

- LOFAR LBA Sky Survey (LoLSS): it plans to cover the entire northern sky in the frequency range 42−66 MHz, with the aim to achieve a resolution of 15″ and an average rms noise of 1 mJy beam^{-1}. LOFAR is the only radio telescope that is currently capable of high-sensitivity, high-resolution observations at frequencies below 100 MHz (see Fig. 2.3). LoLSS will be a revolutionary tool to discover and study ultra-steep spectrum sources, such as high redshift galaxies and quasars, old radio plasma and the magnetosphere of exoplanets. The preliminary data release covers 740 square degrees of the HETDEX spring field region (Fig. 2.4) at a resolution of 47″ with a median rms noise of 5 mJy beam^{-1} (de Gasperin et al., 2021).
- WEAVE-LOFAR is a spectroscopic survey of the LOTSS sky with the WEAVE fibre spectrograph on the William Herschel Telescope. It will provide redshifts for the wide and deep tiers of LOTSS.

Part of the data analysed in this Thesis were observed as part of LoTSS and will be presented in the following chapters.

2.3 Impact on galaxy cluster studies

Diffuse radio emission in galaxy clusters is characterised by a steep spectrum, meaning it is brighter at low frequencies, so an ideal target for LOFAR. With its dense core array

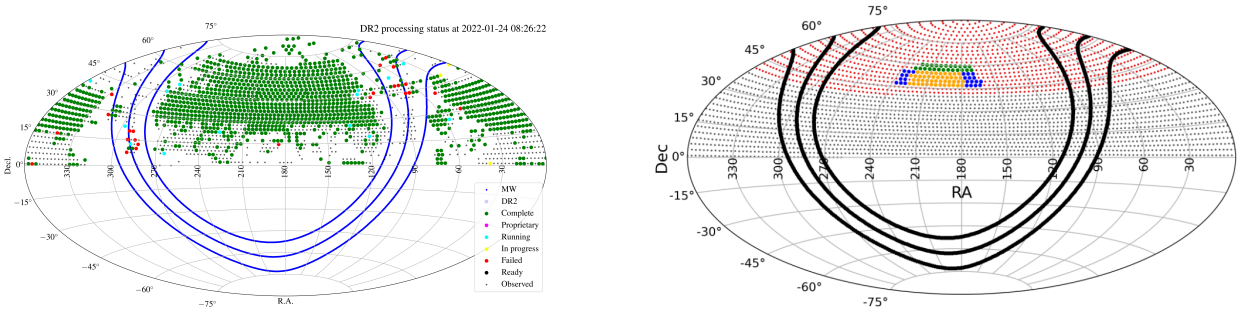

Figure 2.4: *Left:* LoTSS DR2 processing status from https://lofar-surveys.org/status.html. *Right:* LoLSS current and planned sky coverage. Yellow, blue and green dots cover the HETDEX region and constitute the first data release. Red dots are scheduled to be observed by 2022. From de Gasperin et al. (2021). In both the panels solid lines show the position of the Galactic plane with Galactic latitude: −10, 0, +10 degrees.

LOFAR provides exceptional sensitivity to extended sources in the low frequency regime ($\leq$ 200 MHz), expanding for order of magnitudes the number of known giant radio halos and mini halos. According to Cassano et al. (2010), the LOFAR all-sky survey will detect more than 350 radio halos at redshift $\leq$ 0.6. In the HETDEX region 10 Planck PSZ2 clusters with radio halos and 12 candidates were detected (van Weeren et al., 2021). These numbers increase to 53 radio halos and 20 candidates in the second data release (Botteon et al., 2022), among which 35 are new discoveries. Based on these numbers LoTSS should find $\sim$ 260 radio halos, in agreement with theoretical expectations. LOFAR has also made it possible to expand the study of galaxy clusters towards lower masses ($M_{500} \leq 5 \times 10^{14}$ $M_{\odot}$) and higher redshift ($z \geq 0.6$, Cassano et al., Cuciti et al., Di Gennaro et al., in preparation). The improved statistics offered by large samples, will permit, for the first time, to carry out detailed studies of the properties of radio sources in galaxy clusters and investigate their occurrence rates as a fuction of cluster mass, redshift and dynamical state.

Furthermore, LOFAR has discovered new types of diffuse radio sources in galaxy clusters, including radio halos in relaxed clusters (Bonafede et al., 2014; Sommer et al., 2017; Savini et al., 2018, 2019), mega halos (Cuciti et al., submitted) and radio bridges that connect pairs of massive and pre-merging clusters (Govoni et al., 2019; Botteon et al., 2020a)

These results indicate that our comprehension of diffuse radio emission in galaxy clusters is still at the beginning. In the coming years the number of sources discovered in the low frequency regime may still increase thanks to the enhanced sensitivity in the LOFAR2.0 upgrade and the advent of SKA (Square Kilometre Array) and its precursors.

2.4 Data reduction

In this Thesis I made use of both LOFAR LBA and HBA data. To obtain high-fidelity images, observations at low radio frequency require advanced calibration and specific processing techniques to correct for systematic effects. The main source of corruptions is the ionosphere. This introduces a time and directions-dependent delay difference between antennas caused by the variation of the refractive index of the ionospheric plasma along the wave trajectory. Further errors are due to time delay between all CS (connected to the same clock) and any other station, and small differences in the station beam models and shapes. A detailed discussion of the systematic effects inherent to LOFAR data is reported in de Gasperin et al. (2019).

The standard procedure for interferometric data calibration consists in the character-

isation of the telescope's response to systematic effects by observing bright, compact and well-known sources (i.e. calibrators). Generally, a strong unresolved source of known flux density is observed as primary calibrator at the beginning and at the end of the observation, to measure absolute flux calibration, band-pass and residual delays. Therefore, all the effects that are time and direction-independent can be corrected on the target field using the calibrator solutions. To track phase and amplitude variations in time, a secondary (or phase) calibrator located nearby the target source, is observed multiple times on short time intervals to remove the effects of signal corruption in the direction of the target.

The low-frequency and large field-of-view of LOFAR observations require a different calibration strategy. In both HBA and LBA frequency range there are no sources strong enough to dominate the flux within the field of view and close to the target to be used as phase calibrators. Furthermore, the large primary beam of LOFAR requires many different corrections for ionospheric distortions and beam model errors across the field of view. Therefore, the best method to calibrate LOFAR data is to perform a self-calibration using the target field itself to determine time and direction-dependent quantities. In LBA observations, where ionospheric-induced phase variations are higher, the flux density calibrator is observed simultaneously to the target, with half of the available bandwidth on the target field and half on the calibrator. In that way, time variations are tracked and all the solutions to direction-independent systematic effects can be transferred from the calibrator to the target.

The data calibration procedure requires different steps, which are performed with slightly different approaches for LBA and HBA observations, as further detailed below.

2.4.1 LBA data

The calibrator data are reduced following de Gasperin et al. (2019), to isolate the systematic effects of the polarisation alignment, the bandpass and the clock drifts. Since in the low-frequency regime the latter effect is difficult to isolate from the ionospheric delay, the raw scalar phase solutions are transferred to the target. This also gives an initial estimate of the ionospheric delay, using the solutions towards the direction of the calibrator. After the application of the calibrator solutions, the data for the target field require different steps of calibration to correct for differential ionospheric effects. The target field calibration procedure is described in de Gasperin et al. (2020). An initial directions-independent (DI) calibration of the target field removes three systematic effects: the direction-averaged ionospheric delay, the Faraday rotation and beam variations with time and frequency on top of the LOFAR beam model.

The primary errors remaining in the data at this point are the severe differential directions-dependent (DD) effects caused by the ionosphere. To correct for these errors, bright sources in the field of view, called DD-calibrators, selected based on their flux density, are used to estimate the ionospheric effects in their directions. Then, the field of view is divided into facets given by the Voronoi-tesselation of the positions of the DD-calibrators. Each facet is corrected with the calibration solutions of the corresponding DD-calibrator during imaging with `DDFacet` (Tasse et al., 2018). A DD calibrated wide-field image has a full resolution of $15''$.

The final data reduction step is the so-called 'extraction' and self-calibration of the target, where a LBA-specific implementation of the extraction strategy described in van Weeren et al. (2020) is used. In this step, all sources outside the region of interest are subtracted from the full data set, using the model and the calibration solutions derived in the DD calibration. To further refine the image quality of the target, different steps of scalar phase and slow diagonal amplitude self-calibration are performed at increasing

time-resolution.

2.4.2 HBA data

HBA data are processed with the standard Surveys Key Science Project pipeline[1] (see Shimwell et al., 2019; Tasse et al., 2021). The data are firstly corrected for the DI effects following the procedure described in Shimwell et al. (2017): the calibrator data are flagged for interference with AOFLAGGER (Offringa et al., 2012), and calibrated using a model of the appropriate calibrator source, which has a flux density scale set according to Scaife & Heald (2012). The resulting calibration tables are used to derive time-independent amplitude solutions and clock offsets for each station. Similarly, the target data are flagged, corrected for ionospheric Faraday rotation and calibrated using the calibrator solutions. In the final step of the DI calibration pipeline, the data are phase calibrated against a sky model for the target field, generated from the TGSS-ADR1 catalogue (Intema et al., 2017).

The target data are then calibrated for the DD effects through the pipeline that uses `killMS` and `DDF` (Tasse, 2014a,b; Smirnov & Tasse, 2015; Tasse et al., 2018) for DD calibration and imaging, respectively. The pipeline firstly operates on a restricted set of data, which are spaced across the entire bandwidth. These data are self-calibrated to build up a model of the radio emission in the field, which is then used to calibrate the full data set. In the first step `DDF` is used to image the DI calibrated data and create a model of the sky. The sky model is then used to select 45 facets and perform the first phase of DD calibration using `killMS`, which creates an amplitude and phase solution for each of the 45 facets every 60s and 1.95MHz of bandwidth. Several steps of DD calibration, spectral deconvolution and imaging are performed, finding phase and amplitude solutions which are then used to calibrate the entire dataset. The full bandwidth high-resolution imaging is performed with a resolution of 6″.

Finally, to improve the calibration on the target region, all the sources outside a small region centred on the cluster are subtracted, using the DD gains, and then several cycles of phase and amplitude self-calibration are performed in the extracted region using `DPPP` and `WSclean`[2] (van Diepen et al., 2018; Offringa et al., 2014). The flux density scale is set according to Scaife & Heald (2012), and subsequently aligned with LoTSS-DR2 data release (Shimwell et al., 2022), where the flux calibration uncertainty is estimated to be 10 per cent (Hardcastle et al., 2021; Shimwell et al., 2022).

[1] https://github.com/mhardcastle/ddf-pipeline/
[2] https://gitlab.com/aroffringa/wsclean

Chapter 3

Searching large-scale diffuse emission in cool-core clusters with LOFAR

Recent observations of galaxy clusters have revealed the unexpected presence of cluster-scale diffuse radio emission in a few cool-core clusters. These discoveries suggest that some mechanism has (re)accelerated particles on scales larger than the core, in otherwise relaxed clusters. A possible explanation is that these clusters underwent a minor merger that has re-accelerated particles on large-scale without disrupting the central cool-core. As minor mergers are less energetic than the major ones, particles should be accelerated with a lower efficiency, producing steep spectra radio emission ($\alpha \geq 1.5$) and so brighter at low frequencies.

In this Chapter[1] we address two questions: Is this emission common in galaxy clusters that exhibit cool-core and signs of interaction on large-scale? Is there a link between the observed radio emission and the gas dynamics?

3.1 The sample

In order to test the minor-merger scenario as a possible explanation for the presence of large-scale diffuse emission in relaxed clusters, we selected a sample of clusters that have a cool-core and some level of dynamical disturbances. This information has been extracted from X-ray observations, through the computation of the morphological parameters. In particular, we used the concentration parameter (c) and the centroid shift (w), defined in Chapter 1. Large values of c indicate a dense core, typical of cool-core clusters that have not undergone a recent major merger, while large values of w indicate a distribution of gas not spherically symmetric, i.e. a merging cluster. Cassano et al. (2010) found that most of clusters with $c < 0.2$ and $w > 0.012$ (i.e. merging) have a giant radio halo, while no cluster with $c > 0.2$ and $w < 0.012$ (i.e. relaxed clusters) have a radio halo at frequencies $\nu > 610$ MHz. LOFAR observations, instead, have revealed the presence of halo-like emission in clusters classified as relaxed, with $c > 0.3$ and $w > 0.003$ (Savini et al., 2019).

We chose our targets from two X-ray samples of galaxy clusters: the ACCEPT sample (Cavagnolo et al., 2009) and the ME-MACS sample (Mann & Ebeling, 2012; Rossetti et al., 2017). We selected all ME-MACS clusters that are classified as cool-core by Rossetti et al. (2017), according to the concentration parameter ($c \geq 0.075$), and all ACCEPT clusters that are classified as cool-core by Cavagnolo et al. (2009) and Giacintucci et al. (2017), according to the core entropy ($K_0 \leq 30 - 50$ keVcm^2). We computed the

[1]The results presented in this Chapter are reported in an article in preparation.

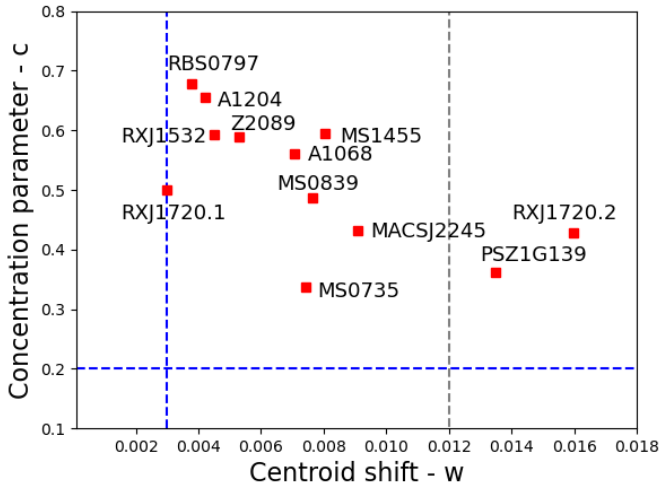

Figure 3.1: Morphological parameters plot of the clusters in our sample. Blue dashed lines indicates the c and w values used to select clusters in our sample. Grey dashed line indicates the w which separates clusters with a radio halo ($w \geq 0.012$) from clusters without a radio halo, according to (Cassano et al., 2010).

morphological parameters c and w of the selected clusters from *Chandra* archival observations that we have reprocessed in the standard way (search and removal of proton flares, correction for exposure map, identification of point sources) using `CIAO`[2] v4.7 (*Chandra* Interactive Analysis of Observation, Fruscione et al., 2006). Exposure-corrected images have been created in the energy band 0.5 – 2 keV, and binned to a common resolution of 4 kpc/pixel. We then selected all clusters with $c > 0.2$, i.e. clusters with a compact core, and $w > 0.003$, i.e. larger than the w of the cluster RX J1720.1+2638, in which diffuse emission outside the cluster core has been observed by Savini et al. (2019). In addition, we considered only clusters that could easily be observed with LOFAR, i.e. with declination greater than 10°, and must have a redshift < 0.4 to resolve emission on scales of 500 kpc at the resolution of 20″. The final sample consists of 12 clusters listed in Tab. 3.1 and shown in Fig. 3.1 in the $c - w$ plot.

3.2 Radio observations

The selected clusters were observed with LOFAR at the frequency of 144 MHz. Four of these were observed by LoTSS, while the rest as part of a dedicated proposal (project LC10_010). The observational details are reported in Table 3.2. For the clusters observed by LoTSS, we indicate both the project ID and the pointings used. Each observation consists of an 8 hr time-on-source book-ended by 10 min scans on the flux density calibrator using HBA stations in the `HBA_DUAL_INNER` mode, implying that only central antennas are used for the remote stations to mimic the size of the core stations. All the data were processed with the standard data reduction illustrated in Section 2.4.2. The flux density scale was set according to Scaife & Heald (2012), and subsequently aligned with LoTSS-DR2 data release, where the flux calibration uncertainty is estimated to be 10 per cent (Hardcastle et al., 2021; Shimwell et al., 2022).

The calibrated data were then imaged at different resolutions using WSClean (Offringa et al., 2014). The high resolution images were produced using a Briggs weighting scheme with robust $= -0.5$, applying an inner uv-cut at 80λ and using a pixel-scale of 1″. For the low resolution images, instead, we used a pixel-scale of 4″, an uv-taper of 20″, and multi-scale deconvolution to better model the diffuse emission. These images were obtained after the subtraction of the central source and of surrounding compact sources which could influence the study of diffuse emission. The source subtraction was computed in

[2] https://cxc.cfa.harvard.edu/ciao/

Table 3.1: Properties of selected clusters.

Cluster name	RA	DEC	z	Scale [kpc/″]	M_{500} [10^{14} $M_\odot$]	c	w
PSZ1G139.61+24	06:22:04.60	+74:40:51.6	0.270	4.17	7.6	0.362	0.0135
MS 0735.6+7421	07:41:44.31	+74:14:39.51	0.216	3.50	5.0	0.3366	0.0074
MS 0839.8+2938	08:42:55.99	+29:27:29.16	0.193	3.21	3.4*	0.4869	0.0076
Z2089	09:00:36.85	+20:53:40.62	0.235	3.67	3.2*	0.5935	0.0045
RBS 0797	09:47:12.72	+76:23:13.85	0.350	4.94	5.6	0.6790	0.0038
A1068	10:40:44.53	+39:57:11.94	0.139	2.45	3.8	0.5611	0.0071
A1204	11:13:20.50	+17:35:40.97	0.171	2.91	3.3	0.6558	0.0042
MS 1455.0+2232	14:57:15.11	+22:20:34.14	0.258	3.99	3.5*	0.5948	0.0080
RX J1532.9+3021	15:32:53.93	+30:21:01.24	0.362	4.89	4.7*	0.5899	0.0053
RX J1720.1+2638	17:20:10.10	+26:37:29.50	0.164	2.81	5.9	0.5	0.0030
RX J1720.2+3536	17:20:16.84	+35:36:26.89	0.391	5.30	6.1	0.4290	0.0159
MACS J2245.0+2637	22:45:04.58	+26:38:04.46	0.304	4.49	4.8*	0.4309	0.0091

Notes. Cluster mass from the *Planck* Sunyaev–Zel'dovich (SZ) cluster catalog (Planck Collaboration et al., 2016). Values marked with $*$ were estimated from the relation between M_{500} and T_X of Vikhlinin et al. (2009). This method tends to underestimate the mass of cool-core clusters by 30% with respect to *Planck* SZ-based estimates (see e.g. Giacintucci et al., 2017; Rossetti et al., 2017)

Table 3.2: Observation details.

Cluster name	Project	Field
PSZ1G139.61+24	LC8_022	P098+74
MS 0735.6+7421	LC10_010	/
MS 0839.8+2938	LT10_010	P129+29, P132+29
Z2089	LC10_010	/
RBS 0797	LC10_010	/
A1068	LC4_034	P157+40, P160+42, P161+40
A1204	LC10_010	/
MS 1455.0+2232	LT10_010	P225+22
RX J1532.9+3021	LC10_010	/
RX J1720.1+2638	LC7_024, LT10_010	P260+28, P261+25
RX J1720.2+3536	LC10_010	/
MACS J2245.0+2637	LC6_015	P341+26, P342+28

the visibility space using a model from high resolution images using `WSclean`. When diffuse emission is present, we applied a cut to the uv-range to exclude short baselines and filter out the emission on $\sim 100-200$ kpc scale. The value of the uv-cut varies from target to target, depending on the extension of the sources that we want to subtract. We then checked the residuals of final images to understand if we over/under subtracted the BCG and in case we repeated the process adjusting the model.

3.3 Results

In this section we briefly present each cluster, reporting information from the literature and results from new LOFAR observations. A summary table with the classification of the radio emission detected with LOFAR at 144 MHz, its linear dimension and total flux density is reported in Table. 3.3. In Fig. 3.2 − 3.13 we present the LOFAR images of each cluster: high resolution image at 144 MHz (upper left panel); low resolution image at 144 MHz (upper right panel); high resolution radio contours overlaid on optical *Pan-STARRS* (Chambers et al., 2016) RGB images, created combining g, r, i bands (lower left panel); low resolution radio contours overlaid on X-ray *Chandra* image (lower right panel).

For the clusters that present diffuse radio emission we extract radial profiles to understand if they consist of a single or two different components. We also extract radial spectral index profiles for those clusters for which a spectral index map of diffuse emission is available. Finally, we estimate the radio power associated to putative giant radio halos and derived upper limits in case of non detection.

3.3.1 Morphology

PSZ1G139.61+24

The cluster PSZ1G139.61+24 (heareafter PSZ1G139), located at z=0.27, presents an elongated X-ray emission in the north-west south-east direction and a cold front towards the north-west (Giacintucci et al., 2017; Savini et al., 2018). The cluster was observed in the radio band with the Giant Metrewave Radio Telescope (GMRT) at 610 MHz and LOFAR at 144 MHz. Both telescopes detect a central mini halo with an extension of ~ 200 kpc, whilst low-frequency LOFAR maps also show diffuse radio emission beyond the cluster core, reaching a total extension of ~ 500 kpc. The central mini halo has a spectral index of $\alpha \sim 1.3$, while the diffuse emission on larger scale has a steeper spectrum with a 2σ lower-limit spectral index of $\alpha \geq 1.7$ (Savini et al., 2018, 2019). We have reprocessed the LOFAR data by Savini et al. (2018, 2019) using the procedure described in Section 2.4.2, obtaining significant improvements in dynamic range and image fidelity (Fig. 3.2). The radio emission is distributed along the north-west south-east direction, following the X-ray emission, and it extends even beyond the cold front, reaching a total extension of ~ 760 kpc. The peak of radio emission is not associated to the brightest cluster galaxy, it is instead associated to another radio galaxy, clearly visible in the higher resolution ($4.5'' \times 3.8''$) zoom box in the upper left panel of Fig. 3.2. There is no obvious optical counterpart of this source, that could be a foreground radio galaxy.

MS 0735.6+7421

The cluster MS 0735.6+7421 (hereafter MS0735), at z=0.216, hosts in its centre a powerful radio galaxy with a defined core and outer lobes (McNamara et al., 2005; Cohen et al., 2005). *Chandra* X-ray observations revealed two giant cavities, each roughly 200

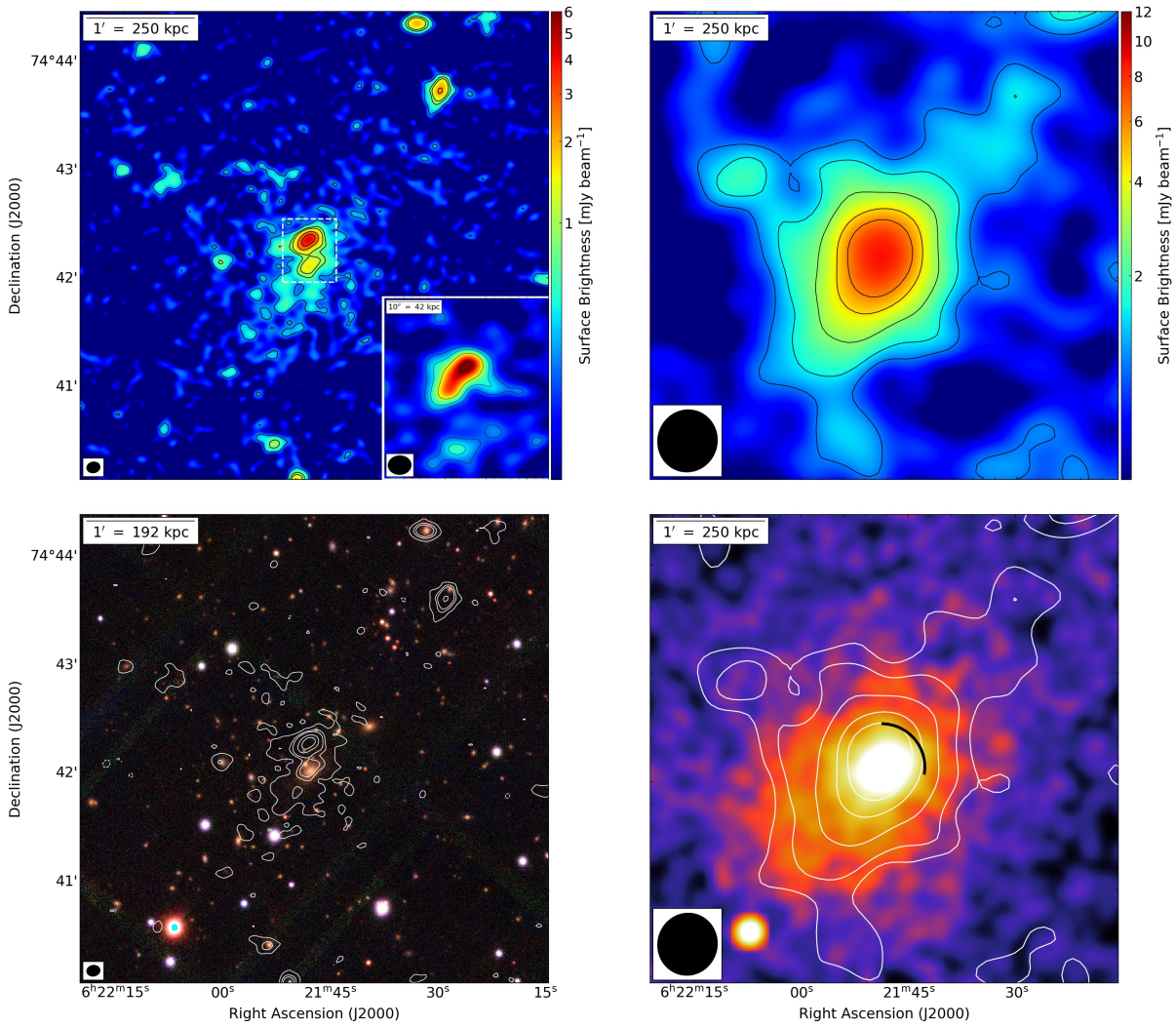

Figure 3.2: PSZ1G139.61+24: *Top left panel*: High-resolution 144 MHz LOFAR image. Levels:[-3, 3, 7, 10, 20, 30]$\times\sigma$ (where $\sigma = 0.11$ mJy beam^{-1}). The beam is $7.4'' \times 6.0''$ and is shown in the bottom left corner of the image. The insert box shows the image of the two central sources at $4.5'' \times 3.8''$ resolution, obtained with Briggs weighting robust=-1.25. *Top right panel*: Low-resolution 144 MHz LOFAR image, obtained after central source and surrounding point sources subtraction. Levels=[-3, 3, 5, 9, 15, 20]$\times\sigma$ (where $\sigma = 0.3$ mJy beam^{-1}). The beam is $34.6'' \times 33''$ and is shown in the bottom left corner of the image. *Bottom left panel*: Optical *Pan-STARRS* RGB image with high-resolution LOFAR contours overlaid. *Bottom right panel*: *Chandra* X-ray image smoothed on a scale of $3''$ with low-resolution LOFAR contours overlaid. The black arc indicates the position of the cold front found by Savini et al. (2018). All the panels depict the same region of the sky.

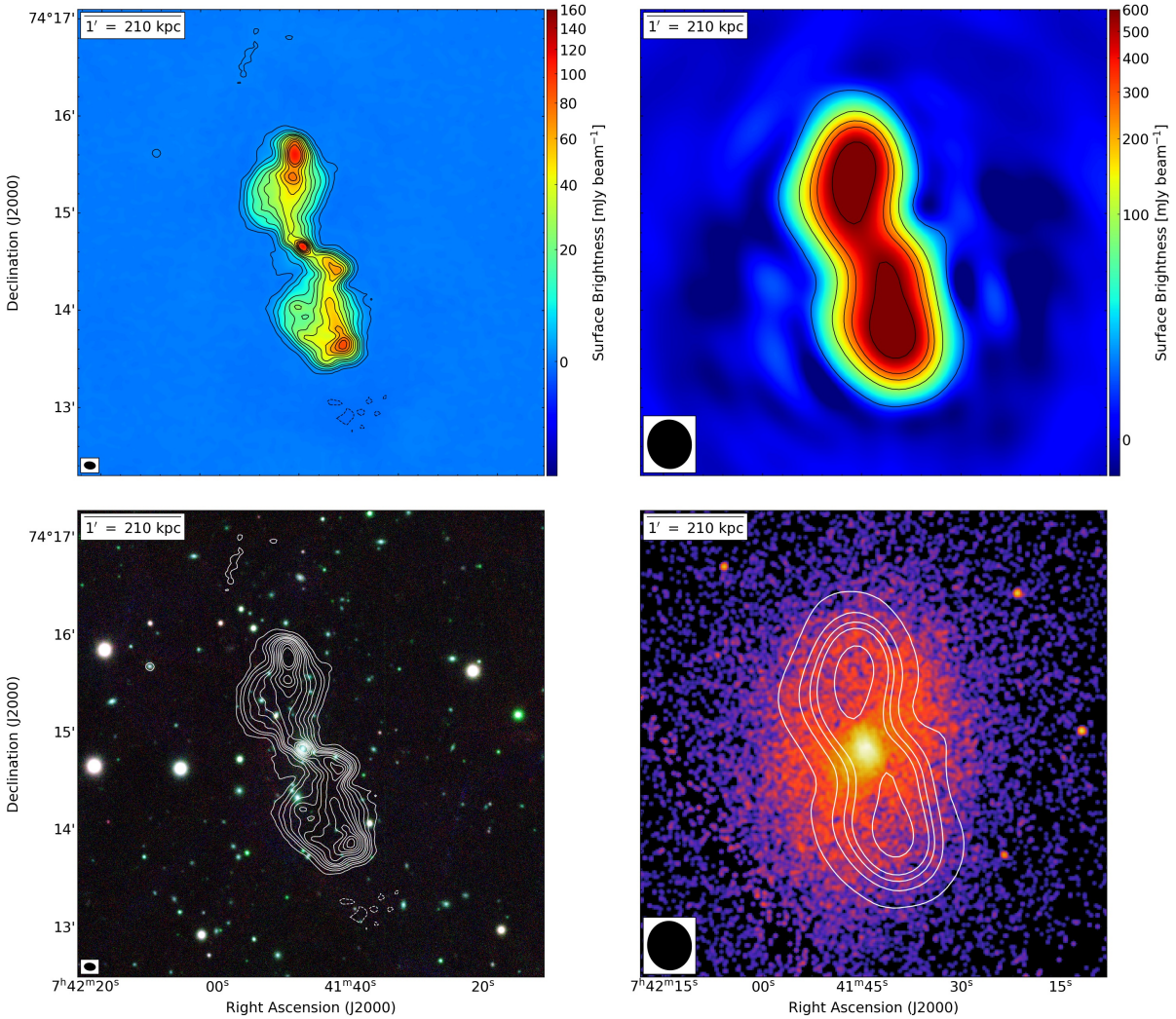

Figure 3.3: MS 0735.6+7421 *Top left panel*: High-resolution 144 MHz LOFAR image. Levels:[-3, 3, 15, 30, 60, 90, 120, 180, 240, 300, 360, 420]$\times\sigma$ (where $\sigma = 0.2$ mJy beam^{-1}). The beam is $6.9'' \times 4.5''$ and is shown in the bottom left corner of the image. *Top right panel*: Low-resolution 144 MHz LOFAR image. Levels=[-3, 3, 20, 40, 60, 120]$\times\sigma$ (where $\sigma = 5$ mJy beam^{-1}). The beam is $30.1'' \times 27.1''$ and is shown in the bottom left corner of the image. *Bottom left panel*: Optical *Pan-STARRS* RGB image with high-resolution LOFAR contours overlaid. *Bottom right panel*: *Chandra* X-ray image smoothed on a scale of $1''$ with low-resolution LOFAR contours overlaid. All the panels depict the same region of the sky.

kpc in diameter that are partially filled by the radio lobes, and a shock front surrounding them (McNamara et al., 2005). Another pair of smaller cavities is located in the inner 20 kpc of the radio jet, indicating the central AGN experienced different phases of jet activity (Vantyghem et al., 2014). The radio lobes at LOFAR frequency (Fig. 3.3) are wider than previously found with the Very Large Array (VLA) at higher frequencies and now completely fill the X-ray cavities. We also discovered an intermediate phase of jet activity, associated to the radio lobe located south-west of the core (Biava et al., 2021b). The position of this lobe corresponds to a new cavity we discovered re-analysing *Chandra* X-ray archival data. A detailed study of the AGN duty-cycle of this source is reported in Chapter 6. However, no diffuse emission in form of halo or mini halo was detected with LOFAR in this cluster.

MS 0839.8+2938

The cluster MS 0839.8+2938 (hereafter MS0839), at z=0.193, was observed with VLA at 1.4 GHz, detecting a central radio galaxy with small radio lobes with a total extension of 80 kpc (Giacintucci et al., 2017). A LOFAR image of this cluster observed with LoTSS was presented by Bîrzan et al. (2020), confirming the presence of a central radio source with small radio lobes. Our image (Fig. 3.4) is made combining two LoTSS pointings and the data are calibrated with more advanced techniques allowing us to achieve a better signal-to-noise ratio. The quality of the image, however, is affected by the presence of a bright radio source in the north not visible in the image. In the higher resolution ($3.7'' \times 2.5''$) zoom box in the upper left panel, obtained with uniform weightings, we can distinguish the central compact source and the associated radio lobes. We then subtracted all the emission visible with uniform weighting and re-imaged the data with a uv-taper of $20''$. In the final image reported in the upper right panel, there is still radio emission which, however, we do not consider as real diffuse emission for the presence of radio lobes and calibration artifacts.

Z2089

The cluster Z2089, at z=0.235, was observed with GMRT at 610 MHz, no radio emission was detected (Venturi et al., 2008), however no radio images are available in the literature. The central source is detected by the FIRST survey, it has an integrated flux density of $S_{1.4\ \mathrm{GHz}} = 8.6$ mJy. With LOFAR (Fig. 3.5), we detect a central compact source, with a small extension ($\sim$ 130 kpc) of radio emission in the north-south direction at low significance. The radio emission associated with the compact central source has a flux density of $S_{144\ \mathrm{MHz}} = 95$ mJy. Therefore it has a steep spectral index of $\alpha \sim 1$ between 144−1400 MHz. This suggests the central source is not resolved and the flux could be dominated by steep radio lobes. At lower resolution no more emission is detected.

RBS 0797

The cluster RBS 0797, at z=0.35, was studied by Gitti et al. (2005) and Doria et al. (2012) performing VLA radio observations at different frequencies (1.4−8.4 GHz) and resolutions (0.4−6.3 arcsec). They found radio emission at different scales: a mini halo with an extension of $\sim$ 220 kpc, extended emission on the north-east south-west direction filling X-ray cavities located at a distance of $\sim$ 24 kpc from the cluster centre (Schindler et al., 2001), and inner jets on scales of $\sim$ 13 kpc pointing north-south, roughly perpendicular to the X-ray cavities. Ubertosi et al. (2021) recently detected a second couple of X-ray cavities in the north-south direction, at roughly the same radial distance as the north-east south-west cavities. Two scenarios have been proposed for the presence of two perpendicular, equidistant pair of cavities: the jet of the central AGN quickly changed direction or there is a binary AGN emitting simultaneously. With LOFAR (Fig. 3.6) we detected the central mini halo with an extension similar to that observed at higher frequency. At lower resolution no more diffuse emission appears. We re-imaged the LOFAR data cutting the baselines shorter than 10 $k\lambda$ to filter out the MH emission and increase the angular resolution. We achieved a resolution of $3.2'' \times 2.2''$, which allows us to detect the north-east south-west radio lobes (insert box in the bottom right panel of Fig. 3.6).

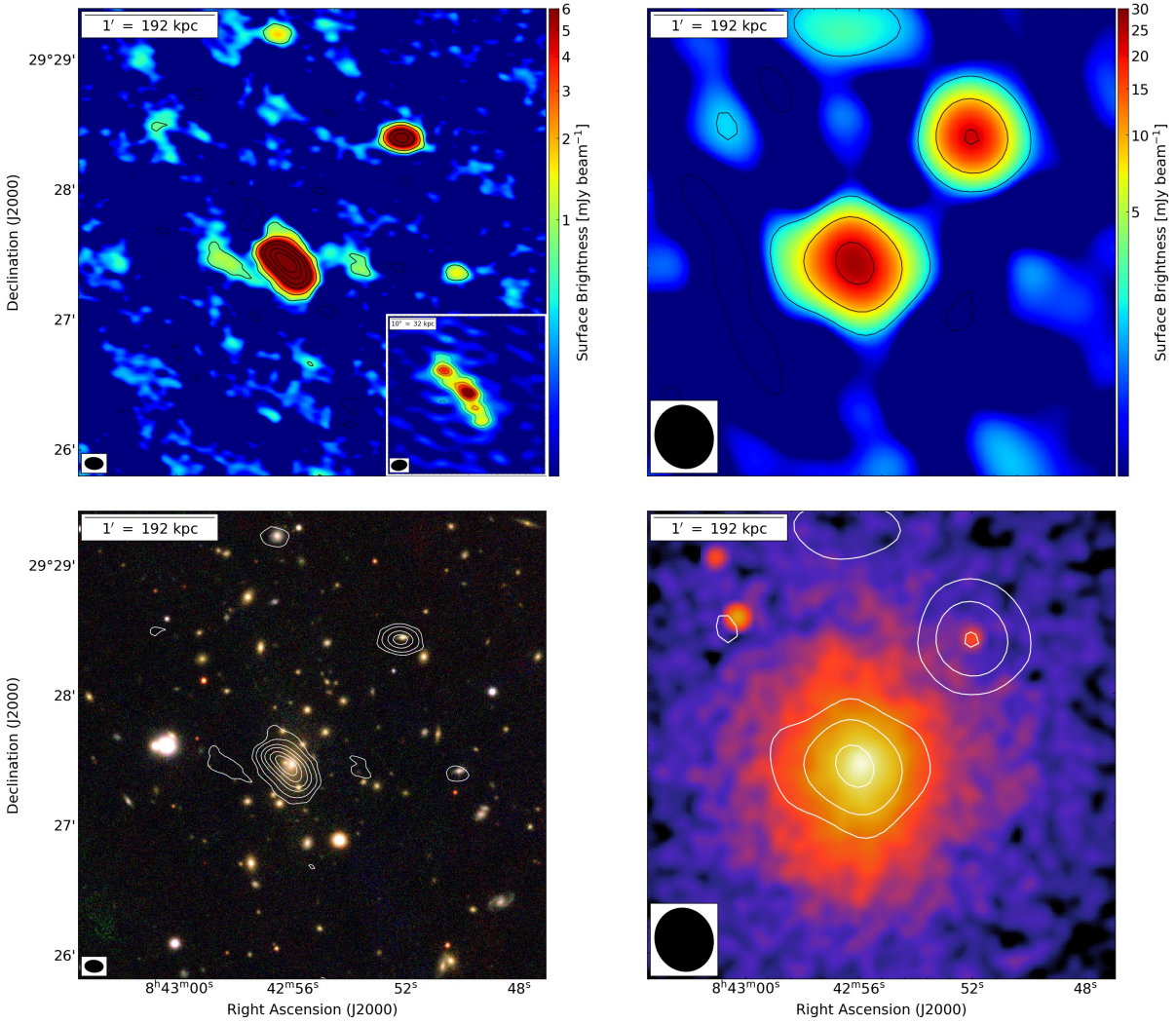

Figure 3.4: MS 0839.8+2938: *Top left panel*: High-resolution 144 MHz LOFAR image. Levels:[-3, 3, 9, 30, 60, 120, 180]$\times\sigma$ (where $\sigma = 0.22$ mJy beam^{-1}). The beam is $8.5'' \times 5.6''$ and is shown in the bottom left corner of the image. The insert box shows the image of the central source at resolution $3.7'' \times 2.5''$ obtained with uniform weightings. *Top right panel*: Low-resolution 144 MHz LOFAR image, obtained after central source subtraction. Levels=[-3, 3, 15, 40]$\times\sigma$ (where $\sigma = 0.55$ mJy beam^{-1}). The beam is $29.6'' \times 26.8''$ and is shown in the bottom left corner of the image. *Bottom left panel*: Optical *Pan-STARRS* RGB image with high-resolution LOFAR contours overlaid. *Bottom right panel*: *Chandra* X-ray image smoothed on a scale of $3''$ with low-resolution LOFAR contours overlaid. All the panels depict the same region of the sky.

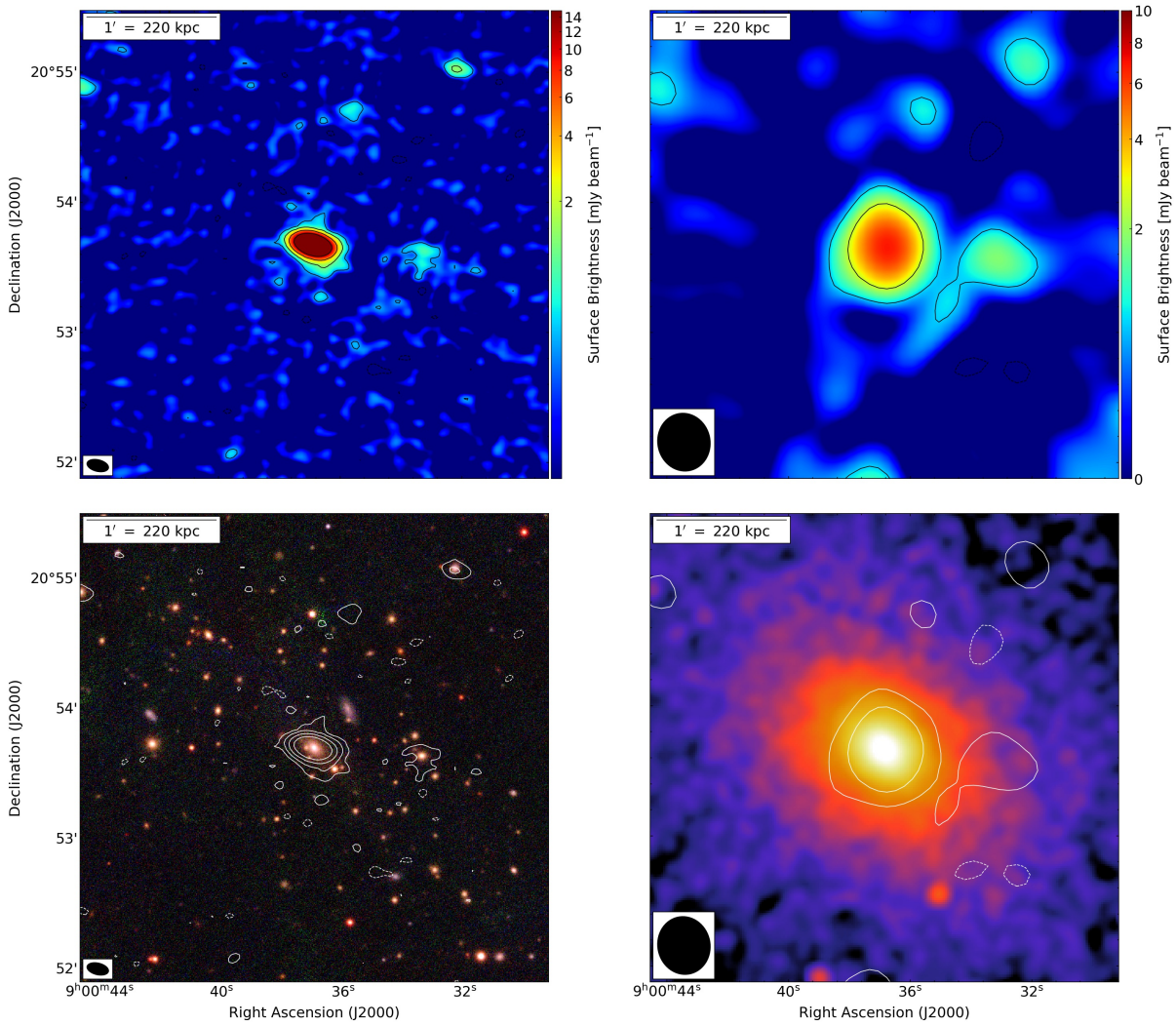

Figure 3.5: Z2089: *Top left panel*: High-resolution 144 MHz LOFAR image. Levels:[-3, 3, 9, 30, 90]$\times\sigma$ (where $\sigma = 0.14$ mJy beam^{-1}). The beam is $10.2'' \times 5.5''$ and is shown in the bottom left corner of the image. *Top right panel*: Low-resolution 144 MHz LOFAR image, obtained after central source subtraction. Levels=[-3, 3, 9]$\times\sigma$ (where $\sigma = 0.28$ mJy beam^{-1}). The beam is $26.8'' \times 24.2''$ and is shown in the bottom left corner of the image. *Bottom left panel*: Optical *Pan-STARRS* RGB image with high-resolution LOFAR contours overlaid. *Bottom right panel*: *Chandra* X-ray image smoothed on a scale of $3''$ with low-resolution LOFAR contours overlaid. All the panels depict the same region of the sky.

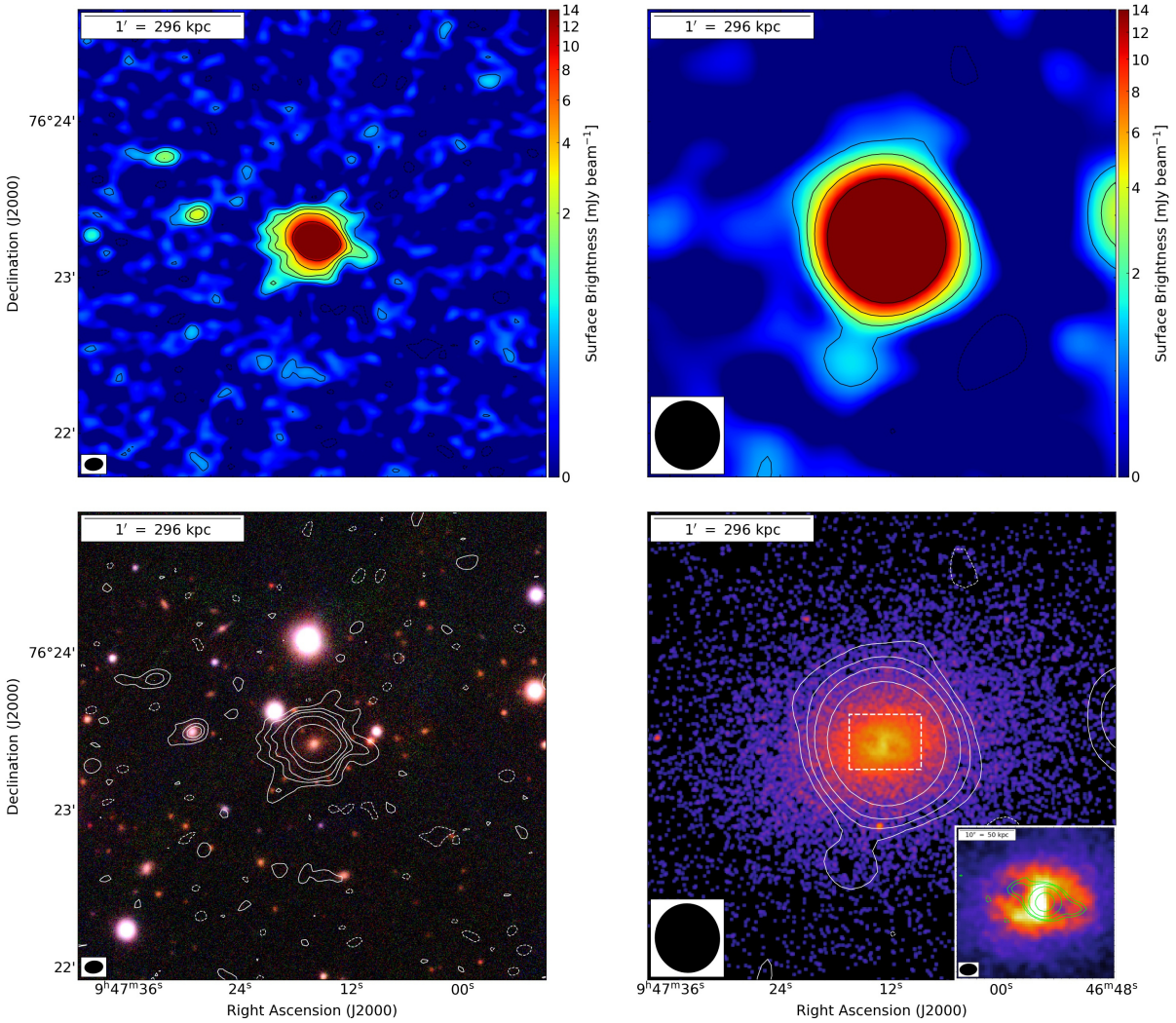

Figure 3.6: RBS797: *Top left panel*: High-resolution 144 MHz LOFAR image. Levels:[-3, 3, 9, 15, 30, 80]$\times\sigma$ (where $\sigma = 0.12$ mJy beam^{-1}). The beam is $7.0'' \times 4.7''$ and is shown in the bottom left corner of the image. *Top right panel*: Low-resolution 144 MHz LOFAR image, obtained after central source and surrounding point sources subtraction. Levels=[-3, 3, 7, 15, 40]$\times\sigma$ (where $\sigma = 0.33$ mJy beam^{-1}). The beam is $26.5'' \times 24.8''$ and is shown in the bottom left corner of the image. *Bottom left panel*: Optical *Pan-STARRS* RGB image with high-resolution LOFAR contours overlaid. *Bottom right panel*: *Chandra* X-ray image smoothed on a scale of $1''$ with low-resolution LOFAR contours overlaid. The insert box shows a zoom of the X-ray image with overlaid the LOFAR contours at $3.2'' \times 2.2''$ resolution, obtained with natural weighting and inner uv-cut. All the panels depict the same region of the sky.

A1068

The X-ray emission of the cluster A1068 (z=0.139) is elongated in the north-west south-east direction and there is evidence of a cold front north-west of the cluster core (Wise et al., 2004; McNamara et al., 2004). The source was observed in radio with the VLA at 1.4 GHz (Govoni et al., 2009), who detected hints of diffuse emission surrounding the central bright source and a companion one.

We re-calibrated *Chandra* X-ray data, finding two cold fronts located on the opposite site of the cluster centre, at distance of 103 and 130 kpc, respectively (black arcs in lower right panel of Fig. 3.7). In our high resolution LOFAR image at 144 MHz (upper left panel of Fig. 3.7), we can clearly distinguish the central galaxy and the companion one, west of the centre, which presents a long tail. Another HT galaxy (z = 0.134, probably a cluster member) is located to the south. The central galaxy is surrounded by diffuse emission, which extends in the north-west south-east direction. For a better visualisation of the diffuse emission, we have subtracted the central source, the two HT galaxies and surrounding sources and re-imaged the data with a *uv*-taper of 20″ (upper left panel of Fig. 3.7). Although some residuals of the central tail have remained, it is clear that the diffuse emission extends beyond the cold fronts, in the same direction as the X-ray emission and has an overall size of $\sim$ 400 kpc. Combining LOFAR data with new upgraded GMRT (uGMRT) data at 400 MHz, we found the central part of diffuse emission has a mean spectral index of $\alpha = 1.4 \pm 0.1$, while the external regions have a steeper spectral index of $\alpha = 1.7 \pm 0.3$ south-east of cluster centre and we estimate a limit of $\alpha \geq 2.6$ in the outermost part of north-west emission, which is not detected with uGMRT. Detailed analysis of this source are reported in Chapter 5.

A1204

The X-ray morphology of the cluster A1204 (z=0.171) is highly spherical with a bright central core. The cluster was observed in the radio band with VLA at 1.4 and 5 GHz. It presents an unresolved central source with a flat spectrum, while no central diffuse emission was detected (Giacintucci et al., 2017). The central source was also detected by the FIRST survey at higher resolution of 5.4″, and it has a flux density of $S_{1400\ \mathrm{MHz}} = 1.9$ mJy. At LOFAR resolution (10″ × 6″, Fig. 3.8) we found that the bright central source is slightly elongated in the east-west direction (size $\sim$ 140 kpc), possibly due to the presence of radio lobes. The flux density of the central compact source is $S_{144\ \mathrm{MHz}} = 9.9$ mJy. Therefore, it has a spectral index of $\alpha \sim 0.7$ between 144−1400 MHz, as is typically observed in the core of active galaxies. No diffuse emission in form of halo is detected around the central galaxy, neither decreasing the resolution.

MS 1455.0+2232

GMRT (610 MHz) and VLA (1400 MHz) observations of MS 1455.0+2232 (hereafter MS1455, z=0.258) indicate the presence of a central mini halo with a linear size of $\sim$ 350 kpc and a spectral index of $\alpha = 1.46$ (Venturi et al., 2008; Giacintucci et al., 2019). A pair of cold fronts surround the mini halo emission (Mazzotta & Giacintucci, 2008). A re-analysis of the X-ray data performed by Riseley et al. (2022) points out that the sloshing region is larger than previously reported by Mazzotta & Giacintucci (2008). The circle in the bottom right panel of Fig. 3.9 delimits that region. In our LOFAR HBA image (Fig. 3.9) the diffuse emission extends far beyond the sloshing region, with a total extension of $\sim$ 560 kpc. This source was also observed with MeerKAT at 1.28 GHz, detecting even more emission than LOFAR (Riseley et al., 2022), thanks to the very high sensitivity of these data (8 μJy beam^{-1} for MeerKAT data compared to 159 μJy beam^{-1} for LOFAR

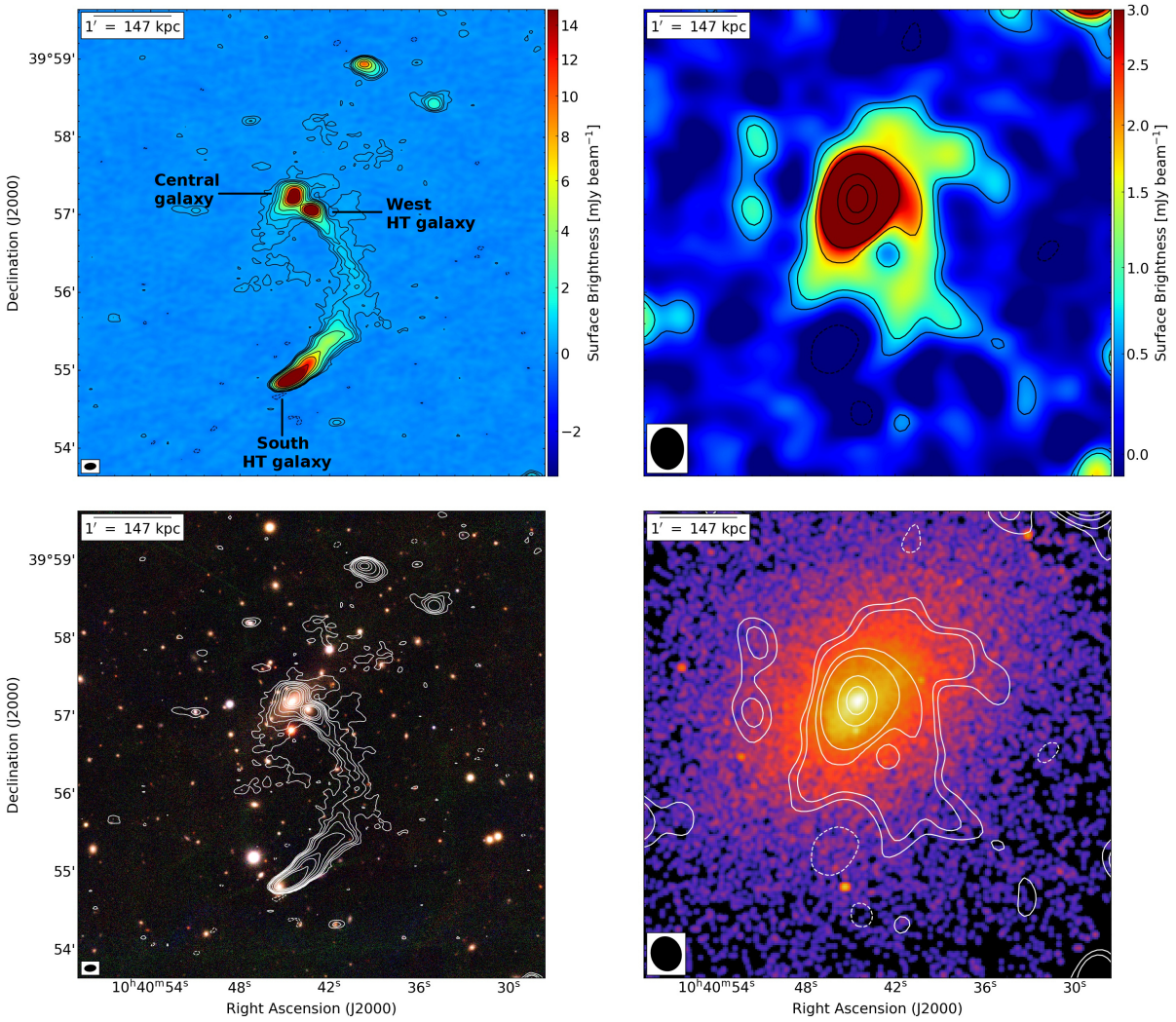

Figure 3.7: A1068: *Top left panel*: High-resolution 144 MHz LOFAR image. Levels:[-3, 3, 6, 9, 15, 30, 60, 90, 150]$\times\sigma$ (where σ = 0.08 mJy beam^{-1}). The beam is 8.8″ × 5.0″ and is shown in the bottom left corner of the image. *Top right panel*: Low-resolution 144 MHz LOFAR image, obtained after central sources and tails subtraction. Levels=[-3, 3, 5, 12, 20, 90, 150]$\times\sigma$ (where σ = 0.15 mJy beam^{-1}). The beam is 32.2″ × 25.3″ and is shown in the bottom left corner of the image. *Bottom left panel*: Optical *Pan-STARRS* RGB image with high-resolution LOFAR contours overlaid. *Bottom right panel*: *Chandra* X-ray image smoothed on a scale of 1″ with low-resolution LOFAR contours overlaid. All the panels depict the same region of the sky.

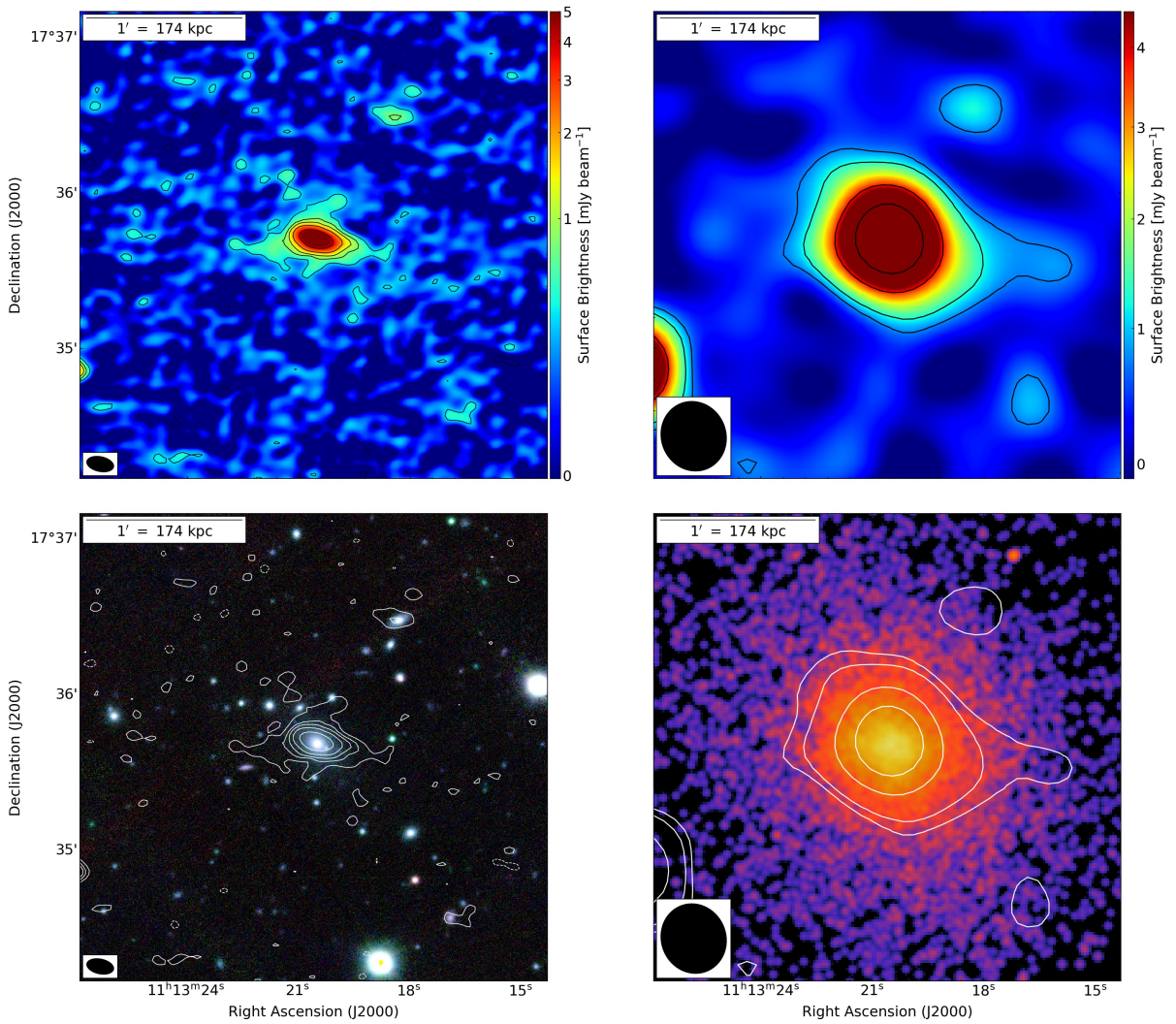

Figure 3.8: A1204: *Top left panel*: High-resolution 144 MHz LOFAR image. Levels:[-3, 3, 6, 9, 15, 30]$\times\sigma$ (where $\sigma = 0.13$ mJy beam^{-1}). The beam is $10.6'' \times 5.7''$ and is shown in the bottom left corner of the image. *Top right panel*: Low-resolution 144 MHz LOFAR image, obtained after subtraction of central source. Levels=[-3, 3, 5, 15, 30]$\times\sigma$ (where $\sigma = 0.25$ mJy beam^{-1}). The beam is $27.1'' \times 24.9''$ and is shown in the bottom left corner of the image. *Bottom left panel*: Optical *Pan-STARRS* RGB image with high-resolution LOFAR contours overlaid. *Bottom right panel*: *Chandra* X-ray image smoothed on a scale of $1''$ with low-resolution LOFAR contours overlaid. All the panels depict the same region of the sky.

data at same resolution of 15″). The diffuse emission has a mean spectral index between 144 and 1283 MHz of $\alpha = 1.1 \pm 0.1$, with larger dispersion in the regions outside the sloshing boundaries. A detailed study of this source is reported in Chapter 5.

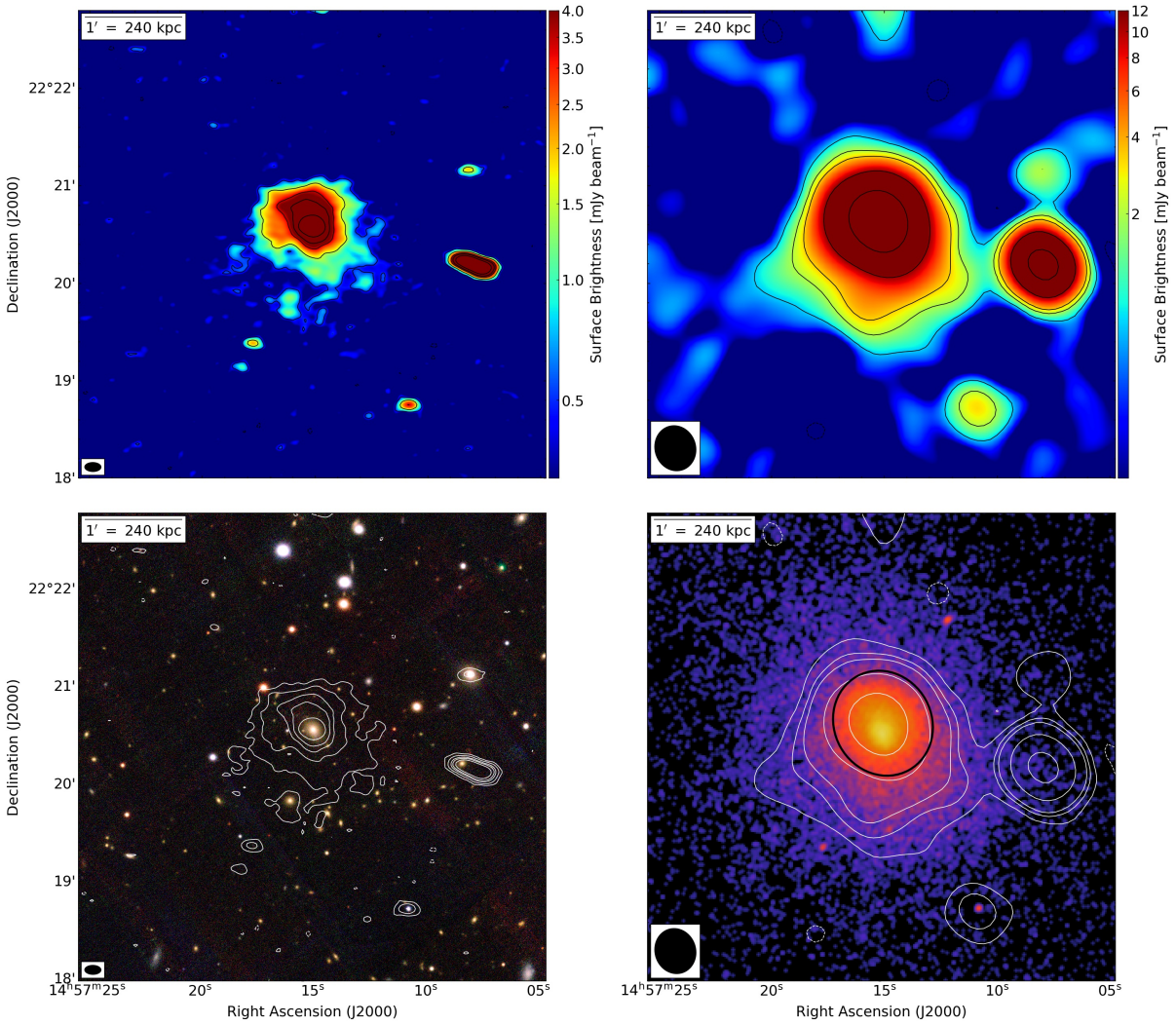

Figure 3.9: MS 1455.0+2232: *Top left panel*: High-resolution 144 MHz LOFAR image. Levels:[-3, 3, 9, 20, 30, 50]×σ (where $\sigma = 0.17$ mJy beam^{-1}). The beam is 10.1″ × 5.6″ and is shown in the bottom left corner of the image. *Top right panel*: Low-resolution 144 MHz LOFAR image, obtained after subtraction of central source and surrounding point sources. Levels=[-3, 3, 9, 15, 50, 150*noise]×σ (where $\sigma = 0.22$ mJy beam^{-1}). The beam is 28.1″ × 25.1″ and is shown in the bottom left corner of the image. *Bottom left panel*: Optical *Pan-STARRS* RGB image with high-resolution LOFAR contours overlaid. *Bottom right panel*: *Chandra* X-ray image smoothed on a scale of 1″ with low-resolution LOFAR contours overlaid. The black circle indicates the boundaries of the sloshing region found by Riseley et al. (2022). All the panels depict the same region of the sky.

RX J1532.9+3021

RX J1532.9+3021 (hereafter RXJ1532) is a luminous X-ray cool-core cluster at z=0.362, which presents two X-ray cavities detected west and east of the core, and a cold front at the edge of the western cavity (Hlavacek-Larrondo et al., 2013). VLA and GMRT observations at 325 MHz, 610 MHz and 1.4 GHz reveal a prominent mini halo in the cluster core, with a total extension of 100 kpc, surrounding the BCG (Hlavacek-Larrondo et al., 2013; Giacintucci et al., 2014a). The mini halo has a total spectral index of $\alpha = 1.20 \pm 0.07$. A second radio galaxy is observed at $\sim 2.6'$ ($\sim$ 800 kpc) projected

distance south-west of the cluster centre. In the same position, a cluster has been detected (GMBCG J233.19725+30.31626; Hao et al., 2010), located at z=0.358, hence compatible with the redshift of RXJ1532. Our LOFAR image (Fig. 3.10) confirms the presence of a central mini halo with a total extension of $\sim$ 240 kpc. No more diffuse emission is detected.

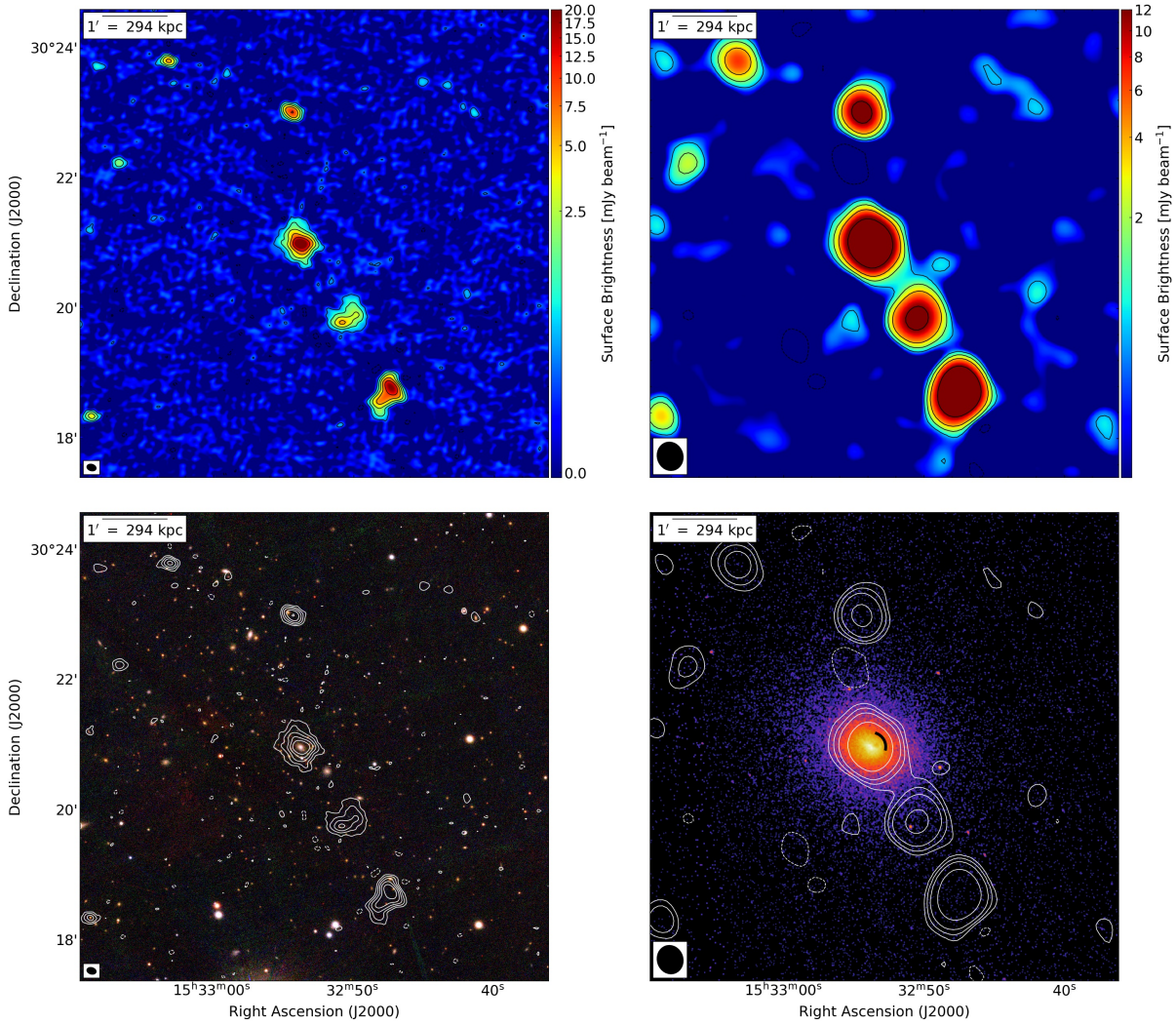

Figure 3.10: RX J1532.9+3021: *Top left panel*: High-resolution 144 MHz LOFAR image. Levels:[-3, 3, 9, 20, 40,80]$\times\sigma$ (where σ = 0.13 mJy beam^{-1}). The beam is 8.8″ × 6.2″ and is shown in the bottom left corner of the image. *Top right panel*: Low-resolution 144 MHz LOFAR image, obtained after subtraction of central source. Levels=[-3, 3, 7, 15, 50,100]$\times\sigma$ (where σ = 0.24 mJy beam^{-1}). The beam is 26.6″ × 23.9″ and is shown in the bottom left corner of the image. *Bottom left panel*: Optical *Pan-STARRS* RGB image with high-resolution LOFAR contours overlaid. *Bottom right panel*: *Chandra* X-ray image smoothed on a scale of 1″ with low-resolution LOFAR contours overlaid. The black arc indicates the position of cold front detected by (Hlavacek-Larrondo et al., 2013). All the panels depict the same region of the sky.

RX J1720.1+2638

RX J1720.1+2638 (hereafter RXJ1720.1) is a cool-core galaxy cluster located at z=0.164, which hosts a bright central mini halo with a size of 70 kpc and a spectral index of $\alpha_{237}^{4850} = 1.0 \pm 0.1$, and a lower surface brightness extension to the east (Giacintucci et al., 2014b). Two cold fronts detected with *Chandra* appear to confine the mini halo (Mazzotta et al., 2001; Mazzotta & Giacintucci, 2008). In the cluster field there is also a HT radio

galaxy, associated with a cluster member galaxy (Owers et al., 2011). LOFAR HBA observations revealed the presence of diffuse emission on larger scales, which extends up to 560 kpc (Savini et al., 2019). Here, we re-analysed LOFAR HBA data combining two observations of this source (Fig. 3.11). To constrain the spectral index of the large-scale emission we requested and obtained LOFAR LBA observations (PI Biava). We found an ultra-steep spectrum with $\alpha \sim 3$ (Biava et al., 2021a). Our analysis, performed combining radio and X-ray data of this cluster, suggests the large-scale diffuse emission resembles a giant radio halo, generated by re-acceleration of particles after a minor merger (Biava et al., 2021a). A detailed study of this cluster is reported in Chapter 4.

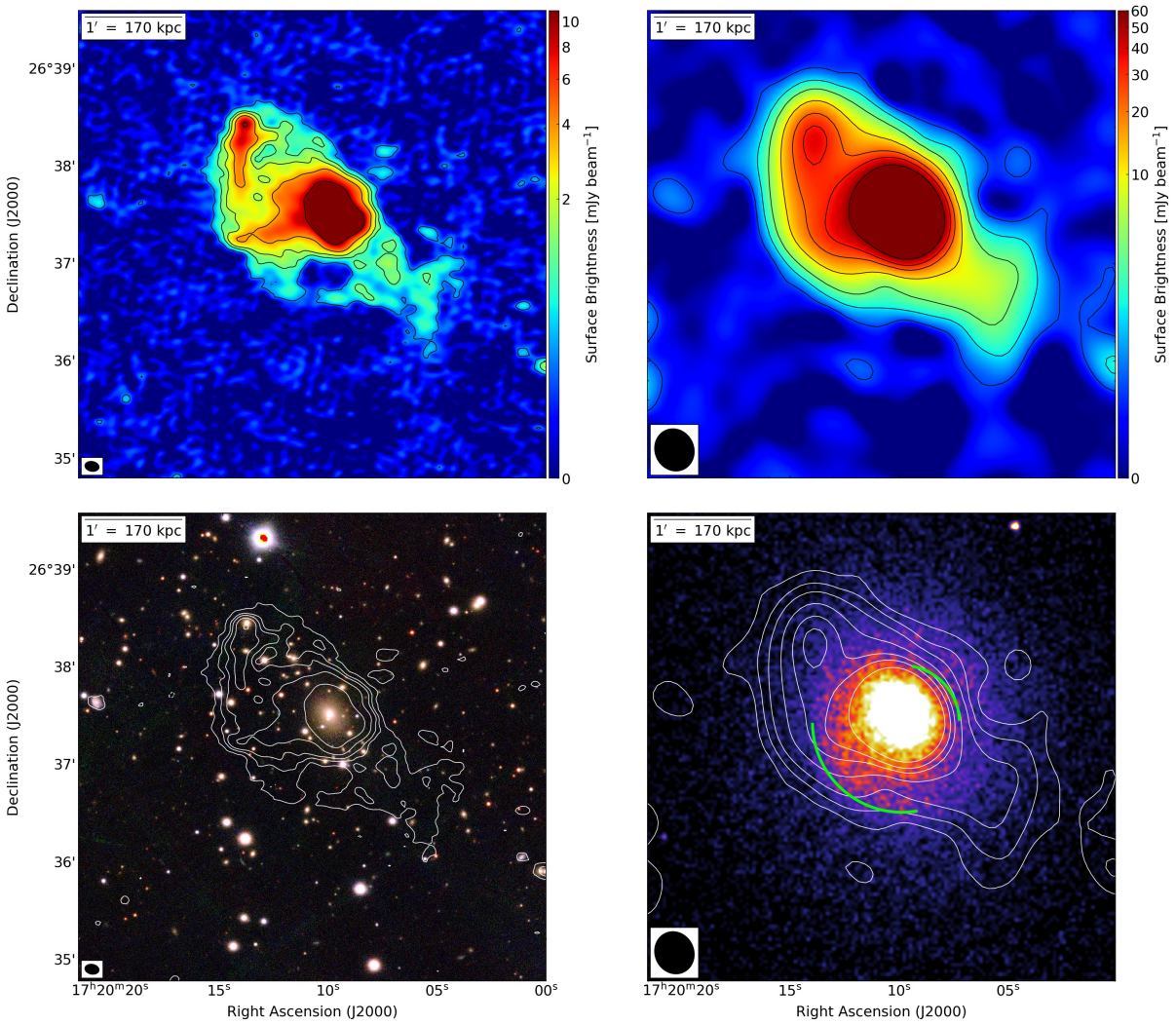

Figure 3.11: RX J1720.1+2638: *Top left panel*: High-resolution 144 MHz LOFAR image. Levels:[-3, 3, 9, 15, 30, 80]$\times\sigma$ (where $\sigma = 0.12$ mJy beam^{-1}). The beam is $8.8'' \times 6.1''$ and is shown in the bottom left corner of the image. *Top right panel*: Low-resolution 144 MHz LOFAR image. Levels=[-3, 3, 9, 20, 50, 100, 150, 250]$\times\sigma$ (where $\sigma = 0.22$ mJy beam^{-1}). The beam is $26.5'' \times 24.0''$ and is shown in the bottom left corner of the image. *Bottom left panel*: Optical *Pan-STARRS* RGB image with high-resolution LOFAR contours overlaid. *Bottom right panel*: *Chandra* X-ray image smoothed on a scale of $3''$ with low-resolution LOFAR contours overlaid. The green arc indicates the position of the cold fronts found by Mazzotta & Giacintucci (2008). All the panels depict the same region of the sky.

RX J1720.2+3536

The thermal emission of RX J1720.2+3536 (hereafter RXJ1720.2, z=0.391) is slightly elongated toward the south. Giacintucci et al. (2017) indicated the presence of a candidate

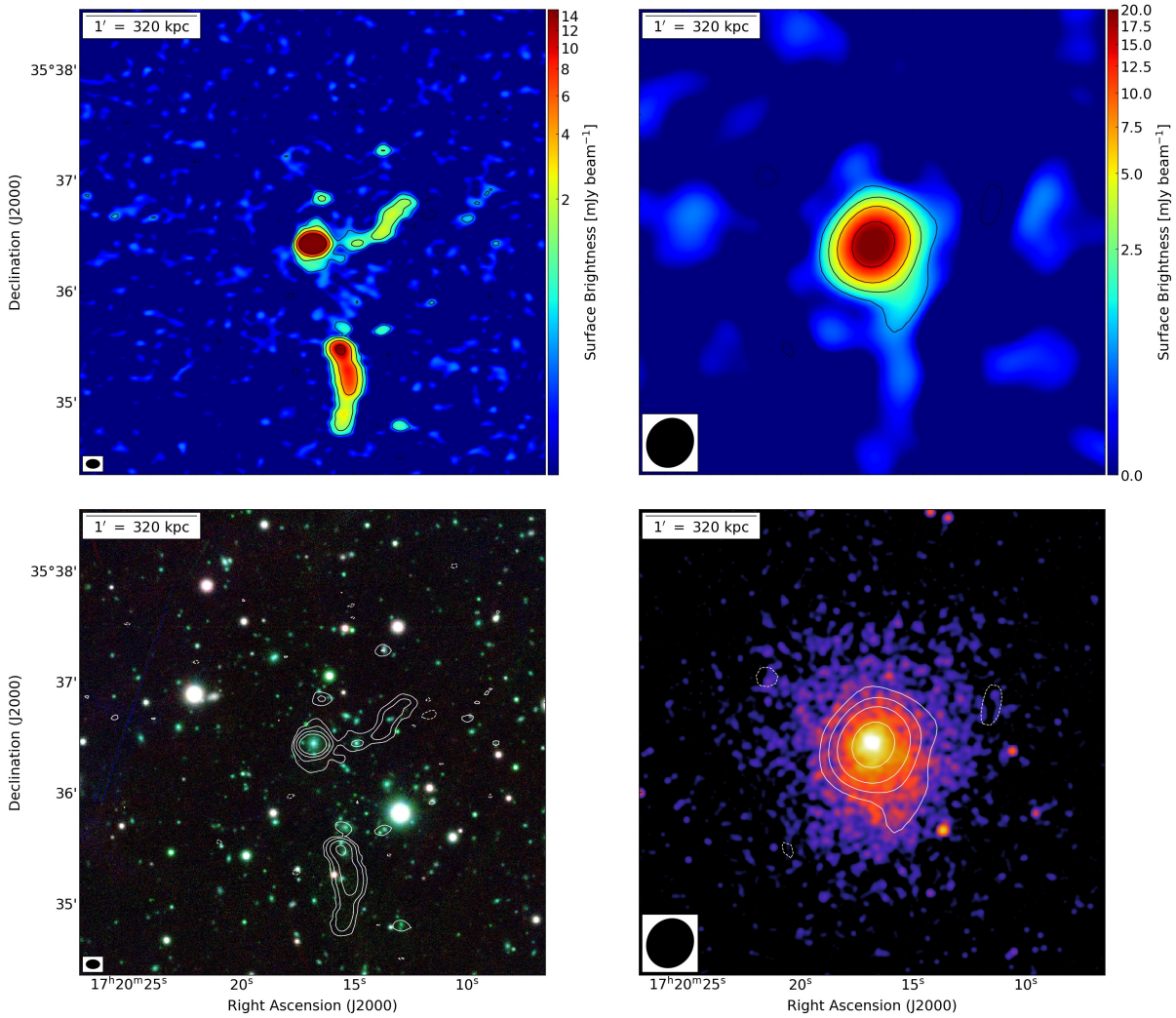

Figure 3.12: RX J1720.2+3536. *Top left panel*: High-resolution 144 MHz LOFAR image. Levels:[-3, 3, 9, 30, 90]×σ (where $\sigma = 0.14$ mJy beam^{-1}). The beam is $7.3'' \times 4.8''$ and is shown in the bottom left corner of the image. *Top right panel*: Low-resolution 144 MHz LOFAR image. Levels=[-3, 3, 9, 20, 50]×σ (where $\sigma = 0.30$ mJy beam^{-1}). The beam is $27.4'' \times 24.7''$ and is shown in the bottom left corner of the image. *Bottom left panel*: Optical *Pan-STARRS* RGB image with high-resolution LOFAR contours overlaid. *Bottom right panel*: *Chandra* X-ray image smoothed on a scale of $3''$ with low-resolution LOFAR contours overlaid. All the panels depict the same region of the sky.

mini halo in this cluster, but no radio images are reported. (Hlavacek-Larrondo et al., 2012) reported the presence of two cavities in the central regions of this cluster, one to the north (at a distance of 19 kpc from the core) and another smaller and less clear to the south-east (6.7 kpc form the core). With our LOFAR data (Fig. 3.12) we do not detect a mini halo at the centre of this cluster, only a central radio source with a small extension in the north-south direction (total extension 140 kpc). The central compact source has a flux density of $S_{144\ \mathrm{MHz}} = 155$ mJy. It is detected also by the FIRST survey with a flux density of $S_{1400\ \mathrm{MHz}} = 16$ mJy. Therefore it has a spectral index of $\alpha \sim 1.0$. In the field there is also a HT radio galaxy on the south and two radio galaxies on the west of the cluster centre, one is compact while the most distant one presents two radio lobes as brilliant as the core. No further diffuse emission is detected at lower resolution.

MACS J2245.0+2637

The cluster MACS J2245.0+2637 (hereafter MACSJ2245), at z=0.304, presents a pronounced cool-core (Ebeling et al., 2010) and a small potential X-ray cavity (Hlavacek-Larrondo et al., 2012). Giacintucci et al. (2017) indicated the absence of diffuse radio emission in this cluster at 610 MHz, but no radio images are reported. With LOFAR (Fig. 3.13), we detected the central radio galaxy and radio emission extending towards the south of uncertain interpretation. At higher resolution of $4.5 \times 3.2''$ (insert box in the upper left panel of Fig. 3.13), we found the central source presents two putative radio lobes which are not aligned. Surrounding the central galaxy there is a hint of diffuse emission with low surface brightness. However, the flux of this component is not dominant even at lower resolution, where the large extension of the radio emission is due to the large beam of the image.

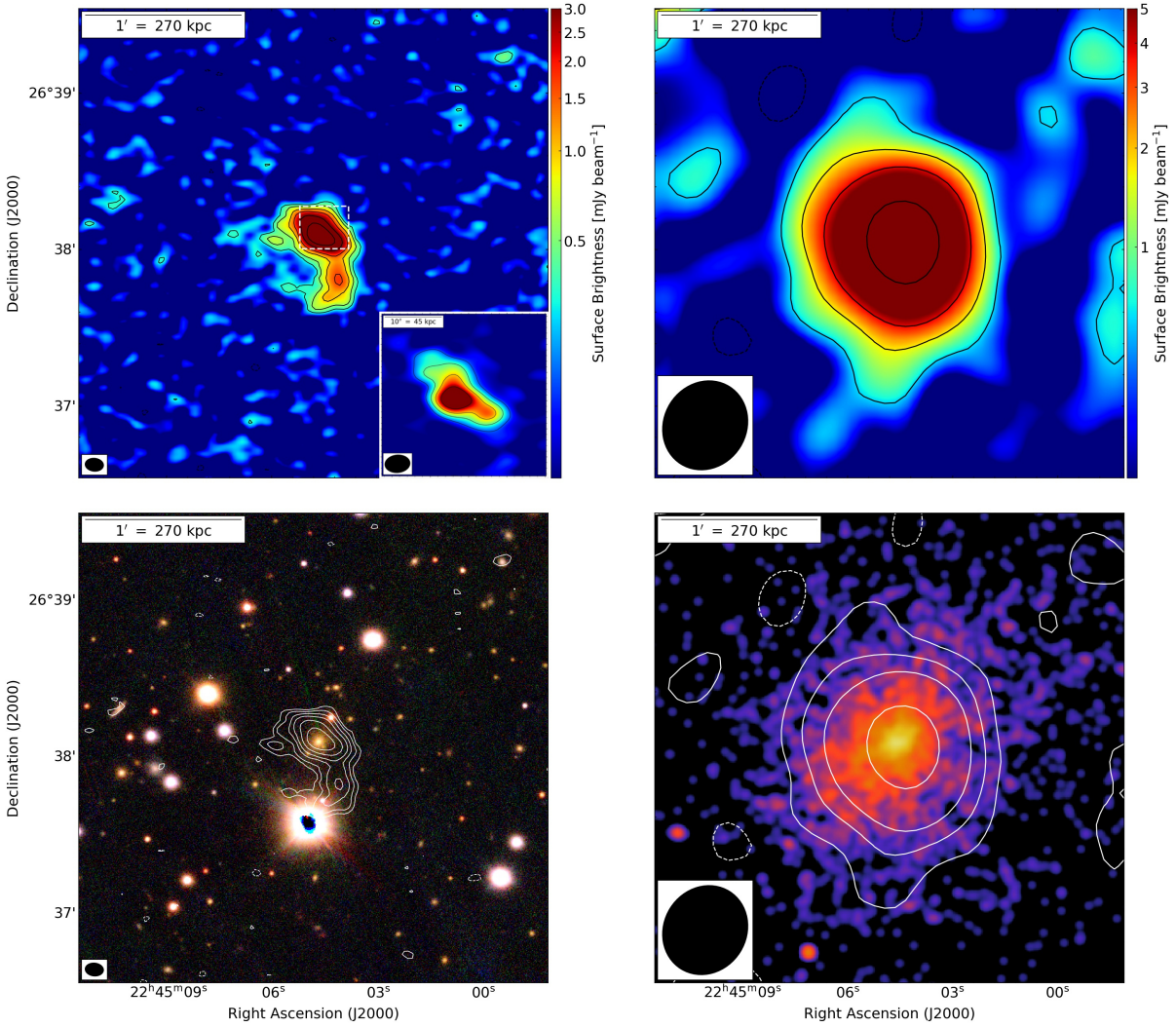

Figure 3.13: MACS J2245.0+2637: *Top left panel*: High-resolution 144 MHz LOFAR image. Levels:[-3, 3, 5, 9, 15, 30, 60]$\times\sigma$ (where σ = 0.11 mJy beam^{-1}). The beam is $7.0'' \times 5.0''$ and is shown in the bottom left corner of the image. The insert box shows the image of the central source at $4.5 \times 3.2''$ resolution obtained with Briggs weighting robust = -1.25 and inner *uv*-cut. *Top right panel*: Low-resolution 144 MHz LOFAR image, obtained after central source subtraction. Levels=[-3, 3, 9, 20, 60]$\times\sigma$ (where σ = 0.19 mJy beam^{-1}). The beam is $35.1'' \times 31.7''$ and is shown in the bottom left corner of the image. *Bottom left panel*: Optical *Pan-STARRS* RGB image with high-resolution LOFAR contours overlaid. *Bottom right panel*: *Chandra* X-ray image smoothed on a scale of $3''$ with low-resolution LOFAR contours overlaid. All the panels depict the same region of the sky.

Table 3.3: LOFAR classification and physical parameters of the detected radio emission.

Cluster name	Classification	D_{max} [kpc]	S_{tot} [mJy]	Notes
PSZ1G139.61+24	MH+H	810	37	Confirmed
MS 0735.6+7421	BCG+lobes	530	4700	No diffuse emission
MS 0839.8+2938	BCG+lobes	110	160	No diffuse emission
Z2089	BCG	130	100	No diffuse emission
RBS 0797	MH	230	270	Confirmed
A1068	MH+H	400	91	Detected new component
A1204	BCG	140	18	No diffuse emission
MS 1455.0+2232	MH+H	560	170	Detected new component
RX J1532.9+3021	MH	240	92	Confirmed
RX J1720.1+2638	MH+H	560	700	Confirmed
RX J1720.2+3536	BCG	140	170	No diffuse emission
MACS J2245.0+2637	cMH	200	49	New detection

3.3.2 Radial profiles

The surface brightness of radio halos decreases with increasing distance from cluster centre. Therefore, their radial profiles are typically fitted with an exponential law (e.g., Murgia et al., 2009) of the form:

$$I(r) = I_0 e^{-r/r_e}, \tag{3.1}$$

where I_0 is the central surface brightness and r_e is the e-folding radius.

We want to investigate if the radio emission in clusters with a MH and large-scale diffuse emission is made of a single or two different components. We then derived their averaged surface brightness radial profiles. We used low-resolution source-subtracted images, convolved with a circular gaussian beam. When the surrounding sources have not been subtracted, or the subtraction has not produced good results, we have masked their emission and we have excluded the masked pixels from the calculation of the surface brightness. We extracted the brightness profiles along various directions to check for spatial differences, as in most of the cases the radio emission is not symmetric with respect to the cluster centre. The regions used to extract the profiles are indicated in Fig. 3.14 and 3.15. We averaged the radio brightness in concentric sectors, centred on the cluster centre and with a width equal to the pixel scale. Thus the values are not statistically independent, but allow us to trace the profiles. The uncertainties represent the error on the mean, calculated as the standard deviation within the single region divided by the square root of the number of beams. We excluded points with surface brightness lower than three times the image noise.

We found a discontinuity in the radial profile of all clusters which presents large-scale diffuse radio emission (PSZ1G139, A1068, MS1455 and RXJ1720.1). The radio emission decreases exponentially with increasing radius, from the cluster centre up to a certain distance where we found an excess of surface brightness, indicating the presence of a second component. This discontinuity, however, is not present along all the directions considered, as we will see in detail below for each cluster.

We then performed a fit on the extracted radial profiles, using a single or double exponential, as appropriate. The results of the fit are reported in Table 3.4. When a

Table 3.4: Radial profile fits.

Cluster name	Sector	Component	Fit	χ^2_{red}
PSZ1G139.61+24	North-west	MH+H	Double exp	1.6
		MH	Single exp	0.35
	South-east	MH	Single exp	0.16
A1068	North-west	MH+H	Double exp	0.75
		MH	Single exp	0.38
	South-east	MH+H	Double exp	0.41
		MH	Single exp	0.17
MS 1455.0+2232	North	MH	Single exp	11
	South	MH+H	Double exp	0.55
		MH	Single exp	0.31
RX J1720.1+2638	South-west	MH+H	Double exp	2.2
		MH	Single exp	0.6

discontinuity is present, we found that the central emission, before the discontinuity, is well fitted by a single exponential fit (red dashed line), as found in other mini halos (e.g., Murgia et al., 2009). We also found that a double exponential fit (orange dash-dotted line) is a good approximation for the profile of the whole emission, indicating that also the external component can be quite well represented by a halo-like profile.

For PSZ1G139 (Fig. 3.14), we detected a discontinuity only in the north-west sector, where there is a cold front. The change in the profile, however, does not occur at the cold front position ($\sim$ 100 kpc from cluster centre, black arc), but at a greater distance from cluster centre ($\sim$ 295 kpc, green arc). The south-east profile, instead, is well fitted by a single exponential profile. We would have expected a discontinuity on smaller scales in both the directions, where LOFAR has detected diffuse emission on a larger scale than GMRT observation (Savini et al., 2018). However, this discontinuity could be present but not visible as it is smoothed at the resolution of 35″. Extracting a profile at higher resolution is trivial for the presence of radio galaxies at the centre of the cluster. To understand if the radio emission responsible of the discontinuity in the radio profile is associated to the cluster or to a background source, we extracted X-ray radial profiles in the same regions used for the radio profiles. We also extracted the X-ray profiles in two control regions, perpendicular to the extension of the radio emission. We smoothed the X-ray map to the same resolution of the radio image (35″). We note that at large distances the X-ray profile in the north direction, where the radio discontinuity is detected, flattens. The same behaviour is observed in one of the control regions, while it is less pronounced in the control region along the west direction. From the X-ray map there still appears to be some emission in both the north and east sectors. This indicates that large-scale radio emission is associated with the cluster. We also note that the X-ray surface brightness in the southern sector is higher than in the other sectors, at the same distance. This is consistent with the fact that the X-ray emission is elongated in this direction, as clearly seen in Fig. 3.2.

In A1068 (Fig. 3.15, upper panels) we detect a discontinuity both in the north-west and south-east sectors, roughly at the same distance from the cluster centre (105 kpc). The radio discontinuities (green arcs) are located in the proximity of the X-ray cold fronts (black arcs).

Compared to the two previous cases where the diffuse emission on a large scale is

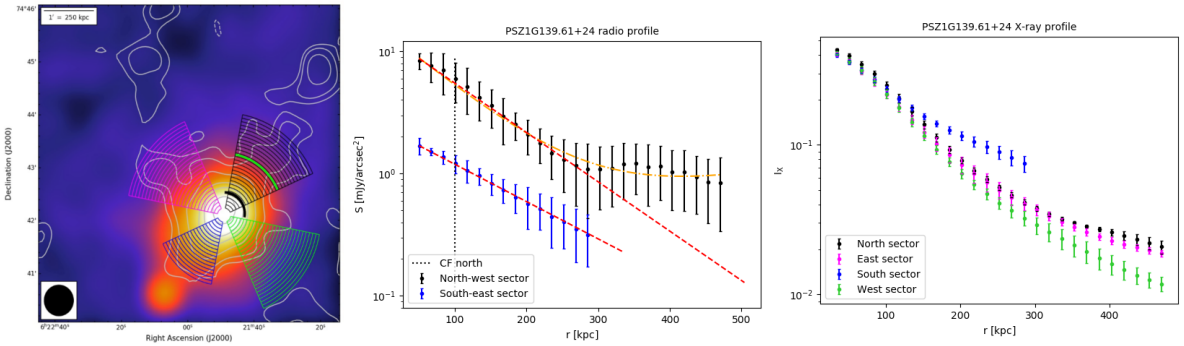

Figure 3.14: Radial profiles of PSZ1G139. *Left panel: Chandra* X-ray map of PSZ1G139 with overlaid LOFAR contours and sectors used to extract radial profiles. The black arc indicates the position of the cold front, while green arc indicates the radius of the radio discontinuity. *Central panel:* Radio radial profiles extracted along the north-west (black) and south-east (blue) sectors. The red dashed line is obtained by a single exponential fit, while orange dash-dotted line is obtained by a double exponential fit. *Right panel:* X-ray radial profiles extract along the north-west (black), north-east (magenta), south-east (blue) and south-west (green) sectors.

detected only at low resolution (35″), in MS1455 and RXJ1720.1 it is clearly seen even at a resolution of 15″. We then extracted the profiles from an image of the clusters at this resolution to be able to detect variations on a smaller scale.

MS1455 (Fig. 3.15, central panels) presents a discontinuity in the southern sector in coincidence with the sloshing boundary ($r = 120$ kpc). In the northern sector, instead, there is no evident discontinuity, however the profile does not follow an exponential law. This difference may be due to the fact that the large-scale emission extends mainly towards the south of the cluster centre.

For RXJ1720.1 (Fig. 3.15, lower panels) we extracted a radial profile only in the south-west direction, as toward north-east there is a HT galaxy that we have not been able to subtract. However, our analysis indicate that the large-scale diffuse emission is also present in that direction (Biava et al., 2021a). Since in this case we have not been able to subtract the central source, we extracted the profile excluding the central annuli. Also in this cluster we found a clear excess of surface brightness in the external regions, respect to an exponential decay. The discontinuity in the profile coincides with the transition zone between mini halo and large-scale emission ($r = 88$ kpc), indicative of a double radio component, as already lightened by the net change in the spectral index inside and outside the cluster core.

Finally, we extracted the profiles for the two clusters (RXJ1532 and RBS797) in which we confirmed the presence of a MH, but we do not detect diffuse emission on larger scales. Unlike the sources previously analysed, the radio emission of RXJ1532 and RBS797 is circularly symmetric around the cluster centre. We then extracted the profiles using four sectors, which cover the full extension of the diffuse emission, to check for dissimilarities in different directions (Fig. 3.16). We do not detect a discontinuity in the radio profiles of RXJ1532 and RBS797 in any of the four sectors tested, all profiles have the same trend. This confirms that all the diffuse emission observed in these clusters belongs to the mini halo.

3.3.3 Spectral index distribution

In this section, we analyse the spectral properties of clusters with a double radio component to better understand their origin. If the radio emission inside and outside the sloshing region has a different nature, we expect a net difference in the spectral index of the two components. On the other hand, a diffusion of particles from the cluster centre to the outskirt, will produce a smooth spectral gradient. Furthermore, the minor merger

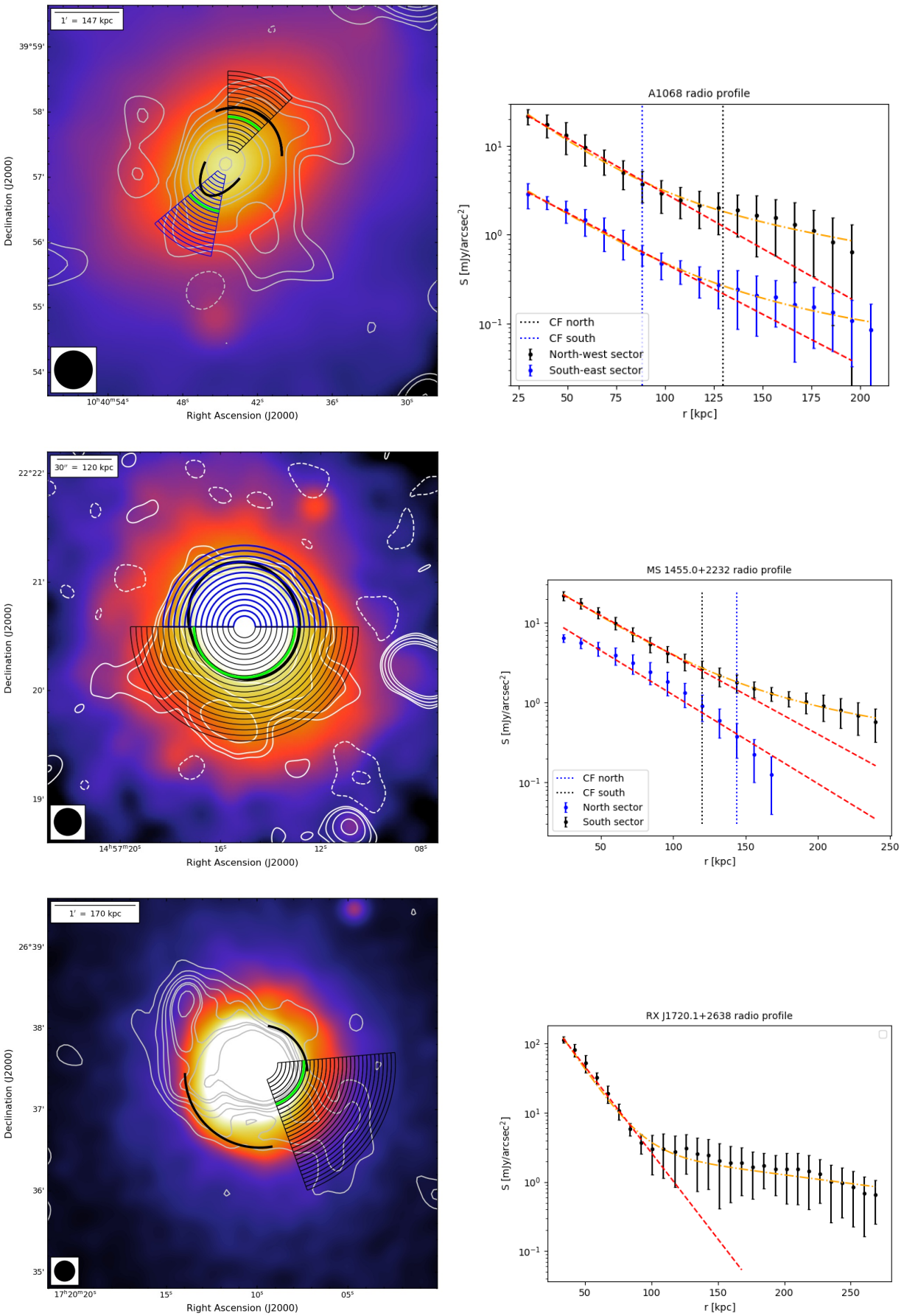

Figure 3.15: Radial profiles of A1068 (*Upper panels*), MS1455 (*Central panels*) and RXJ1720.1 (*Lower panels*). *Left panels: Chandra* X-ray maps with overlaid LOFAR contours and sectors used to extract radial profiles. The black arcs indicate the position of the cold fronts, while green arcs indicate the radius of the radio discontinuity. *Right panels:* Radio radial profiles extracted along the sectors indicated in the left panels. The red dashed line is obtain by a single exponential fit, while orange dash-dotted line is obtained by a double exponential fit.

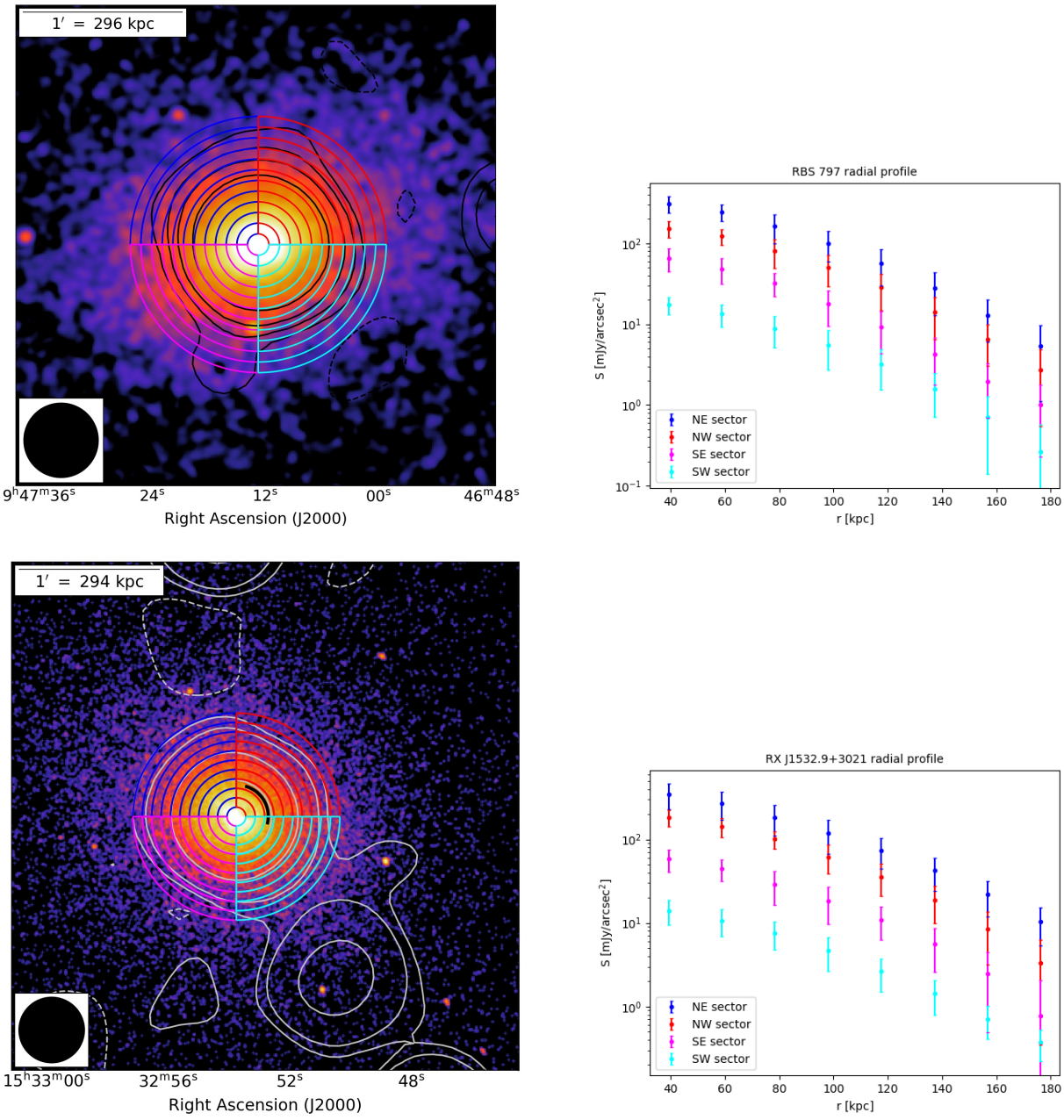

Figure 3.16: Radial profiles of RBS797 (*Upper panels*) and RXJ1532 (*Lower panels*). *Left panels: Chandra* X-ray maps with overlaid LOFAR contours and sectors used to extract radial profiles. The black arc indicates the position of the cold front. *Right panels:* Radio radial profiles extracted along the sectors indicated in the left panels.

scenario predicts a steeper spectral index in the large-scale emission with respect to the the mini halo spectra (e.g., Brunetti et al., 2004).

A detailed spectral analysis of each source is reported in the following Chapters. Here, we investigate the spectral index distribution. We extracted radial spectral index profiles using rectangular regions shown in the left panels of Fig. 3.17, superposed on spectral index maps. In the right panels, we report the mean spectral index inside each box and the associated error, estimated as the standard deviation inside each box divided for the square of the number of the beams in that region.

For A1068 we estimate the spectral index between LOFAR observations at 144 MHz and GMRT observations at 400 MHz. We found a mean central spectral index of $\alpha \sim 1.3$. In the north-west direction the spectral index remains quite constant up to 100 kpc from cluster centre, then it steepens reaching a maximum spectral index of $\alpha \sim 2.1$. As the extreme part of the diffuse emission in that direction is not detected at 400 MHz, we derived a limit of $\alpha \geq 2.6$ considering the GMRT noise and the LOFAR mean flux density in that region. In the south-east direction, instead, the trend is a little different. Moving away from the cluster centre the spectral index flattens slightly, then at a distance of 100 kpc it steepens as in the north direction, reaching a maximum spectral index of $\alpha \sim 1.5$, then decreases again in the outermost regions, where $\alpha \sim 1.3$. We note that the steepening in the spectral index roughly happens at the same distance from the cluster centre in which there is also a discontinuity in the radio profile, indicating the two components have different spectral properties.

For MS1455 we estimated the spectral index between 144 and 1283 MHz. The spectral index is quite uniform throughout the full extension of the diffuse emission, with an average value of $\alpha \sim 0.97$. A steeper region is present to the south, where the mean spectral index is $\alpha \sim 1.34$. However, this steepening is not observed in the whole southern region outside the sloshing edge. We then extracted the spectral index radial profiles along three different directions: in the south direction there is a sharp increase in the spectral index, while in the south-east and south-west directions there are some fluctuations of the spectral index with a slight decrease in coincidence of the sloshing region and then an increase in the outermost region for the south-east direction and an opposite trend in the south-west direction. So there is no evident spectral index change inside and outside the sloshing region.

For RXJ1720.1 we estimated the spectral index between 54 and 144 MHz. There is a steepening in the spectral index from $\alpha \sim 1.3$ at cluster centre, up to $\alpha \sim 3$ at a distance of roughly 100 kpc, where the large-scale diffuse emission becomes dominant. Therefore, the two components have a different nature.

For PSZ1G139, instead, we were not able to create a spectral index map with the data available at the moment, as the large-scale diffuse emission is only detected by LOFAR. Savini et al. (2018), using GMRT 610 MHz and LOFAR 144 MHz data, found a spectral index of $\alpha \sim 1.3$ for the mini halo and estimated a limit of $\alpha \geq 1.7$ for the large-scale diffuse emission. The limit was calculated injecting a mock radio halo in the GMRT (610 MHz) visibilities, as explained in the following section, and measuring the flux density at 2σ. Therefore, also in this case there is a steepening of spectral index in the outer component.

To summarise, we detected a difference in the spectral index in the two components of A1068 and RXJ1720.1, with an ultra-steep spectrum in the large-scale emission, supporting the minor merger scenario. For MS1455, instead, the spectral index is quite uniform and no steepening is observed at sloshing boundaries, suggesting a different origin respect to the previous cases.

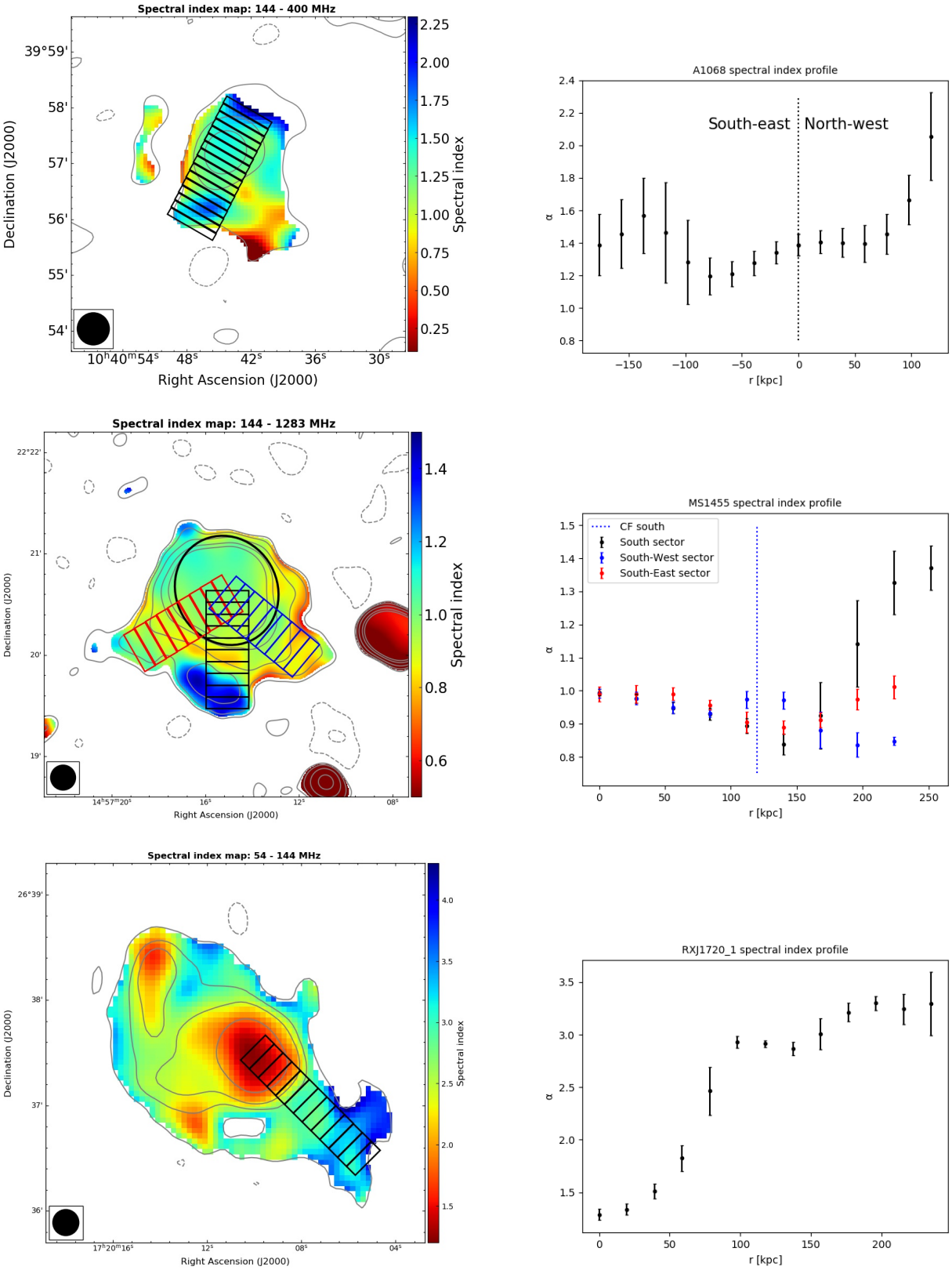

Figure 3.17: Spectral index profiles of A1068 (*upper panels*, MS1455 (*central panels*) and RXJ1720.1 (*lower panels*). *Left panels:* Spectral index maps with overlaid the regions used to extract the spectral index profiles. *Right panels:* Corresponding spectral index profiles.

Table 3.5: Radio halo power.

Cluster	M_{500} [10^{14} $M_\odot$]	Expected P_{150MHz} [10^{24} W/Hz]	Measured P_{150MHz} [10^{24} W/Hz]
PSZ1G139.61+24	7.6	40	5.7
A1068	3.8	0.57	0.67
MS 1455.0+2232	3.5	0.32	11
RX J1720.1+2638	5.9	8.5	12

3.3.4 Radio power and upper-limits

Radio observations and radial profile analysis have revealed the presence of a double radio component, mini halo + giant radio halo, in four clusters.

To compute the radio power of radio halos in our sample, we were not able to fit exponential profiles on the images due to the irregular morphology of the emission and the presence of contaminating sources difficult to exclude. Therefore, we estimated the integrated flux densities of giant radio halos in these clusters from the low resolution LOFAR images, considering all the emission enclosed by 3σ surface brightness contours and then we subtracted the contribution of mini halo and radio galaxies. We note that in that way we are providing a lower limit to the real integrated flux of the giant radio halo, as it is present also in the central regions of the cluster, superposed to the mini halo. So, we added the contribution of the radio halo in the central regions, estimating it has the same mean surface brightness as in the external regions. The final values are reported in Table 3.5, where we also indicated the expected radio power according to the $M_{500} - P_{150\ \mathrm{MHz}}$ relation obtained by van Weeren et al. (2021) on giant radio halos in the LoTSS first data release, for comparison. We note that the biggest difference is found in the power of MS1455, for which we measured a power two order of magnitude higher than the expected power from the correlation. However, the mass of this cluster has been estimated from the $M_{500} - T_X$ correlation of Vikhlinin et al. (2009), which tends to underestimate the mass of cool-core clusters by 30%. With a mass 30% higher, the gap between the measured and expected power would reduce to one order of magnitude, as also found for PSZ1G139. For the other two clusters, instead, the measured radio halo power matches with the value obtained from the correlation.

For the clusters in the sample where no giant radio halos are detected, we provided upper limits on the flux densities. Following the procedure described in Bonafede et al. (2017), we derived upper limits injecting a mock radio halo in the *uv*-plane of each cluster. We modelled the radio brightness profile of the giant radio halo as an exponential law described by Eq. 3.1. We derived r_e from the $P_{1.4GHz} - r_e$ and $M_{500} - P_{150\ \mathrm{MHz}}$ correlations found by Murgia et al. (2009) and Cuciti et al. (2021), respectively. To derive a starting value of I_0, instead, we used the $M_{500} - P_{150\ \mathrm{MHz}}$ correlation derived by van Weeren et al. (2021). For each cluster, we chose a region void of sources to inject the halo, we Fourier transformed the mock halo to add it to the *uv*-data of LOFAR observations that we imaged using a *uv*-taper of $20''$ to improve the sensitivity on diffuse emission. We then increased or decreased the injected value of I_0 until the largest linear scale at 2σ contours ($D_{2\sigma}$) of the injected halo is $\sim R_{\mathrm{H}} = 2.6 \times r_e$, i.e. it is at least half of the expected halo size (Bonafede et al., 2017). In this case we considered the radio halo detected and we used the obtained I_0 to derive the upper limit to the halo power. The results are reported in Table 3.6.

Finally, we investigated the distribution of the observed giant radio halos and mock halos in the radio power–mass diagram (Fig. 3.18). We represented our detection with a

Table 3.6: Radio halo upper limits.

Cluster	M_{500} [10^{14} $M_\odot$]	Expected $P_{150\mathrm{MHz}}$ [10^{24} W/Hz]	Measured $P_{150\mathrm{MHz}}$ [10^{24} W/Hz]	r_e [″]	$D_{2\sigma}$ [″]
MS 0735.6+7421	5.0	3.1	2.2	42	112
MS 0839.8+2938	3.4	0.29	1.3	33	80
Z2089	3.2	0.19	0.67	27	72
RBS 0797	5.6	12.4	4.7	37	98
A1204	3.3	0.03	0.53	26	71
RX J1532.9+3021	4.7	2.1	2.9	28	73
RX J1720.2+3536	6.1	9.8	4.2	33	88
MACS J2245.0+2637	4.8	2.3	3.7	32	86

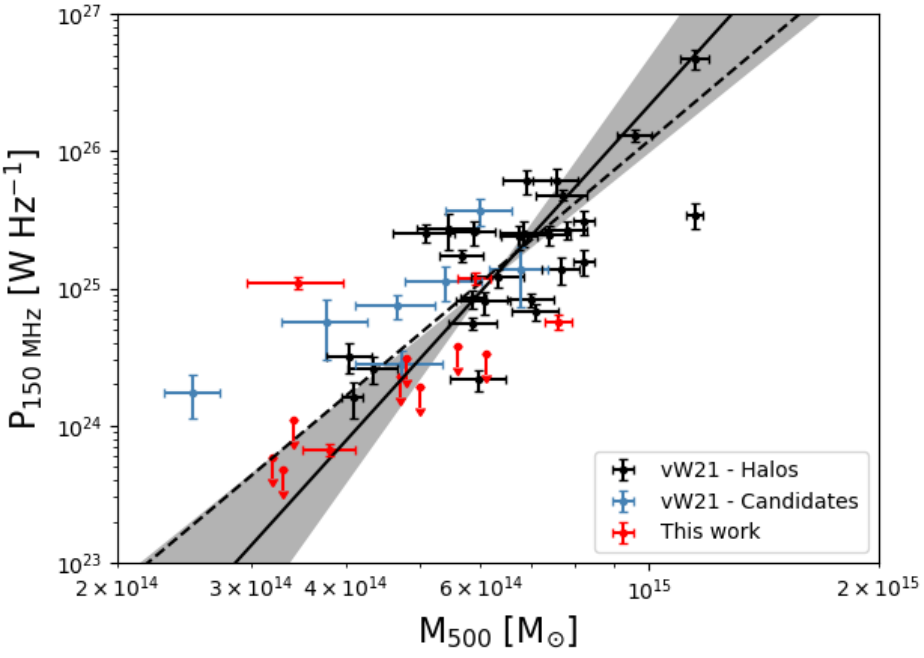

Figure 3.18: Radio power at 150 MHz vs cluster mass (M_{500}). The clusters with a giant radio halo in our sample are indicated in red. For the clusters without giant radio halo detection we derived upper limits (red arrows). Giant radio halos studied in van Weeren et al. (2021) are reported in black and their candidates in blue. Black lines indicate the correlation found by van Weeren et al. (2021) performing a BCES orthogonal fit (solid line) or BCES bisector fit (dashed line) on giant radio halos, candidates excluded. The shaded region shows the 3σ region of the BCES orthogonal fit.

red dot and upper limits with a red arrow. For comparison we also represented the giant radio halos in the sample of van Weeren et al. (2021) (blue dots for confirmed giant radio halos, while cyan dots for candidates). We also reported in the plot the $M_{500} - P_{150\ \mathrm{MHz}}$ correlation found by van Weeren et al. (2021), using a BCES orthogonal regression method and excluding radio halo candidates (black solid line), with corresponding 3σ region (grey shaded area). We also reported their slope derived with a BCES bisector fits (black dashed line), radio halo candidates excluded, for comparison with other works (Bonafede et al., 2017; Cuciti et al., 2021).

Overall, the radio power of our giant radio halos is in agreement with the halo power of van Weeren et al. (2021) sample. The cluster that differs most from the correlation is MS1455, for which the mass should be underestimated, as mentioned before. Our upper limits are consistent with the correlation, so we cannot exclude these clusters should host a giant radio halo under the noise level. More sensitive data are necessary.

3.4 Discussion

In this Chapter we presented LOBAR HBA observations of twelve cool-core clusters selected based on their dynamical status, to search for diffuse emission on cluster-scale. In this section we discuss our results to answer the questions we asked ourselves at the beginning of the Chapter: is cluster-scale emission common in cool-core clusters? Is there a connection between radio emission and the gas dynamics in these sources?

3.4.1 Radio morphology

The clusters in our sample exhibit a variety of radio morphologies. We can identify three different categories of sources:

- **Clusters with a double radio component:**
  RX J1720.1+2638 and PSZ1G139.61+24 were identified by Savini et al. (2019) to host both a central mini halo and diffuse emission on large scales. We found cluster-scale diffuse radio emission in two other clusters: A1068 and MS 1455.0+2232, which were previously classified as candidate mini halo and mini halo, respectively. We note the radio emission of all these clusters is not circularly symmetric with respect to the centre, but is elongated roughly following the X-ray surface brightness distribution. An exception is RXJ1720.1, where the radio emission is elongated in the north-east south-west direction, while the X-ray emission has a more regular morphology. Radial profile analysis reveal a discontinuity in all these clusters, indicating the presence of a double radio component. Our idea is that these cool-core clusters underwent a minor merger which has re-accelerated particles on large-scales leaving the central regions unperturbed. Therefore, a central mini halo and a giant radio halo co-exist. In this case, we would expect to find different spectral index values in the two components. In RX J1720.1+2638 we found a net change of spectral index in the two components, $\alpha \sim 1$ for the mini halo and $\alpha \sim 3$ for the large-scale diffuse emission. Also in A1068 there is a steepening in the external regions, however the change in slope is not as sharp as in the previous case. In MS 1455.0+2232, on the other hand, the spectral index seems fairly uniform throughout the diffuse emission. The large-scale diffuse emission in PSZ1G139.61+24, instead, has not been detected in other observations currently available, so we are unable to reconstruct a spectral map for this source. We can only say that the mini halo has a spectral index of $\alpha \sim 1.3$ and set a limit of $\alpha \geq 1.7$ for the large-scale diffuse emission, suggesting a steepening also in this case.

- **clusters with a central mini halo:**
  we confirm the presence of a central mini halo in the clusters RBS 0797 and RX J1532.9+3021. The radial profiles evidence the presence of a single radio component. In the cluster MACS J2245.0+2637 we detect a hint of diffuse emission around the central source at 2σ significance. We catalogue this source as candidate mini halo. Deeper observations are necessary to confirm the presence of diffuse emission in this cluster.

- **clusters without diffuse emission:**
  in the remaining five clusters of the sample, we did not detect diffuse emission. We derived an upper-limit to the power of the halo in these sources and found that these values are consistent with the $M_{500} - P_{150\ \mathrm{MHz}}$ correlation found by van Weeren et al. (2021). Therefore, we cannot exclude the presence of a radio halo in these sources, based on our observations. Among these clusters, MS 0735.6+7421 presents two giant radio lobes (total extension $\sim$ 550 kpc) and other smaller-scale lobes associated with subsequent phases of the jet activity. MS 0839.8+2938 also features radio lobes, only resolved at $3''$ resolution. Finally, the clusters Z2089, A1204 and RX J1720.2+3536 present small-scale radio emission ($\sim$ 100 kpc) extending from the unresolved central source. This emission may be linked to an old phase of AGN activity, or alternatively originated from hadronic interactions between particles emitted by the central AGN and that present in the ICM. These sources might be further investigated through VLBI (Very Long Baseline Interferometry) observations that allows to reach sub-arcsecond resolution.

3.4.2 Morphological parameters

We want to understand which parameters could be used to discriminate cool-core clusters presenting a double component of diffuse radio emission from the others. In Fig. 3.19 we show again the $c - w$ plot, indicating the clusters of the sample with different colours depending on the radio emission detected with LOFAR: clusters without detected diffuse emission are represented in black, clusters with a mini halo in green (the cMH isshown with an empty green circle), clusters with a double component (MH+H) in red. There is no apparent correlation between the radio morphology and the dynamical status of the cluster, as traced by the morphological parameters. Clusters with a double component are not the most disturbed ones, at least on the scales used in this work to compute the morphological parameters. We note that two clusters, PSZ1G139 and RXJ1720.2, lie beyond the $w \geq 0.012$ line, identified by Cassano et al. (2010) to separate radio halo from non radio halo clusters. However, only PSZ1G139 hosts a double component radio emission, while in RXJ1720.2 no diffuse emission is detected. The other three clusters with a double component, instead, present a low centroid shift value and are located in the $(c - w)$ plane region characterised by clusters without radio halos, according to Cassano et al. (2010), contrary to our findings. Also the cluster with the lowest value of the concentration parameter, MS0735, does not present diffuse radio emission. However, that cluster presents X-ray cavities, surface brightness depressions, which can have affected the estimate of the concentration parameter.

We note there are different definitions in the literature of the concentration parameter, depending on different circular apertures used to compute the peak versus ambient surface brightness. To select our clusters we used the definition reported in Cassano et al. (2010), which used a radius of 100 kpc to delimit the peak surface brightness and a radius of 500 kpc for the ambient surface brightness, while the original definition of Santos et al. (2008), used smaller radius of 40 and 400 kpc. Santos et al. (2008) divided clusters into three categories, based on the concentration parameter value: non cool-core ($c_{40-400} \leq 0.075$),

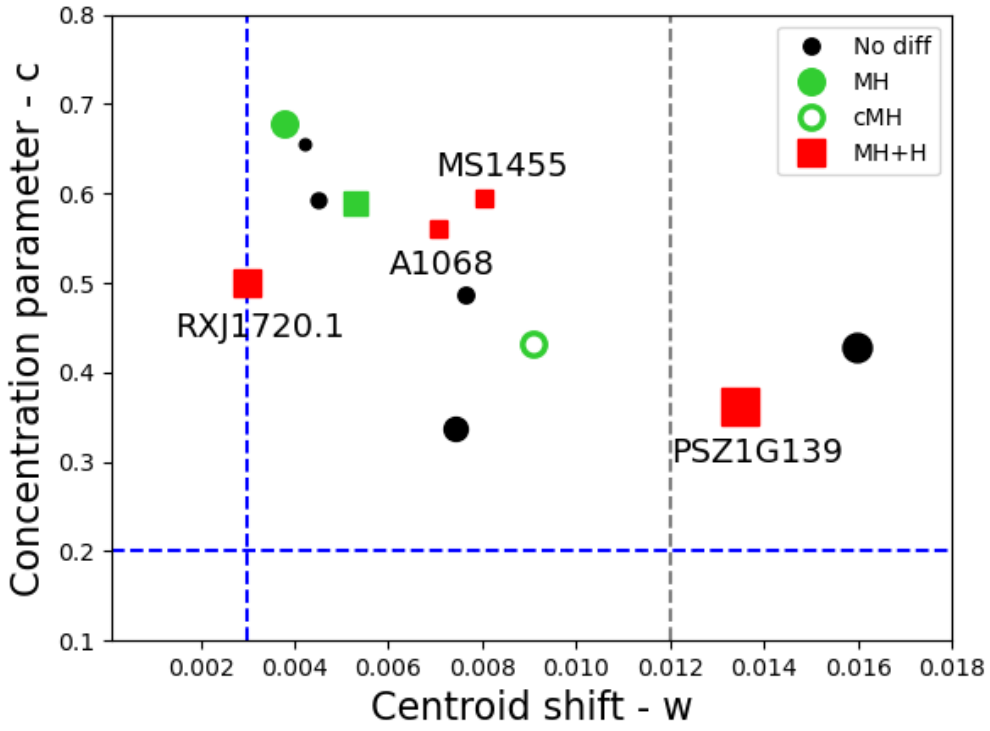

Figure 3.19: Morphological parameters plot of the clusters in the sample. Colours represent different types of radio emission detected with LOFAR: the clusters without detect diffuse emission are represented in black, clusters with a mini halo in green (for the candidate MH we used a marker not filled), clusters with a double component (MH+H) in red. Clusters with detected cold fronts are indicate with a square, otherwise a circle is used. The marker size is proportional to the cluster mass. Blue dashed lines indicate the c and w values used to select clusters in our sample. Grey dashed line separates clusters with a radio halo $w \geq 0.012$ from clusters without a radio halo, according to Cassano et al. (2010).

moderate ($0.075 \leq c_{40-400} \leq 0.155$), and pronounced cool-core ($c_{40-400} \geq 0.155$). Since some of our clusters have a small mass and linear size, the peak surface brightness should be best delimited by a region of smaller radius. We then recalculated the concentration parameters following Santos et al. (2008) definition, founding a systematic decrease in the concentration parameter values of 40−50%. All the clusters in our sample have a concentration parameter $c_{40-400} \geq 0.155$, so also according to Santos et al. (2008) they could be classified as strong cool-core clusters.

Another parameter we considered is the cluster mass (M_{500}). The size of the markers in the $(c - w)$ plane is proportional to the cluster mass. PSZ1G139 and RXJ1720.1 are between the most massive clusters, while A1068 and MS1455 are less massive. So, the cluster mass does not give constrain on the individuation of cool-core clusters with a radio halo.

A feature that instead could indicates the presence of diffuse emission on large scales is the presence of a cold front, X-ray surface brightness discontinuity associated to the sloshing of the cluster core. We indicate with a square in the $(c - w)$ plane the clusters with detected cold fronts, while with a circle the clusters without cold fronts or for which there is no indication in the literature. The four clusters with a double component of diffuse emission present this feature, thus suggesting a link between minor interactions and large-scale diffuse radio emission.

So far there was evidence that diffuse emission in relaxed clusters was confined by cold fronts (e.g., Mazzotta & Giacintucci, 2008). According to ZuHone et al. (2013)

simulations, the sloshing motions generate turbulence in the core regions strong enough to re-accelerate seed electrons and produce diffuse synchrotron emission on scales coincident with the sloshing region. Outside the cold fronts, instead, the turbulence is negligible. With LOFAR, instead, we are able to detect emission on a larger scale, associated with the weaker turbulence that is created outside the sloshing region.

An overall picture is emerging according to which all the relaxed clusters that underwent a minor merger could present this type of emission when observed at low frequency. However, there is another cluster with a confirmed cold front, RXJ1532, for which we only detected the central mini halo. A possibility is that the LOFAR observations are not sensitive enough in this case to detect the fainter large-scale diffuse emission. As we found comparable noise levels in all the observations, the emission in this source should have a steeper spectrum. Otherwise, the turbulence developed in that cluster, as a consequence of a minor merger, is inefficient to accelerate particles on large scales.

A larger sample of relaxed clusters is needed to improve the statistic and better understand the acceleration processes taking place in relaxed clusters.

3.5 Conclusions

In this Chapter, we have presented the results of LOFAR HBA observations of a sample of 12 cool-core clusters. These clusters were selected on the basis of their dynamical state to verify the occurrence of large-scale diffuse radio emission in cool-core clusters and to understand if this emission is related to the thermal gas condition.

Four clusters (one third of the sample) present cluster-scale diffuse radio emission, made of two different components: a central mini halo and halo-like emission on larger scales. We detected this emission for the first time in the clusters A1068 and MS 1455.0+2232, and we confirmed the radio morphology of the clusters RX J1720.1+2638 and PSZ1G139.61+24 (Savini et al., 2019). In two cases, RX J1720.1+2638 and A1068, we also detected a steepening of the spectral index in the external component. In MS 1455.0+2232, on the other hand, the spectral index appears to be rather uniform over the entire extension of the diffuse emission. The power of the giant radio halo component is consistent with the power of giant radio halos detected in merging clusters.

Two clusters (RBS 0797 and RX J1532.9+3021) of the sample host a central mini halo, one confined by a cold front, and we found a new candidate mini halo (MACS J2245.0+2637).

In the other clusters we did not detect diffuse radio emission. Two of these clusters (MS 0735.6+7421 and MS 0839.8+2938) have radio lobes, albeit on different scales. In the remaining three cases (Z2089, A1204 and RX J1720.2+3536) we detected small-scale emission surrounding the central unresolved source, which may be due to an old activity of the central AGN or secondary emission produced by hadronic interactions.

For the clusters in the sample that do not present halo-like diffuse emission, we derived upper-limits to the halo power. The values found are not significative to exclude the presence of a giant radio halo in these clusters.

There is no clear correlation between radio emission and morphological parameters. However, all the clusters with a double component radio emission present cold fronts, X-ray features connected to the sloshing of the cluster core after a minor merger, indicating they are not completely relaxed. Furthermore, the radio emission extends beyond the sloshing region, overcoming the thought that mini halos were confined by cold fronts (e.g., Mazzotta & Giacintucci, 2008).

Further analyses on a larger sample are necessary in order to understand the origin of the radio emission in relaxed clusters.

Chapter 4

The ultra-steep diffuse radio emission observed in the cool-core cluster RX J1720.1+2638 with LOFAR at 54 MHz

In this Chapter[1] we present a detailed study of the cool-core galaxy cluster RX J1720.1+2638, which host both a bright central mini halo and a fainter diffuse emission extending beyond the cluster core that resembles giant radio halo emission. Combining new observations performed with LOFAR LBA at 54 MHz with data at higher frequencies, we were able to constrain the spectral properties of the radio emission for the first time. The large-scale emission presents an ultra-steep spectrum with $\alpha_{54}^{144} \sim 3.2$. Furthermore, we compare radio and X-ray properties through point-to-point analysis. The radio emission inside and outside the cluster core have strictly different properties, as there is a net change in spectral index and they follow different radio-X-ray surface brightness correlations. We argue that the large-scale diffuse emission is generated by particles re-acceleration after a minor merger. While for the central mini halo we suggest that it could be generated by secondary electrons and positrons from hadronic interactions of relativistic nuclei with the dense cool-core gas, as an alternative to re-acceleration models.

4.1 Introduction

RX J1720.1+2638 (hereafter RXJ1720.1) is a cool-core galaxy cluster (cooling time $t_{\rm cool} = 2.36$ Gyr, Giles et al., 2017), which presents a central mini halo and a nearby head-tail radio source north-east of the cluster centre, associated with a cluster member galaxy (Owers et al., 2011). A detailed radio spectral study of the source was performed by Giacintucci et al. (2014b) in the frequency range $237 - 8440$ MHz, using GMRT and VLA data. The mini halo consists of a bright central part, with a spectral index of $\alpha_{237}^{4850} = 1.0 \pm 0.1$ and a lower surface brightness arc-shaped extension to the south-east with a steeper spectral index of $\alpha_{237}^{4850} = 1.4 \pm 0.1$. Two cold fronts detected in the X-ray band with *Chandra* appear to confine the mini halo, suggesting the origin of the mini halo may be connected with gas sloshing that creates the cold fronts (Mazzotta et al., 2001; Mazzotta & Giacintucci, 2008). A multi-object optical spectroscopic study of this cluster identified two group-scale substructures which could have perturbed the cluster core (Owers et al., 2011). The most promising perturber candidate lies ~ 550 kpc north of

[1] based on Biava et al. (2021a)

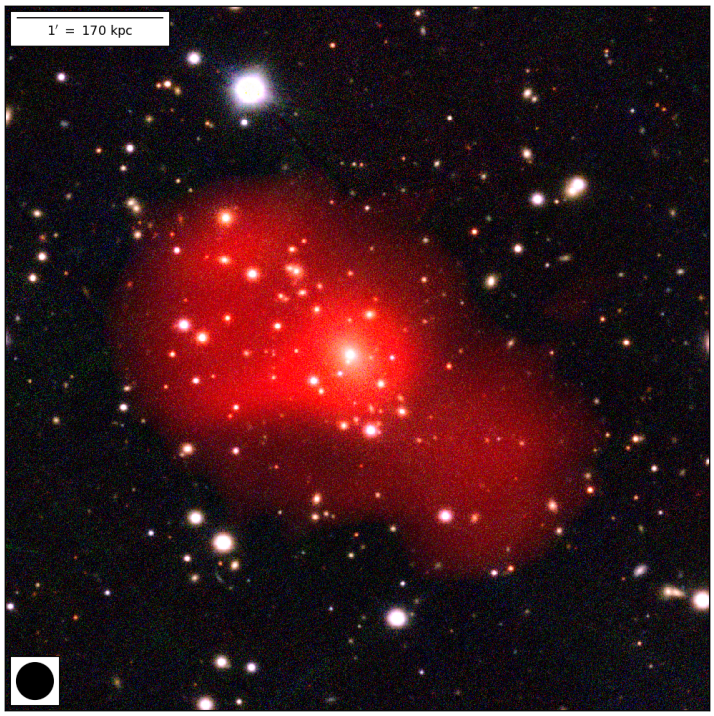

Figure 4.1: Composite image of RXJ1720.1, obtained combining the radio LOFAR LBA image at 15 arcsec resolution in red (see Section 4.2) with optical RGB Pan-STARRS1 images (g, r, i bands; Chambers et al., 2016)

the cluster core, spatially coincident with a peak in the weak lensing maps of Okabe et al. (2010). A weak enhancement in the lensing maps is also present roughly at the position of the substructure located ~ 400 kpc to the south-west, which, however, is dynamically less significant. LOFAR HBA (144 MHz) observations revealed a new diffuse component extending beyond the cluster core, south-west of this, with an overall size of ~ 600 kpc (Savini et al., 2019). Since this emission is not visible at higher frequencies, combining LOFAR 144 MHz and GMRT 610 MHz data, Savini et al. (2019) could only provide a lower limit of the spectral index, of $\alpha \geq 1.5$ in the vicinity of the mini halo up to $\alpha \geq 2.1$ at larger distances. To constrain the spectral properties of the newly discovered emission, observations at lower frequencies are therefore mandatory.

In this Chapter, we calculate for the first time the spectral index of the large-scale diffuse radio emission, combining LOFAR LBA and HBA data. To understand the origin of the diffuse radio emission inside and outside the cluster core, we also analysed archival radio and X-ray data, looking for a spatial correlation between radio and X-ray surface brightness. A composite image of the source, created with our new LOFAR LBA data, is shown in Fig. 4.1.

The cluster RXJ1720.1 (RA: 17:20:10.1 DEC: +26:37:29.5, Piffaretti et al. (2011)) is located at redshift $z = 0.164$ (Harris et al., 1988; Crawford et al., 1999). With the adopted cosmology, this corresponds to a scale of 2.8 kpc arcsec^{-1}.

4.2 Radio observations

In this work we used new LOFAR LBA (54 MHz) observations (PI Biava), complemented by LOFAR HBA (144 MHz), GMRT (610 MHz) and VLA L-band (1480 MHz) and C-band (4860 MHz) observations. All radio observations used are listed below and summarised in Table 4.1.

- **LOFAR LBA** observations were carried out on 2019 September 26 and November 20, for a total observing time of 10 h. The observations were performed in

Table 4.1: Summary of the observational details.

Telescope	Frequency	Configuration	TOS	Observation ID	Reference
LOFAR	54 MHz	`LBA_OUTER`	10h	LC12_018	1
LOFAR	144 MHz	`HBA_DUAL_INNER`	16h	LC7_024, LT10_010	1
GMRT	612 MHz	-	4h	11MOA01	2
VLA	1480 MHz	B	70min	AH190	3
VLA	4860 MHz	C	4min	AE125	3

References: (1) this article, (2) Savini et al. (2019), (3) Giacintucci et al. (2014b).

the frequency range $30 - 78$ MHz in a dual-beam mode, with one beam continuously pointing at the calibrator (3C295) and one beam at the target. We used the `LBA_OUTER` antenna mode, where the outer 48 dipoles of the station are used to minimize the coupling between dipoles, using 24 Core Stations and 14 Remote Stations. The data were taken at 1s integration time and at a frequency resolution of 64 channels per 0.192 MHz sub-band and subsequently averaged to 2 s and 16 ch/sb. The calibration was performed following the procedure described in Section 2.4.1. The flux density scale was set according to Scaife & Heald (2012). The flux calibration uncertainty is estimated to be 10 per cent (de Gasperin et al., 2021). We imaged the data with `WSClean` (Offringa et al., 2014; Offringa & Smirnov, 2017) using a Briggs weighting scheme with robust$=-0.5$, applying an inner uv-cut at 30λ and using a multi-scale deconvolution. The final image of RXJ1720.1 has a resolution of $23'' \times 12''$ and a noise of 1.8 mJy beam^{-1} (see Fig. 4.2, right panel).

- **LOFAR HBA** observations, already presented in Chapter 3, were carried out by LoTSS on 2017 January 25 and 2020 March 6, for a total observing time of 16 hours. The final high-resolution image was produced using a Briggs weighting scheme with robust $=-0.5$, applying an inner uv-cut at 80λ and using a multi-scale deconvolution. The final image has a resolution of $8.8'' \times 6.1''$ and a noise of 0.125 mJy beam^{-1} (see Fig. 4.2, left panel).

- **GMRT** observations at 610 MHz were performed on 2011 July 24. The data, presented in Savini et al. (2019), were calibrated using the Source Peeling and Atmospheric Modeling (SPAM) pipeline (see Intema et al., 2017, for details), that performs both direction-independent and direction-dependent calibrations. The flux density scale was set according to Scaife & Heald (2012). The flux calibration uncertainty is estimated to be 10 per cent.

- **VLA** observations of RXJ1720.1 were performed on different bands and with various configurations. We used the data at 1480 MHz, B configuration, and at 4860 MHz, C configuration. The data sets were reduced with `CASA` (version 5.4, McMullin et al., 2007) following standard procedures after manual flagging. To improve the quality of the final image at 1480 MHz, we performed several cycles of phase self-calibration, to reduce the effects of residual phase variations in the data. Self-calibration was also attempted at 4860 MHz, but the solutions were not applied as the process did not improve the gain solutions due to the low flux density of the source. At both frequencies, the flux density scale was set according to VLA Perley (1990) values in SETJY task. The flux calibration uncertainty is estimated to be 5 per cent at all frequencies.

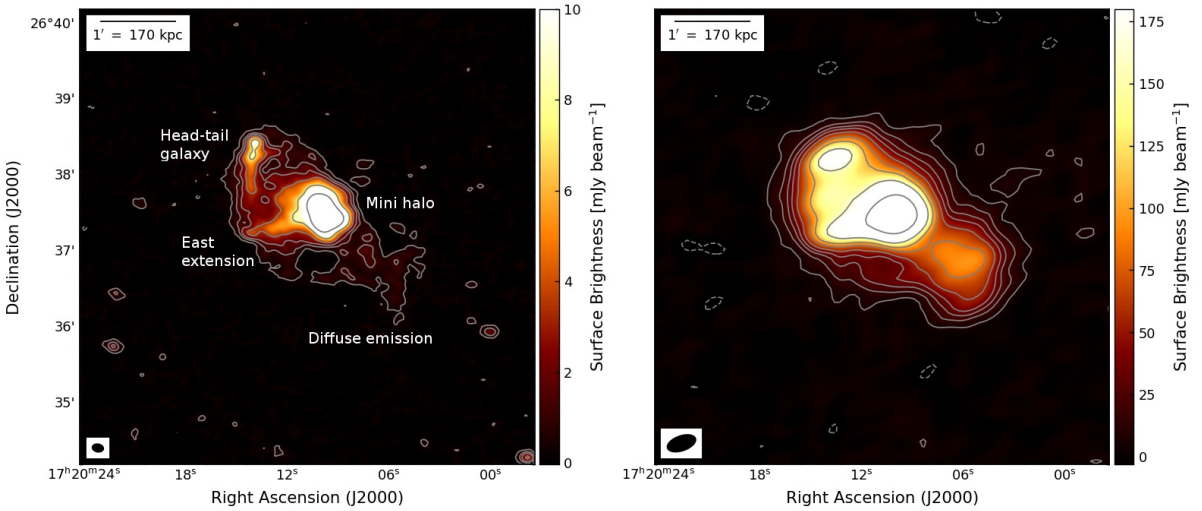

Figure 4.2: Radio maps of RXJ1720.1 at different frequencies. *Left:* LOFAR HBA 144 MHz at $9'' \times 7''$ resolution. Levels:[-1,1,3,5,9,20,50] $\times$ 3σ (where $\sigma = 0.125$ mJy beam^{-1}). *Right:* LOFAR LBA 54 MHz at $23'' \times 12''$. Levels:[-1,1,3,5,7,10,15,20,30,70] $\times$ 3σ (where $\sigma = 1.8$ mJy beam^{-1}). The beam is shown in the bottom left corner of each image.

4.3 Results

4.3.1 Morphology

In Fig. 4.2, we show on the left the LOFAR HBA image at a central frequency of 144 MHz and with a resolution of $9'' \times 7''$, while on the right the LOFAR LBA image at central frequency of 54 MHz and with a resolution of $23'' \times 12''$. Thanks to the high resolution of the HBA image we can identify several radio sources, indicated in the figure. The central diffuse emission is composed of a bright mini halo with a size of $r \sim 25''$ (~ 70 kpc), and a lower surface brightness extension to the east. Both components were already observed at 612 MHz by Giacintucci et al. (2014b). However, in their image the fainter emission has an arc-shaped morphology extending to the south-east. A reanalysis of the same data carried out by Savini et al. (2019) does not show this additional emission towards the south, recovering the morphology that we observe at 144 MHz. North-east of cluster centre there is a head-tail radio galaxy, which appears connected to the mini halo by a faint emission region. However, these two components could overlap for projection effects, without being physically connected. To the south-west of the mini halo, diffuse emission on larger scales is visible. We note that this emission extends also to the north, and essentially surrounds the central mini halo. This diffuse emission is brighter and more evident in the LBA image. Its extension is comparable in the two images ($\sim 200'' \cong 560$ kpc) and is elongated in the north-east south-west direction.

4.3.2 Spectral analysis

In order to understand whether we are observing two different types of emission (a central mini halo and a giant radio halo on larger scales), we investigated the spectral index distribution of the radio emission. To study in detail the different components, we produced two spectral index maps: one at $6''$ resolution between LOFAR HBA (144 MHz) and GMRT (612 MHz) data (Fig. 4.3, left panels) and one at lower resolution of $15''$ between LOFAR LBA (54 MHz) and HBA data (Fig. 4.3, right panels). To create these maps we re-imaged all the radio data with the same *uv*-range ($690 \sim 4000$ λ) and using a uniform weighting scheme. Then we spatially aligned the images with the same

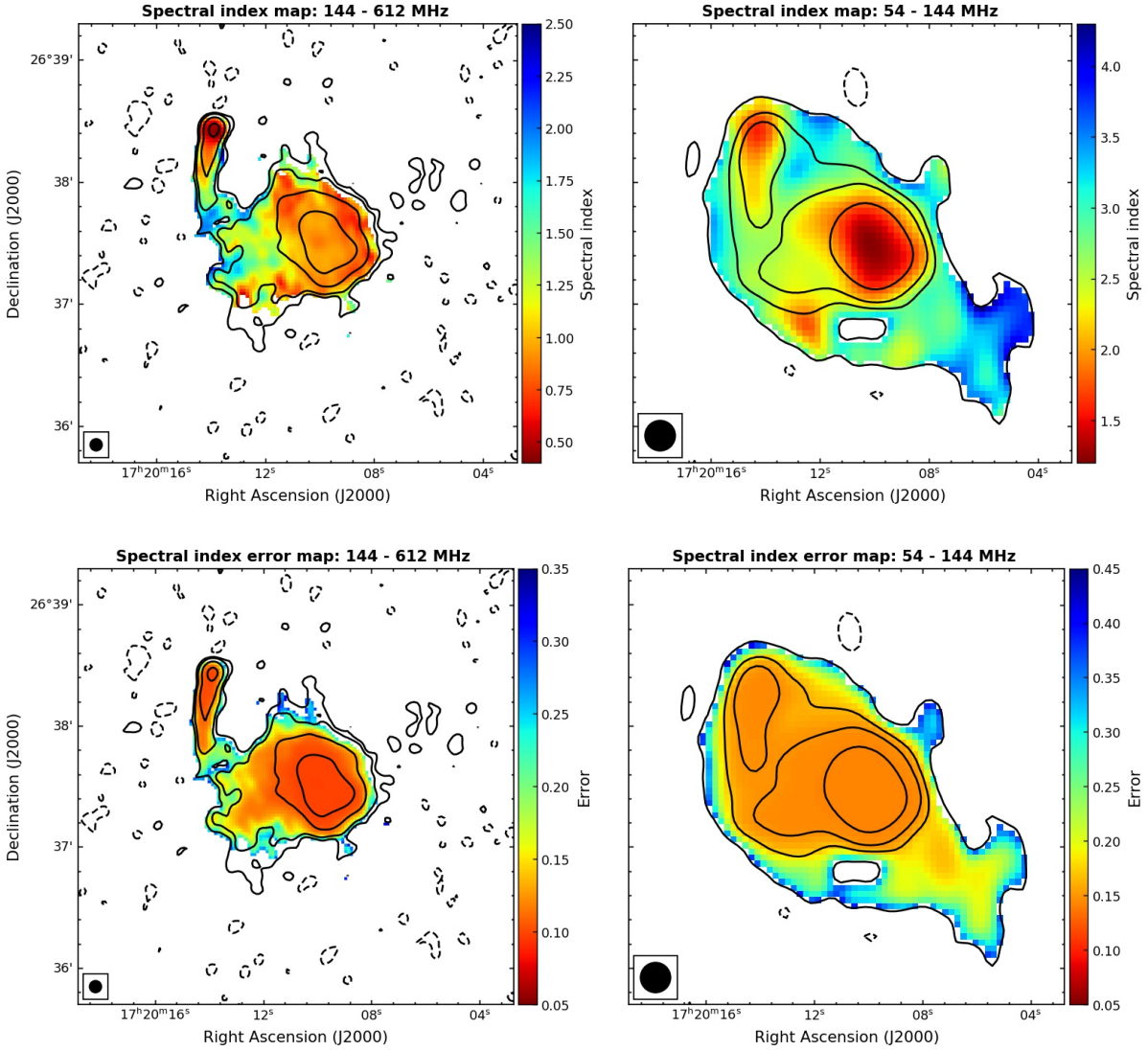

Figure 4.3: Spectral index maps (*Top*) and associated spectral index error maps (*Bottom*) of RXJ1720.1. *Left*: frequency range 144−612 MHz, 6″ resolution. Overlaid are the GMRT 612 MHz contours. *Right:* frequency range 54−144 MHz, 15″ resolution. Overlaid are the LOFAR HBA 144 MHz contours. The beam is shown in the bottom left corner of each map.

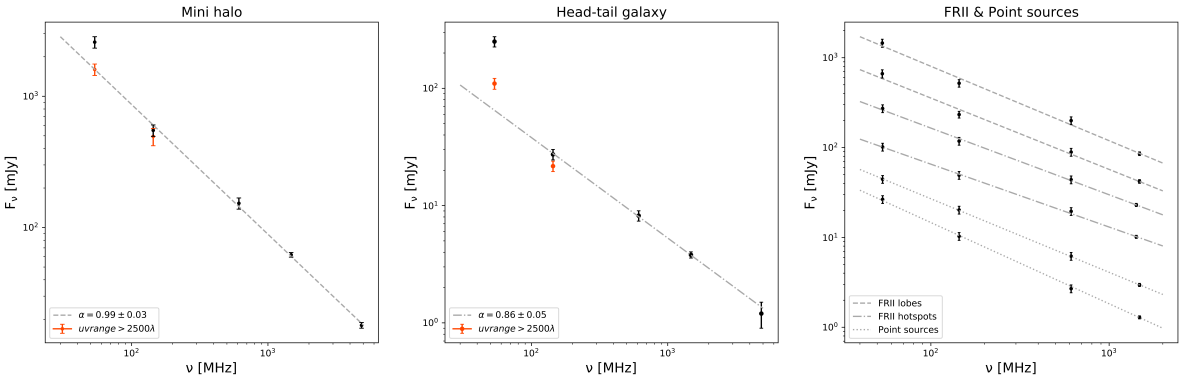

Figure 4.4: *Left:* Integrated flux of the mini halo from the original images (black points) and LOFAR images with uv-range $> 2500\lambda$ (orange points). Dashed line obtained from the weighted least square of the black points. *Middle*: Integrated flux of the core of the head-tail radio galaxy from the original images (black points) and LOFAR images with uv-range $> 2500\lambda$ (orange points). Dashed-dotted line obtained from the weighted least square of the black points. *Right:* Weighted least square of integrated flux of the FRII radio lobes (dashed lines) and hotspots (dashed-dotted lines) and of point sources located near the cluster (dotted lines).

restoring beam, to correct for possible shifts introduced by the phase self-calibration process. Finally, we considered only the emission detected above 3σ and we assumed a flux calibration error of 10 per cent for both LOFAR and GMRT data.

A previous spectral index map of the cluster between 144 and 612 MHz was presented by Savini et al. (2019) with a resolution of $20''$ and they found $\alpha \sim 1$ for the mini halo and put a lower limit of $\alpha \geq 1.5$ for the diffuse emission outside the cluster core. Our increased resolution, sensitivity and frequency coverage allows us to study the spectrum in much more details. In our map between 144 and 612 MHz, the mini halo shows quite a uniform spectral index with a mean value of $\alpha_{144}^{612} = 0.9 \pm 0.1$ and variations of $\Delta\alpha \sim 0.1$ across the region. The east extension of the central emission has a steeper spectral index, with values between $\alpha_{144}^{612} = 1.1 \pm 0.2$ and $\alpha_{144}^{612} = 1.8 \pm 0.2$. This is in agreement with the trend observed by Giacintucci et al. (2014b) at higher frequencies. The core of the head-tail radio galaxy in the north shows a typical spectral index $\alpha_{144}^{612} \sim 0.6$ which steepens along the tail, indicative of ageing, as observed in radio galaxies. To detect the diffuse emission outside the cluster core, we have to go to lower frequencies, in the range 54−144 MHz. This emission shows an ultra-steep spectrum, with a mean spectral index of $\alpha_{54}^{144} = 3.2 \pm 0.2$. This is the first cool-core cluster for which the spectral index of large-scale diffuse emission was estimated, and its large value is in agreement with the lower limit provided by Savini et al. (2018).

In the low-frequency spectral index map (Fig. 4.3, right panel) we noticed a net difference in the spectral index of the mini halo and the diffuse emission on larger scales. This suggests that the radio emission inside and outside the cluster core has a different nature. The strong spectral gradient observed (in projection) across the boundaries of the mini halo rules out the possibility that the electrons producing the emission on larger scale are advected/transported from the mini halo region on larger volumes.

However, in this frequency range the spectral index of the mini halo and of the core of the head-tail radio galaxy is steeper than the one found at higher frequencies. To confirm this behaviour, we created an image of the cluster at all available frequencies (VLA data included) with the same parameters (uv-range = 690 ∼ 40000 λ, uniform weighting scheme, and $15''$ restoring beam) to extract the integrated flux from mini halo region and from the core of the head-tail radio galaxy. From the spectrum of the mini halo, plotted in Fig. 4.4 left panel, we can see that the flux density at 54 MHz is larger than the expected value from a spectral index of about 1, as found in the frequency range

144−4860 MHz (dashed line). In fact, the measured spectral index between 54−144 MHz is $\alpha_{54}^{144} = 1.6 \pm 0.1$, while at higher frequencies it is flatter ($\alpha_{144}^{612} = 0.9 \pm 0.1$, $\alpha_{612}^{1480} = 1.02 \pm 0.12$, $\alpha_{1480}^{4860} = 1.04 \pm 0.05$). A similar offset is observed for the head-tail radio galaxy (Fig. 4.4, middle panel), where $\alpha_{54}^{144} = 2.2 \pm 0.1$, while $\alpha_{144}^{612} = 0.8 \pm 0.1$, $\alpha_{612}^{1480} = 0.9 \pm 0.1$ and $\alpha_{1480}^{4860} = 1.0 \pm 0.2$. The spectra of the core of an active galaxy is expected to follow a pure power-law with a spectral index around 0.6−0.9. Then the spectrum becomes steeper in the high frequency range because of particles ageing. Hence, the steep low-frequency spectral index we observe cannot be explained by the radio galaxy alone, and could be due to the superposition of components with different spectral behaviours.

To understand if there are offsets in the LBA flux density scale, we computed the spectrum of point sources in the proximity of the cluster and of one extended nearby FRII radio galaxy (NVSS J172104+262417). This allows us to check possible systematic errors in the absolute flux calibration, and possible errors introduced by the deconvolution of extended sources. In Fig. 4.4 right panel, we show the spectrum of the point sources and of the radio lobes and the hotspots (comparable to the case of the head-tail radio galaxy in our target) of the extended radio galaxy. For all control sources we did not observe particular offsets of the LBA fluxes, the points are consistent within the error with the higher frequency part of the spectrum, assuming these sources follow a power-law spectrum down to low frequencies. Hence, we can conclude that the offsets observed in the mini halo and head-tail radio galaxy are not affected by systematic errors. We argue that the higher flux density we observed in our target at LBA frequency, it is due to a superposition of two different components along the line of sight: the steep diffuse emission and the mini halo/head-tail core. In support of this, we note that the LBA emission in the mini halo region is comparable to the sum between the flux extrapolated from higher frequencies and the flux of the steep large-scale diffuse emission, scaled for the region area, assuming it has the same brightness as in the regions outside the mini halo. There is therefore evidence that the steep emission observed south-west of the cluster core is substantially present also in the central regions, resembling a giant radio halo. As a further check, we tried to isolate the mini halo flux from that of the steep diffuse emission, re-imaging the LOFAR data with a cut in the *uv*-range. We selected a *uv*-range $> 2500\ \lambda$ (corresponding to ~ 190 kpc), which allows us to somewhat filter out the larger scale steep component of the diffuse emission in the centre of the cluster, without losing the emission coming from the mini halo. We found that with the imposed *uv*-range restriction, the LBA flux density of mini halo and head-tail radio galaxy decreases (Fig. 4.4, orange points in the left and middle panels), confirming our hypothesis.

4.4 Radio and X-ray comparison

X-ray observations show that the cluster has a bright central core and on large scales it is relaxed with a regular morphology (Giacintucci et al., 2014b). X-ray surface brightness and temperature profiles of the cluster revealed the presence of two cold fronts on opposite sides of the X-ray peak: at about 150 kpc to the south-east and at about 100 kpc north-west (Mazzotta et al., 2001; Mazzotta & Giacintucci, 2008).

In Fig. 4.5 we show a *Chandra* X-ray image of the cluster in the $0.5 - 2.5$ keV band, obtained from the combination of three observations (ObsIDs 1453, 3224, and 4631, for a total exposure of 42.5 ks, see Mazzotta & Giacintucci, 2008, for details). On the image we indicate with green lines the position of the cold fronts, and we overlaid the LOFAR LBA contours at 15″ resolution. The diffuse radio emission extends outside the cluster core, as defined by the cold front boundaries, in the north-east south-west direction, perpendicular to the position of the cold fronts, and it lies in a region of lower X-ray surface brightness,

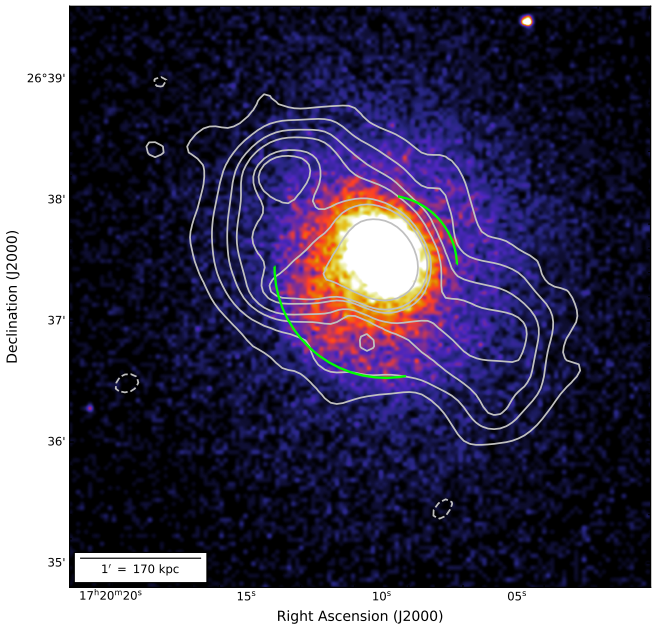

Figure 4.5: *Chandra* X-ray image of RXJ1720.1 in the 0.5−2.5 keV energy band. The background has been subtracted and the image has been corrected for the total exposure and the effective area of the telescope. Each pixel corresponds to 2″. Overlaid are the LOFAR LBA contours at 15″ resolution. Green lines indicate the position of the cold fronts.

with respect to the mini halo. The X-ray image shows neither an excess of emission (i.e., substructures) nor a deficit (i.e., a cavity) in the region of the large-scale diffuse radio emission. We then check the residual image obtained after subtracting a 2D β-model (Cavaliere & Fusco-Femiano, 1976), but also in this case there is no significant feature in correspondence of the LOFAR emission outside the cluster core. However, a cavity could be present but not detectable due to low count rate outside the cluster core or due to projection effects.

4.4.1 X-ray and radio surface brightness correlation

To understand if there is an interplay between thermal and non-thermal emission inside and outside the cluster core, we performed a quantitative comparison between their surface brightness. This connection would induce a spatial correlation between the radio ($I_{\rm R}$) and X-ray surface brightness ($I_{\rm X}$), which could be described by a power law in the log-log space:

$$\log I_{\rm R} = b \log I_{\rm X} + c \ , \tag{4.1}$$

where a slope of $b > 1$ (super-linear relation) indicates that radio brightness declines faster than X-ray brightness or vice versa if $b < 1$ (sub-linear relation). The correlation is related to the particles origin (Dolag & Enßlin, 2000; Govoni et al., 2001; Brunetti et al., 2004; Pfrommer et al., 2008; ZuHone et al., 2013, 2015). Hadronic models predict a super-linear relation, while turbulent re-acceleration scenarios can produce both super-linear and sub-linear relationships depending on the nature of the particles, their distribution in the cluster volume and on the scales considered. A spatial correlation has been observed in several clusters. In the case of giant radio halos a sub-linear or linear scaling is generally found (e.g., Govoni et al., 2001; Botteon et al., 2020b; Rajpurohit et al., 2021b), whereas mini halos present a super-linear scaling between radio and X-rays (Govoni et al., 2009; Ignesti et al., 2020), suggesting an intrinsic difference in the nature of these radio sources.

We performed a point-to-point analysis of the emission in our source, considering its radio components separately. For each component, we constructed a square grid with cell sizes equal to the radio image FWHM and computed the mean surface brightness inside each cell. To determine the best-fitting parameters of the $I_{\rm R}$-$I_{\rm X}$ relation, we used the Linmix software package (Kelly, 2007). Linmix performs a Bayesian linear regression

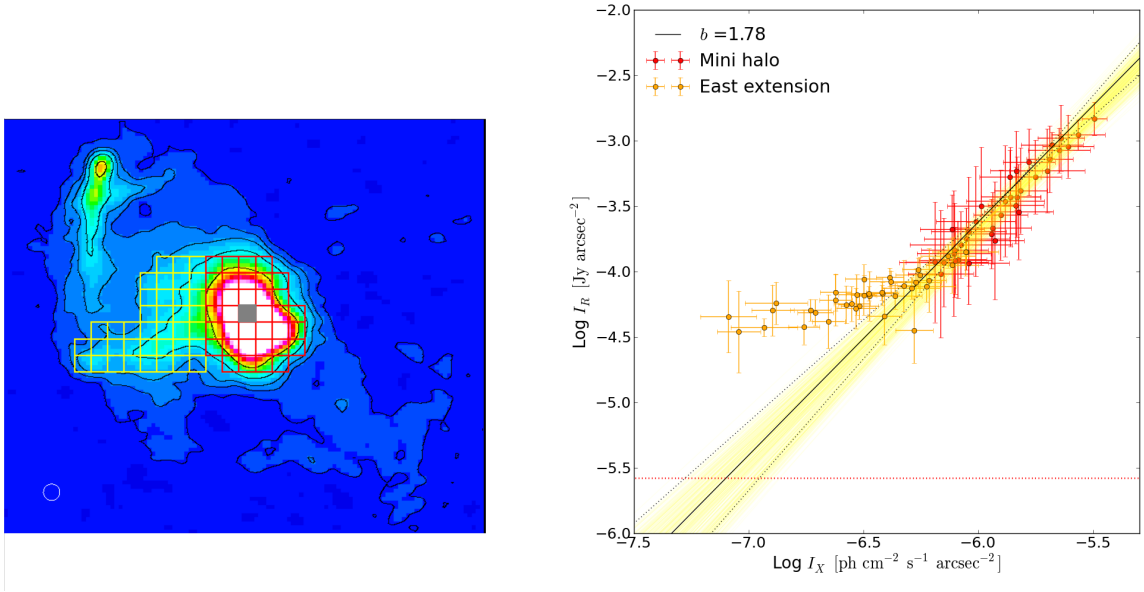

Figure 4.6: Radio-X-ray correlation for the mini halo. *Left:* LOFAR HBA image of RXJ1720.1 at 6″ resolution with contours at 3,9,15,30,60 × σ (where σ = 0.108 mJy beam^{-1}). With overlaid the grid on the mini halo emission in red and on the east extension in yellow. The contribution of the bright central galaxy is excluded from the sampling (grey region). The circle in the lower left corner shows the beam. *Right:* Radio-X-ray surface brightness correlation of the central emission. Red points, with associated statistical errors, are from the mini halo region, while orange points from the east extension. The black line shows the best-fit correlation on mini halo emission, black dotted lines show the 25th and 75th percentile of the posterior distribution. The red dotted line marks 1σ.

taking into account measurement uncertainties on both variables, intrinsic scatter, and upper limits. It calculates the posterior probability distribution of the model parameters, using a Markov Chain Monte Carlo (MCMC) method, and therefore it is accurate for both small and large sample sizes. We considered the mean of the posterior distribution as the best-fit parameters, and the scatter of the 25th and 75th percentile with respect to the mean as an estimate of the slope uncertainty. The correlation strength was measured by using the Pearson and Spearman correlation coefficients.

For the study of the central emission we used a LOFAR HBA image at 6″ resolution. The *Chandra* X-ray image was smoothed to the same resolution. We created a grid at the location of the mini halo emission, indicated with red squares in the left panel of Fig. 4.6, and on the east extension, yellow squares. The right panel of Fig. 4.6 shows the point-to-point comparison between the X-ray and radio surface brightness in log-log scale. Each point represents the brightness in each cell of the grid with associated statistical errors (red points for mini halo and orange points for east extension). We note that the east extension and the mini halo follows different trends, suggesting the two radio emission are different. We then computed the mini halo correlation considering only the red points. In the plot the solid black line represents the best fit of b, and the dotted black lines the 25th and 75th percentile. We list the results of the fit in Table 4.2. We find that the values of $I_{\rm R}$ and $I_{\rm X}$ are strongly positively correlated (correlation coefficients near +1) and the slope is super-linear, $b = 1.78 \pm 0.22$. This implies that the non-thermal and thermal plasma in the mini halo region are connected, and suggests a peaked distribution of relativistic electrons and magnetic field in the cluster core. We note that Ignesti et al. (2020) have already computed a radio X-ray correlation for this source, using GMRT data at 612 MHz, and they found a shallower slope of $b = 1.5 \pm 0.1$. Several factors may be the cause of this difference: they used a different method to estimate the parameters

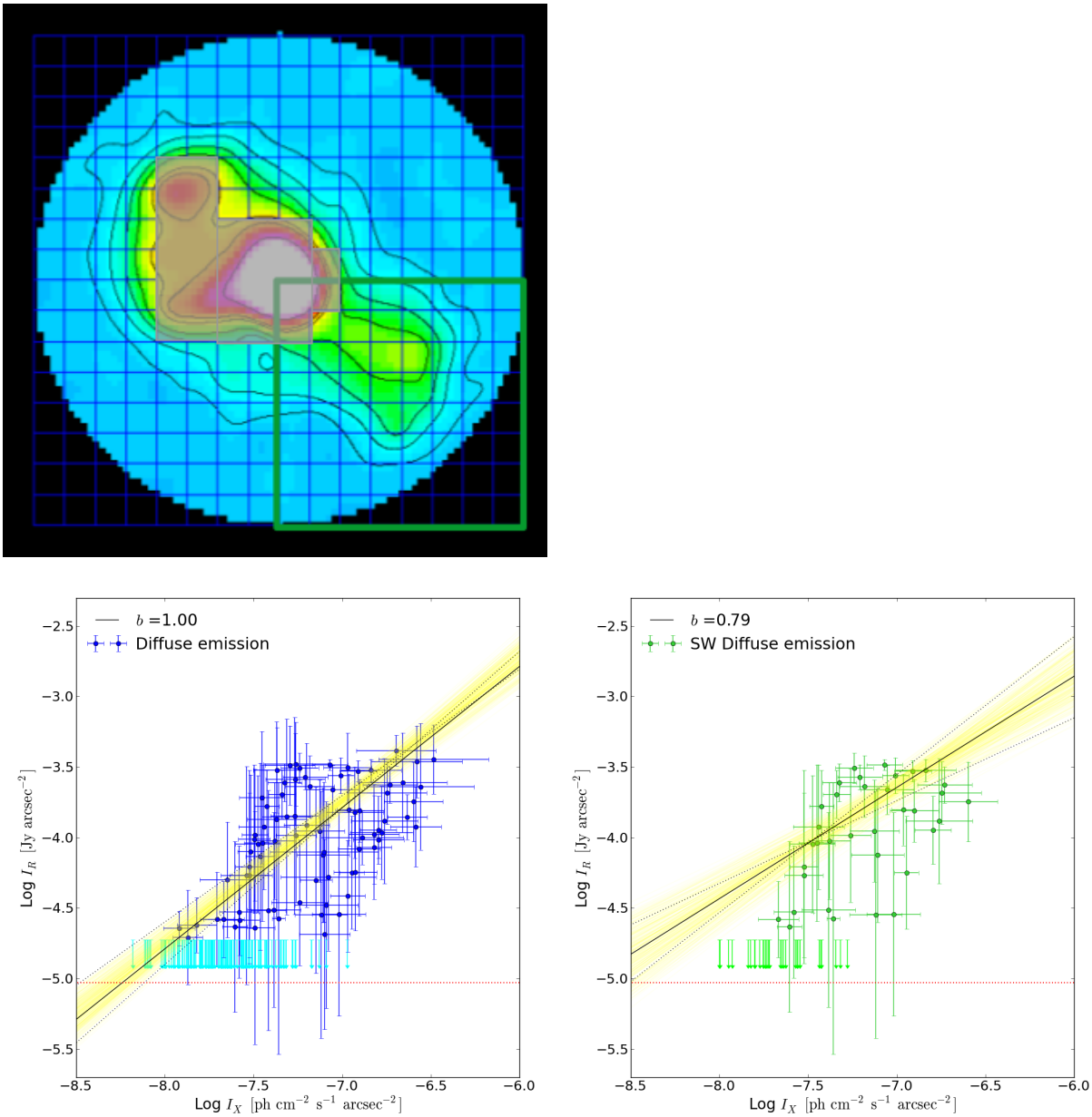

Figure 4.7: Radio-X-ray correlation for the diffuse emission on larger scale. *Top:* LOFAR LBA image of RXJ1720.1, blanked outside a distance from the centre of r = 120″, at 15″ resolution with contours at 3,10,20,30,50,60,100 × σ (where σ = 2.4 mJy beam^{-1}). Overlaid is the grid in blue. The contribution of the mini halo and head-tail radio galaxy is excluded from the sampling (grey region). Green square indicates the region of south-west emission. *Bottom left:* Radio-X-ray surface brightness correlation in the diffuse emission (blue points with associated statistical errors). The cyan arrows are the 2σ upper limits. The black line shows the best-fit correlation derived including upper limits, black dotted lines show the 25th and 75th percentile of the posterior distribution. The red dotted line marks 1σ. *Bottom right:* The same as before, but considering only the south-west (SW) part of diffuse emission (green points with associated statistical errors).

Table 4.2: I_R-I_X correlation.

Region	Frequency ν	Slope b	Pearson coeff. r_p	Spearman coeff. r_s
Mini halo	144 MHz	1.78 ± 0.22	0.96	0.94
East extension	144 MHz	0.61 ± 0.08	0.79	0.80
Diffuse emission	54 MHz	1.00 ± 0.11	0.71	0.67
	144 MHz	1.10 ± 0.14	0.61	0.58
SW Diffuse emission	54 MHz	0.79 ± 0.20	0.76	0.78
	144 MHz	0.87 ± 0.25	0.72	0.67

(BCES) and they computed the surface brightness from a different grid, considering all the radio emission visible at 612 MHz, so including the east extension, and excluding a wider region around the bright central galaxy.

We performed the same analysis for the large-scale diffuse emission. This time we used the LBA image, in which the diffuse emission is more evident, with a resolution of $15''$ and we smoothed the X-ray image to the same resolution. We constructed a grid with cells as large as the beam, covering all the emission inside a circle of 120 kpc, from which we excluded areas containing the mini halo, east extension and head-tail radio galaxy emission. In Fig. 4.7 we show on the top the grid used overlaid on the radio image, while on the bottom left panel we plot the data together with the best fit line of b (black solid line), and the 25th and 75th percentile lines (black dotted lines). Radio values below $2\sigma_{\rm rms}$ are considered as upper limits and included in the fit. We show the results of the fit in Table 4.2. In this case we found a moderate positive correlation (correlation coefficients around 0.7) and a slope $b = 1.00 \pm 0.11$. If instead we consider only the south-west part of the diffuse emission (indicated by a green square in Fig. 4.7, top panel), which is less contaminated by other components, the correlation is sub-linear, with a slope $b = 0.79 \pm 0.20$ (see Fig. 4.7, bottom right panel). We also compute the correlation using the HBA image with a resolution of $15''$, to make a comparison with the results obtained with the LBA image. We found a slope $b = 1.10 \pm 0.14$ ($b = 0.87 \pm 0.25$ for the SW diffuse emission) which is comparable to that obtained at lower frequency, but in this case we obtained a weaker correlation, with correlation coefficients ~ 0.6 (~ 0.7 for the SW diffuse emission). We therefore found for the diffuse emission a less steep correlation, compared to that found for the mini halo, and closer to the values found in the literature for giant radio halos.

We note that using cells with the same size of the radio image FWHM could generate biases because contiguous cells are not statistically independent. This is especially true when the emission is sampled with a small number of cells ($\sim 20 - 30$). To account for this, we repeated the analysis increasing slighter the size of the cells for both mini halo and diffuse emission, founding comparable results. When the size is doubled, on the other hand, we did not have enough points to well constrain the correlation. Another approach to the problem was proposed by Ignesti et al. (2020), with a sampling of the emission of mini halos through non-fixed grids and Monte Carlo analysis. We note that the dispersion of the b values they get in their sample is around 0.14. The slope uncertainties reported in Table 4.2 are therefore wide enough to take this effect into account.

We can therefore confidently say that the mini halo has a super-linear correlation, while the diffuse emission on a larger scale follows a linear/sub-linear trend, suggesting

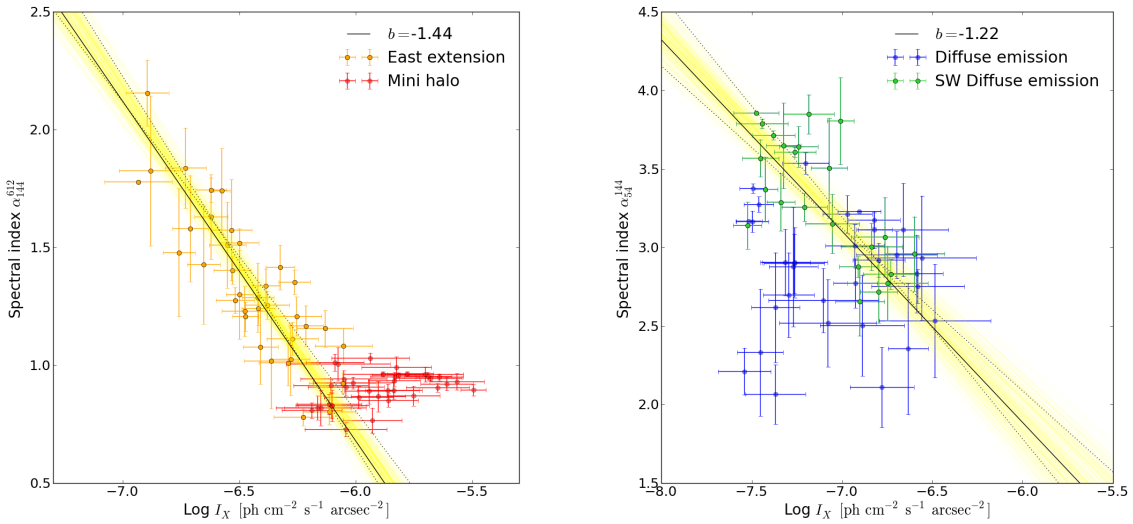

Figure 4.8: *Left:* Spectral index - X-ray surface brightness correlation of the central emission. Orange points, with associated statistical errors, are from the east extension, while red points from the mini halo. The black line shows the best-fit correlation on east extension, black dotted lines show the 25th and 75th percentile of the posterior distribution. *Right:* Spectral index - X-ray surface brightness correlation of the diffuse emission on larger scale (blue points, with associated statistical errors). The points related to the SW part of the diffuse emission are indicated in green. The black line shows the best-fit correlation, black dotted lines show the 25th and 75th percentile of the posterior distribution.

an intrinsic difference in their thermal properties.

4.4.2 X-ray surface brightness vs spectral index

We also studied the point-to-point distribution of the radio spectral index in relation to the thermal emission. For the study of the central radio emission we used the high-frequency spectral index map, between $144-612$ MHz, for which the resolution is higher. For the diffuse emission on larger scale, instead, we used the low-frequency spectral index map, between $54-144$ MHz. To extract the X-ray surface brightness and spectral indices, we used the same grid regions presented in Sec. 4.4.1, considering the radio emission above 3σ level. The results are shown in Fig. 4.8, left panel for the central emission and right panel for diffuse emission on larger scale. There is evidence of an anti-correlation for the east extension (orange points), while for the mini halo radio spectral index and X-ray surface brightness are not correlated (red points). An anti-correlation is also present for the south-west part of the diffuse emission (green points). If, on the other hand, all the diffuse emission is considered (blue points), the scatter of the points is greater and they appear uncorrelated, suggesting a contamination of other components to this emission. To compute the significance of the correlation, we estimated the Spearman and Pearson correlation coefficients and fitted the data with a relation of the form:

$$\alpha = b \log I_{\rm X} + c. \tag{4.2}$$

As in the previous section, we performed a linear regression using Linmix. The resultant parameters are reported in Table 4.3. There is a moderate negative correlation between the spectral index and X-ray surface brightness of the two components with a super-linear best-fit slope, indicating that the spectral index is flatter at high X-ray surface brightness and steepens in low X-ray brightness regions. Recently, an anti-correlation between these two quantities has been observed for the radio halo in MACS J0717.5+3745 (Rajpurohit

Table 4.3: α-I_X correlation.

Region	Frequency ν	Slope b	Pearson coeff. r_p	Spearman coeff. r_s
Mini halo	144-612 MHz	0.18 ± 0.07	036	0.42
East extension	144-612 MHz	-1.44 ± 0.14	-0.86	-0.87
Diffuse emission	54-144 MHz	-0.62 ± 0.16	-0.32	-0.34
SW Diffuse emission	54-144 MHz	-1.22 ± 0.20	-0.71	-0.67

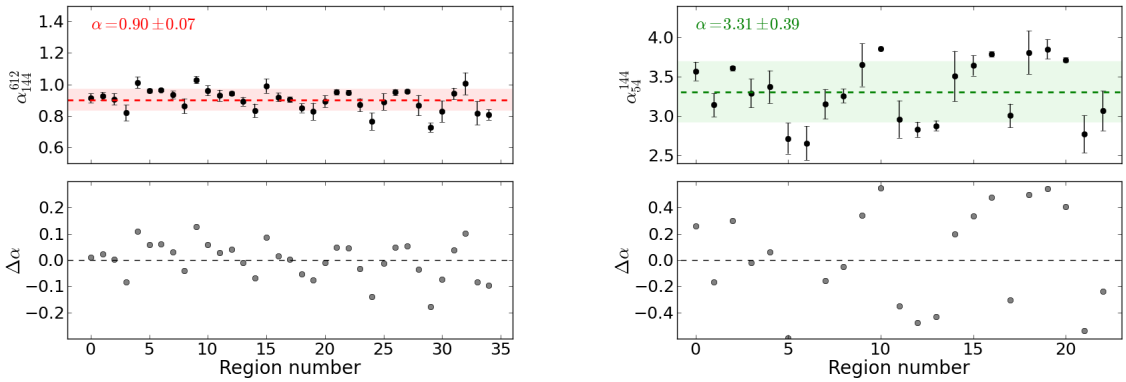

Figure 4.9: Spectral index distribution across the mini halo (*Left*, α_{144}^{612}) and across the SW diffuse emission (*Right*, α_{54}^{144}). The spectral indices were extracted in regions indicated in Fig. 4.6 (red squares) and in Fig. 4.7 (green square), respectively. The dashed horizontal line indicates the mean spectral index, while the coloured region represents the standard deviation. The lower panels show the residuals of α with respect to the mean spectral index.

et al., 2021a), conversely for the halo in Abell 2255 Botteon et al. (2020b) found a positive correlation.

In Fig. 4.9 we show the spectral index distribution across the mini halo (left panel) and the SW diffuse emission (right panel). On mini halo scale there is a small scatter in the spectral index distribution ($\Delta\alpha \sim 0.1$), while a large scatter is observed in the spectral index of SW diffuse emission, with values in the range $2.6 \leq \alpha \leq 3.9$.

4.5 Discussion

In this work we presented new LOFAR LBA observations of the galaxy cluster RXJ1720.1, which presents a central mini halo and fainter diffuse emission on larger scales. We performed spectral analysis of the source and a comparison between radio and X-ray properties to try to understand the origin of this hybrid morphology. Our results reveal that the mini halo and the more diffuse emission show distinct features, suggesting the radio emission inside and outside the cluster core have a different origin. They could be either generated by different mechanisms, such as hadronic origin for the mini halo and turbulence for the more extended emission, either by the same mechanism, such as turbulence, with different origins or the same origin but in different conditions of e.g. magnetic field or distribution of seed electrons. Another possibility is that different micro-physical conditions of the ICM in the cluster volume can change the acceleration rate of the particles (Brunetti & Lazarian, 2011).

4.5.1 Central emission

The central emission of RXJ1720.1 consists of a bright central mini halo and a fainter emission extending to the east, delimited by two cold fronts. The east extension was previously interpreted as a continuation of the mini halo (Giacintucci et al., 2014b). However, our results showed that the mini halo and the east extension present different trend for the $I_R - I_X$ and $\alpha - I_X$ correlations. So we decided to exclude this emission from the analyses concerning the mini halo. The east extension on the other hand follows correlations that are more similar to those of the SW diffuse emission. This could indicate that also the east extension is powered by the same mechanism responsible for the SW diffuse emission. In any case, because of the nearby AGN tail, it is likely that we are observing the superposition of the halo with the tail. As these emissions cannot be separated, we focused our analysis on the SW diffuse emission only (see Section 4.5.2).

The mini halo has a mean spectral index of $\alpha_{144}^{612} = 0.9 \pm 0.1$ with little spectral index variations. It follows a super-linear correlation between radio and X-ray surface brightness, indicating that the relativistic electrons and magnetic field are more concentrated around the central AGN. The relativistic particles injected by the central AGN can then play a role both directly generating secondary electrons or as seed particles re-accelerated by turbulence.

A test of hadronic models (Pfrommer & Enßlin, 2004; Enßlin et al., 2011; ZuHone et al., 2015) for mini halos can be obtained from the γ-rays due to the decay of π^0 that are produced by the same chain of secondary electrons. Ignesti et al. (2020) calculated the γ-ray emission of a sample of mini halos. Their predicted fluxes are below the *Fermi*-LAT [2] detection limit, hence the hadronic model does not violate the current non-detection of diffuse γ-ray emission. We used the formalism in Brunetti et al. (2017) to calculate the expected γ-ray flux from the mini halo region of RXJ1720.1 assuming a pure hadronic origin of the mini halo. The expected γ-rays are a factor 10 below *Fermi*-LAT sensitivity (assuming 15 yrs of data) assuming an average magnetic field of $B_0 = 1$ μG in the core of the cluster (Fig. 4.10). Larger γ-ray fluxes are predicted for weaker magnetic fields, yet we found that for $B_0 \leq 0.5$ μG the hadronic model predicts γ-rays below the current *Fermi*-LAT sensitivity. The γ-ray flux would be even lower in the case cosmic-ray protons and their secondaries are re-accelerated by turbulence in the core (Brunetti & Lazarian, 2011; Pinzke et al., 2017).

In conclusion, although in previous literature a re-acceleration of seeds electrons origin of the mini halo in RXJ1720.1 was favoured (Giacintucci et al., 2014b; ZuHone et al., 2013), we found that also a hadronic origin may provide a valid interpretation.

4.5.2 Diffuse emission outside the cluster core

Low-frequency observations with LOFAR have revealed the presence of fainter diffuse emission outside the cluster core of RXJ1720.1. This emission extends in the north-east south-west direction, reaching a total extension of 600 kpc, and has an ultra-steep spectrum, with a mean spectral index of $\alpha_{54}^{144} = 3.2 \pm 0.2$. The X-ray emission instead has a regular morphology on large scales. We propose two possible scenarios:

- The cluster underwent a minor merger that injected turbulence into the medium and re-accelerated particles on large scales. In this case the large-scale diffuse emission is similar to a giant radio halo. In fact it extends up to 600 kpc and there is evidence of steep emission even in the central regions of the cluster. Moreover, we found a modest linear/sub-linear correlation between radio and X-ray surface brightness. This emission shows an ultra-steep spectrum $\alpha_{54}^{144} = 3.2 \pm 0.2$, as observed in rare

[2] Large Area Telescope (LAT) on-board of the *Fermi* satellite

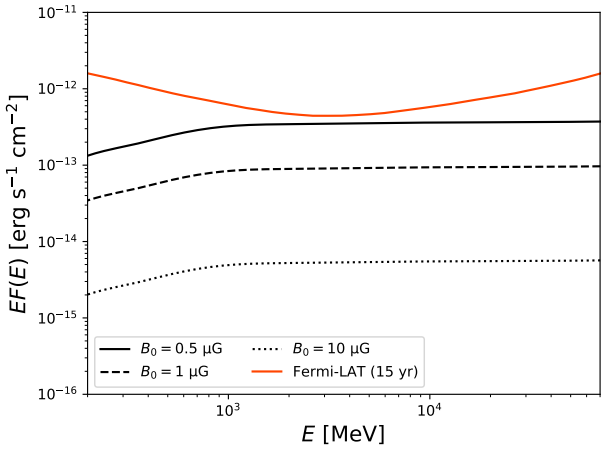

Figure 4.10: γ-rays spectrum for the mini halo considering a central magnetic field of $B_0 = 0.5$ μG (black solid line), $B_0 = 1$ μG (black dashed line) and of $B_0 = 10$ μG (black dotted line) compared with the *Fermi*-LAT 15 yrs detection limit (orange line).

cases of very gentle particle re-acceleration (de Gasperin et al., 2017; Hodgson et al., 2021). In our source, the turbulence could be generated as a consequence of a minor/off-axis merger. Steep-spectrum diffuse emission is indeed predicted by re-acceleration models in connection with less energetic merger events (e.g., Cassano et al., 2006; Brunetti et al., 2008; Wilber et al., 2018). The minor merger has then dissipated enough energy into the ICM to accelerate particles in a large volume, without disrupting the cool-core of the cluster. In this scenario, therefore, both a mini halo and a giant radio halo coexist, as proposed for the cool-core cluster PSZ1G139.61+24.20 (Savini et al., 2018). The large-scale sloshing should have left an imprint also in the distribution of the thermal emission. However, the X-ray map of RXJ1720.1 does not show an excess of surface brightness at the location of the SW diffuse radio emission. Evidence in support of this scenario is the detection of group-scale substructures with optical spectroscopy (Owers et al., 2011), that may have perturbed the medium and produced the emission we observed in the radio band. The most likely perturber is a substructure located south-west of cluster centre at a distance of $\sim$ 400 kpc, in the same direction of the large-scale diffuse radio emission we observed. A slight increase observed in the weak lensing map of Okabe et al. (2010) supports this hypothesis.

- The radio emission located south-west of the cluster core is the relic of a giant bubble generated by the jet activity of the central AGN. The very steep spectrum we found for this emission suggests that the bubble is very old. The radiative age of a bubble can be calculated from the frequency at which the spectrum of a synchrotron-emitting population, initially described by a power-law with a spectral index between $0.6 - 0.8$, steepens due to energy losses. Assuming an initial power-law of $\alpha = 0.7$ and an equipartition magnetic field of $B_{\rm eq} \sim 5.7 \mu$G, we estimated a bubble age of $t \sim 350$ Myr. The counter-part of this bubble is located north-east of the centre, where we also found evidence of steep emission between the mini halo and the head-tail radio galaxy. This scenario is supported by the recent discovery of a giant X-ray cavity in the Ophiucus galaxy cluster (Werner et al., 2016; Giacintucci et al., 2020), filled by radio emission with a steep spectrum ($\alpha = 2.4 \pm 0.1$). In our source no X-ray cavity has been identified. However, it could be present but not detectable due to small contrast in the X-ray image outside the cluster core or due to projection effects. Other results against this scenario are: the detection of ultra-steep emission in the mini halo region, which suggests a spherical morphology like a halo rather than two bubbles; the radio and X-ray surface brightness are positively

correlated, not expected in the presence of a bubble.

In conclusion, we provide evidence that the large-scale diffuse emission should be generated by re-acceleration of particles after a minor/off-axis merger.

4.6 Conclusions

In this Chapter, we have presented new LOFAR LBA observations of the source RX J1720.1+2638. These data, combined with archival data at higher frequencies, allow us to perform a resolved spectral study and investigate the possible origins of this peculiar source. A comparison between radio and X-ray properties completes this work. The main results are summarised below:

- RXJ1720.1 is a cool-core cluster with an hybrid morphology in the radio band, it is composed of a central bright mini halo and fainter diffuse emission, only detected with LOFAR, extending outside the cluster core in the north-east south-west direction. The mini halo and the diffuse emission on larger scales show different features, suggesting they have a different nature.
- The mini halo has a spectral index of $\alpha_{144}^{612} = 0.9 \pm 0.1$, the correlation between radio and X-ray surface brightness is super-linear and the γ-ray fluxes we derived do not violate *Fermi*-LAT detection limits. Our results indicate that the mini halo could have a hadronic origin, as a valid alternative to the re-acceleration models previously proposed in the literature.
- For the first time we estimated the spectral index of the diffuse emission outside the cluster core, finding an ultra-steep spectrum, with a mean spectral index of $\alpha_{54}^{144} = 3.2 \pm 0.2$.
- There is neither an excess or a deficit of X-ray emission in the region of the large-scale diffuse emission, but we found a positive correlation between radio and X-ray surface brightness.
- We argue that the large-scale diffuse emission was generated by re-acceleration of particles after a minor merger. We also speculated that it could be a relic bubble, but there is no observational evidence to support this hypothesis.

Chapter 5

Radio and X-ray analysis of the cool-core clusters A1068 and MS 1455.0+2232

In this Chapter[1] we report the analysis performed on the cool-core clusters A1068 and MS 1455.0+2232. The diffuse emission of both clusters extends beyond the sloshing region and consists of a double component. For both the clusters we re-processed *Chandra* X-ray data. We found two cold fronts in A1068 and constrained in more detail the cold fronts position in MS 1455.0+2232. Furthermore, we performed spectral analysis of the diffuse emission, combining LOFAR HBA data presented in Chapter 3 with data ad higher frequencies. In A1068 the spectral index increases at larger distances from the centre, while in MS 1455.0+2232 this trend is less constrained. Finally, we performed a point-to-point comparison of the radio and X-ray surface brightness for the source MS 1455.0+2232.

5.1 Introduction

A1068 is a cool-core galaxy cluster located at redshift $z = 0.14$ ($1'' \cong 2.45$ kpc with the adopted cosmology). The cooling-time in the core is very short, $t \geq 9 \times 10^7$ yr, and there is a spatial correspondence between regions of observed star formation and short cooling times (Wise et al., 2004; McNamara et al., 2004). The X-ray emission of A1068 exhibits a strong central peak coincident with the central cD galaxy and has an highly elliptical morphology, with the major axis along the north-west south-east direction (Wise et al., 2004). This morphology is also reflected in the abundance map of the elements, where there is a clear metal increase along the major axis. The cluster presents a declining temperature gradient, with the coolest temperature of $T \sim 2.5$ keV at cluster centre. There are, however, asymmetries in the gas temperature map: south-east of the cluster centre, at a distance of $r \sim 20''$ (50 kpc), there is an arc-shaped region of low temperature ($T \sim 2 - 3$ keV), while at north-west the temperature increases rapidly, reaching a maximum of $T \sim 5$ keV at a distance of $r \sim 10''$ (25 kpc) from the cluster centre. Such temperature jump is coincident with a surface brightness discontinuity, suggesting the presence of a cold front (Wise et al., 2004).

The cluster was observed in the radio band with VLA at 1.4 GHz by Govoni et al. (2009). The central emission exhibits two peaks associated to the cD galaxy and another bright cluster-member galaxy. Around the central emission there is a hint of diffuse emission with an extension of roughly 100 kpc.

[1]The analysis of MS 1455.0+2232 are reported in (Riseley et al., 2022), to which I collaborated. The analysis of A1068 are still in progress and will be reported in a dedicated article.

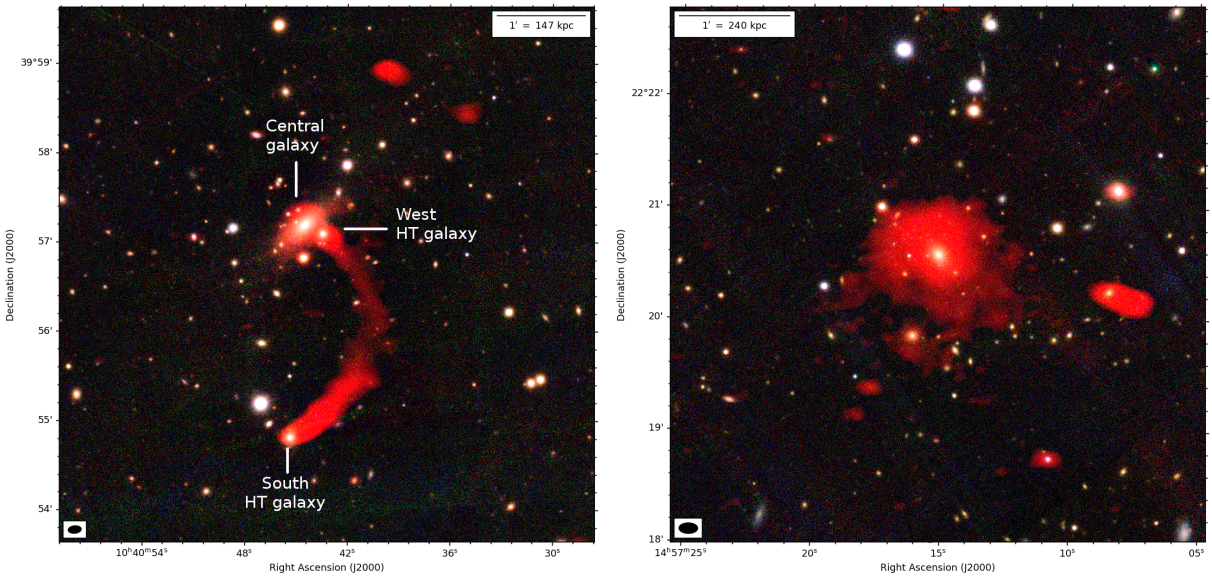

Figure 5.1: *Left panel:* Composite image of A1068, obtained combining the radio LOFAR HBA imate at $8.8'' \times 5.0''$ resolution in red with optical RGB Pan-STARR image (g,r,i bands, Chambers et al., 2016) *Right panel:* Composite image of MS1455, obtained combining the radio 144 MHz LOFAR image at $10.0'' \times 5.6''$ resolution in red with optical RGB Pan-STARR image (g,r,i bands, Chambers et al., 2016).

In Fig. 5.1 (left panel) we show a composite image of A1068 with our 144 MHz LOFAR data in red overlaid on an optical RGB image reconstructed using *i*-, *r*- and *g*-band images from *Pan-STARRS* (Chambers et al., 2016).

MS 1455.0+2232 (hereafter MS1455) is a cool-core cluster located at redshift $z = 0.26$ ($1'' \cong 4$ kpc with the adopted cosmology), hosting a pair of cold fronts on opposite sides of the cluster centre (Mazzotta et al., 2001; Mazzotta & Giacintucci, 2008).

The mini halo in MS1455 was first reported by Venturi et al. (2008) using 610 MHz observations performed with GMRT (Swarup, 1990). Venturi et al. identified it as a 'core-halo' structure, measuring a largest angular size of 90″ (347 kpc). More recently, Giacintucci et al. (2019) presented a re-analysis of archival narrow-band 1.4 GHz VLA A- and C-configuration observations. The mini halo is only partially resolved in their C-configuration image, and appears less extended ($60'' \cong 231$ kpc in diameter) than at lower frequencies. Giacintucci et al. (2019) estimate a spectral index of $\alpha_{610}^{1400} = 1.5 \pm 0.2$.

In Fig. 5.1 (right panel) we show a composite image of MS1455 with our 144 MHz LOFAR data in red overlaid on an optical RGB image reconstructed using *i*-, *r*- and *g*-band images from *Pan-STARRS* (Chambers et al., 2016).

5.2 Data

5.2.1 Radio data

For the analysis of the clusters we used the LOFAR HBA (144 MHz) data observed with LoTSS presented in Chapter 3.

For A1068, we complemented LOFAR data with new uGMRT Band 3 data (300−500 MHz, PI Biava). uGMRT observations were carried out on 2021 January 29 using the GMRT Wideband Backend (GWB). The cluster was observed for a total integration time of 11 hours. The sources 3C286 and 3C48 were used as flux-density calibrators. The

uGMRT data were processed using the SPAM[2] pipeline (Intema, 2014; Intema et al., 2017), that corrects for both ionospheric direction-independent and direction-dependent effects. The calibrated data were then imaged at different resolutions using WSClean (Offringa et al., 2014).

For MS1455, instead, we complemented LOFAR observation with new MeerKAT data at 1283 MHz. Observations were performed on 2021 April 25 (SB 20210301-0026) using the L-band receivers, with 4096 channels covering a frequency range 872−1712 MHz. Following standard MeerKAT practice, bandpass calibrators were observed roughly every three hours during the observing run. These were the bright radio sources PKS B0407−658 and PKS B1934−638, the latter of which was also used to set the absolute flux density scale. The compact radio source J1445+0958 was observed for two minutes at a half-hour cadence to provide an initial calibration of the time-varying instrumental gains. The total integration time on MS1455 was 5.5 hours. Initial calibration and flagging was performed using the Containerized Automated Radio Astronomy Calibration (`CARACal`) pipeline[3] (Józsa et al., 2020, 2021). Once applied the calibration tables to our target, we generated an initial sky model using `DDFacet` (Tasse et al., 2018). We averaged our data by a factor of eight in frequency, yielding 512 output channels of 1.67 MHz width. Self-calibration was carried out using the `killMS` software package (`kMS` Tasse, 2014a; Smirnov & Tasse, 2015). We performed three rounds of direction-independent (DI) phase-only self-calibration and two rounds of DI amplitude-and-phase self-calibration. Imaging was performed with `DDFacet` using `robust` = −0.5 weighting (Briggs, 1995) in order to achieve a balance between resolution, signal-to-noise, and sensitivity to diffuse radio emission. We used the sub-space deconvolution (`SSD`, Tasse et al., 2018) algorithm in order to more accurately reconstruct the emission from the various resolved radio sources across the field of view. While we had achieved a generally high dynamic range after DI self-calibration, we noted some residual DD errors in the wider field. To correct for these, we tessellated the sky into 16 directions and performed two rounds of DD calibration, applying gains in both amplitude and phase during each imaging step. Once no further improvement was achieved from our self-calibration process, we generated an 'extracted' dataset covering the immediate region around MS1455 by subtracting our best sky model of all sources more than 0.2 degree from the cluster. Final imaging was performed with `WSclean` (Offringa et al., 2014; Offringa & Smirnov, 2017), using multi-scale clean in order to optimally recover diffuse radio emission. The MeerKAT data presented in this work had the flux density scale set using observations of PKS B1934−638, tied to the Reynolds (1994) scale. We adopt a typical 5 per cent uncertainty in the flux scale of our MeerKAT images.

5.2.2 X-ray data

We re-analysed archival *Chandra* data of A1068 (ObsID 1652), originally presented in Wise et al. (2004) and MS1455 (ObsID 4192), originally presented in Mazzotta & Giacintucci (2008). The A1068 observation was performed on 2001 February 4, is ∼ 27 ks long, and used *Chandra* ACIS-S in FAINT mode. The MS1455 observation took place on 2003 September 5, is 95 ks long, and used *Chandra* ACIS-I in VFAINT mode. Data were processed using CIAO v4.13 with CalDB v4.9.0. We searched for time periods affected by soft proton flares by inspecting the light curve extracted in the 0.5−7.0 keV band. To maximise the signal-to-noise ratio from the ICM emission, exposure corrected images were created in the 0.5−2.0 keV energy band. Point sources were detected with the `wavdetect` task, visually inspected, and removed from the image by replacing them

[2] http://www.intema.nl/doku.php?id=huibintemaspam
[3] https://github.com/caracal-pipeline/caracal

with random values extracted from neighbouring pixels.

We produced X-ray surface brightness gradient maps using the adaptively smoothed Gaussian Gradient Magnitude (GGM) filter recently introduced by Sanders et al. (2021). This method adds in quadrature the gradients computed along the x- and y-axes from the $\log_{10}$ value of an adaptively-smoothed X-ray image of the cluster (we adopted a smoothing signal-to-noise ratio of 25).

5.3 Results

5.3.1 A1068

5.3.1.1 Radio morphology

In the upper panels of Fig. 5.2 we represent high-resolution images of LOFAR observations at 144 MHz on the left and GMRT data at 400 MHz on the right. Two bright sources dominate the radio emission at cluster centre (see also Fig. 5.1): on the left the cD galaxy, which has a morphology slightly elongated to the north; on west a cluster-member head-tail radio galaxy. South of the cluster centre there is another head-tail radio galaxy. Around the central galaxy, we detected small-scale diffuse emission. This emission is clearly visible in the high-resolution GMRT image.

To enhance the sensitivity to diffuse emission, we created low-resolution uv-tapered images, shown in the central row of Fig. 5.2. In the LOFAR image the diffuse emission is detected on a larger scale, reaching a total extension of 400 kpc and is elongated in the north-west south-east direction. In the uGMRT image, instead, it has a smaller extension of 245 kpc, suggesting a steep spectrum.

To analyse in detail the diffuse emission in A1068 we subtracted the central source and the two tails. The final source-subtracted low-resolution images are shown in the lower panels of Fig. 5.2. There are still some residuals of the tails. However, we can study the diffuse emission by neglecting the part contaminated, to the right of the cluster centre.

In Chapter 3 we found a discontinuity in the radial profile of the radio emission in both north-west and south-east directions, indicative of the presence of a double component in the diffuse emission.

5.3.1.2 Radio spectral study

Combining LOFAR and uGMRT data, we created spectral index maps of the source at different resolutions, shown in Fig. 5.3 (upper panels) together with associated error maps (lower panels). The signal under 3σ is blanked. At a resolution of $6''$ (left panel) we can distinguish the core of the central galaxy, which has a spectral index of $\alpha = 0.6 \pm 0.1$ and the surrounding diffuse emission which has a mean spectral index of $\alpha = 1.6 \pm 0.1$. The core of the central head-tail galaxy has a spectral index similar to the BCG, $\alpha = 0.7 \pm 0.1$, and then there is a steepening along the tail, reaching a maximum spectral index of $\alpha = 1.6 \pm 0.2$, indicating electron ageing, as expected. The same trend is observed in the head-tail galaxy on the south.

We also produced a map at lower resolution of $35''$ (right panel of Fig. 5.3) after source subtraction. We overlapped in black the LOFAR contours after source subtraction and in grey the LOFAR contours before source subtraction. As there are still some residual of the two tails, we did not consider the contaminated region, where we obtained the flattest values of spectral index. So we considered only the diffuse emission which extends in the north-west south-east direction. It has a quite uniform spectral index of $\alpha = 1.4 \pm 0.1$ in

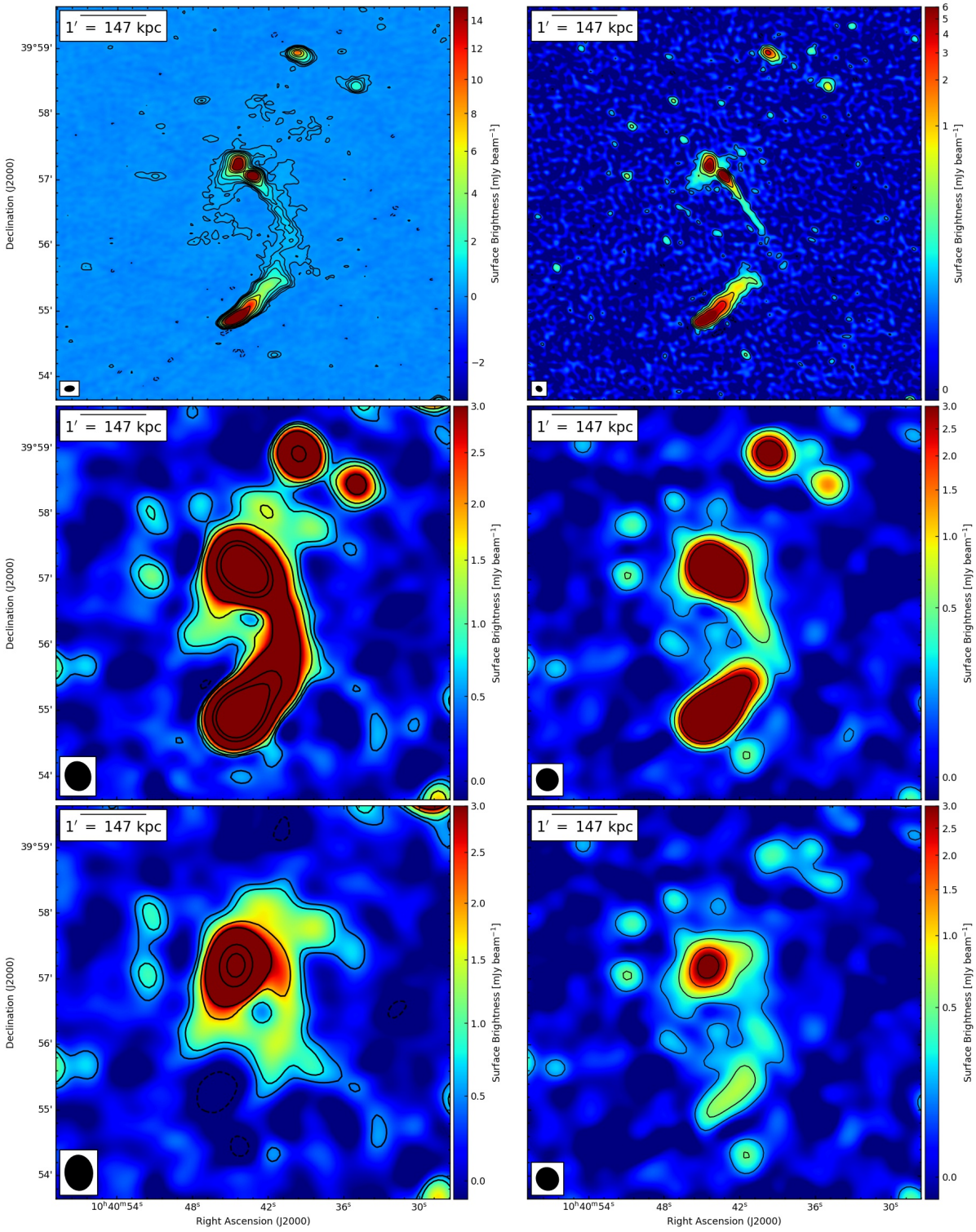

Figure 5.2: A1068 images at different frequencies and resolutions: *Top left panel*: High-resolution 144 MHz LOFAR image. Levels:[-3, 3, 6, 9, 15, 30, 60, 90, 150]$\times\sigma$ (where $\sigma = 0.08$ mJy beam^{-1}). The beam is $8.8'' \times 5.0''$ and is shown in the bottom left corner of the image. *Top right panel*: High-resolution 400 MHz uGMRT image. Levels:[-3, 3, 15, 50, 150]$\times\sigma$ (where $\sigma = 0.018$ mJy beam^{-1}). The beam is $5.7'' \times 4.4''$ and is shown in the bottom left corner of the image. *Central left panel*: Low-resolution 144 MHz LOFAR image. Levels=[-3, 3, 5, 12, 20, 90, 150]$\times\sigma$ (where $\sigma = 0.15$ mJy beam^{-1}). The beam is $32.2'' \times 25.3''$ and is shown in the bottom left corner of the image. *Central right panel*: Low-resolution 400 MHz uGMRT image. Levels=[-3, 3, 9, 30, 60]$\times\sigma$ (where $\sigma = 0.054$ mJy beam^{-1}). The beam is $21.3'' \times 19.8''$ and is shown in the bottom left corner of the image. *Bottom left panel*: Low-resolution 144 MHz LOFAR image, obtained after central sources and tails subtraction. *Bottom right panel*: Low-resolution 400 MHz uGMRT image, obtained after central sources and tails subtraction. The same portion of the sky is represented in all the panels.

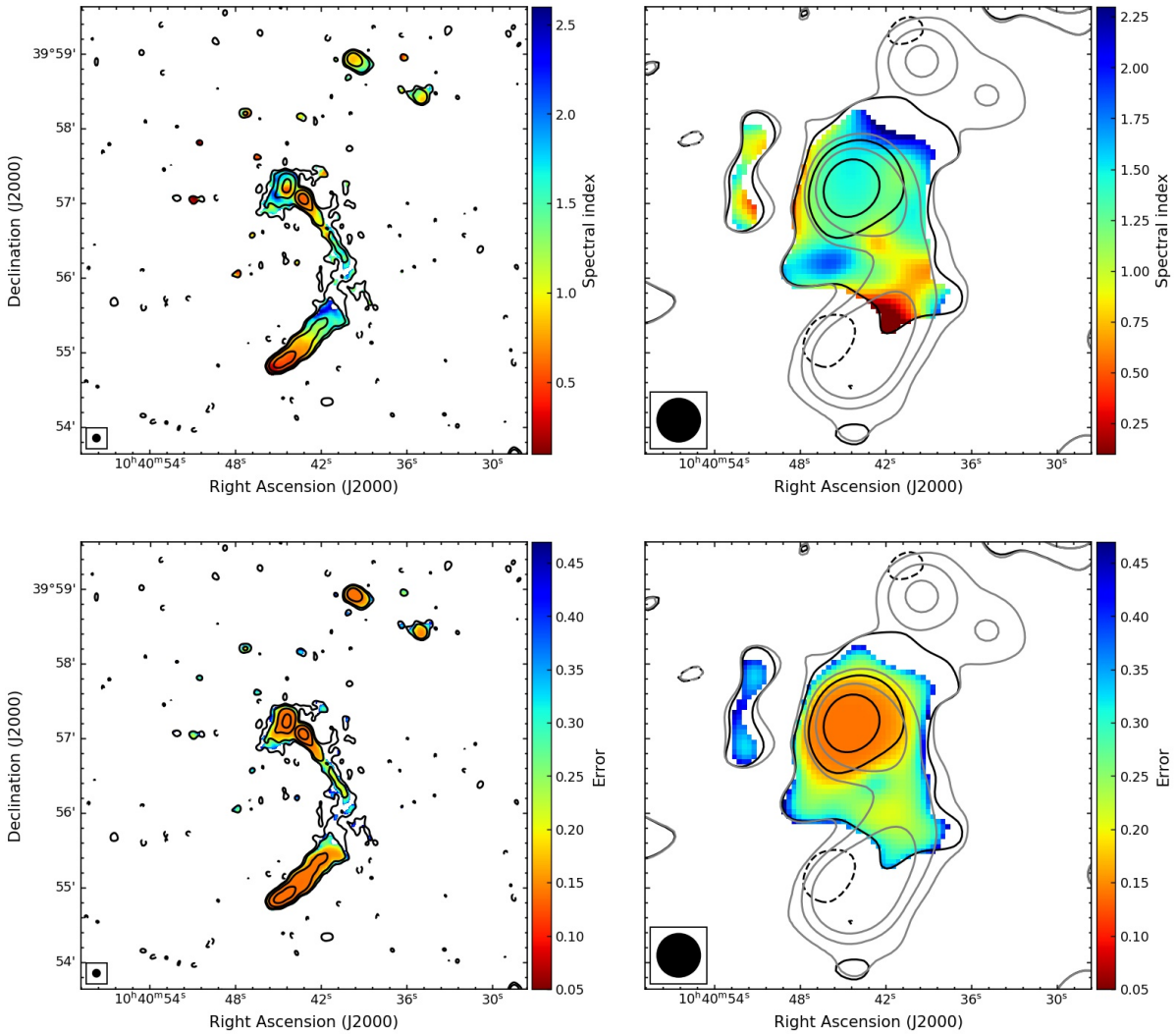

Figure 5.3: Spectral index maps (*top panels*) and associated spectral index error maps (*bottom panels*) of A1068 between 144 and 400 MHz at different resolutions. *Left panels:* 6″ resolution spectral maps with overlaid LOFAR contours. Levels:[-3, 3, 7, 30, 150]×σ (where σ = 0.09 mJy beam^{-1}). *Right panels:* 35″ resolution source-subtracted spectral maps with overlaid in black LOFAR contours of the source-subtracted image and in grey LOFAR contours of the original image, for comparison. Levels:[-3, 3, 15, 50]×σ (where σ = 0.25 mJy beam^{-1}).

the central region, then it steepens in the outermost regions, where $\alpha \sim 1.7 \pm 0.3$ south-east of cluster centre and $\alpha = 2.0 \pm 0.3$ north-west. The extreme part of the north-west emission, however, is not detected with uGMRT, so we derived a limit to its spectral index of $\alpha \geq 2.6$ considering the 3σ LOFAR emission and the uGMRT noise.

5.3.1.3 X-ray features

Fig. 5.4 shows the *Chandra* X-ray surface brightness map in the 0.5−2.0 keV energy band in the upper left panel and the X-ray surface brightness gradient map in the upper right panel. The central part of the X-ray emission is highly elongated in the north-west south-east direction, while on larger scales the ellipticity is less accentuated. The gradient surface brightness map helps to individuate discontinuities in the X-ray surface brightness, where the gradient value is higher. We note that there is an elliptic structure of high surface gradient south-east of the cluster centre. North-west and south-east of the cluster centre there are instead two regions of low gradient, resembling holes, which

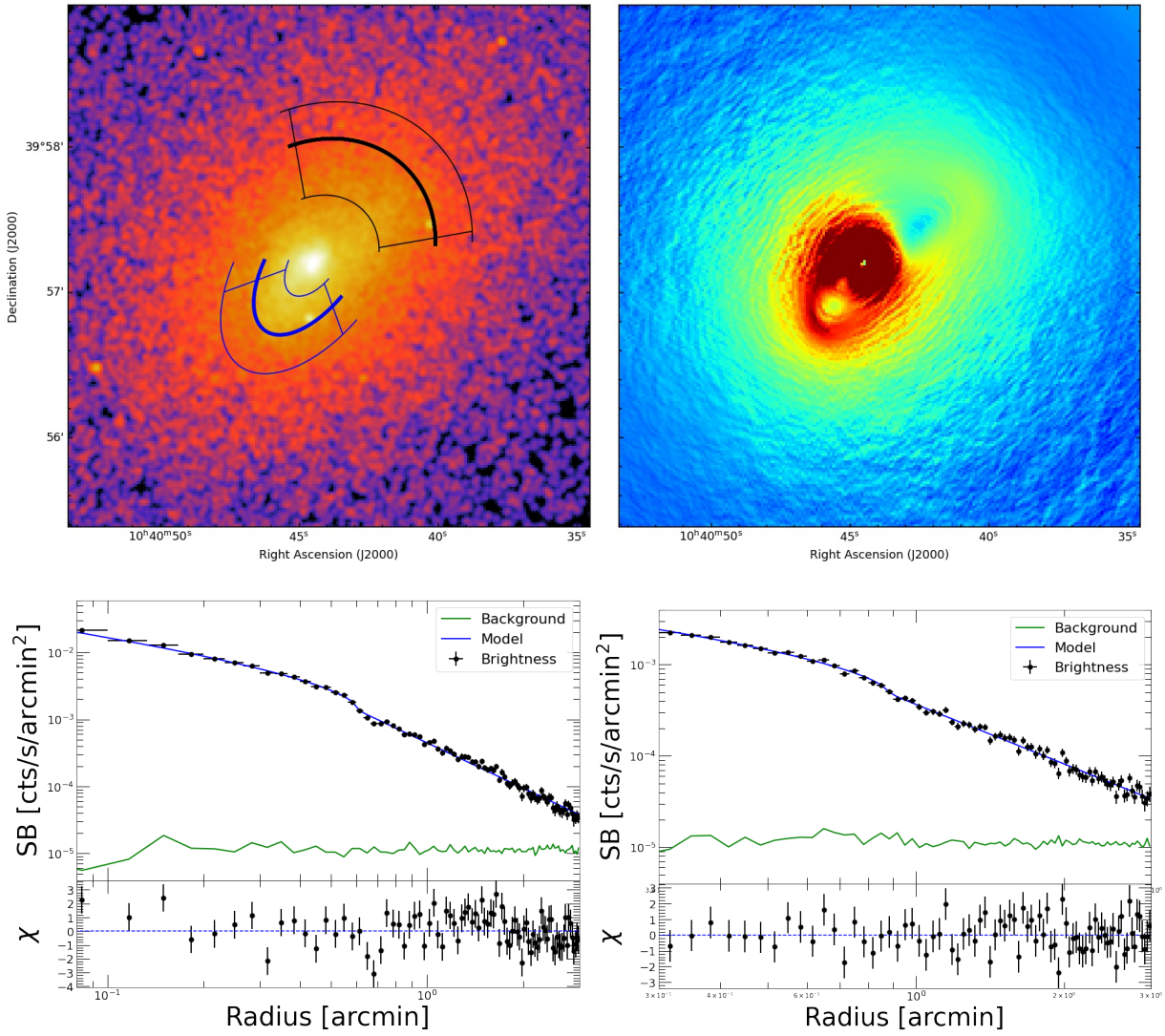

Figure 5.4: *Upper left panel:Chandra* 0.5–2.0 keV image. *Upper right panel* X-ray surface brightness gradient map. *Lower left panels:* best-fitting broken power-law (blue line) model with associated residuals, of the extracted SB profile in south-east sector, indicated in blue in the *upper left panel*. The position of the cold front is represented by a blue arc. *Lower right panel:* same as before, but for the north-west sector, indicated in black in the *upper left panel*. The position of the cold front is represented by a black arc.

indicate regions where the gas is denser and elongated by the sloshing.

We investigated the possible presence of cold fronts. Driven by the surface brightness gradient map, we checked for a surface brightness discontinuity in the region of high gradient south-east of the core. We extracted the surface brightness profile in the sector indicated in blue in the upper left panel of Fig. 5.4, using elliptical annuli optimised to follow the X-ray morphology, with a bin-size of 2″. The profile extraction and fitting were performed with `pyproffit` (Eckert et al., 2020) on the exposure-corrected image of the cluster. The south-east profile, reported in bottom left panel of Fig. 5.4, shows a clear discontinuity. This profile is well fitted by a broken power-law (in blue) with a jump in projected density of 1.34 ± 0.04 at a distance of 90 kpc. Spectral analysis provides temperatures in the inner and outer regions of $kT_{\rm in} = 2.9 \pm 0.2$ and $kT_{\rm out} = 4.4 \pm 0.4$, respectively. Such a temperature jump is specific of a cold front, in the case of a shock front, instead, we would have found a reversed temperature jump. Therefore, there is a cold front south-east of the cluster centre, at a distance of 90 kpc, indicated with a blue arc in the upper left panel of Fig. 5.4.

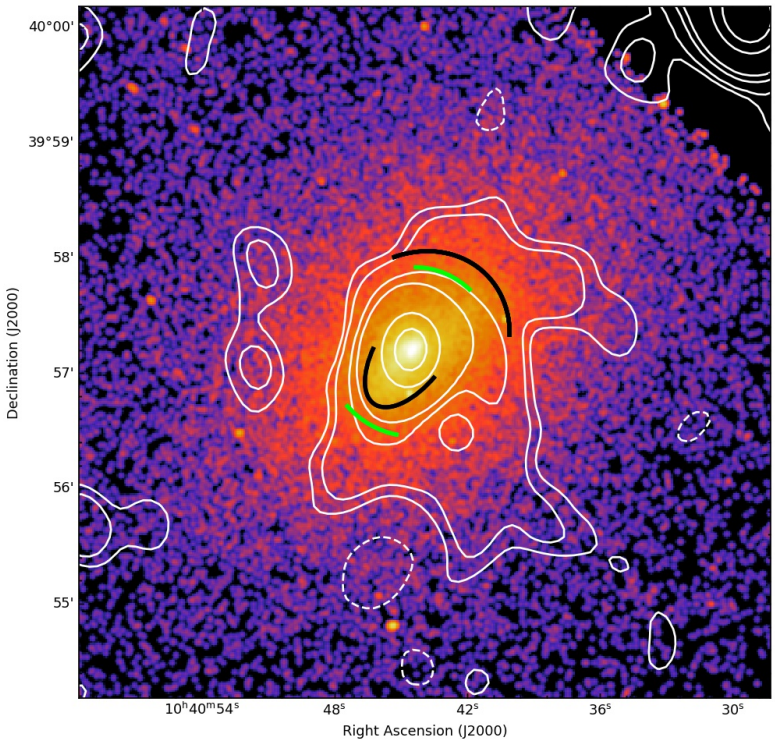

Figure 5.5: *Chandra* 0.5-2.0 keV image with overlaid in white the LOFAR HBA contours at 144 MHz with 35″ resolution. Black arcs represent the positions of the detected cold fronts, while green arcs represent the positions of discontinuities in the radio profiles.

We noticed another feature in the gradient map, a cocoon at lager distance oriented in the north-west south-east direction, which encircles the central emission. As this feature is present along all the directions, we checked for possible surface brightness discontinuities in four sectors, along the north-west, north-east, south-east and south-west directions. To follow the X-ray morphology, this time we extracted the profiles using more circular annuli. We found a discontinuity in the profile extracted in the north-west sector, indicated in black in the upper left panel of Fig. 5.4. This profile, reported in the bottom right panel of Fig. 5.4, is well-fitted by a broken power-law, with a jump in the projected density of 1.26 ± 0.04 at a distance of 130 kpc from the cluster centre. In this case, however, the inner and outer temperatures are consistent, not allowing us to firmly assert the nature of the surface brightness discontinuity. Given he morphology of the X-ray emission (elongated in the north-west south-east direction) and the presence of a cool-core, we argue that a cold front is the most likely interpretation.

In Fig. 5.5 we overlap LOFAR 144 MHz radio contours on the X-ray surface brightness map and we also indicate the cold fronts detected (black arcs). We note that the radio emission extends beyond the cold fronts in both directions. In Chapter 3 we have identified the presence of a discontinuity in LOFAR radial profiles at a distance of roughly 100 kpc in both south-east and north-west directions. The radio discontinuities (green arcs in Fig. 5.5) are close to the X-ray cold fronts (black arcs).

5.3.2 MS 1455.0+2232

5.3.2.1 Radio morphology

Figure 5.6 (upper panels) presents our high resolution MeerKAT and LOFAR images of MS1455 prior to source subtraction, imaged using `robust` $= -0.5$. With the excellent sensitivity afforded by our observations, the mini halo in MS1455 is recovered at high signal-to-noise at both 1283 MHz and 144 MHz. We also identified multiple compact and extended sources in the wider field, including a likely cluster-member head-tail radio galaxy to the west of the mini halo. The mini halo itself is asymmetric at both 1283 MHz

and 144 MHz, appearing generally brighter to the north of the cluster centre (where is located the compact radio source associated with the BCG) with more extended fainter emission toward the south. This fainter emission has not been conclusively reported in previous radio studies at comparable resolution (Mazzotta & Giacintucci, 2008; Venturi et al., 2008; Giacintucci et al., 2019) although we note a tentative detection at low resolution ($\sim 15''$) by Venturi et al. (2008) at 610 MHz.

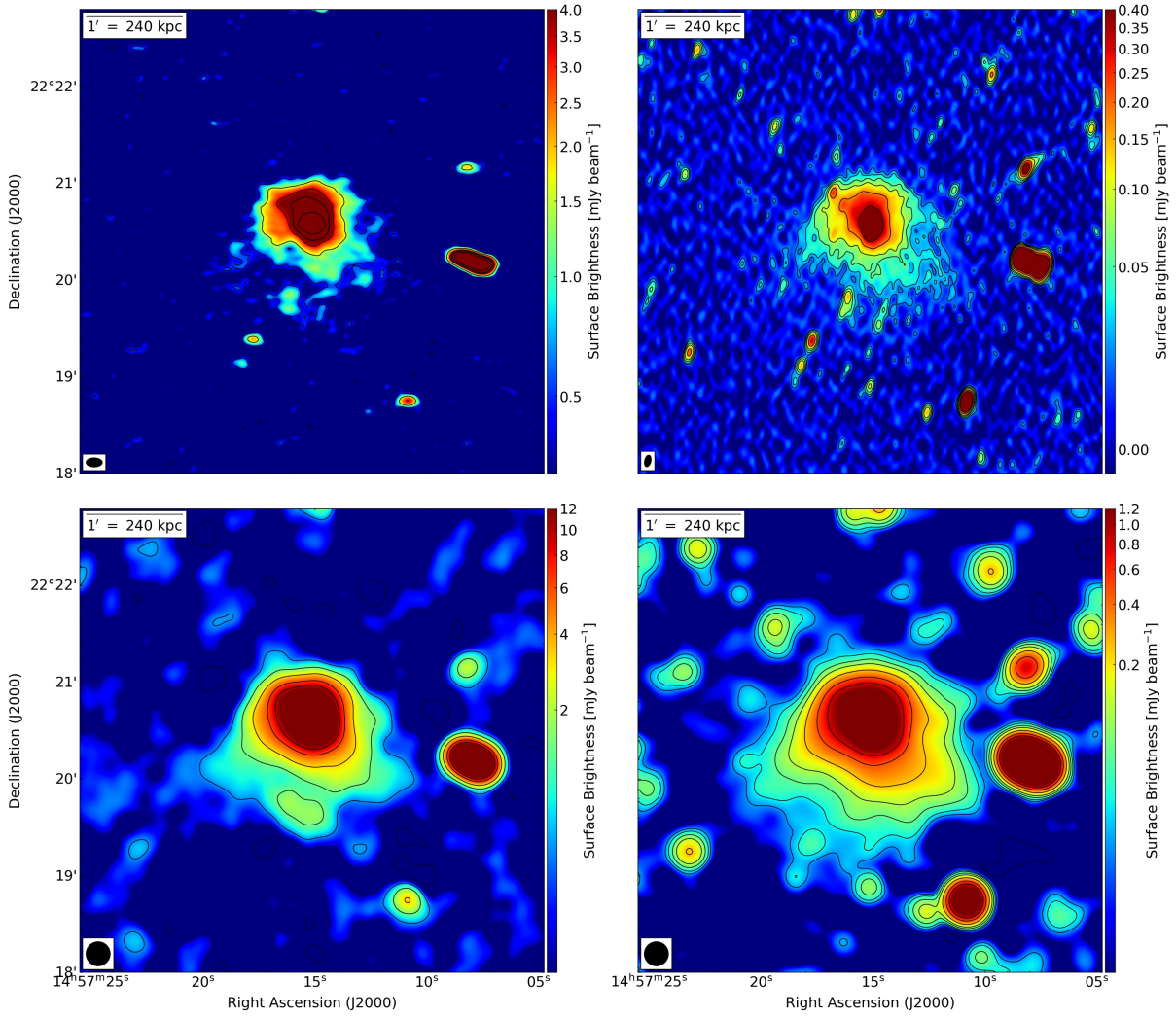

Figure 5.6: MS1455 images at different frequencies and resolutions: *Top left panel*: High-resolution 144 MHz LOFAR image. Levels:[-3, 3, 9, 20, 30, 50]$\times\sigma$ (where $\sigma = 0.17$ μJy beam^{-1}). The beam is $10.1'' \times 5.6''$ and is shown in the bottom left corner of the image. *Top right panel*: High-resolution 1283 MHz MeerKAT image. Levels:[-3, 3, 5, 9, 15, 30, 60]$\times\sigma$ (where $\sigma = 5.9$ μJy beam^{-1}). The beam is $7.4'' \times 4.0''$ and is shown in the bottom left corner of the image. *Bottom left panel*: Low-resolution 144 MHz LOFAR image after source subtraction. Levels=[-3, 3, 9, 20, 40, 60]$\times\sigma$ (where $\sigma = 159$ μJy beam^{-1}). The beam is $15'' \times 15''$ and is shown in the bottom left corner of the image. *Bottom right panel*: Low-resolution 1283 MHz MeerKAT image. Levels=[-3, 3, 5, 9, 15, 30, 60, 100]$\times\sigma$ (where $\sigma = 8$ μJy beam^{-1}). The beam is $15.0'' \times 15.0''$ and is shown in the bottom left corner of the image.

Figure 5.6 (lower panels) presents our source-subtracted, *uv*-tapered images of MS1455 at $15''$ resolution. With the enhanced sensitivity to very low surface brightness radio emission, the diffuse radio emission of the mini halo is detected to a much greater extent. From our MeerKAT image at 1283 MHz, we measured a largest angular scale (LAS) of $152''$, corresponding to a largest linear size (LLS) of 586 kpc with our cosmology. This is 69 per cent larger than previously reported by Venturi et al. (2008) at 610 MHz, who

measured a LAS (LLS) of 90″ (347 kpc). At 144 MHz, the LAS is 122″ (471 kpc).

We note that it is unusual to find non-thermal cluster phenomena that are more extended at higher frequencies than lower frequencies. The faint, steep-spectrum radio sources often associated with clusters typically trace weak and/or inefficient (re-)acceleration processes in the ICM, and are more commonly found to decrease in size with increasing frequency (reflecting the nature of the acceleration mechanism, e.g. Rajpurohit et al., 2021b,a). However, our MeerKAT images achieve a very low rms noise of 7.3 μJy beam^{-1} at 1283 MHz; as such, a source that has a 1σ flux density at each frequency would have a spectral index of $\alpha = 1.37$. This means that the larger extent at higher frequencies does not necessarily imply a spectral flattening.

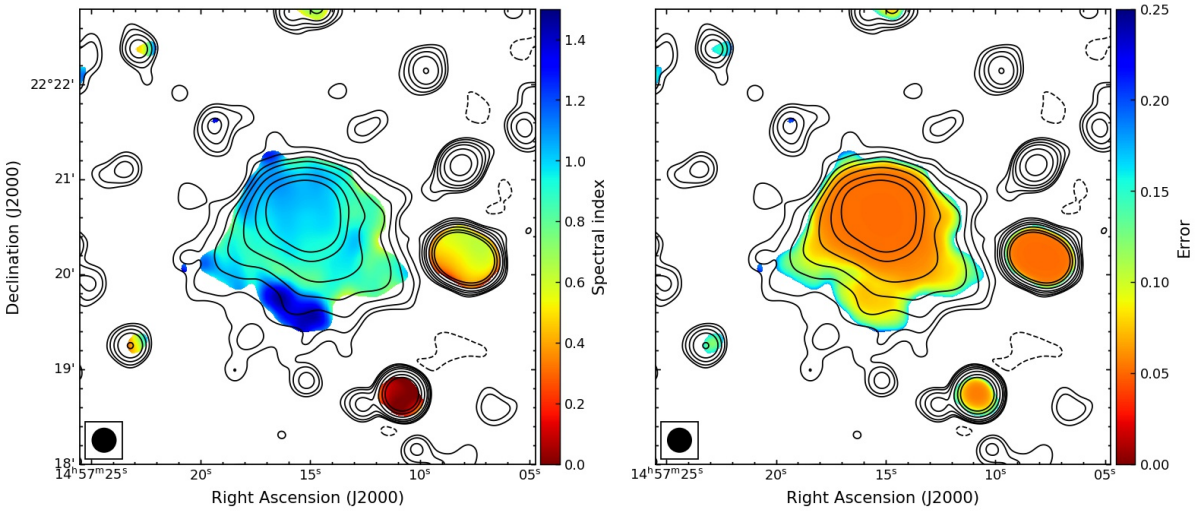

Figure 5.7: Spectral index map (*left*) and associated error mao (*right*) of the diffuse emission in MS1455 at a resolution of 15″, derived using our MeerKAT (1283 MHz) and LOFAR (144 MHz) data. Contours show MeerKAT surface brightness at 1283 MHz as per Fig. 5.6. Pixels below 3σ in each radio image are blanked.

5.3.2.2 Radio spectral study

Integrating above the 3σ contour in the corresponding MeerKAT and LOFAR images of the mini halo in Figure 5.6, we found a total flux density recovered by MeerKAT of $S_{1283\ \mathrm{MHz}} = 18.7 \pm 0.9$ mJy. For LOFAR, we measured a total integrated flux density of $S_{144\ \mathrm{MHz}} = 154.5 \pm 15.6$ mJy. Thus, our integrated spectral index for the mini halo in MS1455 is $\alpha^{144}_{1283} = 0.97 \pm 0.05$.

This is significantly flatter than was previously reported by Giacintucci et al. (2019) for this cluster: $\alpha^{610}_{1400} = 1.5 \pm 0.2$. The cause of this difference is in the higher sensitivity of our data. In fact, only the brightest central region of the mini halo is recovered by the VLA C-configuration observations presented by Giacintucci et al.; as such they recovered an integrated 1400 MHz flux density $S_{1400\mathrm{MHz}} = 8.5 \pm 1.1$ mJy, half the value we found with our deeper MeerKAT observations.

Figure 5.7 presents the spectral index map between 144 MHz and 1283 MHz at 15″ resolution, as well as the associated error map. We found a mean spectral index of $\alpha = 0.97 \pm 0.09$. Overall, the spectral index across the majority of the mini halo is largely uniform at this resolution.

We found that the average spectral index is slightly steeper exterior to the sloshing spiral boundaries ($\alpha_{\mathrm{out}} = 1.0 \pm 0.1$) than interior ($\alpha_{\mathrm{in}} = 0.94 \pm 0.07$), although these are consistent at 1σ. The standard deviation in spectral index is also a factor two greater

exterior to the spiral ($\sigma_\alpha \sim 0.06$) than interior ($\sigma_\alpha \sim 0.03$).

Toward the southernmost edge of the mini halo we found a relatively steep spectral index of $\alpha = 1.37 \pm 0.08$. However, we do not currently have the signal-to-noise to investigate this further; deeper low-frequency observations would be required to study the spectral index behaviour in the cluster outskirts in more detail and confirm this steepening.

Due to the sensitivity difference between our MeerKAT and LOFAR images, the outermost regions of the diffuse emission are undetected at 144 MHz; however, given that they are undetected by LOFAR they cannot have an ultra-steep spectrum. To quantify the spectral index limit in the outer reaches of the diffuse emission, we took the typical surface brightness measured by MeerKAT and assumed a 2.5σ limit from our LOFAR map. This yields an upper limit to the spectral index of $\alpha \gtrsim 1.3$. Deeper observations with LOFAR would be required to map the spectral index in these regions; however, the spectral index in these outer regions is clearly shallower than the ultra-steep values of $\alpha \sim 2-3$ measured in the outer regions of RX J1720.1+2638 (see Chapter 4).

5.3.2.3 X-ray properties

Fig. 5.8 shows the *Chandra* X-ray surface brightness map in the 0.5−2.0 keV band in the left panel and the X-ray surface brightness gradient map in the right panel.

The X-ray gradient map is particularly useful to highlight the surface brightness discontinuities in the ICM, such as shocks and cold fronts, and study their connection with the radio emission. Our image clearly shows a spiral-like structure that is often associated with core-sloshing in relaxed clusters: a sloshing spiral (e.g., Sanders et al., 2016b,a; Werner et al., 2016; Douglass et al., 2018).

The sloshing spiral is asymmetric around its peak: it occupies an elliptical region $66'' \times 60''$ (at PA $\sim$ 29 degrees) centred on (RA=14:57:15.14, DEC=+22:20:37.6). This corresponds to a physical scale of 254 kpc × 232 kpc. Our new analysis revealed that the cold fronts previously identified by Mazzotta & Giacintucci (2008) (black arcs in the right panel) form part of the larger spiral structure in MS1455; this kind of structure almost perfectly matches prototypical core-sloshing spirals seen in numerical simulations (e.g. Ascasibar & Markevitch, 2006; ZuHone et al., 2013).

The diffuse emission in MS1455 extends far beyond the boundaries of the sloshing spiral (black region in the left panel of Fig. 5.8): the diffuse synchrotron emission fills almost the entire X-ray-emitting region (above a count rate of 5×10^{-6} counts s^{-1}). To the north, it extends for $20''$ (77 kpc) beyond the boundary of the sloshing spiral. However, to the south the diffuse emission extends $56''$ (216 kpc) beyond the outer edge of the sloshing spiral, as traced by our MeerKAT data at 1283 MHz.

5.3.3 Radio and X-ray comparison

5.3.3.1 Point-to-Point Correlation: Surface Brightness

In giant radio halos, the synchrotron emission often shows a similar morphology and extent to the observed X-ray emission (van Weeren et al., 2019, and references therein). Mini halos show a similar trend, albeit covering a smaller fraction of the cluster volume, although that may be due to the relatively limited sensitivity of many historic observations (e.g., Giacintucci et al., 2019; Ignesti et al., 2020; Biava et al., 2021a). This implies a connection between the thermal and non-thermal components in the ICM. Fig. 5.9 (upper panels) shows the *Chandra* X-ray image of MS1455 in the 0.5−2.0 keV band, smoothed to a resolution of $15''$, with source-subtracted radio contours overlaid (MeerKAT contours

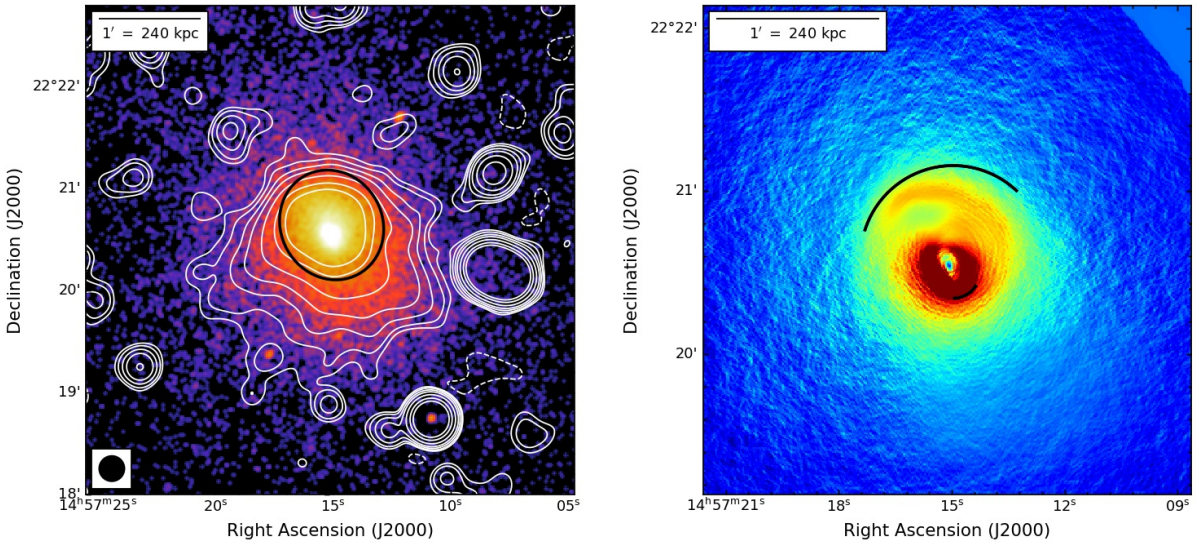

Figure 5.8: *Left panel: Chandra* 0.5−2.0 keV X-ray map with overlaid the MeerKAT 1283 MHz contours at 15″ resolution. The black regions indicates the edges of the sloshing spiral. *Right panel:* X-ray surface brightness gradient map. Black arcs trace the cold fronts identified by Mazzotta et al. (2001); our new analysis revealed that these trace features visible in the larger-scale sloshing spiral.

on the left and LOFAR contours on the right). The diffuse emission in MS1455 fills the entire volume of the X-ray emitting region, indicating a strong connection.

We studied the radio/X-ray connection using the point-to-point correlation between the radio surface brightness ($I_{\rm R}$) and X-ray surface brightness ($I_{\rm X}$) at 15″ resolution. Following recent similar studies (e.g. Ignesti et al., 2020; Botteon et al., 2020b; Biava et al., 2021a; Rajpurohit et al., 2021b,a, although most of these have focussed on giant haloes), we placed adjacent boxes of 15″ width across the diffuse emission, covering all regions above an X-ray flux limit of $\sim 5 \times 10^{-4}$ counts s^{-1}, excising those regions contaminated by residual emission from radio galaxies. We indicated with different colours the boxes inside (pink) and outside (cyan) the sloshing region, as shown in Fig. 5.9 (upper panels).

The $I_{\rm R}/I_{\rm X}$ plane for the MS1455 diffuse emission is presented in the bottom panels of Fig. 5.9. Our new highly-sensitive radio data show a positive correlation between radio and X-ray surface brightness, suggesting a strong connection between the thermal and non-thermal components in the diffuse emission of MS1455. We found the two component of radio emission, inside and outside the sloshing region, are roughly aligned, with only the four points of highest X-ray surface brightness which are deviating. To quantify the connection, we fitted a power-law relation (in log-log space) of the form:

$$\log(I_{\rm R}) = c + b\log(I_{\rm X}), \tag{5.1}$$

where the slope b describes the scaling between the thermal and non-thermal components of the ICM. The slope of this correlation is related to the underlying particle acceleration mechanism (e.g. Govoni et al., 2001; Brunetti et al., 2004; ZuHone et al., 2013, 2015). Broadly-speaking, the turbulent (re-)acceleration scenario can produce either a sub-linear or super-linear slope depending on the nature and distribution of the relativistic electrons throughout the cluster volume. Generally, the hadronic model predicts a super-linear relation due to the central CRp injection profile and equipartition assumption.

Physically, the slope relates to the relative distribution of non-thermal and thermal components. A super-linear slope (i.e. $b > 1$) would indicate that the magnetic field and/or CRe distribution is more peaked than the thermal plasma distribution, whereas a

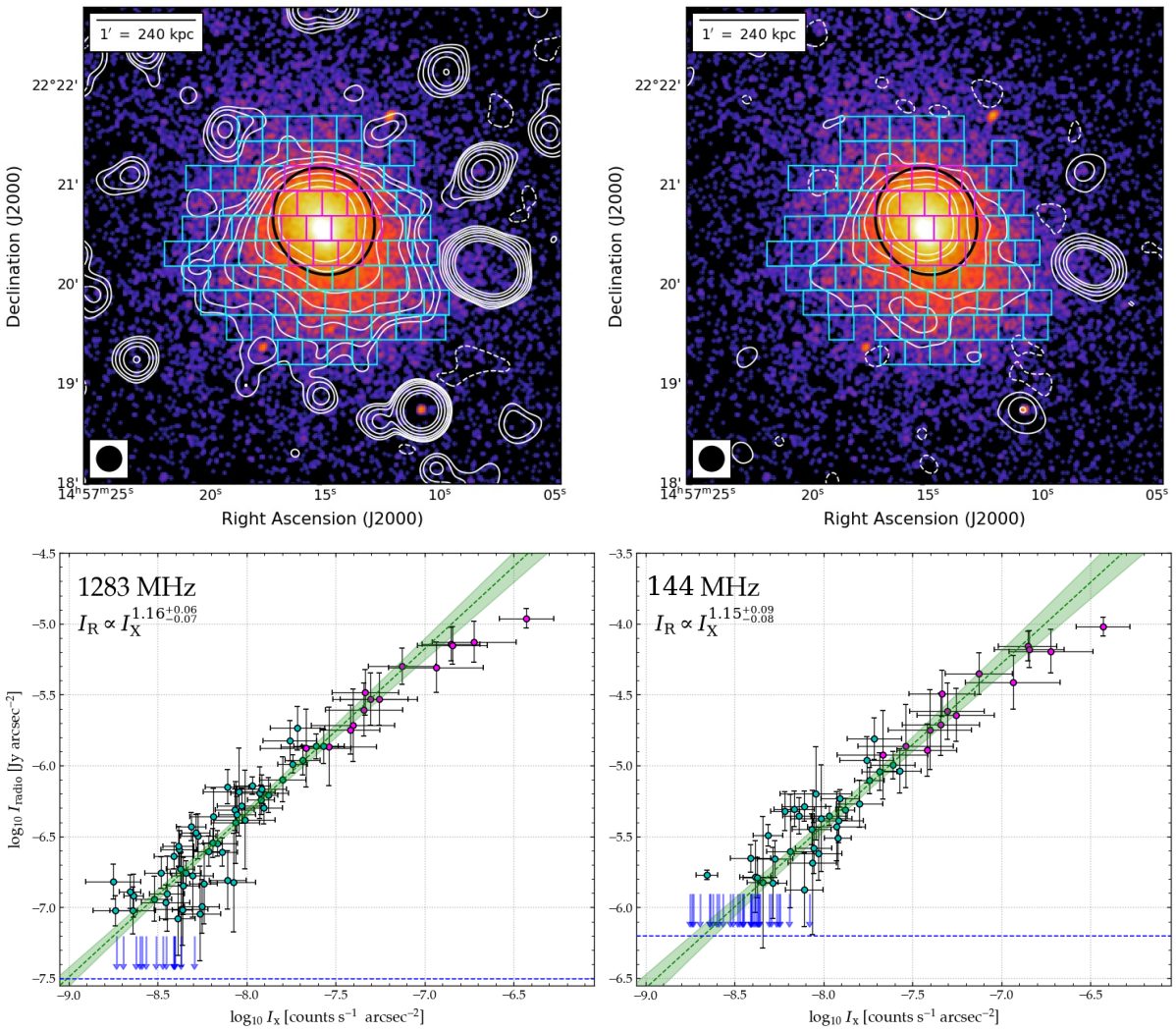

Figure 5.9: Radio/X-ray surface brightness correlation for the diffuse emission in MS1455. *Upper panels: Chandra* X-ray surface brightness map in the 0.5−2 keV band, smoothed with a 15″ FWHM Gaussian to match the resolution of our radio data. Contours denote the source-subtracted radio data (*left*: MeerKAT; *right*: LOFAR) at 15″ resolution, starting at 3σ, as per Figure 5.6. Boxes show the regions used to profile the radio/X-ray correlations, with magenta boxes indicating regions within the boundary of the sloshing spiral (identified by the black ellipse) and cyan boxes indicating regions outside. *Lower panels* shows the I_R/I_X plane at 1283 MHz, measured from our MeerKAT image (left) and the same plane at 144 MHz measured from our LOFAR image (right), both at 15″ resolution. Point markers are colourised according to the extraction regions in the upper panels. Magenta points lie within the bounds of the sloshing spiral; cyan points lie outside. For regions where the radio surface brightness is below the 3σ level in the corresponding image, we adopt a 2σ upper limit in this analysis; these are indicated by blue arrows, and the dashed blue line indicates the 1σ level. Dashed green line shows the best-fit power-law relation and the shaded green region shows the 1σ uncertainty. The slope of the best-fit power-law is $b_{1283\ \mathrm{MHz}} = 1.16^{+0.06}_{-0.07}$ at 1283 MHz and $b_{145\ \mathrm{MHz}} = 1.15^{+0.09}_{-0.08}$ at 145 MHz.

sub-linear slope (i.e. $b < 1$) would indicate the converse. However, different magnetic field profiles and/or CRp density profiles (which might arise due to the relative contribution from cluster-member galaxies) can yield different correlation slopes (e.g. Ignesti et al., 2020; Timmerman et al., 2021).

We determined the best-fit values of a and b, and quantified the strength of our correlation, using the LINMIX software package (Kelly, 2007). LINMIX performs Bayesian linear regression, accounting for uncertainties on both variables, intrinsic scatter and (importantly) upper limits to the dependent variable (I_R). We used the MCMC implementation incorporated in LINMIX to determine the best-fit values for a and b. We quote the median values of a and b from our MCMC run as our 'best-fit' values, and used the 16th and 84th percentiles to determine the uncertainties. Finally, the correlation strength was quantified by measuring the Spearman and Pearson rank coefficients.

Table 5.1 presents the results of our fitting routine. We measured a slope of $b_{144\ \mathrm{MHz}} = 1.15^{+0.09}_{-0.08}$ for the LOFAR/*Chandra* surface brightness plane and $b_{1283\ \mathrm{MHz}} = 1.16^{+0.06}_{-0.07}$ for the MeerKAT/*Chandra* surface brightness plane. We find that the radio and X-ray surface brightness is well-correlated at each frequency, with a Pearson (Spearman) coefficients of $r_p = 0.89$ ($r_s = 0.95$) at 144 MHz and $r_p = 0.91$ ($r_s = 0.94$) at 1283 MHz. At each frequency, the slope is super-linear, consistent with the typical behaviour of mini halos in the I_R/I_X plane (e.g., Govoni et al., 2009; Ignesti et al., 2020; Biava et al., 2021a). This super-linear correlation is generally believed to favour the hadronic model over the turbulent re-acceleration scenario, although we note that under some conditions, the turbulent (re-)acceleration model can replicate a super-linear slope. These conditions include scenarios where turbulence is stronger in the central region and/or where the spatial distribution of CRe is more peaked toward the cluster centre than the thermal electron distribution (e.g. simulations by ZuHone et al., 2013).

The mini halo sample of Ignesti et al. (2020) includes MS1455. The analyses are not straightforward to compare due to the dramatic difference in surface brightness sensitivity achieved by our MeerKAT and LOFAR images compared to the narrow-band GMRT images used by Ignesti et al. (2020). Similarly, the methods employed differ somewhat. Ignesti et al. (2020) used two different methods to study the point-to-point correlation, the results of which exhibit a mild tension: the BCES Bisector method found a best-fit slope $k = 0.8 \pm 0.1$, whereas they derived a correlation slope of $k = 1.0 \pm 0.1$ from the subsequent Monte-Carlo analysis using the Point-to-point TRend EXtractor (PT-REX; Ignesti, 2022). In either case, our LINMIX regression yields a fit that is steeper than that found by Ignesti et al. (2020).

Our new broad-band data not only allow us to study the point-to-point comparison in exquisite detail, but also to investigate whether there is any evolution in the correlation with frequency. Our analysis indicates no significant evolution in the slope with frequency — the slope of the correlation is consistent at 1283 MHz and 144 MHz. However, the comparison between our MeerKAT and LOFAR images shows that we cannot yet map the full extent of the diffuse emission at 144 MHz; deeper observations with LOFAR, and/or follow-up observations at complementary frequencies would be required to investigate this further. This implies that we are not seeing any evidence of spectral steepening, consistent with evidence presented earlier, although we again note that higher-frequency observations (e.g. at S- or C-band) would be required to investigate further.

5.3.3.2 Point-to-Point Correlation: Spectral Index

Our highly-sensitive data also allow us to study the point-to-point relation between the radio spectral index and the X-ray surface brightness. We performed this analysis using our images at 15″ resolution and the same regions indicated in Fig. 5.9. Few

Table 5.1: I_R-I_X and α-I_X correlations

Image	Slope	Spearman coeff.	Pearson coeff.
	b	r_S	r_P
1280 MHz	$1.16^{+0.06}_{-0.07}$	0.91	0.94
144 MHz	$1.15^{+0.09}_{-0.08}$	0.89	0.95
α (outer)*	$0.21^{+0.11}_{-0.11}$	0.28	0.28

Notes. The fit for the spectral index point-to-point analysis was performed using only measurements outside the sloshing spiral (cyan points in Fig. 5.10)

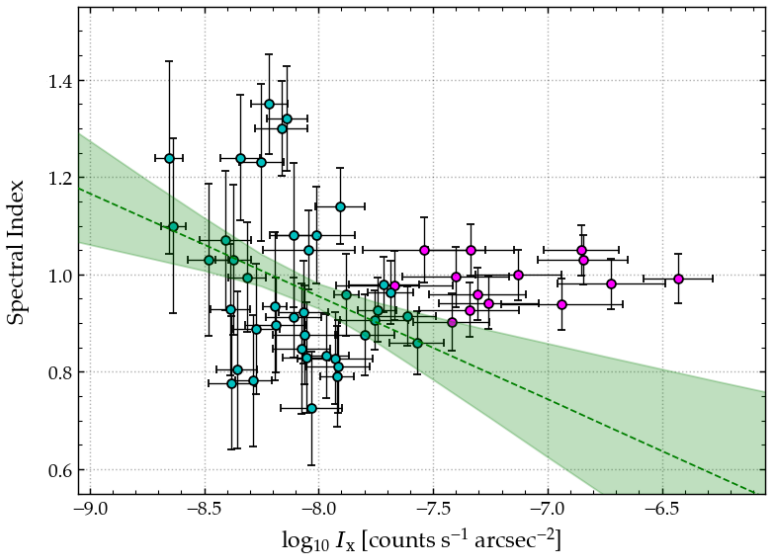

Figure 5.10: Radio spectral index/X-ray surface brightness correlation for the diffuse emission in MS1455. Points are colourised according to extraction region, as per Figure 5.9. Magenta (cyan) points denote regions inside (outside) the boundary of the sloshing spiral. Dashed green line shows the best-fit to Equation 5.2 for the cyan points and the shaded green region shows the 1σ uncertainty. Magenta points show no correlation.

such studies exist in the literature for mini halos, though Biava et al. (2021a) found no strong correlation between spectral index and X-ray surface brightness for the mini halo in RX J1720.1+2638. Outside of the mini halo however, Biava et al. (2021a) found a moderate-to-strong anti-correlations for the different diffuse radio emission substructures outside the core of RX J1720.1+2638. For radio halos, the picture is mixed. Some halos show positive correlation (Botteon et al., 2020a), some show an anti-correlation (Rajpurohit et al., 2021a) and others show both correlation and anti-correlation for different sub-regions (Rajpurohit et al., 2021b).

We quantified the relation between radio spectral index α and X-ray surface brightness by fitting a power-law in linear-log space as follows:

$$\alpha = c + b\log(I_X) \tag{5.2}$$

The result of our point-to-point analysis is presented in Fig. 5.10, and the correlation slope b and Spearman and Pearson coefficients are reported in Table 5.1. When we fit a single relation to all points, the slope $b = 0.01^{+0.03}_{-0.03}$ is consistent with no correlation. The Spearman and Pearson coefficients are similarly very weak, as we find $r_S = 0.07$ and $r_P = -0.01$. However, Fig. 5.10 suggests that regions inside and outside the sloshing spiral may exhibit different behaviour: regions outside the sloshing spiral (cyan points in Figure 5.10) appear to show a tentative correlation with X-ray surface brightness, similar to the 'eastern extension' of the mini halo in RX J1720.1+2638 (Biava et al., 2021a). While the correlation is weak ($r_S = 0.28$ and $r_P = 0.28$), we found a best-fit

slope $b = 0.21^{+0.11}_{-0.11}$. This fit is presented in Fig. 5.10. The magenta points show no correlation.

Fig. 5.10 also demonstrates that the standard deviation in spectral index increases in the fainter X-ray regions outside the sloshing spiral, as mentioned previously in Section 5.3.2.2. Overall, this evidence supports the multi-component diffuse emission interpretation, though the limited sensitivity of our LOFAR data prevents us from exploring this in more detail at present.

5.4 Discussion

In this Chapter we presented follow-up radio observations and new X-ray analysis of the cool-core clusters A1068 and MS1455. LOFAR radial profiles have pointed out that the diffuse emission in these clusters is made up of two components (Chapter 3).

A1068 presents diffuse radio emission extending in the north-west south-east direction roughly following the X-ray morphology. This suggest that the thermal and non-thermal components of the ICM are linked and have experienced a perturbation in that direction. The abundance map of Wise et al. (2004) highlights this hypothesis: the heavy elements, usually concentrated on cluster core, have been redistributed by sloshing in a more elongated configuration. A re-analysis of the *Chandra* X-ray data pointed out the presence of two cold fronts: one located south-east of the cluster centre at a distance of 90 kpc, and an second one in the north-west direction at a larger distance of 130 kpc. The discontinuities in radio and X-ray surface brightness occur at comparable distance from the cluster centre. Hence this cluster hosts radio emission that goes beyond the CFs.

MS1455 presents diffuse radio emission extending toward the south beyond the sloshing boundary, coincident with the discontinuity in the LOFAR radial profile. On the north instead the radio emission is confined by the cold front.

In both sources we have therefore found that not all radio emission is confined within the sloshing region, as it was supposed in the past (e.g., Mazzotta & Giacintucci, 2008). Therefore, new more sensitive observations are able to detect even the faint emission associated with the weaker turbulence that is created outside the sloshing region.

Our *Chandra* re-analysis has therefore revealed that both the clusters are experiencing core sloshing; as such, turbulence likely plays a role in powering the diffuse emission. The presence of breaks in the radio surface brightness profiles corresponding to the cold fronts indicates that there must be a strong connection between the dynamics of the thermal gas and the non-thermal components.

This is confirmed by the radio/X-rays point-to-point correlation we computed for MS1455. We found that radio and thermal surface brightness are closely related and follow a super-linear correlation, as typically found in mini halos. Unlike RX J1720.1+2638, however, we have not found a difference in slope for the regions inside and outside the sloshing boundary. For A1068 we were not able to perform this type of analysis as its small extension could be sampled by too few regions to get some information.

In the turbulent (re-)acceleration scenario, we might expect to see spatial variations in the radio emission (at a given frequency) and thus fluctuations in the spectral index distribution.

In A1068 we found a steepening in the spectral index in the external regions, resembling the trend observed in RX J1720.1+2638. MS1455, instead, presents a broadly uniform spectral index across much of the diffuse emission volume. Only in the southernmost region we found a steeper spectral index. The spectral index distribution of MS1455 seems more consistent with an hadronic scenario, where the long-living CRp are in principle able to achieve a spatially-smooth distribution that exhibits a similar spectral slope

throughout the volume of the cluster. However, the absence of strong spectral variations may be reconciled with (re-)acceleration assuming that different turbulent cells are integrated along the line of sight. Furthermore, the presence of cold fronts is not predicted in the hadronic model, so a combination of hadronic emission plus turbulent acceleration, perhaps dominant on different scales (e.g. Brunetti & Lazarian, 2011; Zandanel et al., 2014), provides the best explanation.

The diffuse emission in MS1455 therefore seems to have a different nature from the emission observed in RX J1720.1+2638, where the two components (MH + H) have different properties. A1068 instead seems to be more similar to RX J1720.1+2638, at least from a spectral point of view. However, further analyses in a wider frequency range are necessary for a greater understanding of these peculiar sources.

5.5 Conclusions

To summarise, in this Chapter we have presented radio spectral analysis of the cool-core galaxy cluster A1068 using LOFAR 144 MHz and uGMRT 400 MHz data and of MS 1455.0+2238 using LOFAR 144 MHz and MeerKAT 1283 MHZ observations. These data, combined with archival X-ray data from *Chandra*, have allowed us to perform a comprehensive and detailed study of the connection between the thermal and non-thermal properties of the diffuse emission.

We found that the diffuse emission of both clusters fills the majority of the X-ray emitting region traced by *Chandra*, suggesting a strong connection between the thermal and non-thermal properties of the ICM. In our LOFAR images, the diffuse emission of A1068 has a total extension of 400 kpc, while the diffuse emission of MS1455 is wide in the MeerKAT image, reaching a total extension of 586 kpc.

Our re-analysis of *Chandra* observations has revealed striking evidence for a large-scale asymmetric sloshing spiral in MS 1455.0+2232, identified in the X-ray gradient map. In A1068, instead, the thermal emission has been dragged in the north-west south-east direction by a turbulent motion. Furthermore, we identified two cold fronts in A1068.

In both clusters, the diffuse radio emission extends beyond cold fronts and is characterised by a double radio component.

We found a spectral steepening at large distances in A1068, while MS1455 presents a broadly uniform spectral index map.

Finally, we have studied the spatial correlation between X-ray surface brightness and radio properties in MS1455. Our analysis reveals a tight correlation in the I_R/I_X plane with a super-linear slope at both 1283 MHz and 144 MHz. We found a single correlation for emission inside and outside the sloshing region. While, for the X-ray surface brightness/radio spectral index correlation, we found a weak correlation for regions outside the sloshing boundaries and no correlation inside.

A1068 presents properties similar to RX J1720.1+2638, with different spectral index in the two radio components, while in MS1455 the radio emission inside and outside the sloshing region has a similar behaviour.

Further analyses are necessary to understand if the diffuse emission in these sources originates from the same acceleration mechanism in different physical conditions, or if different mechanisms are involved.

Chapter 6

Constraining the AGN duty cycle in the cool-core cluster MS 0735.6+7421 with LOFAR data

In this Chapter[1] we present a detailed study of the famous radio galaxy at the centre of the cool-core galaxy cluster MS 0735.6+7421. This cluster does not present diffuse emission, but hosts one of the most powerful known AGNs. This source has been well studied in the X-rays, but not in the radio band. Thanks to LOFAR data we have, for the first time, the resolution and low frequency signal necessary to perform a resolved spectral study of this source. Previous analysis revealed the presence of two pairs of cavities, filled with synchrotron emission, indicating a re-activation of the AGN outburst. At the LOFAR frequency, the source presents two large outer radio lobes that are wider than at higher frequencies, and a smaller intermediate lobe that is located south-west of the core. A new inspection of X-ray data allowed us to identify an intermediate cavity that is associated with this lobe. It indicates a further phase of jet activity. The radio lobes have a steep spectrum even at LOFAR frequencies, reaching $\alpha_{144}^{610} = 2.9$ in the outer lobes and $\alpha_{144}^{610} = 2.1$ in the intermediate lobe. Fitting the lobe spectra using a single injection model of particle ageing, we derived a total age of the source between 170 and 106 Myr. This age agrees with the buoyancy and sound-crossing timescales derived from X-ray data. The resolution of the spectral age map we performed allows us to reconstruct the duty cycle of the source. In three phases of jet activity, the AGN was active for most of the time with only brief quiescent phases that ensured the repeated heating of the central gas. Finally, we estimated the minimum energy inside the outer lobes. We found that a source of additional pressure support must be present to sustain the bubbles against the pressure of the external medium.

6.1 Introduction

MS 0735.6+7421 (hereafter MS0735), is a cool-core galaxy cluster located at redshift $z = 0.216$, corresponding to a scale of $1'' = 3.53$ kpc, with the adopted cosmology.

This cluster was first identified as a cooling flow candidate by Donahue et al. (1992) and was then confirmed by Donahue & Stocke (1995). Based on data obtained with VLA, the central radio source (4C +74.13) was identified as a radio galaxy with a clearly defined core and outer lobes (Cohen et al., 2005). Cohen et al. (2005) also found a significant

[1] based on (Biava et al., 2021b)

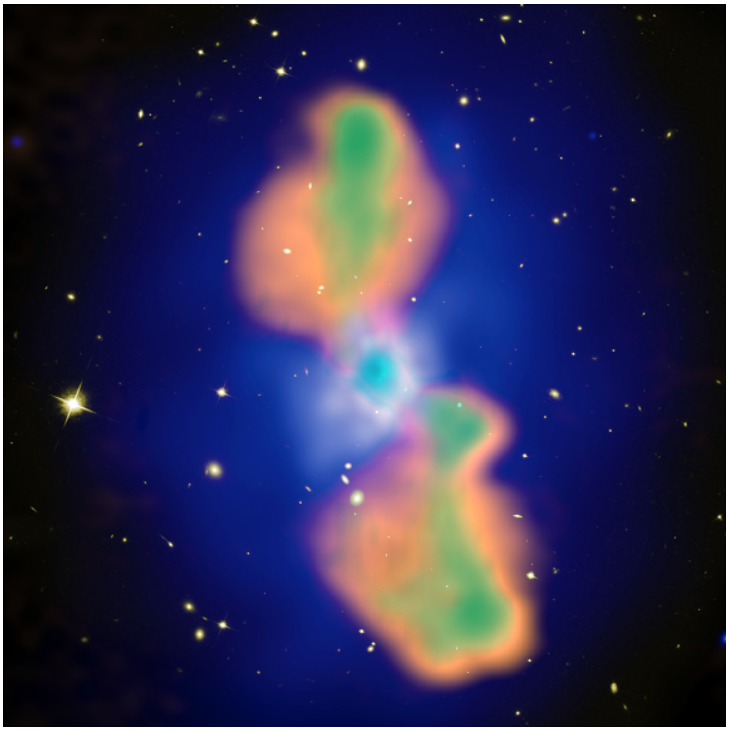

Figure 6.1: Composite image of MS0735, obtained by combining the *Chandra* X-ray image (blue), the I-band image taken by the Hubble Space Telescope (white), the radio wavelengths observed with LOFAR at 144 MHz (orange) and those observed with the VLA at 325 MHz (green). The LOFAR lobes are wider than at 325 MHz, and they perfectly fill the cavities.

extension of the central emission towards the south-west, which may be the result of the jet interacting with the ICM, or an inner lobe generated by a more recent radio outburst. Using VLA data at 325 MHz and 1425 MHz, with a resolution of 21″, the authors found steep spectra in all the main features of the source: $\alpha_{325}^{1425} = 1.54 \pm 0.04$ for the central region, and $\alpha_{325}^{1425} = 3.17 \pm 0.05$ and $\alpha_{325}^{1425} = 3.13 \pm 0.05$ for the northern and southern outer lobes, respectively.

Chandra X-ray observations revealed two giant cavities, each roughly 200 kpc in diameter, and a shock front surrounding them (McNamara et al., 2005). The radio lobes partially fill the cavities, suggesting that the gas was displaced and compressed by the advancing radio jets. The total energy involved in the process is $\sim 6 \times 10^{61}$ erg, making this one of the most powerful known outbursts, together with the Ophiuchus galaxy cluster (Giacintucci et al., 2020). The total energy is enough to quench the cooling flow and to heat the gas within 1 Mpc by ~ 0.25 keV per particle. *XMM* data confirmed these results and showed that most cooling-flow clusters are likely experiencing such powerful outbursts during episodes lasting for a small fraction ($\sim 10\%$) of their age (Gitti et al., 2007).

Using deep *Chandra* observations, Vantyghem et al. (2014) detected a second pair of cavities located along the radio jets in the inner 20 kpc, which corroborated the hypothesis of a renewed period of AGN activity. The authors estimated the cavity ages using the buoyancy, sound crossing, and refill timescales. The mean ages of the northern and southern outer cavities are 150 Myr and 170 Myr, respectively, while the age of the surrounding shock front (110 Myr), which should be comparable to the true cavity age, is shorter than the mean rise time. This means that the cavity ages are slightly overestimated while the power to inflate the bubbles (for the northern cavity, 9×10^{45} erg s^{-1}; for the southern cavity, 8×10^{45} erg s^{-1}) is underestimated. For the inner cavities, Vantyghem and collaborators found a mean age of 48 Myr (northern cavity) and 42 Myr (southern cavity). The power of these cavities (northern 2.8×10^{44} erg s^{-1} and southern 2.4×10^{44} erg s^{-1}) is 30 times smaller than the outer cavity power, implying that the jet power has varied significantly over time (Vantyghem et al., 2014). The outburst interval, estimated as the difference between the ages of the outer and inner cavities, is 110 Myr. It

is shorter than the central cooling time, which prevents most of the surrounding gas from cooling. Repeated heating of the central gas supplies enough energy to prevent cooling, and may explain the lack of star formation in the system (McNamara et al., 2009).

However, the ages derived from the cavity rise time are approximate and are an indirect probe of the AGN duty cycle. A first estimate of the radiative age of the lobes from radio data was performed by Bîrzan et al. (2008). Based on integrated spectral analysis of VLA data at 235 MHz and 1400 MHz, they estimated a synchrotron age of 97 Myr, which reduces to 50 Myr if adiabatic losses are considered.

Integrated models of spectral ageing have long been used to determine the age of radio galaxies. However, they provide a poor, frequency-dependent description of the spectrum of a source compared to recent well-resolved studies that use modern analysis techniques on small spatial scales (Harwood, 017a).

A composite image of the source, created with our new LOFAR data at 144 MHz together with archival VLA 325 MHz data, is shown in Fig. 6.1.

We note that LOFAR snapshot observations of MS0735 have previously been shown by Kokotanekov et al. (2017). This observation was performed during the first LOFAR all-sky survey, the Multifrequency Snapshot Sky Survey (MSSS; see Heald et al., 2015). The MSSS image of MS0735 has a resolution of 27.8″ and an rms noise of 30 mJy beam^{-1} at 140 MHz, neither of which is sufficient for a resolved spectral study.

6.2 Data

To investigate the spectral properties and estimate the radiative age of the radio lobes of MS0735, we used new 144 MHz LOFAR data together with archival data from the VLA and the GMRT radio relescopes, covering the frequency range 144−8460 MHz. We reprocessed archival observations performed with the VLA at 325, 1420, and 8460 MHz and the GMRT at 235 and 610 MHz. In the following sections, we describe these observations and the data reduction procedures. A summary of the radio observational details is reported in Table 6.1. We present the final images throughout our frequency range in Fig. 6.2 and 6.3. Their properties are listed in Table 6.2.

Finally, we compare the radio morphology of the source with X-ray features, shown in Fig. 6.4, and the radiative age of the radio lobes with X-ray cavity timescales, using *Chandra* X-ray observations of this source presented in Vantyghem et al. (2014). We describe these observations only briefly.

6.2.1 LOFAR observation

LOFAR observations of this source were already presented in Chapter 3, here we only reported some technical details. For the data calibration refer to Section 2.4.2. The source was observed on 23 May 2018 using the LOFAR High Band Antennas (HBA) in the `HBA_DUAL_INNER` mode. The target was observed for a total integration time of 8 h, using all the LOFAR stations: core stations, remote stations, and international stations. International stations were not used in this work and were flagged before calibration. The observations were performed using a dual-beam mode setup, co-observing with the LOFAR Two-Metre Sky Survey (LoTSS; Shimwell et al., 2017). We observed in the frequency range 110−190 MHz, divided into 244 sub-bands of 64 channels each, with a sampling time of 1 s.

The flux density scale was set according to Scaife & Heald (2012), and was subsequently verified through comparison with the TIFR GMRT Sky Survey (TGSS, Intema et al., 2017). The flux calibration error is estimated to be 10% (Hardcastle et al., 2021).

Table 6.1: Summary of the observational details.

Telescope	Frequency	Configuration	Target TOS	Observation date
LOFAR	144 MHz	HBA-dual inner	8h	23 May 2018
GMRT	235 MHz	-	6h	4 December 2009
VLA	325 MHz	A	2.4h	24 December 2004
VLA	325 MHz	B	3.6h	4 December 2003
VLA	325 MHz	C	4h	24 December 2006
GMRT	610 MHz	-	6h	4 December 2009
VLA*	1420 MHz	A	2h	24 October 2004
VLA	1420 MHz	B	5h	19 August 2006
VLA	1420 MHz	C	3.4h	15 April 2004
VLA*	8460 MHz	A	1.7h	17 October 2004
VLA*	8460 MHz	D	4.5h	28 November 2005

Notes. *Observations considered only for the analysis of the central emission.

6.2.2 VLA observations and data reduction

MS0735 has previously been observed by the VLA in a number of different bands and configurations. We used the following specific datasets:

- 325 MHz, A-configuration, observed on 24 December 2004.
  The observation was performed using 26 antennas for a total time on target of 2.4 h, divided into four scans alternated by 2-minute observations of the phase calibrator (0749+743). The flux density calibrator (3C286) was observed at the end of the observation for 6 minutes. The frequency band was divided into two spectral windows of 31 channels each for a total bandwidth of 3 MHz. The data were recorded using a dual-mode polarization.

- 325 MHz, B-configuration, observed on 4 December 2003.
  The target was observed for 3.6 h divided into three scans alternated with 3 minutes of phase calibrator (0749+743) observations. The flux density calibrator (3C147) was observed at the beginning and end of the observing run. Twenty-six antennas were used. The observing band was divided into two sub-bands with 15 channels each of 391 kHz width for a total bandwidth of 12 MHz.

- 325 MHz, C-configuration, observed on 24 December 2006.
  The observation was performed using 25 antennas, some equipped with the old VLA receivers, whereas the others were made with the new receivers. EVLA-VLA baselines were affected by closure errors. We corrected for this effect using the flux density calibrator (3C286). The source was observed in 14 time-scans for a total time of 4 h. The phase calibrator (3C184) was observed for 2 minutes before every target scan, while the flux density calibrator was observed at the beginning and end of the observing run for 4 minutes each time. The data were recorded using two sub-bands of 31 channels each for a total bandwidth of 6 MHz.

- 1420 MHz, A-configuration, observed on 24 October 2004.
  The observation was performed using 26 antennas and two single-channel sub-bands with a width of 25 MHz each. The source was observed for roughly 2h, alternated

by 2-minute observations of the phase calibrator (0749+743). The flux density calibrator (3C286) was instead observed at the end of the observation for 3 minutes.

- 1420 MHz, B-configuration, observed on 19 August 2006.
  Observation performed using 25 antennas, 4 of which were equipped with the old VLA receivers. These were flagged from the dataset because they clearly provided a different response with respect to the upgraded antenna, and no suitable calibrator was observed to correct for this effect. The data were recorded in two single-channel sub-bands with a width of 50 MHz. The source was observed for a total time of 5h divided into 12-minute time-scans. The flux density calibrator (3C286) was observed at the beginning and end of the observation (4 minutes each time), while the phase calibrator (0954+745) was observed alternating with the source for 3 minutes every time-scan.

- 1420 MHz, C-configuration, observed on 15 April 2004.
  Observation performed using 27 antennas, two sub-bands of seven channels each for a total bandwidth of 22 MHz. The data were recorded for a total integration time on target of 3.4 h divided into five time-scans. The flux density calibrator (3C147) was observed at the beginning and at the end of the observing run for a total time of 10 minutes; the phase calibrator (0841+708) was observed for 2 minutes alternating with scans on target.

- 8460 MHz, A-configuration, observed on 17 October 2004.
  The source was observed for 1.7h using 25 antennas. The data were recorded in two single-channel sub-bands with a width of 25 MHz each. The phase calibrator (0749+743) was observed alternating with the target for 2 minutes each time, while the flux density calibrator (3C286) was observed at the end of the observation for 2 minutes.

- 8460 MHz, D-configuration, observed on 28 November 2005.
  The observation was performed using 23 antennas and two single-channel spectral windows centred at 8440 MHz and 8490 MHz with a bandwidth of 50 MHz each. The target was observed for 4.5 h divided into ten scans interspersed with 2-minute phase calibrator (0721+713) observations. The flux density calibrator (3C147) was observed for 8 minutes at the beginning of the run.

All datasets were reduced with Common Astronomy Software Applications (`CASA`, version 5.4; McMullin et al., 2007) using the following steps: after manual flagging, we performed calibration in the standard manner. The flux density scale was set according to Perley & Butler (2013) for all datasets except for the data at 325 MHz, for which we used the scale of Scaife & Heald (2012). The flux calibration error is estimated to be 5% for P band and L band and 2% for X band (Scaife & Heald, 2012; Perley & Butler, 2013).

Following standard calibration, we performed several cycles of phase-only and amplitude-and-phase self-calibration at 325 MHz and 1420 MHz. Self-calibration was also attempted at 8460 MHz, but due to the low flux density of the source, the process did not improve the gain solutions and the solutions were not applied. Finally, we combined all individual datasets at matching frequencies (325 MHz, 1420 MHz, and 8460 MHz) and jointly deconvolved them to improve the *uv*-coverage.

6.2.3 GMRT observations and data reduction

The source was observed with the GMRT at 235 MHz and 610 MHz on 4 December 2009 in dual-frequency mode using the GMRT Hardware Backend (GHB). In observations

performed with GHB, the 32 MHz bandwidth is typically split over an upper-side band (USB) and lower-side band (LSB), both recorded in separate LTA files.

For the data at 235 MHz we were able to calibrate only the USB because good calibrator scans are lacking in the LSB. The bandwidth is thus limited to 16 MHz. The target was observed in nine time-scans for a total integration time of 6 h. The source 3C286 was used as flux-density calibrator and observed at the end of the observing run for 12 minutes.

The flux calibration error is estimated to be 10% (Chandra et al., 2004). We processed the data using the Source Peeling and Atmospheric Modelling (`SPAM`; Intema, 2014; Intema et al., 2017) pipeline that corrects for ionospheric direction-dependent effects. The output calibrated visibility data were then imported into `CASA` for imaging.

Table 6.2: Image properties.

Telescope	ν [MHz]	uv-range [λ]	Beam size	Rms [mJy beam^{-1}]	Fig.
LOFAR	144	$48 \sim 480000$	7.0"×4.5"	0.2	6.2
GMRT	235	$30 \sim 19173$	20"×12"	2.7	6.3
VLA	325	$37 \sim 40186$	7"×5"	0.53	6.3
GMRT	610	$80 \sim 49375$	7"×4"	6.0×10^{-2}	6.3
VLA	1420	$157 \sim 54376$	10"×10"	4.2×10^{-2}	6.3
VLA	8460	$807 \sim 29186$	9"×7"	1.2×10^{-2}	6.3

6.2.4 X-ray observations

We used the *Chandra* data already published in Vantyghem et al. (2014) to perform some further analysis as described in Sect. 6.3.2. The source was observed seven times with *Chandra* in June 2009 for a cumulative exposure time of 477 ks. Each observation was calibrated in the standard way (see Vantyghem et al., 2014, for more details) and was then imaged by summing events in the energy range 0.5–7.0 keV. These images were then combined to create a single mosaic image to study the X-ray emission. Point sources were identified and removed. Finally, the best-fitting double-β model was subtracted from the cluster emission, producing the residual image we report in the left and middle panels of Fig. 6.4.

6.3 Results

6.3.1 Radio morphology

In Fig. 6.1 we show a composite image of MS0735, obtained by combining the Hubble Space Telescope I-band image (yellow), the *Chandra* X-ray image (blue), and the radio image at two different frequencies, LOFAR 144 MHz (orange) and VLA 325 MHz (green), at a similar resolution of $7'' \times 5''$, to compare the extension of the radio emission. The radio lobes at LOFAR frequency are clearly wider than previously found with the VLA at higher frequencies and now completely fill the X-ray cavities. In Fig. 6.2 we show the high-resolution image of MS0735 as seen with the LOFAR-HBA at a central frequency of 144 MHz. The two radio lobes, called the northern and southern outer lobes, extend in the north-south direction for $\sim 150'' \cong 530$ kpc from the bright central emission. At

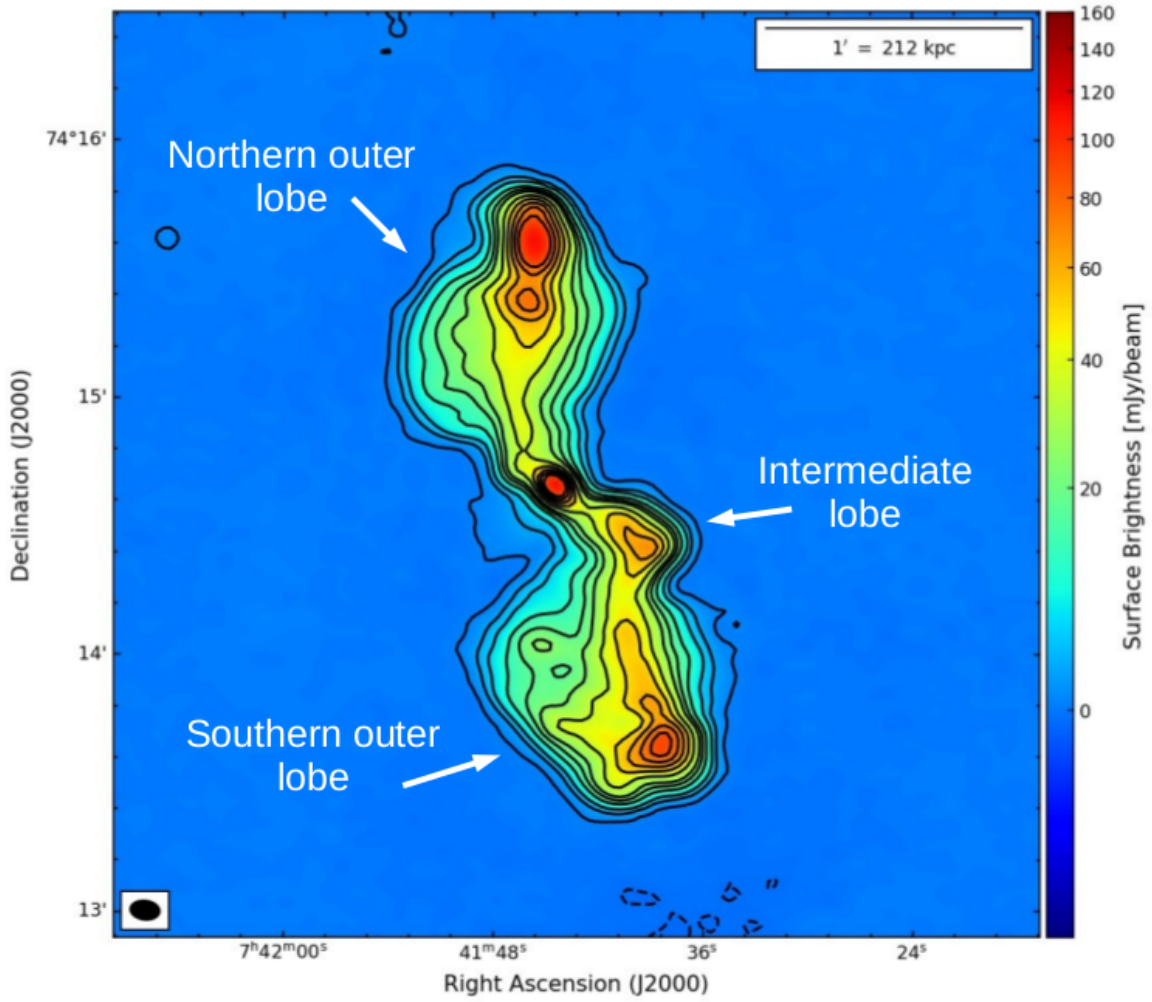

Figure 6.2: LOFAR 144 MHz radio map of MS0735 at resolution of $7.0'' \times 4.5''$. Contour levels: $[-1,1,5,10,20,30,40,60,80,100,120,140] \times 3\sigma$ (where $\sigma = 0.2$ mJy beam^{-1}). The beam is shown in the bottom left corner.

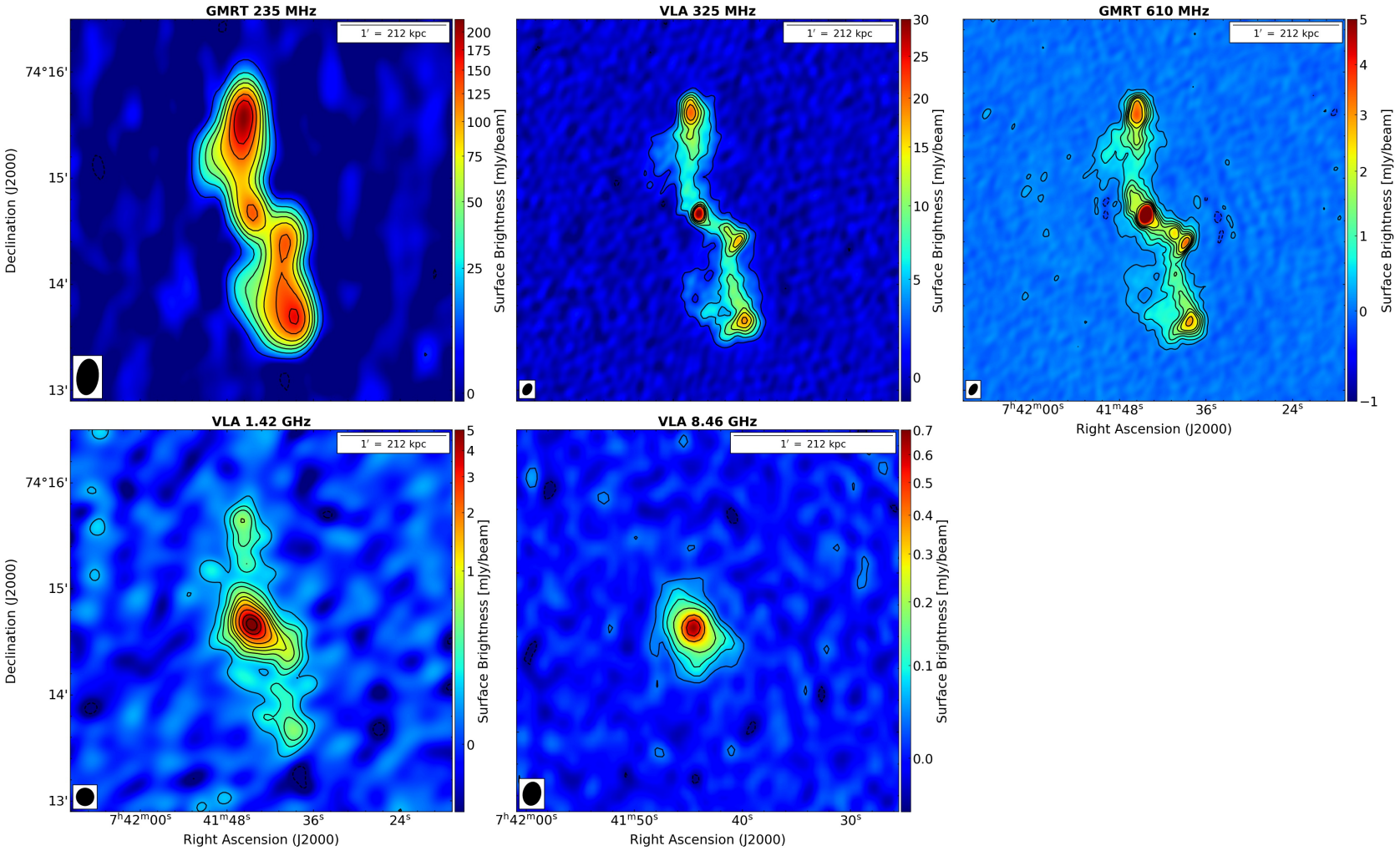

Figure 6.3: Radio maps of MS0735 at different frequencies. *Top left*: GMRT 235 MHz at $20'' \times 12''$ resolution. Levels: $[-1, 1, 3, 5, 7, 10, 15, 20, 30] \times 3\sigma$ (where $\sigma = 2.7$ mJy beam^{-1}). *Top middle*: VLA 325 MHz image at $7'' \times 5''$ resolution. Levels: $[-1, 1, 3, 5, 7, 9, 11, 15, 20] \times 3\sigma$ ($\sigma = 0.53$ mJy beam^{-1}). *Top right*: GMRT 610 MHz at $7'' \times 4''$ resolution. Levels: $[-1, 1, 3, 5, 7, 9, 11, 15, 18, 30, 50] \times 3\sigma$ ($\sigma = 6.0 \times 10^{-2}$ mJy beam^{-1}). *Bottom left*: VLA 1420 MHz at $10'' \times 10''$ resolution. Levels: $[-1, 1, 2, 3, 5, 7, 9, 13, 20, 30, 40] \times 3\sigma$ ($\sigma = 4.2 \times 10^{-2}$ mJy beam^{-1}). *Bottom right*: VLA 8460 MHz at $9'' \times 7''$ resolution. Levels: $[-1, 1, 2, 3, 5, 10, 15] \times 3\sigma$ ($\sigma = 1.18 \times 10^{-2}$ mJy beam^{-1}). The beam is shown in the bottom left corner of each image.

the extreme edge of the lobes an increase in surface brightness is visible, which can be interpreted as hotspots.

At this resolution the extended emission south-west of the core is clearly visible, which was previously noted at higher frequencies by Cohen et al. (2005). This was suggested to either be a signature of a second epoch of AGN activity or a bending of the southern jet direction because of the interaction with the ICM. Our new analysis of the X-ray data, as discussed in Sect. 6.3.2, points to the presence of a further cavity corresponding to this radio emission, which was not noticed before. Together with the radio morphology observed at high resolution (see LOFAR and VLA images, 6.2 and 6.3), this supports the idea that this emission represents a radio lobe associated with a further phase of jet activity that occurs between the two jet activities that were previously discovered by Vantyghem et al. (2014). It is visible in the central panel of Fig. 6.4, where the LOFAR contours are superposed on the X-ray image, and the radio emission fills the newly detected cavity, represented with a red ellipse. From here on, we refer to this emission as to the intermediate lobe. At its edge seems to be a hotspot, based on the increase in surface brightness. The bending of this emission with respect to the outer lobes indicates that the reactivated jet has changed its direction. No counterpart of this intermediate lobe, north-east of the core, is detected. This could be due to projection effects, for instance, Doppler boosting (e.g. Blandford & Königl, 1979; Orr & Browne, 1982; Kellermann & Owen, 1988; Hardcastle et al., 1998).

From Vantyghem et al. (2014) we know that a third series of cavities is present in the innermost regions of the source. These are shown in the right panel of Fig. 6.4 with green ellipses, where the soft band X-ray image is superposed with the LOFAR contours. The limited resolution of the radio images does not allow us to detect the corresponding inner lobes or jets, however.

The central panel of Fig. 6.4 also shows that all the radio emission is confined to the surrounding cocoon. The high energy associated with the outburst has displaced and compressed the material in the cluster atmosphere, creating a confining shell that hinders the advance of any radio plasma.

We also checked for more diffuse emission by re-imaging the LOFAR data at lower resolution. The overall morphology of the source in this case is consistent with what was previously observed at 325 MHz (Cohen et al., 2005). While the radio lobes are more extended at 144 MHz, we find no evidence of any older outbursts.

In Fig. 6.3 we show images of MS0735 at different frequencies, made from the archival data described earlier. At higher frequencies, the morphology of the source changes: the central region (which includes the core and the inner jets) becomes dominant, while the lobes become less prominent, until they are no longer visible at 8460 MHz. To verify that this variation is real or due to different observational setups, we re-imaged all the datasets using the same *uv*-range, with a `uniform` weighting scheme, and convolved all images to the same resolution (see the low-resolution column of Table 6.4). The morphological differences remain even in this case, indicating that the lack of lobe emission at 8460 MHz is really due to the spectral steepening and not to instrumental effects. This implies a sharp cut-off in the spectrum of the outer lobes that is typical of aged plasma.

When we consider the morphology at different frequencies, MS0735 may overcome the boundaries of the Fanaroff-Riley (FR) classification (Fanaroff & Riley, 1974) in that it could be at different points of the activity cycle. The outer lobes exhibit the classical morphology of FRII radio galaxies, with lobes and hotspots (visible also in the VLA and GMRT images up to 1420 MHz). The second phase of activity may have created another FRII, presenting an increase in brightness in the intermediate lobe, but at 610 MHz, the jets are clearly visible, which is unusual for this class of source. It is therefore possible that the source was born as an FRII, and was then slowed down by the dense

surrounding medium at the centre of the cool-core cluster. In this scenario, the source could have turned into an FRI-type radio galaxy during subsequent phases of jet activity (e.g. Laing, 1994; Kaiser & Best, 2007; Meliani et al., 2008; Wang et al., 2011; Turner & Shabala, 2015; Kapińska et al., 2017).

Understanding the nature of the source and its variation throughout its life is beyond the scope of this paper. For our purposes, that is, estimating the radiative life of the outer lobes and of the intermediate lobe, we assume that the source is an FRII, so the particle acceleration took place in the hotspots. In the following sections, we discuss this point further.

6.3.2 X-ray features

Vantyghem et al. (2014) detected two large cavities, with a diameter of $\sim$ 200 kpc and a shock front enveloping the cavities. They are both clearly visible in the left and middle panels of Fig. 6.4. The projected sizes and positions of the cavities were determined by eye by approximating the surface brightness depressions with elliptical regions, see the blue ellipses in Fig. 6.4. The northern cavity is best represented by an ellipse with a semi-major axis a = 109 $\pm$ 16 kpc, semi-minor axis b = 106 $\pm$ 16 kpc, and projected distance from the AGN, R = 150 kpc. The southern cavity is best represented by an ellipse with a = 120 $\pm$ 15, b = 100 $\pm$ 21, and R = 186 kpc. The cocoon shock front is approximated by an ellipse with a semi-major axis a = 320 kpc and a semi-minor axis b = 230 kpc.

The deep *Chandra* image in the soft band (0.3 - 1.0 keV), right panel of Fig. 6.4, revealed two smaller cavities located along the radio jets in the inner 20 kpc. Their positions and sizes are shown in all the panels of Fig. 6.4 with green ellipses. These cavities are best represented by an ellipse with a = 13.3 $\pm$ 1.6 kpc, b = 10.1 $\pm$ 2.3 kpc, and a projected distance of R = 19.3 kpc from the cluster centre for the inner northern cavity and a = 15.5 $\pm$ 2.2, b = 10.5 $\pm$ 3.3, and R = 25.0 kpc for the inner southern cavity.

We performed a further visual inspection of the X-ray residual image that led to the possible detection of an additional cavity, located to the south-west of the core at an intermediate distance from the cluster centre with respect to that of the two cavities reported in Vantyghem et al. (2014). No corresponding cavity to the north-east of the core has been detected. This newly identified cavity (referred to as the intermediate cavity), represented with a red ellipse in Fig. 6.4, is distinct from the region used for the analysis of the outer cavity to the south (Vantyghem et al., 2014), represented with a blue ellipse. Because the radio emission is less sensitive to projection effects than depressions in the X-ray image, we considered different dimensions for the intermediate cavity (as done, e.g. in Gitti et al., 2010), ranging from the size of the apparent depression seen in the residual X-ray image (solid red ellipse) to the extension of the intermediate radio lobe (dashed red ellipse in middle panel of Fig. 6.4). Our analysis provides a range of values for a semi-major axis a = 39 - 56 kpc, semi-minor axis b = 35 - 48 kpc, and distance from the cluster centre R = 85 - 100 kpc.

We estimated the energetics and age of this newly detected intermediate cavity following the same procedure as was used by Vantyghem et al. (2014) for the other cavities. The minimum total energy required to create a cavity for a relativistic gas is $E_{\rm cav} = 4pV$, where p is the cavity pressure and V is its volume. Assuming pressure equilibrium, the pressure is estimated from the deprojected pressure profile of the surrounding ICM (Fig. 7 of Vantyghem et al., 2014) at a radius corresponding to the distance of the cavity centre. The cavity volume is calculated using the geometric mean between oblate and prolate ellipsoids, $V = 4/3\pi(ab)^{3/2}$. The age of the cavity is estimated using three characteristic timescales: the sound crossing time, buoyancy time, and refill time (e.g.

Table 6.3: Cavity properties.

Cavity	a [kpc]	b [kpc]	R [kpc]	$E_{\rm cav}$ [10^{59} erg]	$t_{\rm buoy}$ [Myr]	$t_{\rm c_s}$ [Myr]	$t_{\rm ref}$ [Myr]	$P_{\rm cav,buoy}$ [10^{44} erg s^{-1}]
N outer	109 ± 16	106 ± 16	150	440 ± 200	91	120	240	160 ± 70
S outer	120 ± 15	100 ± 21	186	440 ± 200	110	140	250	130 ± 60
Intermediate	48 ± 9	42 ± 7	85−100	23−60	62−64	53−69	103−120	12−30
N inner	13.3 ± 1.6	10.1 ± 2.3	19.3	3.6 ± 2.0	33	19	74	3.6 ± 2.0
S inner	15.5 ± 2.2	10.5 ± 3.3	25.0	3.6 ± 2.4	41	25	78	2.9 ± 2.0

Notes. For each cavity we list the semi-minor axis (a), semi-major axis (b), distance from cluster centre (R), energy of the cavity ($E_{\rm cav}$), buoyancy timescale ($t_{\rm buoy}$), sound crossing timescale ($t_{\rm c_s}$) refilling timescale ($t_{\rm ref}$), and power of the cavity ($P_{\rm cav,buoy} = E_{\rm cav}/t_{\rm buoy}$). The values for the outer and inner cavities are taken from Table 2 of Vantyghem et al. (2014).

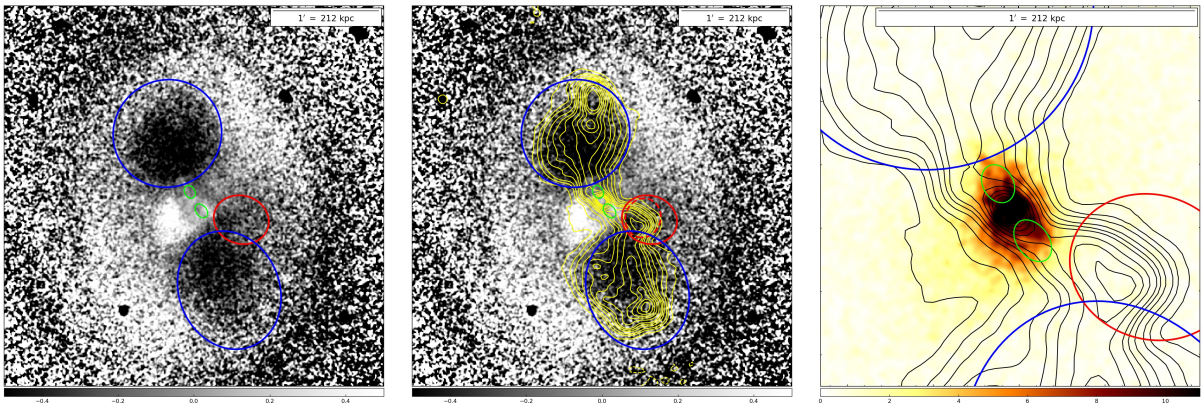

Figure 6.4: *Chandra* images of MS0735. *Left:* Residual image after subtracting a double−β model from the X-ray image (0.5−7 keV). The image is in units of counts pixel^{-1} and is Gaussian-smoothed with a 1 arcsec kernel radius. The dark regions to the north and south correspond to two large cavities, marked by blue ellipses. A surface brightness edge surrounds these cavities and corresponds to a weak shock front. The red ellipse marks the newly discovered intermediate cavity south-west of the core, while green ellipses show the inner cavities. *Middle:* Same as before, with the LOFAR contours at 144 MHz superposed, and the smaller region outlined by the dashed red ellipse is considered to place a lower limit on the size of the intermediate cavity. *Right:* Soft-band (0.3−1.0 keV) image in units of counts pixel^{-1}, Gaussian-smoothed with a 1 arcsec kernel radius. Two regions of low surface brightness, interpreted as a pair of cavities originating from a recent AGN outburst, are indicated with green ellipses. The LOFAR contours at 144 MHz and the blue and red ellipses showing the outer and intermediate cavities, respectively, are superposed.

Bîrzan et al., 2004). At the distance of the intermediate cavity, we estimated a sound velocity of $c_s = 1210 - 1260$ km s^{-1}. The gravitational acceleration, g, used to calculate the buoyancy and refill timescales was determined using the MS0735 mass profile from Hogan et al. (2017). Finally, we estimated the power required to inflate the cavity, as $P_{\rm cav} = 4pV/t_{\rm buoy}$, where we used the buoyancy timescale as reference for the cavity age. The properties and energetics of the intermediate cavity derived in this work, along with those of the inner and outer cavities studied by Vantyghem et al. (2014), are reported in Table 6.3.

The X-ray data have thus revealed that there were at least three AGN outbursts in MS0735. Only few sources with multiple cavities are currently known, for example Hydra A (Nulsen et al., 2005; Wise et al., 2007; Gitti et al., 2011) and NGC 5813 (Randall et al., 2011, 2015). The presence of different episodes of jet activity is important to ensure the continuous heating of the central gas and so to prevent it from cooling.

6.3.3 Radio spectral study

To perform a spectral study of the source, we re-imaged all the radio data with the same restoring beam ($16'' \times 10''$, PA 0°), *uv*-range ($157 \sim 19173$ λ), and used a `uniform` weighting scheme. We excluded the data at 8460 MHz, where the emission of the lobes is not visible. Finally, we spatially aligned all the images to correct for possible shifts introduced by the phase self-calibration process, using only the central compact emission as reference because no point sources are visible in the vicinity of the target. After this procedure, the spatial difference between the images was reduced to less than 0.1 pixel.

For a more detailed study of the central regions of the source, we furthermore created another set of images at higher resolution, excluding the GMRT data at 235 MHz. The exclusion of this frequency has very little effect on the results of the study because it lies between two points at frequencies very close to each other. These high-resolution images have a restoring beam of $6.5''$. The parameters of the two sets of images are listed in Table 6.4.

Table 6.4: Summary of imaging parameters.

Parameter	High resolution	Low resolution
Frequency range	144 - 1420 MHz (excluding 235 MHz)	144 - 1420 MHz (all)
Restoring beam	$6.5'' \times 6.5''$	$16'' \times 10''$, PA 0°
uv-range	$157 \sim 19173$ λ	$157 \sim 40186$ λ
Weighting	`uniform`	`uniform`

From the images at lower resolution, we measured the total flux density of the source and of the outer lobes, reported in Table 6.5 and plotted in Fig. 6.5. We also set an upper limit for the lobes emission at 8460 MHz, estimated as the product between the rms noise at 8460 MHz and the lobe area expressed in units of beams ($3\sigma \times N_{\rm beam}$).

We used the Broadband Radio Astronomy Tools (`BRATS`)[2] software package (Harwood et al., 2013, 2015) to estimate the spectral age of the source. BRATS allows performing a detailed spectral analysis on a pixel-by-pixel basis. In this way, we mapped the source properties (e.g. spectral index, spectral age) throughout the source extension. The detection limit was set to three times the noise, estimated as the rms in an empty region in the field.

[2] http://www.askanastronomer.co.uk/brats/

Table 6.5: Total flux density of MS0735 and of the outer lobes.

Telescope	ν [MHz]	Total [Jy]	Northern outer lobe [Jy]	Southern outer lobe [Jy]
LOFAR	144	4.7 ± 0.5	1.3 ± 0.1	1.2 ± 0.1
GMRT	235	1.6 ± 0.2	$(4.8 \pm 0.5) \times 10^{-1}$	$(4.4 \pm 0.4) \times 10^{-1}$
VLA	325	$(6.5 \pm 0.3) \times 10^{-1}$	$(1.8 \pm 0.1) \times 10^{-1}$	$(1.8 \pm 0.1) \times 10^{-1}$
GMRT	610	$(1.4 \pm 0.1) \times 10^{-1}$	$(3.1 \pm 0.3) \times 10^{-2}$	$(3.0 \pm 0.3) \times 10^{-2}$
VLA	1420	$(2.0 \pm 0.2) \times 10^{-2}$	$(1.7 \pm 0.1) \times 10^{-3}$	$(1.6 \pm 0.1) \times 10^{-3}$
VLA	8460	$(1.20 \pm 0.03) \times 10^{-3}$	$(\sim 6.1 \times 10^{-6})$	$(\sim 6.9 \times 10^{-6})$

Notes. 3σ upper limit are shown at 8460 MHz for the lobes flux density because they are not detected.

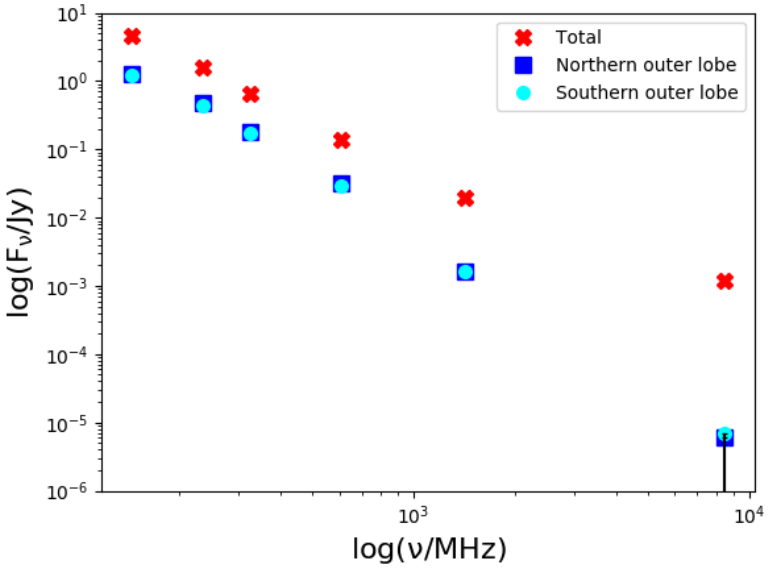

Figure 6.5: Total flux density distribution of MS0735 between 144 MHz and 1420 MHz (in red) and of the northern and southern outer lobes (in blue and cyan, respectively). We have also set a 3σ upper limit for the flux of the lobes at 8460 MHz because they are not detected.

6.3.3.1 Spectral index maps

To investigate the spatial distribution of the spectral index, we made a high-resolution (6.5″) two-frequency spectral index map using LOFAR 144 MHz and GMRT 610 MHz images (see the left panel of Fig. 6.6). To our knowledge, this is the first time that a spectral index study of MS0735 extended to this low frequency is presented at high resolution.

Previous work that was based on integrated spectra found an ultra-steep radio spectrum for this source ($\alpha_{325}^{1425} = 2.45 \pm 0.04$ Cohen et al. 2005, $\alpha_{327}^{1400} = 2.48 \pm 0.04$ Bîrzan et al. 2008). Our resolved spectral study confirms that this trend extends to 144 MHz, with spectral index values reaching $\alpha_{144}^{610} = 3.1 \pm 0.3$. Curiously, the spectrum remains very steep even at the location of the core, where the spectral index is $\alpha_{144}^{610} = 1.5 \pm 0.1$, as previously observed at higher frequency ($\alpha_{325}^{1425} = 1.54 \pm 0.04$, Cohen et al. 2005). This steep value suggests superposition of the core and the lobe emission. The emission from the central region is further analysed in the next section.

In addition, we note a gradient of the spectral index along the main axis of the source. Starting from a value of $\alpha_{144}^{610} = 2.3 \pm 0.1$ in the hotspots, at the edges of the outer lobes, it steepens when the core is approached, reaching a maximum value of $\alpha_{144}^{610} = 2.9 \pm 0.3$ in the outer lobes, then flattens again in the central regions and in the intermediate lobe, where the spectral index is $\alpha_{144}^{610} = 2.1 \pm 0.1$. This trend suggests two different episodes of jet activity. If there were only one phase of jet activity, we would expect a gradual increase in the spectral index from the hotspot, where the particles are last accelerated, to the core where the oldest particles are found. Instead, the spectral index in the central regions is flatter than in the outer lobes, indicating the presence of younger particles, which were therefore emitted later. These ultra-steep spectral indices in hotspots occur in $\leq 0.5\%$ of cases (Hogan et al. 2015). This likely indicates that the acceleration of particles is no longer active in these regions, otherwise we would expect a spectral index in the range 0.6-0.8, as observed for typical FRII-type radio galaxies (Jaffe & Perola, 1973; Carilli et al., 1991; Komissarov & Gubanov, 1994).

In the middle and right panels of Fig. 6.6, we show the low-frequency spectral index map between 144 MHz and 235 MHz and the high-frequency spectral index map between 610 MHz and 1420 MHz, respectively, both at the resolution of $16'' \times 10''$. When the frequency range between 144 and 235 MHz is narrowed, the spectrum is less steep than that represented in the map obtained between 144 and 610 MHz. This is especially true in the hotspot of the northern outer lobe where the spectral index reaches the minimum value of $\alpha_{144}^{235} = 0.75 \pm 0.40$, much closer to typical values. The hotspot in the southern outer lobe is instead less pronounced and has a steeper spectral index, $\alpha_{144}^{235} = 1.6 \pm 0.4$. This difference may be due to projection effects in the southern outer lobe, with an overlap along the line of sight of particles of different ages, making the spectrum steeper. At higher frequencies, the spectrum is instead very steep, and we recover the values found by Cohen et al. (2005) for the centre and the outer lobes. For the main features of the source, we list in Table 6.6 the average spectral index at low and high frequencies and their difference, which represents the spectral curvature of these regions (SPC $= \alpha_{\rm high} - \alpha_{\rm low}$). For the two outer lobes and the intermediate lobe, the high-frequency spectral index is steeper than that observed at low frequency, and despite the large uncertainties, the spectral curvature is high, indicating emission from an aged population of electrons.

6.3.4 Central emission

As explained above, the central region of MS0735 exhibits a steep radio spectrum, with $\alpha = 1.5 \pm 0.1$ between 144−610 MHz, which is much steeper than that of typical AGN cores. However, we note that at the resolution of $6.5'' \cong 23$ kpc, the actual core is

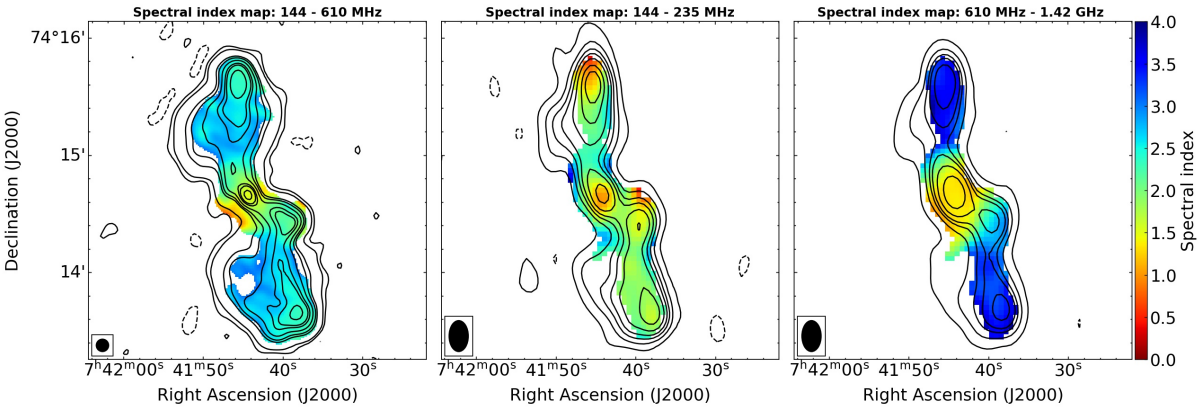

Figure 6.6: Spectral index maps of MS0735. *Left:* High-resolution spectral index map between 144 MHz and 610 MHz, resolution = 6.5″. The LOFAR contours are overlaid. *Middle:* Low-frequency spectral index map between 144 MHz and 235 MHz, resolution = 16″ × 10″. The 235 MHz contours are overlaid. *Right:* High-frequency spectral index map between 610 MHz and 1420 MHz, resolution = 16″ × 10″. The 610 MHz contours are overlaid. The beam is shown in the bottom left corner of each map.

Table 6.6: Spectral indices ($\alpha_{\rm low}$, $\alpha_{\rm high}$) and spectral curvature (SPC) for the main features of MS0735.

Region	$\alpha_{\rm low}$	$\alpha_{\rm high}$	SPC
Centre	1.2±0.4	1.4±0.1	0.2±0.5
Northern outer lobe	2.1±0.4	3.4±0.6	1.3±0.9
Northern hotspot	0.75±0.40	3.4±0.6	2.6±0.9
Southern outer lobe	2.0±0.4	3.4±0.6	1.4±0.9
Southern hotspot	1.6±0.4	3.4±0.6	1.8±0.9
Intermediate lobe	1.5±0.4	2.8±0.3	1.3±0.7

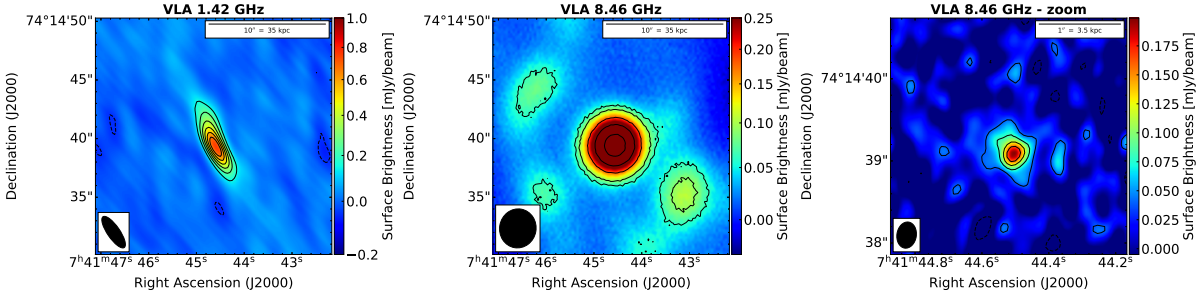

Figure 6.7: Radio maps of the central emission of MS0735. *Left*: VLA 1420 MHz at 3.1″ × 1.1″. Levels: [−1, 3, 5, 7, 9, 11, 13] ×3σ (σ = 17 μJy beam^{-1}). *Middle*: VLA 8460 MHz at 3.3″ × 3.1″ resolution. Levels: [−1, 1, 1.5, 3, 5, 8] ×3σ (σ = 20 μJy beam^{-1}). *Right*: Zoom of VLA 8460 MHz at 0.32″ × 0.24″ resolution. Levels: [−1, 1, 2, 3, 4] ×3σ (σ = 13 μJy beam^{-1}). The beam is shown in the bottom left corner of each image.

likely not resolved, and the observed emission (and thus apparent steep spectrum) could result from the superposition of different populations of electrons from the inner jets or lobes. The detection of inner cavities in fact demonstrates that there has been more recent jet activity (Vantyghem et al., 2014).

To investigate this region further, we analysed high-resolution archival VLA observations of the source. These observations (at 1420 MHz for array A and 8460 MHz for array A, listed in Sect. 2.2) were performed without the use of short baselines, so the diffuse emission is filtered out, allowing us to study the real compact emission of the nuclear region.

In Fig. 6.7 we show the radio map of the central emission at 1420 MHz (left panel), at $3.1'' \times 1.1''$ resolution, at 8460 MHz (middle panel) $3.3'' \times 3.1''$ resolution, and the emission at 8460 MHz (right panel), at $0.32'' \times 0.24''$ resolution. To measure the flux densities of the central emission component at 1420 MHz and 8460 MHz, we used images produced with a common uv-range ($17926 \sim 353657\ \lambda$) and a resolution of $2'' \cong 7$ kpc.

We obtain a spectral index of 0.75 ± 0.08 for this central component. This supports the idea that even at this resolution, the emission we observe is not purely core emission, which would have a much flatter spectrum (e.g. Blandford & Königl, 1979; Hogan et al., 2015), but rather a superposition of emission from the core and the inner part of the jets.

6.3.5 Radiative age

For a synchrotron-emitting electron population, initially distributed along a power law, the energy-loss rate scales as $E/(dE/dt) \propto 1/E$. This leads to a faster cooling of high-energy electrons, and in absence of further particle acceleration, produces a spectrum that is initially described by a power law and becomes increasingly curved over time. A break in the spectrum develops at frequency ν_b, which relates to the time elapsed since the injection and to the magnetic field as $\nu_\mathrm{b} \propto B^{-3}t^{-2}$. This means that if we know the magnetic field strength, we can derive the age of a radio source from the shape of its spectrum.

A modern approach to deriving the spectral age of the source consists of fitting the observed radio spectrum with a modelled spectrum that is obtained by numerical integration of the equations that describe the radiative losses of the plasma. `BRATS` follows this approach and allows fitting the observed radio spectrum with different spectral ageing models, obtaining a spectral age map of the source. On small scales, particles can likely be assumed to be part of a single injection event.

Three single-injection models are usually considered: the JP (Jaffe & Perola, 1973), KP (Kardashev, 1962; Pacholczyk, 1970) and Tribble (Tribble, 1993) models. The JP and KP models consider synchrotron and inverse-Compton losses in a constant magnetic field environment, where the radio-emitting electron population has a fixed pitch angle (in the KP model) or a continuously isotropized pitch angle distribution (in the JP model). The JP model is more realistic from a physical point of view because an anisotropic pitch angle distribution will become more isotropic due to scattering.

The Tribble model is a more complex model that attempts to account for a spatially non-uniform magnetic field by integrating the standard JP losses over a Maxwell–Boltzmann magnetic field distribution. The model implemented in the `BRATS` code is a specific version that is the low-field, high-diffusion case (Harwood et al., 2013; Hardcastle, 2013).

Major differences between the models are visible at frequencies higher than the break frequency (ν_b), while at lower frequencies all models are expected to have a spectral index equal to the injection index (α_inj), which describes the initial distribution of the electron population. We tested all the models and found that the final numbers are consistent within 10%. Therefore we report for simplicity only the results obtained by fitting the

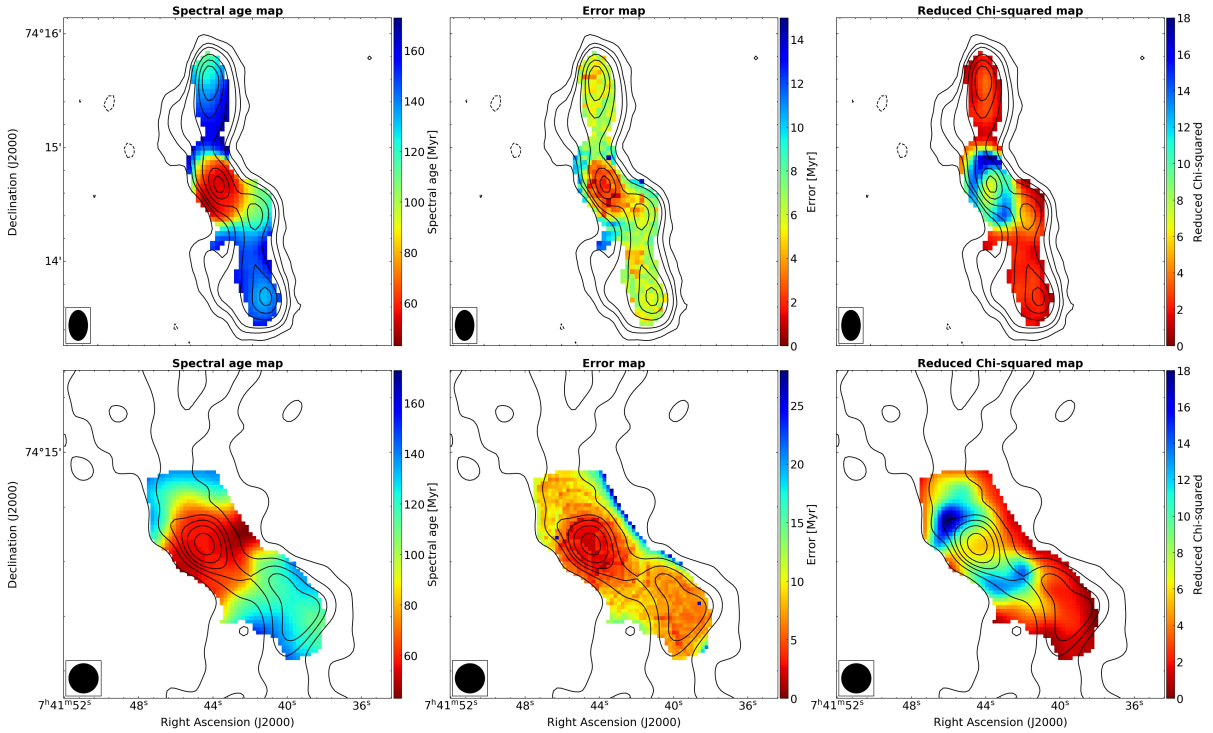

Figure 6.8: Tribble spectral ageing maps (*left*) and corresponding error maps (*middle*) and reduced chi-squared maps (*right*) of the entire source at a resolution of $16'' \times 10''$ (*top panels*) and of the central regions at a higher resolution of $6.5''$ (*bottom panels*). The 325 MHz contours are overlaid. For the fit we set $\alpha_{\rm inj} = 0.75$ and $B_{\rm eq} = 5.9$ μG.

Tribble model, which, as tested on other sources in the literature (e.g. Harwood et al., 2013), provides both a good fit to observations and a more physically realistic description of the source.

We fit the models over a range of injection indices and found that the lowest chi-squared value is obtained with $\alpha_{\rm inj} = 1.5$. This injection index is much steeper than classical values (between 0.5 and 0.7, see e.g. Jaffe & Perola, 1973; Carilli et al., 1991; Komissarov & Gubanov, 1994) and cannot physically be explained with current particle acceleration models. It is also steeper than the highest value found up to now, 1.2 for the cluster-centre radio galaxy 3C28 (Harwood et al., 2015), whose physical interpretation has been attributed to the jet terminating in a weak shock. However, the injection index can also be constrained by the low-frequency spectrum of the regions where particles are accelerated, that is, in the hotspots or jets if the source is an FRII or FRI, respectively. The MHz-frequency part of the spectrum is the least affected by the ageing and can preserve information on the shape of the original energy distribution of the injected particles. We therefore used an injection index of 0.75 for our modelling, which is the lowest spectral index value found in the hotspot of the northern outer lobe in the frequency range 144-325 MHz and is also consistent with values from the literature that were recently found from resolved spectral studies of FRII radio galaxies (0.75−0.85; Harwood et al., 2013, 2015, 017b; Shulevski et al., 2017).

To derive the magnetic field in the outer lobes, we assumed equipartition between particles and magnetic field. To perform this analysis we assumed a power-law particle distribution of the form $N(\gamma) \propto \gamma^{-\delta}$ between a minimum and maximum Lorentz factor of $\gamma_{\rm min} = 100$ and $\gamma_{\rm max} = 10^7$ (Falcke & Biermann, 1995; Reynolds et al., 1996; Dunn et al., 2006). The particle energy power-law index (δ) is related to the injection index by $\delta = 2\alpha_{\rm inj} + 1$. We also assumed that the particle energy was equally divided between

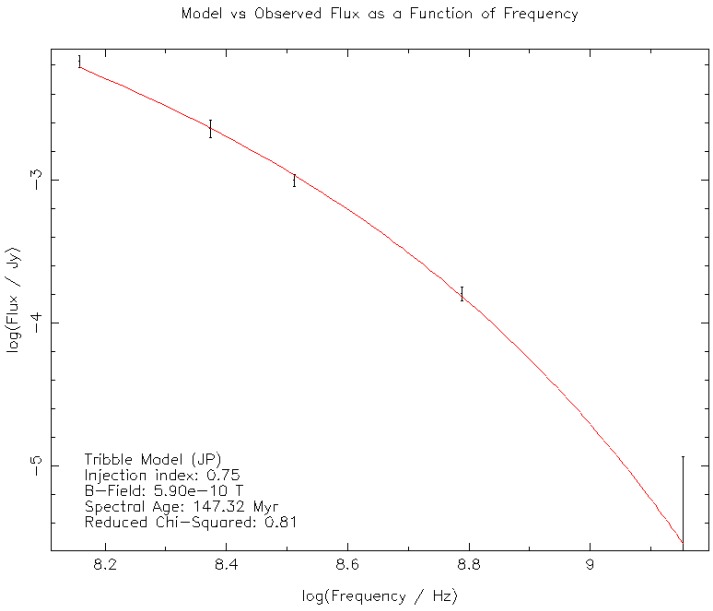

Figure 6.9: Flux density distribution of an example region in the southern outer lobe, fitted with the Tribble model, setting $\alpha_{\rm inj} = 0.75$ and $B_{\rm eq} = 5.9$ μG.

electrons and protons, setting $k = E_{\rm p}/E_{\rm e} = 1$. Finally, we derived the flux density and the volume of the lobes at the LOFAR frequency, approximating the lobe geometry to a prolate ellipsoid with $V = (4\pi/3)ab^2$, where a and b are the semi-major and semi-minor axes, respectively. For the northern lobe $a = 31.5''$ and $b = 24.6''$, while for the southern lobe $a = 27''$ and $b = 26''$. The total flux of the lobes at 144 MHz is 3.3 Jy. For $\alpha_{\rm inj} = 0.75$, we derive a magnetic field strength of $B_{\rm eq} \sim 5.9$ μG, in agreement with the equipartition magnetic field of 4.7 μG derived by Bîrzan et al. (2008).

To derive the age of the intermediate lobe, we used the values of the injection index and magnetic field derived for the outer lobes, and we repeated the fit on the high-resolution images of the source. In Fig. 6.8 we show the spectral age map, error map, and chi-squared map of the whole source (*upper panels*) and of the high-resolution zoom on the central regions (*bottom panels*). The results of the fit are reported in Table 6.7, while in Fig. 6.9 we show one representative spectral plot of a well-fitted single region in the southern outer lobe for the purpose of illustration.

We can reconstruct the first phase of jet activity from the ages obtained in the outer lobes. The oldest age found in the lobes represents the total age of the source, while the youngest age represents the OFF time, that is, the time elapsed since the last particle acceleration in the outer lobes. Consequently, we can estimate the duration of the first active phase (ON time) as the difference between the oldest and the youngest age found in the outer lobes: $t_{\rm ON} = t_{\rm max} - t_{\rm min}$, following the approach in Shulevski et al. (2017) and Brienza et al. (2020). The total age, OFF age, and ON age for the northern and southern outer lobes are reported in Table 6.7.

To estimate the spectral age of the intermediate lobe, we refer to the high-resolution spectral age map shown in the bottom panels of Fig. 6.8. However, this region shows only a slight age gradient from the hotspot towards the centre that is not significant enough to obtain robust values for the oldest and youngest age, due to both resolution and the presence of different components (southern outer lobe, intermediate lobe, and central emission). Therefore we can only give an estimate of the duration of the second phase of jet activity and cannot distinguish between the active and off time.

To complete the spectral age study of MS0735, we also considered a second category of models that assumed a continuous injection of particles: the continuous injection (CI),

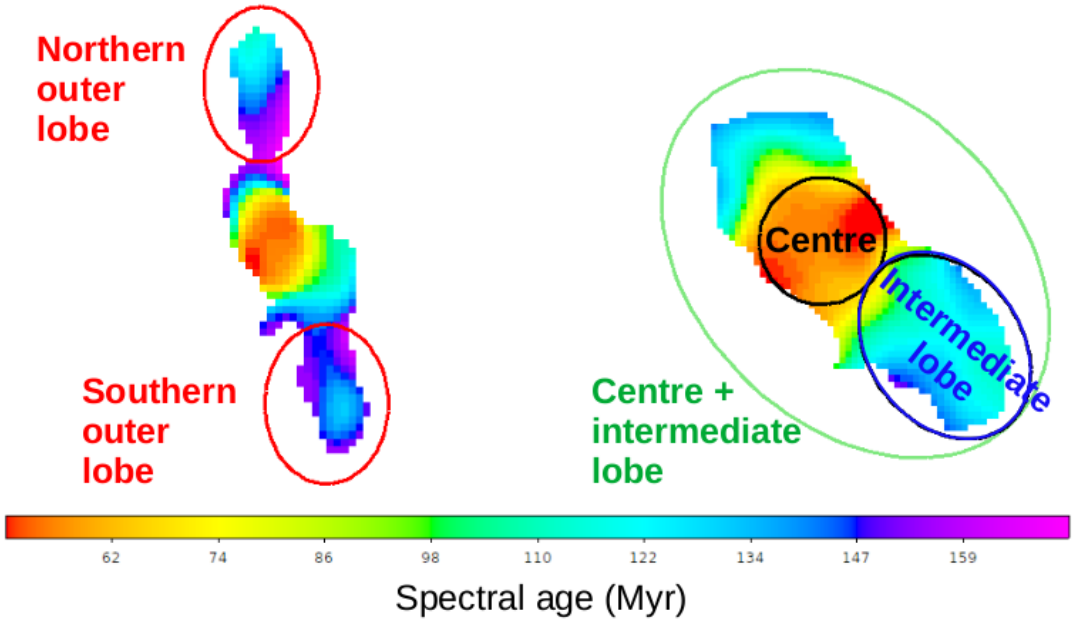

Figure 6.10: Representation of the regions used to measure the integrated flux density of the main features of the source, selected based on their age. The flux density of the outer lobes is measured from the low resolution images, while we used the higher resolution images to measure the flux of the centre and of the intermediate lobe.

and the so-called CIoff models (Pacholczyk, 1970; Komissarov & Gubanov, 1994). With respect to single-injection models, the source in the CI models is fuelled at a constant rate by the nuclear activity for a duration $t_{\rm ON}$ (the 'continuous injection phase'). In this phase the radio spectrum presents a first break frequency that depends on the total age of the source $t_{\rm tot}$:

$$\nu'_{\rm break} \propto \frac{B}{(B^2 + B^2_{\rm CMB})^2 t^2_{\rm tot}}, \tag{6.1}$$

where $B_{\rm CMB} = 3.18(1+z)^2$ is the inverse-Compton equivalent magnetic field. Below and above $\nu'_{\rm break}$ the spectral indices are $\alpha_{\rm inj}$ and $\alpha_{\rm inj} + 0.5$, respectively.

While in the CI model the source is continuously fuelled by fresh particles, in the CIoff, at the time $t_{\rm ON}$, the power supply of the nucleus is switched off and a new phase of duration $t_{\rm OFF}$ begins (the 'dying phase'). A new break frequency then appears beyond which the radiation spectrum drops precipitously,

$$\nu''_{\rm break} = \nu'_{\rm break} \left(\frac{t_{\rm tot}}{t_{\rm OFF}} \right)^2, \tag{6.2}$$

with $t_{\rm tot} = t_{\rm ON} + t_{\rm OFF}$. Thus, the CIoff model is described by four parameters: the injection index, the two break frequencies, and the normalization. As in the JP model, the synchrotron and inverse-Compton losses are modelled using a continuously isotropized pitch angle.

These models are applicable only if the injected particles are confined to the fitted regions, so we can fit them only to the integrated flux of selected regions, shown in Fig. 6.10.

We selected different sub-regions within the 'Centre + intermediate lobe' region depicted in Fig. 6.10, in order to determine whether the intermediate lobe is still being fuelled by the jet. The integrated flux densities for these regions are presented in Fig.

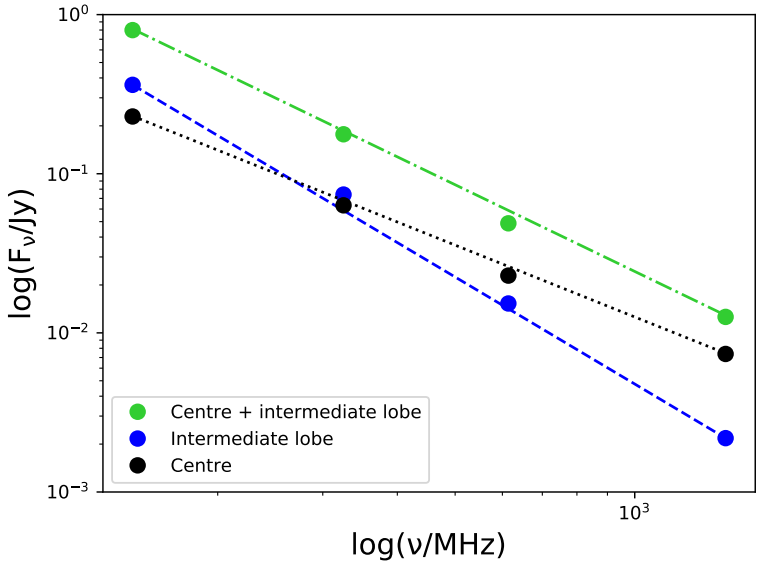

Figure 6.11: Integrated flux density as a function of frequency for the central regions shown in Fig. 6.10. The centre region is represented with the black dotted line; the intermediate lobe with the blue dashed line, and the total flux of these regions with the green dash-dotted line. In all the cases, the spectra show no evidence of curvature and/or spectral breaks; they are well-described by a power-law with a slope of $\alpha = 1.5$ for the centre, $\alpha = 2.23$ for the intermediate lobe and $\alpha = 1.79$ for centre + intermediate lobe. The size of the points represents the dimension of the flux density error.

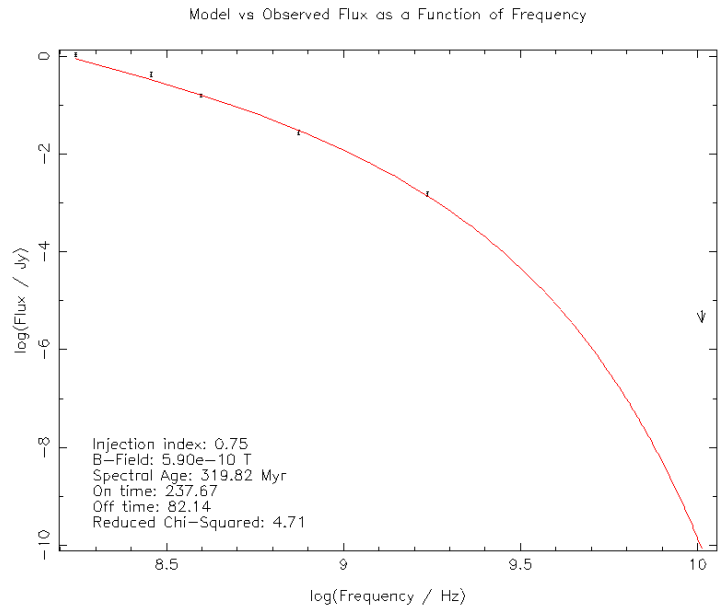

Figure 6.12: Results of the CIoff model fit on the northern outer lobe, using $\alpha_{\rm inj} = 0.75$.

Table 6.7: Tribble and CIoff fitting results and correction for adiabatic expansion.

$\alpha_{\rm inj} = 0.75$ $B_{\rm eq} = 5.9$ μG											
		Tribble model					CIoff model				
Region	Age	$\nu_{\rm break}$ [MHz]	t [Myr]	$\nu_{\rm break}^{\rm corr}$ [MHz]	$t^{\rm corr}$ [Myr]	$\chi^2_{\rm red}$	$\nu_{\rm break}$ [MHz]	t [Myr]	$\nu_{\rm break}^{\rm corr}$ [MHz]	$t^{\rm corr}$ [Myr]	$\chi^2_{\rm red}$
Northern outer lobe	Tot	159	170 ± 6	413	106 ± 4	1.04	13.6	475 ± 200	0.8	2369 ± 800	4.71
	Off	347	115 ± 7	902	71 ± 4	1.95	466	81 ± 1	28	405 ± 4	–
	On	–	55 ± 15	–	35 ± 8	–	–	394 ± 201	–	1964 ± 804	–
Southern outer lobe	Tot	166	163 ± 7	481	98 ± 4	1.09	10.2	548 ± 200	0.6	2770 ± 800	5.68
	Off	259	133 ± 6	751	78 ± 4	2.52	473	80 ± 1	28	405 ± 4	–
	On	–	30 ± 15	–	20 ± 8	–	–	468 ± 201	–	2365 ± 804	–
Intermediate lobe	Tot	308	122 ± 7	431	103 ± 6	2.60	–	–	–	–	–

Notes. The break frequency ($\nu_{\rm break}$) and the synchrotron age (t) derived from the fitting model, the adiabatic-loss corrected break frequency ($\nu_{\rm break}^{\rm corr}$) and synchrotron age ($t^{\rm corr}$) and finally the reduced chi-squared of the fit ($\chi^2_{\rm red}$). Those parameters are derived for both the total age (Tot), the dying phase (Off) and the active phase (On) of the lobes using two different models (Tribble and CIoff), setting $\alpha_{\rm inj} = 0.75$ and $B_{\rm eq} = 5.9$ μG.

6.11. Our results suggest that each sub-region within the inner part of MS0735 is well-described by a single power-law fit, with a slope of $\alpha = 1.5$ for the Centre, $\alpha = 2.23$ for the intermediate lobe and $\alpha = 1.79$ for Centre + intermediate lobe, showing no evidence of a spectral break. This could be explained by ongoing injection of particles, or alternatively through the superposition of various components from different phases. Hence, we can not estimate the spectral ages from the integrated flux densities of these regions.

Conversely, the outer lobes exhibit curved spectra, indicating aged emission, which is consistent with the lack of detection at 8460 MHz (see bottom right panel of Fig. 6.3). We fitted the spectra of the outer lobes using the CI and CIoff models, fixing the injection index to the same values as we used for the resolved spectral study ($\alpha_{\rm inj} = 0.75$ and 1.5). For both outer lobes we find that the CI model does not provide a good fit to the data, while the CIoff model provides a better fit. The particle supply in the outer lobes is expected to have switched off, as both the radio and X-ray data revealed subsequent phases of jet activity. Furthermore, similar to the Tribble model discussed before, the best fit of the CIoff model is obtained with $\alpha_{\rm inj} = 1.5$

The CIoff model fitting results with $\alpha_{\rm inj} = 0.75$ are reported in Table 6.7, while the fit of the northern outer lobe flux density is shown in Fig. 6.12. We note that the reduced chi-squared of this fit ($\chi^2_{\rm red} = 4.71$) is greater than that obtained from the single-region Tribble model fit ($\chi^2_{\rm red} = 2.66$), shown in Fig. 6.9. This is true for all the regions in the outer lobes, as is visible from the map in the top right panel of Fig. 6.8, where the reduced chi-squared value is always lower than 4.

As shown in Table 6.7, our $\alpha_{\rm inj} = 0.75$ fit provides a very low first break frequency ($\nu_{\rm break} \sim 10-15$ MHz) that falls outside the frequency range sampled by our observations. The associated total age of the source ($t \sim 0.5$ Gyr) is therefore very old. Even considering the high uncertainties for this value, the discrepancy with the oldest age derived in the resolved spectral study is very large.

6.3.6 Correction for adiabatic losses

We assumed for the spectral ages derived in the previous section that particles only undergo synchrotron and inverse-Compton energy losses. However, previous X-ray observations have indicated that the cavities filled by the outer lobes were created by low-density bubbles of radio plasma that were inflated by the jet and displaced the surrounding gas by rising buoyantly and expanding adiabatically. Adiabatic losses should therefore be taken into account.

The effect of adiabatic losses is to reduce the particle energy and the magnetic field in radio lobes (Scheuer & Williams, 1968). The shape of the synchrotron spectrum is preserved, but it is shifted towards lower (or higher) frequencies if there is a single (or continuous) injection of particles (Kardashev, 1962; Murgia et al., 1999). The radiative ages estimated from standard models of spectral ageing without considering the adiabatic expansion exceed (or underestimate) the true age of the source if the synchrotron-emitting electrons are generated in a short-term (or continuous injection) event.

The radiative ages estimated in the previous section can be corrected for by multiplying the break frequency with a corrective factor F,

$$\nu^{corr}_{\rm break} = \nu^{obs}_{\rm break} \times F, \tag{6.3}$$

where for a single injection of particles,

$$F = \left(\frac{\Delta^{2n} - 1}{2n} \right)^2, \tag{6.4}$$

Table 6.8: Corrective factors for the adiabatic losses.

Region	p_1 [erg cm^{-3}]	Δ	$F_{\rm Tribble}$	$F_{\rm CIoff}$
Northern outer lobe	7.3×10^{-11}	1.65	2.6	0.06
Southern outer lobe	6.9×10^{-11}	1.67	2.9	0.06
Intermediate lobe	9.5×10^{-11}	1.54	1.4	0.06

while for a continuous injection of particles,

$$F = \frac{1}{4n^2}. \tag{6.5}$$

Here, Δ is the linear expansion factor for a volume of plasma and n is the exponent of the magnetic field variation $B(t) = B_0\Delta^{-n} = B_0(t/t_0)^{-n}$. We set $n = 2$, assuming that the magnetic flux is conserved during the expansion.

Following the procedure of Bîrzan et al. (2008), we calculated Δ as the ratio between the final radius of the bubble at the end of the adiabatic expansion (r_1) and the initial radius of the bubble at the start of the adiabatic expansion (r_0), which we assumed to be the cluster centre. According to the adiabatic expansion law,

$$\Delta = \frac{r_1}{r_0} = \left(\frac{p_1}{p_0}\right)^{-1/3\gamma}, \tag{6.6}$$

where the ratio of specific heats γ is assumed to be 4/3, p_1 is the gas pressure at the location of the X-ray cavity, and $p_0 = 5.4 \times 10^{-10}$ erg/cm^3 is the gas pressure at the centre of the cluster (derived from X-ray observations; see Vantyghem et al., 2014, and Sect. 6.3.2). For the intermediate lobe the detected pressure is less reliable because of the uncertainty about the cavity size and the scatter in the density profile at that distance.

The assumption that the particles are all injected at the central pressure and expand to the current X-ray pressure at each lobe position likely overestimates the adiabatic correction, which is generally modest. This is especially true in our case because the source is at the centre of a cool-core cluster, where the gas pressure is high enough to confine the lobes. This means that the lobes remain luminous for a longer time than remnant lobes in more rarefied environments.

In Table 6.8 we list the pressure at the location of the intermediate and outer cavities (p_1), the linear expansion factor (Δ), and the corrective factors ($F_{\rm Tribble}$ and $F_{\rm CIoff}$) for the two outer lobes and the intermediate lobe. The corrected break frequencies and ages are reported in Table 6.7.

6.4 Discussion

We have studied the peculiar radio source at the centre of the cool-core cluster MS0735. A detailed study of the source in the radio band, together with a re-inspection of the X-ray data, revealed that the source was subjected to at least three different phases of jet activity. From the radio spectrum we derived estimates of the radiative age of the source under different hypotheses in order to reconstruct its duty cycle and to provide an independent comparison with previously established age estimates from the cavities detected in X-rays. We also aimed to estimate the power of the jet to confirm whether the energy released in the ICM during the jet activity is enough to stop the cooling flow, and to verify whether the bubbles are in pressure equilibrium with the surrounding medium.

6.4.1 Spectral ages and duty cycle

A first attempt to derive the spectral age of the source MS0735 was performed by Bîrzan et al. (2008). Because data at only two frequencies were available at the time, it was not possible to derive the break frequency from the integrated spectra of the outer lobes. The spectral age was therefore estimated using the relation of Myers & Spangler (1985), assuming $\alpha_{\rm inj} = 0.5$. The frequency coverage and high resolution of the data presented in this work allowed us to reconstruct the radiative history of the source.

The source MS0735 has experienced at least three different episodes of jet activity throughout its life. The outer lobes, the best known regions of this source, perfectly match the outer cavities and represent the first phase of jet activity visible today. These regions present a very steep and curved spectrum, indicating that particle injection has stopped. We can therefore give an estimate of their age and reconstruct the duty cycle of the first phase of jet activity. From the spectral ageing modelling of the northern outer lobe spectrum we derived that the first outburst started around $t_{\rm tot} = 170 \pm 6$ Myr ago and lasted about $t_{\rm ON} = 55 \pm 15$ Myr before switch-off ($t_{\rm OFF} = 115 \pm 7$ Myr). Similar values are found from the southern outer lobe (see Table 6.7). These numbers were obtained assuming only the presence of synchrotron and inverse-Compton losses and neglecting the adiabatic losses due to the bubble expansion. Therefore the ages reported above could be considered as an upper limit for the true radiative age of the source. The age values of the northern outer lobe corrected for adiabatic losses are $t_{\rm tot} = 106 \pm 3$ Myr, $t_{\rm OFF} = 71 \pm 3$ Myr, and $t_{\rm ON} = 35 \pm 6$ Myr (see Sect. 6.3.6). These values were obtained using an upper limit for the lobe expansion and can therefore been considered as a lower limit to the actual lobe age. In summary, the total age of the outer lobes lies in the range $106\,{\rm Myr} \lesssim t_{\rm tot} \lesssim 170\,{\rm Myr}$, and the first phase of jet activity lasted around $35\,{\rm Myr} \lesssim t_{\rm ON} \lesssim 55\,{\rm Myr}$.

The second phase of jet activity is associated with the intermediate lobe, which also presents an overall steep spectrum, and fills the new discovered intermediate cavity. The age gradient in this region cannot be well constrained because the available resolution is too low. Therefore we only provide an estimate of the start of the second phase of jet activity, which lies in the range $103\,{\rm Myr} \lesssim t_{\rm tot} \lesssim 122\,{\rm Myr}$, depending on the contribution of the adiabatic expansion. We note that these values are comparable with the age of the outer lobes, indicating that jet activity has immediately been reactivated, with an inactivity time of about a few and 10 Myr.

The third phase of the jet activity is represented by the inner lobes, for which we are not able to give an estimate of the age, however, because they are not resolved. The central regions of the source are poorly described by the Tribble model, as indicated by the high chi-squared values we obtained (lower right panel of Fig. 6.8). They result from the likely superposition of particles that were emitted at different times. However, the measurement at high resolution of a central spectral index of 0.75 suggests active jets on scales of some kiloparsec. Furthermore, the detection of inner cavities on the same scale ensures the reactivation of jet activity. The age of the inner cavities could then be used to give a constraint on the duration of the second phase. Based on the age of the southern inner cavity (25−78 Myr, depending on the scenario, Vantyghem et al., 2014) and that of the intermediate lobe, the jet cannot be active for more than $t_{\rm ON} \leq 44 - 78$ Myr.

Overall, our new analysis suggests that the source is going through a very rapid cycle where the central AGN is active most of the time, interrupted only by brief quiescent phases. These several close episodes of jet activity ensure a continuous source of heating to the central gas, preventing it from cooling.

We recall that our discussion of the source age and duty cycle is based on the results of the resolved spectral study, which we consider more reliable. The analysis of the

integrated spectrum has provided less certain results. The total times derived from the fit of the CIoff model are three times higher than those derived from the resolved study and are therefore unrealistic. Furthermore, the chi-squared values of the CIoff fit for the integrated spectra of the outer lobes are higher than those obtained from the Tribble model fit for single regions. Harwood (017a) reported that a discrepancy between the spectral ages derived from integrated and resolved analysis is expected. An integrated study is not able to provide good constraints with respect to the model parameters. Furthermore, the goodness-of-fit is highly dependent on frequency coverage if the spectrum is not well constrained around the spectral break, as is our case for the first break frequency.

When compared with other radio galaxies, the timescales we observe for MS0735 are in accordance with the typical activity time, between dozens and some hundred million years, and the inactivity time is between a few and some dozen million years (e.g. Konar et al., 2013; Orrù et al., 2015; Shulevski et al., 2017; Brienza et al., 2018, 2020; Maccagni et al., 2020). Unfortunately, not many similar studies on radio galaxies at the centre of clusters are available, so we cannot make a direct comparison. The only clusters that were studied are 3C438 and 3C28 (Harwood et al., 2015), which present a single phase of jet activity and are younger (oldest age in the lobes of ~ 4 and ~ 17 Myr, respectively), and 3C388 (Brienza et al., 2020), which instead is a restarted source with a total age of 82 Myr and a longer activity time than the quiescent period, as seen in our source. However, the sample is not large enough to draw general conclusions.

6.4.2 Comparison with X-ray estimates

An independent estimate of the source age was made by Vantyghem et al. (2014) from the X-ray data, providing different timescales for the formation of the outer cavities. We can then compare the total radiative age we derived for the outer lobes with the age derived from X-rays for the corresponding cavities. To our knowledge, no studies of sources in clusters are available in which this type of comparison has been made. It was only performed for a source in a galaxy group (Kolokythas et al., 2020). It is therefore important to understand whether the two estimates are consistent, as Kolokythas and collaborators have found.

Three different timescales were used to derive the age of the cavities: the buoyancy, sound crossing, and refill timescale. In general, the ages calculated using the speed of sound are the shortest, those based on the refilling timescale are the longest, and the buoyancy timescale, which is based on the terminal velocity of the bubbles, lies in between. However, in the case of the outer cavities of MS0735, the terminal velocity is supersonic, so that the buoyancy timescale is the shortest. Neglecting the expansion history of the bubble in the buoyancy timescale therefore underestimates the true cavity age. All timescales are reported in Table 6.9.

When we compared the age estimates of the outer lobes or cavities, we realised that the buoyancy (91 Myr) and sound crossing timescales (120 Myr) are comparable with the derived range of radiative ages (106−170 Myr), while the refilling timescale (240 Myr) is much longer. We note that it appears from the X-ray analysis that the refilling timescale is overestimated because it is longer than the age of the surrounding shock front ($t_{\rm shock} = 110$ Myr), which should be comparable to the true cavity age (Vantyghem et al., 2014). We therefore suggest that the refilling scenario is the least reliable.

A comparison can also be made for the age of the intermediate lobe or cavity. We followed the procedure used by Vantyghem et al. (2014) to compute the three different timescales for this new cavity, reported in Table 6.9. In contrast to the outer lobes, the range of radiative ages that we found for this lobe (103−122 Myr) is comparable to the

Table 6.9: Radio lobe versus X-ray cavity age estimates.

Region	$t_{\rm rad}$ [Myr]	$t_{\rm buoyancy}$ [Myr]	$t_{\rm Cs}$ [Myr]	$t_{\rm refill}$ [Myr]
Northern outer lobe/ Northern outer cavity	106−170	91	120	240
Southern outer lobe/ Southern outer cavity	98−163	110	140	250
Intermediate lobe/ Intermediate cavity	103−122	62-64	53-69	103-120

Notes. For the age of the radio lobe ($t_{\rm rad}$) derived from our analysis we report a range of values. The highest value is derived with a simple radiative Tribble model fit, while the lowest is corrected for adiabatic losses. The three X-ray cavity age estimates are based on the buoyancy timescale ($t_{\rm buoyancy}$), the sound crossing timescale ($t_{\rm Cs}$), and the refill timescale ($t_{\rm refill}$). The southern and northern outer cavity timescales are derived by Vantyghem et al. (2014), while we estimate the timescales for the intermediate cavity reporting a range of values for the different dimensions of the cavity considered.

estimates provided by the refilling scenario.

For the inner cavities, on the other hand, we cannot make comparable statements as we were unable able to estimate the age of the radio emission on the same scale. Overall, we note that the two ways of estimating the age of a source give consistent results. When the radiative age is better constrained, it allows reducing the number of methods for calculating the age of the cavity. However, our results are not sufficient to determine which is the most realistic.

6.4.3 Energetics

In this section we estimate the energetics of the source, starting from the radio properties of the outer lobes. Deriving the total power of the source is important to understand whether the gas heating by AGN is enough to quench the cooling flow in the cluster centre, as is observed from the X-rays. The X-ray analysis of this source has revealed that the energy released by the AGN outburst ($\sim 8 \times 10^{61}$ erg) is enough to quench a cooling flow for several billion years (McNamara et al., 2005; Gitti et al., 2007; Vantyghem et al., 2014). When we take the mean of the buoyancy timescales of the outer cavities ($t \sim 100$ Myr) as an estimate of the cavity age, the mechanical power required to inflate the bubbles is $P = E/t = 1.4 \times 10^{46}$ erg s^{-1}. The same estimate can be performed based on the radio data presented in this work as follows.

It is difficult to estimate the total power of the source because different components contribute to it. First of all, we can compute the total radio luminosity for the outer lobes by integrating the flux between the rest-frame frequencies of 10 and 10000 MHz as

$$L_{\rm rad} = \frac{4\pi D_{\rm L}^2 S_{\nu_0}}{(1+z)^{(1-\alpha)}} \int_{\nu_1}^{\nu_2} (\nu/\nu_0)^{-\alpha} d\nu, \tag{6.7}$$

where we used the flux density measured at 144 MHz as the flux reference (S_{ν_0}), and set the spectral index to $\alpha = 2.9$. This is the value derived in the outer lobes, using our data at 144 MHz and 610 MHz (because this spectral index is probably measured above the break frequency, integrating to low frequency will overestimate the luminosity). We obtain a total radio luminosity of $L_{\rm rad} = 7 \times 10^{43}$ erg s^{-1}.

The energy dissipated into synchrotron radiation is only a minor fraction of the jet power. The bulk of the jet power is converted into energizing the lobes, which contain both relativistic particles and a magnetic field. The total energy is hence given by the sum of these contributions $E_{\rm tot} = (1+k)E_{\rm e} + E_{\rm B}$, where k is the ratio between the energy of

protons and electrons, which we have set equal to one. Both the particle and the magnetic field energy depend on the magnetic field strength, which is difficult to measure, so that an estimate can be derived by invoking minimum-energy arguments. The condition of minimum energy approximately corresponds to energy equipartition between particles and magnetic field. For the equipartition magnetic field strength derived in Sect. 6.3.5, $B_{\rm eq} \sim 5.9$ μG, the minimum energy contained in the lobes is $E_{\rm min} \sim 9 \times 10^{59}$ erg. Furthermore, we can use our estimate of the lobe age to determine the average jet power over the lifetime of MS0735.

Using the total age of northern outer lobe ($t_{\rm tot} = 62 - 170$ Myr), we derive a range for the power $P_{\rm jet} \sim 2 - 5 \times 10^{44}$ erg s^{-1}, which is two orders of magnitude lower than the power derived from the X-rays and comparable with the X-ray bolometric luminosity within the cooling radius (2.6×10^{44} erg s^{-1}), balancing radiative losses. However, we must consider that in our calculation we used the minimum energy inside the lobes, which means that the power that is injected might be larger. Furthermore, neither estimate accounts for the power emitted to drive shocks into the external medium, as observed from X-ray data.

From the minimum energy we can also estimate the minimum pressure inside the lobes, the sum of the contribution of the magnetic field and of the plasma (for a relativistic plasma $p = U/3$, where U is the energy density). This yields $p \sim 2 \times 10^{-12}$ erg cm^{-3}, which is again two orders of magnitude lower than the gas pressure of the external medium derived from the X-rays ($\sim 2 \times 10^{-10}$ erg cm^{-3}). This is clearly unphysical because in this case, the bubbles would collapse under the pressure of the external medium.

In our estimates we considered that the particle energy is equally divided between electrons and protons (k=1) and that the lobes are completely filled with radio plasma (filling factor $\phi = 1$). To reach pressure equilibrium, keeping the equipartition principle valid, we can decrease the filling factor and increase the contribution of the protons. In this case, we would assume $k \geq 2000$ and $\phi \leq 30\%$, generating much higher magnetic field strengths ($B_{\rm eq} \sim 60$ μG) and therefore unrealistic short plasma ages (~ 3 Myr). Furthermore, the strongest evidence that this is not the case is given by the fact that FRII radio galaxies have light jets (Hardcastle et al., 2002; Croston et al., 2004, 2005, 2018). This means that either equipartition does not apply in the outer lobes of MS0735 or that there is additional pressure support (e.g. from entraining of hot thermal gas).

In the case of FRII sources, where it was possible to directly measure the magnetic field strength from observations of inverse-Compton emission, it has been shown that the typical magnetic field strength is a factor 2-3 below the equipartition values (e.g. Croston et al., 2005; Kataoka & Stawarz, 2005; Migliori et al., 2007; Ineson et al., 2017; Turner et al., 2018), suggesting that the lobes contain electron energy densities higher than what is implied by the minimum energy condition. Accordingly, the total energy would be higher than the minimum energy by a factor of about 2 on average. However, the departure from equipartition is not sufficient to provide the solution to the underpressured lobes of MS0735.

In conclusion, additional pressure support is required to keep bubbles in equilibrium. This could be provided by hot thermal gas entrained by the jet, as has been proposed to compensate for the large pressure disparity observed in a few other sources, for example the intermediate FRI/FRII source Hydra A (Croston & Hardcastle, 2014) and the FRII source 3C438 (Harwood et al., 2015). To entrain material, a jet must move slowly, but the material of FRII sources is assumed to remain relativistic up to great distances. However, MS0735 does not show the typical morphology of an FRII, as already noted. A slow-moving jet might therefore provide a solution to both the pressure gap and its atypical morphology.

6.5 Conclusions

We have presented new LOFAR observations of the source MS 0735.6+7421. These data, combined with archival GMRT and VLA data at higher frequencies, allowed us to perform a resolved spectral study of this source, expanding previous work both in frequency range and in resolution. The main results are summarised below.

- Our new LOFAR data show two giant outer radio lobes, much wider than at higher frequencies, with a hotspot at the extremity. These lobes fill the X-ray outer cavities perfectly. There is also evidence of an intermediate lobe south of the core, confirmed by our discovery of a corresponding cavity after a re-inspection of the X-ray data. This means that the source experienced a further phase of jet activity, in addition to the two activities that were known before from a previous analysis of X-ray data.

- Previous work has pointed out the steep spectrum for this source. Our work confirms this result. The spectrum is steep down to 144 MHz both in the outer lobes ($\alpha_{144}^{610} \sim 2.9$) and in the more central regions ($\alpha_{144}^{610} \sim 2.1$). Additionally, the hotspots in the outer lobes show a steep spectral index ($\alpha_{144}^{610} \sim 2.4$), indicating that the particle acceleration mechanisms in these regions has ceased to operate. However, the spectral index flattens at low frequencies to a value of $\alpha_{144}^{235} \sim 0.75$.

- Our high-resolution images of the central emission at 1420 MHz and 8460 MHz show a spectral index of $\alpha_{1420}^{8460} = 0.75 \pm 0.08$. This suggests that within the central component, the actual AGN core and the inner active jets are blended.

- We used single-injection models to estimate the radiative age of the radio lobes and found a total age for the outer lobes in the range 106-170 Myr and for the intermediate lobe in the range 103-122 Myr, depending on the effect of adiabatic losses. We compared radiative ages with X-ray estimates from cavity timescales. The age range of the outer lobes we found agrees well with buoyancy and sound crossing timescales derived from X-rays (Vantyghem et al., 2014).

- We reconstructed the duty cycle of the source, finding that the first phase of jet activity lasted for about $t_{\rm ON} = 35 - 55$ Myr. We also set an upper limit on the duration of the second phase ($t_{\rm ON} \leq 44 - 78$ Myr). The two episodes are separated by a brief quiescent phase of a few million years. The source therefore has a duty cycle close to unity, and the AGN was active for most of the time.

- By comparing the pressure estimates inside the cavities, derived from the minimum total energy and from the thermal gas, we found that additional pressure support, for instance from entraining of hot thermal gas, is necessary to maintain the bubbles.

We have demonstrated the importance of performing a resolved spectral study to reconstruct the duty cycle of a radio source. This is necessary to understand the AGN feedback. With the high resolution and sensitivity reached with the new generation of radio telescopes (LOFAR, the Karl G. Jansky VLA, the uGMRT, and in the near future with the advent of the Square Kilometre Array; SKA), resolved spectral studies will be enabled for an increasing number of sources, allowing us to perform the first statistical studies of these objects. It will also shed new light on the history of very well-known sources such as MS0735.

Thesis conclusions

In the recent years, with the advent of the LOw Frequency ARray (LOFAR), new types of radio sources have been observed. Some were expected from theories and simulations but never detected before, such as radio bridges or ultra-steep spectrum radio halos, while others are unexpected detection. In particular, Mpc-scale diffuse radio emission, typically located in merging clusters, has been surprisingly observed in relaxed cool-core clusters with no signs of major merger. This discovery bridges the long-standing distinction between giant radio halo and mini halo emission in galaxy clusters, thought to originate from different formation mechanisms. Before this Thesis, only four cases where known, while we added here two new discoveries. In this Thesis, I tried for the first time to understand their origin, analysing the dynamic state of the clusters.

This Thesis is dedicated to the study of these peculiar sources, with the aim to characterise their morphological and spectral properties and verify their occurrence. During the PhD, I have calibrated and analysed LOFAR observations at 144 MHz of a sample of 12 cool-core galaxy clusters, selected based on their dynamical properties. The results based on these observations are reported in Chapter 3. One third of the clusters in the sample present cluster-scale diffuse emission. In two cases, we observed this emission for the first time. The diffuse emission in these clusters is characterised by two components: a central mini halo and fainter diffuse emission on larger-scale that resembles a giant radio halo.

These double radio component galaxy clusters experienced a minor merger event, indicated by the presence of cold fronts, X-ray features connected to the sloshing of the cluster core. Diffuse emission in these sources is detected even beyond the sloshing region, overcoming the vision that mini halos are confined by cold fronts. This demonstrates the great potential of LOFAR in detecting the diffuse emission associated with less energetic phenomena.

Thermal and non-thermal emission is strictly connected in these sources, supported by the strong correlations found in MS 1455.0+2232 and RX J1720.1+2638 between the two components, and the spatial coincidence between cold fronts and radio surface brightness discontinuities in A1068 and MS 1455.0+2232.

I complemented LOFAR data with follow-up observations at other frequencies with LOFAR, MeerKAT and uGMRT telescopes, which we have requested and obtained in the last few years. These data allow us to constrain for the first time the spectral index of large-scale emission in three of the four clusters with a double component of radio emission. A detailed study of these sources is reported in Chapters 4 and 5. In two cases, A1068 and RX J1720.1+2638, we detected a difference of spectral index in the two components, with an ultra-steep spectrum in the halo-like component. This result supports the minor merger scenario, where the turbulence induced by a minor merger could accelerate particles on cluster-scales leaving the core of the cluster unperturbed. In

MS 1455.0+2232, instead, a quite uniform spectral index is observed, suggesting another mechanism contributed to the creation of the large-scale emission.

The radio power at LOFAR frequency of the radio halo component is consistent with estimates on giant radio halos observed in merging clusters. For the other sources in the sample, which host a simple mini halo or no diffuse emission, we derived an upper limit to the radio halo power. The values obtained do not allow to exclude the possible presence of large-scale diffuse emission in these sources. Deeper observations are needed to draw firm conclusions.

Finally, the resolution and high sensitivity at low frequency of LOFAR data, allow us to investigate the connection between AGN bubbles and the local environment in the cluster MS 0735.6+7421 (Chapter 6). We reconstructed the duty cycle of the central AGN. The source experienced at least three phases of jet activity, with the AGN being active for most of the time. This ensures the repeated heating of the central gas required to balance cooling.

Future prospects

The results of this Thesis make evident the connection of cluster-scale diffuse radio emission in relaxed clusters and minor merger events. Furthermore, they confirm the great potential of low frequency observations in detecting faint diffuse emission.

One main question is therefore: do all the clusters that underwent a minor merger present this type of emission when observed at low frequency? An answer to this question can be found by observing at low frequency those clusters that show cold fronts or signs of dynamical interaction. The advent of the Square Kilometre Array (SKA) and its precursors will allow to expand the sample including sources in the southern hemisphere.

The sources we have studied do not all have the same characteristics. A larger sample would therefore allow a better comprehension of the particle acceleration mechanisms in relaxed clusters.

Acknowledgements

This Thesis is part of the project DRANOEL (Deciphering RAdio NOn-Thermal Emission on the Largest-scale), financed by the European Research Council (ERC-2016-STG 714245) LOFAR, the Low Frequency Array designed and constructed by ASTRON (Netherlands Institute for Radio Astronomy), has facilities in several countries, that are owned by various parties (each with their own funding sources), and that are collectively operated by the International LOFAR Telescope (ILT) foundation under a joint scientific policy. This research made use of the LOFAR IT computing infrastructure supported and operated by INAF, and by the Physics Dept. of Turin University (under the agreement with Consorzio Interuniversitario per la Fisica Spaziale) at the C3S Supercomputing Centre, Italy. The Jülich LOFAR Long Term Archive and the German LOFAR network are both coordinated and operated by the Jülich Supercomputing Centre (JSC), and computing resources on the supercomputer JUWELS at JSC were provided by the Gauss Centre for supercomputing e.V. (grant CHTB00) through the John von Neumann Institute for Computing (NIC). The scientific results reported in this Thesis are based in part on data obtained from the VLA Data Archive and the GMRT Data Archive. This research has made use of data obtained from the Chandra Data Archive and the Chandra Source Catalog, and software provided by the Chandra X-ray Center (CXC) in the application packages CIAO and Sherpa. This research made use of the following Python packages: APLpy (Robitaille & Bressert, 2012), Astropy (Astropy Collaboration et al., 2013) and NumPy (van der Walt et al., 2011).

Bibliography

Arnaud M., Evrard A. E., 1999, MNRAS, 305, 631

Ascasibar Y., Markevitch M., 2006, ApJ, 650, 102

Astropy Collaboration et al., 2013, A&A, 558, A33

Baldi R. D., Capetti A., Giovannini G., 2015, A&A, 576, A38

Biava N., et al., 2021a, MNRAS, 508, 3995

Biava N., et al., 2021b, A&A, 650, A170

Bîrzan L., Rafferty D. A., McNamara B. R., Wise M. W., Nulsen P. E. J., 2004, ApJ, 607, 800

Bîrzan L., McNamara B. R., Nulsen P. E. J., Carilli C. L., Wise M. W., 2008, ApJ, 686, 859

Bîrzan L., et al., 2020, MNRAS, 496, 2613

Blandford R. D., Königl A., 1979, ApJ, 232, 34

Blasi P., Colafrancesco S., 1999, Astroparticle Physics, 12, 169

Blumenthal G. R., Faber S. M., Primack J. R., Rees M. J., 1984, Nature, 311, 517

Böhringer H., et al., 2010, A&A, 514, A32

Bonafede A., et al., 2014, MNRAS, 444, L44

Bonafede A., et al., 2017, MNRAS, 470, 3465

Botteon A., et al., 2020a, MNRAS, 499, L11

Botteon A., et al., 2020b, ApJ, 897, 93

Botteon A., et al., 2022, A&A, 660, A78

Brienza M., et al., 2018, A&A, 618, A45

Brienza M., et al., 2020, A&A, 638, A29

Briggs D. S., 1995, PhD thesis, "High fidelity deconvolution of moderately resolved sources, New Mexico Institute of Mining Technology, Socorro, New Mexico, USA,

Brocksopp C., Kaiser C. R., Schoenmakers A. P., de Bruyn A. G., 2007, MNRAS, 382, 1019

Brunetti G., Jones T. W., 2014, International Journal of Modern Physics D, 23, 1430007

Brunetti G., Lazarian A., 2011, MNRAS, 412, 817

Brunetti G., Setti G., Comastri A., 1997, A&A, 325, 898

Brunetti G., Setti G., Feretti L., Giovannini G., 2001, MNRAS, 320, 365

Brunetti G., Blasi P., Cassano R., Gabici S., 2004, MNRAS, 350, 1174

Brunetti G., Venturi T., Dallacasa D., Cassano R., Dolag K., Giacintucci S., Setti G., 2007, ApJ, 670, L5

Brunetti G., et al., 2008, Nature, 455, 944

Brunetti G., Cassano R., Dolag K., Setti G., 2009, A&A, 507, 661

Brunetti G., Blasi P., Reimer O., Rudnick L., Bonafede A., Brown S., 2012, MNRAS, 426, 956

Brunetti G., Zimmer S., Zandanel F., 2017, MNRAS, 472, 1506

Burns J. O., 1998, Science, 280, 400

Carilli C. L., Perley R. A., Dreher J. W., Leahy J. P., 1991, ApJ, 383, 554

Cassano R., Brunetti G., Setti G., 2006, MNRAS, 369, 1577

Cassano R., Ettori S., Giacintucci S., Brunetti G., Markevitch M., Venturi T., Gitti M., 2010, ApJ, 721, L82

Cassano R., Brunetti G., Norris R. P., Röttgering H. J. A., Johnston-Hollitt M., Trasatti M., 2012, A&A, 548, A100

Cassano R., et al., 2013, ApJ, 777, 141

Cavagnolo K. W., Donahue M., Voit G. M., Sun M., 2009, ApJS, 182, 12

Cavaliere A., Fusco-Femiano R., 1976, A&A, 500, 95

Cavaliere A., Fusco-Femiano R., 1978, A&A, 70, 677

Chambers K. C., et al., 2016, arXiv e-prints, p. arXiv:1612.05560

Chandra P., Ray A., Bhatnagar S., 2004, ApJ, 612, 974

Churazov E., Brüggen M., Kaiser C. R., Böhringer H., Forman W., 2001, ApJ, 554, 261

Ciotti L., Ostriker J. P., Proga D., 2010, ApJ, 717, 708

Ciotti L., Pellegrini S., Negri A., Ostriker J. P., 2017, ApJ, 835, 15

Cohen A. S., Clarke T. E., Feretti L., Kassim N. E., 2005, ApJ, 620, L5

Crawford C. S., Allen S. W., Ebeling H., Edge A. C., Fabian A. C., 1999, MNRAS, 306, 857

Croston J. H., Hardcastle M. J., 2014, MNRAS, 438, 3310

Croston J. H., Birkinshaw M., Hardcastle M. J., Worrall D. M., 2004, MNRAS, 353, 879

Croston J. H., Hardcastle M. J., Harris D. E., Belsole E., Birkinshaw M., Worrall D. M., 2005, ApJ, 626, 733

Croston J. H., Ineson J., Hardcastle M. J., 2018, MNRAS, 476, 1614

Cuciti V., Cassano R., Brunetti G., Dallacasa D., Kale R., Ettori S., Venturi T., 2015, A&A, 580, A97

Cuciti V., et al., 2021, A&A, 647, A51

Dallacasa D., et al., 2009, ApJ, 699, 1288

De Young D. S., 1984, Phys. Rep., 111, 373

Dennison B., 1980, ApJ, 239, L93

Dolag K., Enßlin T. A., 2000, A&A, 362, 151

Donahue M., Stocke J. T., 1995, ApJ, 449, 554

Donahue M., Stocke J. T., Gioia I. M., 1992, ApJ, 385, 49

Doria A., Gitti M., Ettori S., Brighenti F., Nulsen P. E. J., McNamara B. R., 2012, ApJ, 753, 47

Douglass E. M., Blanton E. L., Randall S. W., Clarke T. E., Edwards L. O. V., Sabry Z., ZuHone J. A., 2018, ApJ, 868, 121

Dunn R. J. H., Fabian A. C., Celotti A., 2006, MNRAS, 372, 1741

Ebeling H., Edge A. C., Mantz A., Barrett E., Henry J. P., Ma C. J., van Speybroeck L., 2010, MNRAS, 407, 83

Eckert D., Finoguenov A., Ghirardini V., Grandis S., Kaefer F., Sanders J., Ramos-Ceja M., 2020, The Open Journal of Astrophysics, 3, 12

Edge A. C., 2001, MNRAS, 328, 762

Enßlin T., Pfrommer C., Miniati F., Subramanian K., 2011, A&A, 527, A99

Ettori S., Donnarumma A., Pointecouteau E., Reiprich T. H., Giodini S., Lovisari L., Schmidt R. W., 2013, Space Sci. Rev., 177, 119

Fabian A. C., 1994, ARA&A, 32, 277

Fabian A. C., 2012, ARA&A, 50, 455

Fabian A. C., Sanders J. S., Taylor G. B., Allen S. W., Crawford C. S., Johnstone R. M., Iwasawa K., 2006, MNRAS, 366, 417

Falcke H., Biermann P. L., 1995, A&A, 293, 665

Fanaroff B. L., Riley J. M., 1974, MNRAS, 167, 31P

Farnsworth D., Rudnick L., Brown S., Brunetti G., 2013, ApJ, 779, 189

Forman W., Jones C., 1982, ARA&A, 20, 547

Fruscione A., et al., 2006, in Silva D. R., Doxsey R. E., eds, Society of Photo-Optical Instrumentation Engineers (SPIE) Conference Series Vol. 6270, Society of Photo-Optical Instrumentation Engineers (SPIE) Conference Series. p. 62701V, doi:10.1117/12.671760

Ghisellini G., Tavecchio F., Foschini L., Ghirlanda G., 2011, MNRAS, 414, 2674

Giacintucci S., Markevitch M., Venturi T., Clarke T. E., Cassano R., Mazzotta P., 2014a, ApJ, 781, 9

Giacintucci S., Markevitch M., Brunetti G., ZuHone J. A., Venturi T., Mazzotta P., Bourdin H., 2014b, ApJ, 795, 73

Giacintucci S., Markevitch M., Cassano R., Venturi T., Clarke T. E., Brunetti G., 2017, ApJ, 841, 71

Giacintucci S., Markevitch M., Cassano R., Venturi T., Clarke T. E., Kale R., Cuciti V., 2019, ApJ, 880, 70

Giacintucci S., Markevitch M., Johnston-Hollitt M., Wik D. R., Wang Q. H. S., Clarke T. E., 2020, ApJ, 891, 1

Giles P. A., et al., 2017, MNRAS, 465, 858

Giovannini G., Bonafede A., Feretti L., Govoni F., Murgia M., Ferrari F., Monti G., 2009, A&A, 507, 1257

Gitti M., Feretti L., Schindler S., 2005, in American Astronomical Society Meeting Abstracts. p. 177.13

Gitti M., McNamara B. R., Nulsen P. E. J., Wise M. W., 2007, ApJ, 660, 1118

Gitti M., O'Sullivan E., Giacintucci S., David L. P., Vrtilek J., Raychaudhury S., Nulsen P. E. J., 2010, ApJ, 714, 758

Gitti M., Nulsen P. E. J., David L. P., McNamara B. R., Wise M. W., 2011, ApJ, 732, 13

Govoni F., Enßlin T. A., Feretti L., Giovannini G., 2001, A&A, 369, 441

Govoni F., Murgia M., Markevitch M., Feretti L., Giovannini G., Taylor G. B., Carretti E., 2009, A&A, 499, 371

Govoni F., et al., 2019, Science, 364, 981

Hao J., et al., 2010, ApJS, 191, 254

Hardcastle M. J., 2013, MNRAS, 433, 3364

Hardcastle M. J., Croston J. H., 2020, arXiv e-prints, p. arXiv:2003.06137

Hardcastle M. J., Alexander P., Pooley G. G., Riley J. M., 1998, MNRAS, 296, 445

Hardcastle M. J., Birkinshaw M., Cameron R. A., Harris D. E., Looney L. W., Worrall D. M., 2002, ApJ, 581, 948

Hardcastle M. J., et al., 2021, A&A, 648, A10

Harris D. E., Dewdney P. E., Costain C. H., McHardy I., Willis A. G., 1988, ApJ, 325, 610

Harwood J. J., 2017a, MNRAS, 466, 2888

Harwood J. J., Hardcastle M. J., Croston J. H., Goodger J. L., 2013, MNRAS, 435, 3353

Harwood J. J., Hardcastle M. J., Croston J. H., 2015, MNRAS, 454, 3403

Harwood J. J., et al., 2017b, MNRAS, 469, 639

Heald G. H., et al., 2015, A&A, 582, A123

Hlavacek-Larrondo J., Fabian A. C., Edge A. C., Ebeling H., Sanders J. S., Hogan M. T., Taylor G. B., 2012, MNRAS, 421, 1360

Hlavacek-Larrondo J., et al., 2013, ApJ, 777, 163

Hodgson T., Bartalucci I., Johnston-Hollitt M., McKinley B., Vazza F., Wittor D., 2021, ApJ, 909, 198

Hogan M. T., et al., 2015, MNRAS, 453, 1201

Hogan M. T., et al., 2017, ApJ, 851, 66

Hota A., et al., 2011, MNRAS, 417, L36

Hudson D. S., Mittal R., Reiprich T. H., Nulsen P. E. J., Andernach H., Sarazin C. L., 2010, A&A, 513, A37

Ignesti A., 2022, New A, 92, 101732

Ignesti A., Brunetti G., Gitti M., Giacintucci S., 2020, A&A, 640, A37

Ineson J., Croston J. H., Hardcastle M. J., Mingo B., 2017, MNRAS, 467, 1586

Intema H. T., 2014, in Astronomical Society of India Conference Series. p. 469 (arXiv:1402.4889)

Intema H. T., Jagannathan P., Mooley K. P., Frail D. A., 2017, A&A, 598, A78

Jaffe W. J., 1977, ApJ, 212, 1

Jaffe W. J., Perola G. C., 1973, A&A, 26, 423

Jones C., Forman W., 1999, ApJ, 511, 65

Józsa G. I. G., et al., 2020, CARACal: Containerized Automated Radio Astronomy Calibration pipeline (ascl:2006.014)

Józsa G. I. G., et al., 2021, MNRAS, 501, 2704

Kaiser C. R., Best P. N., 2007, MNRAS, 381, 1548

Kale R., Shende K. M., Parekh V., 2019, MNRAS, 486, L80

Kapińska A. D., et al., 2017, AJ, 154, 253

Kardashev N. S., 1962, Soviet Ast., 6, 317

Kataoka J., Stawarz Ł., 2005, ApJ, 622, 797

Kellermann K. I., Owen F. N., 1988, Radio galaxies and quasars.. pp 563–602

Kelly B. C., 2007, ApJ, 665, 1489

King I. R., 1972, ApJ, 174, L123

Kokotanekov G., et al., 2017, A&A, 605, A48

Kolokythas K., et al., 2020, MNRAS, 496, 1471

Komissarov S. S., Gubanov A. G., 1994, A&A, 285, 27

Konar C., Hardcastle M. J., Jamrozy M., Croston J. H., 2013, MNRAS, 430, 2137

Laing R. A., 1994, in Bicknell G. V., Dopita M. A., Quinn P. J., eds, Astronomical Society of the Pacific Conference Series Vol. 54, The Physics of Active Galaxies. p. 227

Leccardi A., Rossetti M., Molendi S., 2010, A&A, 510, A82

Lovisari L., et al., 2017, ApJ, 846, 51

Maccagni F. M., et al., 2020, A&A, 634, A9

Mann A. W., Ebeling H., 2012, MNRAS, 420, 2120

Markevitch M., Vikhlinin A., 2007, Phys. Rep., 443, 1

Mazzotta P., Giacintucci S., 2008, ApJ, 675, L9

Mazzotta P., Markevitch M., Vikhlinin A., Forman W. R., David L. P., van Speybroeck L., 2001, ApJ, 555, 205

McDonald M., Gaspari M., McNamara B. R., Tremblay G. R., 2018, ApJ, 858, 45

McMullin J. P., Waters B., Schiebel D., Young W., Golap K., 2007, in Shaw R. A., Hill F., Bell D. J., eds, Astronomical Society of the Pacific Conference Series Vol. 376, Astronomical Data Analysis Software and Systems XVI. p. 127

McNamara B. R., Nulsen P. E. J., 2007, ARA&A, 45, 117

McNamara B. R., O'Connell R. W., 1989, AJ, 98, 2018

McNamara B. R., et al., 2000, ApJ, 534, L135

McNamara B. R., Wise M. W., Murray S. S., 2004, ApJ, 601, 173

McNamara B. R., Nulsen P. E. J., Wise M. W., Rafferty D. A., Carilli C., Sarazin C. L., Blanton E. L., 2005, Nature, 433, 45

McNamara B. R., Kazemzadeh F., Rafferty D. A., Bîrzan L., Nulsen P. E. J., Kirkpatrick C. C., Wise M. W., 2009, ApJ, 698, 594

Meliani Z., Keppens R., Giacomazzo B., 2008, A&A, 491, 321

Meneghetti M., Rasia E., Merten J., Bellagamba F., Ettori S., Mazzotta P., Dolag K., Marri S., 2010, A&A, 514, A93

Migliori G., Grandi P., Palumbo G. G. C., Brunetti G., Stanghellini C., 2007, ApJ, 668, 203

Miley G., 1980, ARA&A, 18, 165

Mitchell R. J., Culhane J. L., Davison P. J. N., Ives J. C., 1976, MNRAS, 175, 29P

Molendi S., Pizzolato F., 2001, ApJ, 560, 194

Murgia M., Fanti C., Fanti R., Gregorini L., Klein U., Mack K. H., Vigotti M., 1999, A&A, 345, 769

Murgia M., Govoni F., Markevitch M., Feretti L., Giovannini G., Taylor G. B., Carretti E., 2009, A&A, 499, 679

Myers S. T., Spangler S. R., 1985, ApJ, 291, 52

Nulsen P. E. J., David L. P., McNamara B. R., Jones C., Forman W. R., Wise M., 2002, ApJ, 568, 163

Nulsen P. E. J., McNamara B. R., Wise M. W., David L. P., 2005, ApJ, 628, 629

Offringa A. R., Smirnov O., 2017, MNRAS, 471, 301

Offringa A. R., de Bruyn A. G., Zaroubi S., 2012, MNRAS, 422, 563

Offringa A. R., et al., 2014, MNRAS, 444, 606

Okabe N., Takada M., Umetsu K., Futamase T., Smith G. P., 2010, PASJ, 62, 811

Omma H., Binney J., Bryan G., Slyz A., 2004, MNRAS, 348, 1105

Orr M. J. L., Browne I. W. A., 1982, MNRAS, 200, 1067

Orrù E., et al., 2015, A&A, 584, A112

Owers M. S., Nulsen P. E. J., Couch W. J., 2011, ApJ, 741, 122

Pacholczyk A. G., 1970, Radio astrophysics. Nonthermal processes in galactic and extragalactic sources

Pearce C. J. J., et al., 2017, ApJ, 845, 81

Peebles P. J. E., Yu J. T., 1970, ApJ, 162, 815

Perley R. A., Butler B. J., 2013, ApJS, 204, 19

Peterson J. R., Fabian A. C., 2006, Phys. Rep., 427, 1

Peterson J. R., Kahn S. M., Paerels F. B. S., Kaastra J. S., Tamura T., Bleeker J. A. M., Ferrigno C., Jernigan J. G., 2003, ApJ, 590, 207

Petrosian V., 2001, ApJ, 557, 560

Petrosian V., Bykov A. M., 2008, Space Sci. Rev., 134, 207

Pfrommer C., Enßlin T. A., 2004, Journal of Korean Astronomical Society, 37, 455

Pfrommer C., Enßlin T. A., Springel V., 2008, MNRAS, 385, 1211

Piffaretti R., Arnaud M., Pratt G. W., Pointecouteau E., Melin J. B., 2011, A&A, 534, A109

Pinzke A., Oh S. P., Pfrommer C., 2017, MNRAS, 465, 4800

Planck Collaboration et al., 2016, A&A, 594, A27

Press W. H., Schechter P., 1974, ApJ, 187, 425

Raja R., et al., 2020, MNRAS, 493, L28

Rajpurohit K., et al., 2021a, A&A, 646, A135

Rajpurohit K., et al., 2021b, A&A, 654, A41

Randall S. W., et al., 2011, ApJ, 726, 86

Randall S. W., et al., 2015, ApJ, 805, 112

Rasia E., et al., 2006, MNRAS, 369, 2013

Rasia E., et al., 2012, New Journal of Physics, 14, 055018

Rasia E., Borgani S., Ettori S., Mazzotta P., Meneghetti M., 2013, ApJ, 776, 39

Reynolds J. E., 1994, ATNF Internal Memo AT/39.3/040, A Revised Flux Scale for the AT Compact Array. Australia Telescope National Facility

Reynolds C. S., Fabian A. C., Celotti A., Rees M. J., 1996, MNRAS, 283, 873

Riseley C. J., et al., 2022, MNRAS, 512, 4210

Robitaille T., Bressert E., 2012, APLpy: Astronomical Plotting Library in Python (ascl:1208.017)

Rossetti M., et al., 2016, MNRAS, 457, 4515

Rossetti M., Gastaldello F., Eckert D., Della Torre M., Pantiri G., Cazzoletti P., Molendi S., 2017, MNRAS, 468, 1917

Ruel J., et al., 2014, ApJ, 792, 45

Sadler E. M., Ekers R. D., Mahony E. K., Mauch T., Murphy T., 2014, MNRAS, 438, 796

Sanders J. S., et al., 2016a, MNRAS, 457, 82

Sanders J. S., Fabian A. C., Russell H. R., Walker S. A., Blundell K. M., 2016b, MNRAS, 460, 1898

Sanders J. S., et al., 2021, arXiv e-prints, p. arXiv:2106.14534

Sanderson A. J. R., Ponman T. J., Finoguenov A., Lloyd-Davies E. J., Markevitch M., 2003, MNRAS, 340, 989

Santos J. S., Rosati P., Tozzi P., Böhringer H., Ettori S., Bignamini A., 2008, in Kodama T., Yamada T., Aoki K., eds, Astronomical Society of the Pacific Conference Series Vol. 399, Panoramic Views of Galaxy Formation and Evolution. p. 375

Sarazin C. L., 1986, Reviews of Modern Physics, 58, 1

Savini F., et al., 2018, MNRAS, 478, 2234

Savini F., et al., 2019, A&A, 622, A24

Scaife A. M. M., Heald G. H., 2012, MNRAS, 423, L30

Scheuer P. A. G., Williams P. J. S., 1968, ARA&A, 6, 321

Schindler S., Castillo-Morales A., De Filippis E., Schwope A., Wambsganss J., 2001, A&A, 376, L27

Schoenmakers A. P., de Bruyn A. G., Röttgering H. J. A., van der Laan H., 2000, MNRAS, 315, 395

Serlemitsos P. J., Smith B. W., Boldt E. A., Holt S. S., Swank J. H., 1977, ApJ, 211, L63

Shimwell T. W., et al., 2017, A&A, 598, A104

Shimwell T. W., et al., 2019, A&A, 622, A1

Shimwell T. W., et al., 2022, arXiv e-prints, p. arXiv:2202.11733

Shulevski A., et al., 2017, A&A, 600, A65

Smirnov O. M., Tasse C., 2015, MNRAS, 449, 2668

Sommer M. W., Basu K., Intema H., Pacaud F., Bonafede A., Babul A., Bertoldi F., 2017, MNRAS, 466, 996

Swarup G., 1990, Indian Journal of Radio and Space Physics, 19, 493

Tadhunter C., 2016, A&A Rev., 24, 10

Tasse C., 2014a, arXiv e-prints, p. arXiv:1410.8706

Tasse C., 2014b, A&A, 566, A127

Tasse C., et al., 2018, A&A, 611, A87

Tasse C., et al., 2021, A&A, 648, A1

Thierbach M., Klein U., Wielebinski R., 2003, A&A, 397, 53

Timmerman R., van Weeren R. J., McDonald M., Ignesti A., McNamara B. R., Hlavacek-Larrondo J., Röttgering H. J. A., 2021, A&A, 646, A38

Tribble P. C., 1993, MNRAS, 261, 57

Turner R. J., Shabala S. S., 2015, ApJ, 806, 59

Turner R. J., Shabala S. S., Krause M. G. H., 2018, MNRAS, 474, 3361

Ubertosi F., et al., 2021, ApJ, 923, L25

Vantyghem A. N., McNamara B. R., Russell H. R., Main R. A., Nulsen P. E. J., Wise M. W., Hoekstra H., Gitti M., 2014, MNRAS, 442, 3192

Venturi T., Giacintucci S., Brunetti G., Cassano R., Bardelli S., Dallacasa D., Setti G., 2007, A&A, 463, 937

Venturi T., Giacintucci S., Dallacasa D., Cassano R., Brunetti G., Bardelli S., Setti G., 2008, A&A, 484, 327

Venturi T., et al., 2017, A&A, 603, A125

Vikhlinin A., Kravtsov A., Forman W., Jones C., Markevitch M., Murray S. S., Van Speybroeck L., 2006, ApJ, 640, 691

Vikhlinin A., et al., 2009, ApJ, 692, 1033

Walker S., et al., 2019, Space Sci. Rev., 215, 7

Wang Y., Knigge C., Croston J. H., Pavlovski G., 2011, MNRAS, 418, 1138

Werner N., et al., 2016, MNRAS, 460, 2752

White D. A., Fabian A. C., 1995, MNRAS, 273, 72

Wilber A., et al., 2018, MNRAS, 473, 3536

Wise M. W., McNamara B. R., Murray S. S., 2004, ApJ, 601, 184

Wise M. W., McNamara B. R., Nulsen P. E. J., Houck J. C., David L. P., 2007, ApJ, 659, 1153

Zandanel F., Pfrommer C., Prada F., 2014, MNRAS, 438, 124

ZuHone J. A., Markevitch M., Brunetti G., Giacintucci S., 2013, ApJ, 762, 78

ZuHone J. A., Brunetti G., Giacintucci S., Markevitch M., 2015, ApJ, 801, 146

de Gasperin F., et al., 2017, Science Advances, 3, e1701634

de Gasperin F., et al., 2019, A&A, 622, A5

de Gasperin F., et al., 2020, A&A, 642, A85

de Gasperin F., et al., 2021, A&A, 648, A104

de Young D. S., 2002, The physics of extragalactic radio sources

van Diepen G., Dijkema T. J., Offringa A., 2018, DPPP: Default Pre-Processing Pipeline (ascl:1804.003)

van Haarlem M. P., et al., 2013, A&A, 556, A2

van Weeren R. J., de Gasperin F., Akamatsu H., Brüggen M., Feretti L., Kang H., Stroe A., Zandanel F., 2019, Space Sci. Rev., 215, 16

van Weeren R. J., et al., 2020, arXiv e-prints, p. arXiv:2011.02387

van Weeren R. J., et al., 2021, A&A, 651, A115

van der Walt S., Colbert S. C., Varoquaux G., 2011, Computing in Science and Engineering, 13, 22